

# Dissipative Particle Dynamics: Theory, algorithms and application to sickle cell anemia

by

Huan Lei

B.Sc., University of Science and Technology of China, P.R.China, 2005

M.Sc., Brown University, RI, 2009

A dissertation submitted in partial fulfillment of the  
requirements for the degree of Doctor of Philosophy  
in the Division of Applied Mathematics at Brown University

PROVIDENCE, RHODE ISLAND

May 2012

Abstract of “Dissipative Particle Dynamics: theory, algorithms and application to sickle cell anemia” by Huan Lei, Ph.D., Brown University, May 2012

Dissipative Particle Dynamics (DPD) is a mesoscopic simulation method, potentially very effective in simulating mesoscale hydrodynamics and soft matter. This thesis addresses open theoretical and algorithmic questions of DPD and demonstrates the new developments with applications to blood flow in health as well as in sickle cell anemia. The first part investigates the intrinsic relation of DPD to the microscopic Molecular Dynamics (MD) method through the Mori-Zwanzig theory. We provide a physical explanation for the dissipative and random forces by constructing a mesoscopic system directly from a microscopic one. The relationship between DPD and MD is quantified and the many-body effect on the hydrodynamics of the coarse-grained system is discussed. We then address algorithmic issues and develop a simple approach for imposing proper no-slip boundary conditions for wall-bounded fluid systems and outflow boundary conditions for open fluid systems. The second part deals with blood flow applications. First, we use DPD and multi-scale red blood cell models to investigate the transition of blood flow from Newtonian to non-Newtonian behavior as the arteriole size decreases. Then, we develop a multi-scale model for the sickle red blood cells (RBCs), accounting for diversity in shapes and polymerization of hemoglobin. Subsequently, we use this model to investigate abnormal rheology and hemodynamics of the sickle blood flow under different physiological conditions. Despite the increased flow resistance, no occlusion was observed in a straight tube under any conditions unless an adhesive dynamics model was explicitly incorporated into our simulations. This new adhesion model includes both sickle RBCs as well as leukocytes. The former interact with the vascular endothelium, with the deformable sickle cells (SS2) exhibiting larger adhesion. The adherent SS2 cells further trap rigid irreversible sickle cells (SS4) resulting in vaso-occlusion in vessels less than  $15\mu m$ . Under inflammation, adherent leukocytes may also trap SS4 cells resulting in vaso-occlusion in even larger vessels.

© Copyright 2012 by Huan Lei

This dissertation by Huan Lei is accepted in its present form  
by the Division of Applied Mathematics as satisfying the  
dissertation requirement for the degree of Doctor of Philosophy.

Date \_\_\_\_\_  
George Em Karniadakis, Director

Recommended to the Graduate Council

Date \_\_\_\_\_  
Martin Maxey, Reader

Date \_\_\_\_\_  
Ming Dao, Reader

Approved by the Graduate Council

Date \_\_\_\_\_  
Peter M. Weber, Dean of the Graduate School

## The Vita of Huan Lei

Born on April 10, 1986 in Hubei, China.

### Education

- M.Sc. in Applied Mathematics, Brown University, May 2009.
- B.Sc. in Special Class for the Gifted Young, University of Science and Technology of China, P.R. China, June 2005.

### Publications

- Direct construction of mesoscopic models from microscopic simulations. H. Lei, B. Caswell, G. E. Karniadakis, *Phys. Rev. E* **81** 026704, 2011.
- Time-dependent and outflow boundary conditions for dissipative particle dynamics H. Lei, D. A. Fedosov, G. E. Karniadakis, *Journal of Computational Physics* **230** 3765, 2011.
- Multiscale modeling of red blood cell mechanics and blood flow in malaria D. A. Fedosov, H. Lei, B. Caswell, S. Suresh, and G. E. Karniadakis, *PLoS Computational Biology* **7** e1002270, 2011.
- Quantifying the biophysical characteristics of sickle anemia blood flow H. Lei, G. E. Karniadakis, *Biophysical Journal*, **102** 185, 2012.
- Predicting the morphology of sickle red blood cell using coarse-grained model of the intracellular aligned hemoglobin polymers H. Lei, G. E. Karniadakis, *Soft Matter* accepted (to appear), 2012.

### Selected conference presentations

- Direct construction of mesoscopic models from microscopic simulations. Discrete Simulation of Fluid Dynamics, Rome, Italy, 2010.

- Occlusion of Small Vessels by Malaria-Infected Red Blood Cells. Division of Fluid Dynamics, APS, Long beach, California, 2010.
- Rheologic and dynamic properties of sickle blood flow. Society of Experimental Mechanics, Uncasville, Connecticut, 2011.
- Dissipative Particle Dynamics Modeling of Healthy and Sickle disease Blood Flow in Arterioles and Capillaries. International Congress on Industrial and Applied Mathematics, Vancouver, Canada, 2011.

## Acknowledgments

First of all, I would like to express my deepest gratitude to my advisor, Professor George Karniadakis for his invaluable guidance, support and encouragement during my study at Brown. He is a brilliant scholar and also a wonderful mentor. He led me into the foremost frontier of the research field and gave me the opportunity to work on some of the most challenging problems in this field. While working with him, I am filled with admiration for his profound knowledge, creative thinking and deep understanding in fields of mathematics, scientific computation, physics and biology. His influence has been beyond science, and will be throughout my academic career. It is a great honor for me to be one of his students.

I would like to thank my dissertation committee members, Professor Martin Maxey and Doctor Ming Dao for taking time to read my thesis and give me many valuable suggestions. Professor Martin Maxey is one of the most trusted and respected teacher I have ever met. I learned a lot from the discussions with him on various fluid mechanics problems related to my research work. Doctor Ming Dao provided me lots of important experimental results on sickle red blood cells which inspired my research work on the numerical modeling and simulation of sickle cell anemia. I am very grateful to him for his guidance in this research project.

I want to thank my preliminary examination committee members, Professor Michael Kosterlitz, Professor Dmitri Feldman, Professor Chi-Wang Shu and Professor Chau-Hsing Su. I would also like to thank all the faculty and staff members of the Division of Applied Mathematics, and particularly, Madeline Brewseter, Jean Radican, Laura Leddy and Stephanie Han.

I want to express my great appreciation to all the past and current CRUNCH group members. Special thanks to Dmitry Fedosov, Kyong Min Yeo, Wenxiao Pan, Igor Pivkin, Hyongsu Baek, Xiaoliang Wan, Guang Lin, Zhongqiang Zhang, Yue Yu, Summer Zheng, Xiu Yang, Xuejin Li and Mingge Deng for their support and

help in my graduate study.

I want to thank Dr. Xiaoyan Li for helpful discussion on Chap. 2 and Xin Yi for helpful discussion on Chap. 6 and Chap. 7. Special thanks to Dr. Sarah Du and Dr. Zhangli Peng for sharing their research results and thoughts.

Needless to say, my dear parents have been my warmest spiritual reliance at all times. They raised me for nineteen years and saw me off to a foreign country on the other side of the Earth. Since I first left my home in China seven years ago, I have been unable to take care of them as a son is supposed to do. They have never even mentioned this but directed all their effort and hope in their son's successful future. They were delighted by whatever progress that I made and were anxious for whichever frustration that I endured. There is no way that I can deliver my deepest love and respect to them.

Lastly, I would like to thank my wonderful friends Deqing Sun, Wanchun Wei, Dafei Jin, Heng Xu, Yun Wang, Xiaoyan Li, Lei Yang, Li Gao, Yi Dong, Guanglai Li, Baofeng Zhang, Shubao Liu for all the happiness that they brought to me during the past years, particularly in those fun events: weekend shopping and dining, birthday parties, tennis and badminton games, fishing, hiking ... I will always cherish these moments in my heart.

This thesis work is supported by the NSF grant CBET-0852948 and by the NIH grant R01HL094270.

*Dedicated*  
*to*  
*my father in heavon*

# Contents

<b>Acknowledgments</b>	<b>vi</b>
<b>1 Introduction</b>	<b>1</b>
1.1 Overview of Dissipative Particle Dynamics . . . . .	1
1.2 Background information of sickle cell anemia . . . . .	4
1.3 Outline . . . . .	6
<b>2 Direct construction of Dissipative Particle Dynamics system from microscopic system</b>	<b>8</b>
2.1 Introduction . . . . .	8
2.2 Theoretical background . . . . .	11
2.3 Microscopic model . . . . .	13
2.3.1 Lennard-Jones system . . . . .	13
2.3.2 Simulation Results . . . . .	16
2.4 Coarse Grained Models . . . . .	21
2.4.1 Mean force field approach . . . . .	21
2.4.2 Langevin thermostat approach . . . . .	23
2.4.3 Dissipative Particle Dynamics (DPD) . . . . .	26
2.5 Other potentials . . . . .	34
2.6 Summary and Discussion . . . . .	35

<b>3</b>	<b>No-slip and outflow boundary conditions for Dissipative Particle Dynamics</b>	<b>39</b>
3.1	Introduction . . . . .	39
3.2	DPD method . . . . .	41
3.3	No-slip boundary conditions . . . . .	43
3.3.1	Boundary method . . . . .	43
3.3.2	Numerical verification . . . . .	47
3.4	Outflow boundary conditions . . . . .	53
3.4.1	Boundary method . . . . .	53
3.4.2	Simulation results . . . . .	56
3.5	Summary and Discussion . . . . .	68
<b>4</b>	<b>Mesosopic simulation of blood flow in small tubes</b>	<b>71</b>
4.1	Introduction . . . . .	71
4.2	Microstructure of blood flow . . . . .	73
4.2.1	Velocity and shear rate distribution . . . . .	73
4.2.2	Cell density and local hematocrit distribution . . . . .	75
4.2.3	Cell deformation and orientation . . . . .	78
4.3	Continuum approximation . . . . .	80
4.3.1	Local shear viscosity . . . . .	80
4.3.2	Continuum approximation with slip boundary velocity . . . . .	83
4.4	Conclusion . . . . .	87
<b>5</b>	<b>A multi-scale model for sickle red blood cell</b>	<b>89</b>
5.1	Introduction . . . . .	89
5.2	Multiscale model . . . . .	92
5.2.1	RBC membrane . . . . .	92
5.2.2	Sickle cell membrane . . . . .	94
5.2.3	Adhesion model . . . . .	96

5.2.4	Scaling of model and physical units . . . . .	97
5.3	Results . . . . .	98
5.3.1	Morphology of sickle red blood cell . . . . .	98
5.3.2	Shear viscosity of SS-RBC suspensions . . . . .	103
5.3.3	SS-RBC suspensions in tube flow . . . . .	108
5.3.4	Effect of the adhesive interaction: a simplified example . . . . .	112
5.4	Discussion . . . . .	116
<b>6</b>	<b>Predicting the heterogeneous morphologies of sickle red blood cells</b>	<b>119</b>
6.1	Introduction . . . . .	120
6.2	Numerical model . . . . .	123
6.2.1	Aligned Hemoglobin Polymer . . . . .	124
6.2.2	Simulation setup and physical parameters . . . . .	126
6.3	Results . . . . .	129
6.3.1	Sickle cell morphology . . . . .	129
6.3.2	Quantifying the cell membrane distortion . . . . .	135
6.4	Discussion . . . . .	142
<b>7</b>	<b>Effects of Adhesion</b>	<b>148</b>
7.1	Introduction . . . . .	148
7.2	Adhesive dynamics of single sickle red blood cell . . . . .	151
7.2.1	Shear flow system . . . . .	151
7.2.2	Static incubation . . . . .	160
7.3	Sickle blood in tube flow . . . . .	163
7.4	Summary . . . . .	177
<b>8</b>	<b>Summary and Perspective</b>	<b>181</b>
8.1	Concluding remarks . . . . .	181
8.2	Future research . . . . .	183

# List of Tables

2.1	Dynamic properties for the MD system with $k_B T = 3.0$ , $N_c = 10$ ; $D$ , $\eta$ and $S_c$ stand for diffusivity, dynamic viscosity, and Schmidt number, respectively. . . . .	20
2.2	Dynamic properties for MD and CG system with $k_B T = 3.0$ , $N_c = 10$	34
4.1	Flow rate $Q$ and maximum flow velocity $U_m$ calculated in DPD simulations and with the <i>Newtonian<sup>S</sup></i> and <i>Newtonian<sup>N</sup></i> models at $H^T = 0.3$ . The slip velocity $U_{slip}$ for the <i>Newtonian<sup>S</sup></i> model is also shown. For each tube size $D$ the pressure gradient $\Delta P/\Delta x$ is fixed. The tabulated values for $D = 20$ and $100 \mu m$ correspond to the velocity profiles of figure 4.8. . . . .	86
5.1	Stretching force (pN) applied on the anchor points for each type of the cell morphology. . . . .	99
5.2	The fitting parameters for the cell membranes with different morphologies. The label “S”, “E” and “G” represent the sickle, elongated and granular shape respectively. The upper label “u” and “l” represent the upper and lower part of the cell surface. The unit of $x$ , $y$ and $z$ is in micrometer. . . . .	103

5.3	The parameters of Eq. (5.13) representing the boundary of cell on the x-y plane, where the surface of the cell membrane is defined. The label “S”, “E” and “G” represent the sickle, elongated and granular shape, respectively. $Z^T$ and $Z^m$ are the average/maximum cell thickness. $\langle C_H \rangle$ is the average value of the mean curvature over the cell surface. $\epsilon$ is the $L_2$ error of the polynomial fitting. . . . .	103
5.4	Simulation (in DPD units) and physical (in SI units) parameters for blood flow with adhesive interaction with vascular endothelium. . . .	114
6.1	Simulation parameters for each type of SS-RBC. The symbol “MCHC” represents mean corpuscular hemoglobin concentration values. The symbol “E”, “S”, “H” and “G” represents the elongated, sickle, holly leaf and granular shape of the SS-RBC. $\mu$ and $\mu_0$ represent the shear modulus of the deoxygenated SS-RBC and healthy RBC respectively. $\theta_0$ and $w$ represent the spontaneous deflection angle and the angular width of the aligned hemoglobin polymer domains, respectively. . . .	138
7.1	Simulation (in DPD units) and physical (in SI units) parameters for blood flow with adhesive interaction with coated ligand particles. . .	154
7.2	DPD simulation parameters for the adhesive dynamics of single sickle red blood cells. . . . .	155

# List of Figures

2.1	A sketch of the force between two clusters. Small spheres represent atomistic particles while shells represent CG particles. The force vectors drawn in the figure correspond to the instantaneous forces obtained from the MD simulation. The total force $\mathbf{F}_{\mu\nu}$ between two clusters is generally not parallel to the radial vector $\mathbf{e}_{\mu\nu}$ . . . . .	15
2.2	Potential of the average pair force scaled by temperature, with $\rho = 0.8$ , $N_c = 10$ , $R_g = 0.95$ (left) and $R_g = 1.4397$ (right). . . . .	17
2.3	Potential of the average pair force scaled by $N_c$ with $k_B T = 3.0$ , $\rho = 0.8$ , $N_c = 10$ , $R_g = 0.95$ (left) and $R_g = 1.4397$ (right). . . . .	17
2.4	Potential of the average pair force for different densities with $N_c = 10$ , $k_B T = 3.0$ , $R_g = 0.95$ (left) and $R_g = 1.4397$ (right). . . . .	18
2.5	Radial distribution function $g(r)$ computed for different temperatures, with $\rho = 0.8$ , $N_c = 10$ , $R_g = 0.95$ and $R_g = 1.4397$ . For the latter case, the three curves coincide. . . . .	19
2.6	Velocity profiles obtained using the periodic Poiseuille flow method. The square and circle symbols represent velocity profiles for $\rho = 0.8$ and $\rho = 0.4$ , respectively. The lines are quadratic fit curves for each case. The body force $g_z$ is added on each atomistic particle; $g_z$ is chosen as 0.02 and 0.005 for $\rho = 0.8$ and $\rho = 0.4$ , respectively. The box size is changed to $30 \times 15 \times 15$ in this test and the temperature is $k_B T = 3.0$ . . . . .	20

2.7	Pressure computed by MD and CG simulations for $N_c = 10$ , $k_B T = 3.0$ with $R_g = 0.95$ and $R_g = 1.4397$ . . . . .	22
2.8	Radial distribution function of the coarse-grained particles for $\rho_c = 0.08$ and $\rho_c = 0.04$ , with $R_g = 0.95$ (left) and $1.4397$ (right). The lines denote the MD simulation results. The symbols correspond to MD simulations. . . . .	23
2.9	Computation of the Langevin thermostat coefficient. (a-b): Time correlation of the velocity and random force on each cluster for $\rho = 0.8$ , $N_c = 10$ , $k_B T = 3.0$ . The solid line denotes ensemble correlation of the x-component of total random force on a cluster. The dashed line denotes the velocity correlation of the x-component. (c-d): Time integration of correlation defined by $\gamma(t) = \beta \int_0^t \langle \delta F_{\mu x}^Q(0) \delta F_{\mu x}^Q(t-s) \rangle ds$ . The result converges when $t \approx 3.0$ for $R_g = 0.95$ and $t \approx 15.0$ for $R_g = 1.4397$ . . . . .	24
2.10	Upper: Time correlation of the pairwise random force between two clusters for $\rho = 0.8$ , $N_c = 10$ , $k_B T = 3.0$ , with (a) $R_g = 0.95, r = 2.65$ and (b) $R_g = 1.4397, r = 2.25$ . The solid line is the radial part and the dash line is the perpendicular part. The velocity correlation function decays slower than the random force as shown. Lower: time integration of the correlation function with (c) $R_g = 0.95, r = 2.65$ and (d) $R_g = 1.4397, r = 2.25$ . . . . .	30
2.11	Radial and shear friction coefficients for $R_g = 0.95$ ; the solid line is a fit to: (a) $\rho_c = 0.08$ , $\gamma_{\parallel}(r) = a(1 - r/b)^4$ , where $a = 1.06 \times 10^3$ , $b = 3.6$ ; $\gamma_{\perp}(r) = a(1 - r/b)^3$ , where $a = 80.1$ , $b = 3.5$ (b) $\rho_c = 0.08$ ; $\gamma_{\parallel}(r) = a(1 - r/b)^4$ , where $a = 0.97 \times 10^3$ , $b = 3.6$ , $\rho = 0.4$ ; $\gamma_{\perp}(r) = a(1 - r/b)^3$ , where $a = 35.6$ , $b = 3.5$ . . . . .	31

2.12	Mean square displacement of the clusters and CG particles for different densities with $R_g = 0.95$ (left) and $R_g = 1.4397$ (right); $N_c = 10$ , $k_B T = 3.0$ . . . . .	32
2.13	Velocity correlation function of the clusters and CG particles for different densities with $R_g = 0.95$ (left) and $R_g = 1.4397$ (right); $N_c = 10$ , $k_B T = 3.0$ . . . . .	32
2.14	Velocity profile for periodic Poiseuille flow method for MD and DPD model. Body forces $f_{MD}$ and $f_{CG}$ are applied on each MD and CG particle, respectively. Upper: $R_g = 0.95$ , $\rho = 0.4$ , $f_{MD} = 0.005$ , $f_{CG} = 0.05$ ; $R_g = 0.95$ , $\rho = 0.8$ , $f_{MD} = 0.02$ , $f_{CG} = 0.2$ . Lower: $R_g = 1.4397$ , $\rho = 0.4$ , $f_{MD} = 0.01$ , $f_{CG} = 0.1$ ; $R_g = 1.4397$ , $\rho = 0.8$ , $f_{MD} = 0.02$ , $f_{CG} = 0.4$ . . . . .	33
2.15	Left: Effective potential $V_{eff}(r)$ obtained from the pair distribution function of MD simulation and mean field potential $\langle V(r) \rangle$ obtained from Eq. 2.14 with $R_g = 1.2$ , $k_B T = 3.0$ , $N_c = 10$ and $\rho = 0.8$ . $V_{eff}(r)$ shows an artificially longer tail compared with $\langle V(r) \rangle$ . Right: Pair distribution function measured by MD, $V_{eff}(r)$ and $\langle V(r) \rangle$ . . . . .	36
2.16	Velocity correlation function (left) and mean square displacement (right) measured by MD, effective potential $V_{eff}(r)$ and mean field potential $\langle V(r) \rangle$ for $R_g = 1.2$ , $k_B T = 3.0$ , $N_c = 10$ and $\rho = 0.8$ . . . . .	36
3.1	A sketch of the shear flow illustrated by DPD particles. The arrows represent the magnitude and direction of the particles' average velocities. The solid line represents a reference plane for the target particle while the total interaction of the target particle with the DPD particles below the reference plane (the gray area) is calculated using Eq. (3.8). . . . .	43

3.2	The dissipative force coefficient for a single DPD particle in shear flow with respect to the distance to the reference plane calculated by Eq. (3.10). . . . .	44
3.3	Left: velocity profile of the plane Couette flow. Right: density and temperature profiles. The triangle symbols represent the numerical results by DPD using Eq. (3.13). The circle symbols correspond to the numerical results by Eq. (3.13) without the random force term. The diamond symbols show the numerical results by the adaptive boundary method used in [49]. The solid lines are the analytical solution.	47
3.4	Left: velocity profiles of the sudden start-up of Couette flow at different times. The symbols correspond to the simulation results, while the solid lines represent the analytical solution of the Navier-Stokes equation. Right: instantaneous temperature of the system at different times. . . . .	49
3.5	Velocity profiles of the oscillatory Stokes flow at times $t = \frac{k}{10}T$ , where $k = 0, 1, 2, \dots, 7$ and $T$ is the oscillation period. The symbols are the numerical results, while the solid lines represent the analytical solution given in Eq. (3.14). . . . .	50
3.6	Left: velocity profiles of the flow driven by an oscillating pressure gradient. The symbols, from the bottom to the top, correspond to the simulation results obtained at $t = \frac{k}{4}T$ , where $k$ equals to 1, 0, 2, 3. The solid lines represent the exact solution for the Womersley flow given in Eq. (3.15). Right: instantaneous temperature of the DPD system at different times. . . . .	51

3.7	A sketch of the domain of an open flow system. The solid lines are the wall boundaries. The plane P represents the inlet through which DPD particles enter the domain with a specified velocity profile. The plane Q represents a pseudo-plane where the flow is fully developed. A and B correspond to two regions adjacent to the plane Q, where the flow is also fully developed. . . . .	52
3.8	Velocity profiles (left) and density profiles (right) of the fully developed Poiseuille flow. The DPD results are shown for the planes $x = 10.0$ and $x = 18.0$ . The solid lines correspond to the analytical solution. . . . .	57
3.9	Pressure profile for the Poiseuille flow along the x direction. The symbols represent the numerical results by DPD extracted at $y = 5$ and $y = 8$ , and the solid line represents the analytical solution. . . .	58
3.10	Streamlines (left) and velocity profiles (right) for backward facing step flow at $Re = 20, 40$ and $60$ . The velocity profiles are extracted at different planes as labeled in the plots. The symbols correspond to the DPD results and the solid lines represent the numerical solution of NS equation. The inset plot in the velocity plot of $Re = 40$ shows normalized recirculation lengths of the step flow as a function of $Re$ number. The square symbols correspond to the DPD results and the triangle symbols are the NS results. . . . .	60
3.11	Pressure profiles for the step flow for Reynolds numbers $Re = 20, 40, 60$ . The symbols represent DPD simulations, while the solid lines correspond to the NS results. . . . .	61

3.12	Top: 2D contour plot of velocity for both x (left) and y (right) directions for a symmetrically bifurcated channel flow obtained by DPD and NS equation. Bottom: 1D plot of the velocity profile at PP', DD', and UU' cuts. The symbols are the DPD results and the solid lines represent the NS results. . . . .	63
3.13	Top: 2D contour plot of velocity for both x (left) and y (right) directions for a non-symmetrically bifurcated channel flow obtained by DPD and NS equation. The flow rates of the two outflow boundaries scale as 1 : 2. Bottom: 1D plot of the velocity profile at PP', DD', and UU' cuts. The symbols are the DPD results and the solid lines represent the NS results. . . . .	65
3.14	Top: 2D contour plot of velocity for both x (left) and y (right) directions for an non-symmetrically bifurcated channel flow obtained by DPD and NS equation. The flow rates of the two outflow boundaries scale as 1 : 3. Bottom: 1D plot of the velocity profile at PP', DD', and UU' cuts. The symbols are the DPD results and the solid lines represent the NS results. . . . .	66
3.15	Pressure distribution along the centerline CC' of the channel shown in Fig. 3.13. The flow rate ratio at the outflow boundaries scales as 1 : 2 (left) and 1 : 3 (right). The solid line corresponds to the NS results. . . . .	67
3.16	The velocity profiles extracted from the Womersley flow with $\Omega = 2\pi/200$ (left) and $\Omega = 2\pi/50$ (right). Left: the solid lines, from top to bottom, represent the theoretical predictions at $t = T/4, 0, 2T/4$ and $3T/4$ . The square and circle symbols represent the numerical results extracted at $x = 10$ and $x = 18$ . Right: the solid lines, from top to bottom, represent the theoretical predictions at $t = T/3, 0, 2T/3$ , the symbols represent the DPD results extracted at $x = 10$ . . . . .	68

4.1	Velocity profiles for $D = 20$ (left) and $100\mu m$ (right) with $H^T = 0.3$ . The blue dash curves represent the parabolic fitting to the simulation results. The data is also fitted with parabolic curves (blue dashed lines) and the tangent lines at the wall with slopes $\tau_w/\mu$ , while the vertical dashed line indicates the cell-free layer thickness. . . . .	74
4.2	Shear rate distributions for blood flow in tubes of various diameters at $H^T = 0.3$ . For $D = 100 \mu m$ the vertical dashed lines indicate: the CFL thickness near the wall, and the limit of the linear portion of the distribution near the centerline. . . . .	75
4.3	Central cut-plane snapshots along the tube axis for $D = 40 \mu m$ ((a) and (b)), and $100 \mu m$ ((c) and (d)) at $H^T = 0.3$ . (a) and (c) are the half-tube images, while (b) and (d) are thin slices across the cut. CFL thickness is shown by dashed lines parallel to the walls. . . . .	76
4.4	Radial RBC-density distributions normalized by the mean prescribed density for $D = 20, 40 \mu m$ (left) and $D = 100, 150\mu m$ (right) for $H^T = 0.3$ . . . . .	77
4.5	Local hematocrit distributions normalized by $H^T$ for $D = 20, 40 \mu m$ (left) and $D = 100, 150\mu m$ (right) for $H^T = 0.3$ . . . . .	78
4.6	Asphericity (left) and cell orientation angle (right) distributions for different tube diameters with $H^T = 0.3$ The horizontal dashed line denotes the equilibrium RBC asphericity equal to approximately 0.15. . . . .	79

4.7	(a): relative viscosity (the cell suspension viscosity normalized by the solvent viscosity) distribution along the radial direction for $D = 20, 40, 100,$ and $150\mu m$ at $H^T = 0.3$ . The dash line represents the separation of the “blood core”, “linear” and the blood plasma region for $D = 150\mu m$ . (b): relative viscosity from the shear-rates distribution. For reference the horizontal dashed line is the plasma viscosity. The vertical dashed line gives the position of the CFL for $D = 150\mu m$ . Experimental values are shown as points. . . . .	82
4.8	The velocity profile of the blood flow for $D = 20, 100\mu m$ . The symbols represent the numerical results obtained by the numerical simulation from the DPD simulation. The dash lines represent the results from the continuum model with slip boundary condition defined by Eq. (4.3) and Eq. (4.7). The dash dot lines represent the results from the continuum model with no-slip boundary condition defined by Eq. (4.11). The vertical dash line represents the position of the slip boundary $R_B = (1 - \delta_2)R$ , where $\delta_2$ defined by Eq. (4.7). . . . .	85
5.1	Left: triangulated mesh of the RBC membrane. The label “A”, “B”, “C” and “D” represents the four anchor points where the stretching force is applied. Right: Successive snapshots of a RBC during the morphological transition to the “sickle” shape. . . . .	95

5.2	Asphericity and elliptical shape factors for the different shapes of the sickle cells. The label “G”, “S” and “E” represents the granular, sickle and elongated shape of the sickle cells respectively, and the inset sketches represent their morphologic projections on the x-z and x-y planes; the inset images represent the experimental observations on different morphologic states of deoxygenated SS-RBC by scanning electron microscopy, reproduced from DK Kaul and H Xue, <i>Blood</i> , 1991 77:1353-1361, by permission. The label “B” corresponds to the original biconcave shape, whose morphological projection is shown in Fig. 5.1. . . . . .	100
5.3	Upper: fitted surface of cell membrane for the sickle shape of SS-RBC. Lower: For illustration purposes, the upper and lower surface is shifted by 1 and $-1$ in the z direction respectively. The blue dots represent the cell vertices obtained from the procedure described in the current work. . . . .	102
5.4	Cell vertices (blue dots) and the fitted surface of the cell membrane for the <i>elongated</i> (upper) and <i>granular</i> (lower) shape of SS-RBC. . . .	102
5.5	Shear viscosity of the healthy blood and SS-RBC suspensions with Hct = 45%. The dash lines represent the fitted curve to the simulation result by $\eta = be^{-a/\gamma^{0.5}} + c$ , where $\gamma$ is the shear rate. $a$ , $b$ and $c$ equal to 1.43, $-6.04$ , $8.78$ for healthy blood and 1.08, $-5.5$ , $23.9$ for deoxygenated SS-RBC suspension. The inset plot shows a snapshot of the “granular” SS-RBCs in shear flow. . . . .	105
5.6	Shear viscosity of the sickle blood flow with different cell morphologies reported in Ref. [87], Hct = 40%. . . . .	107
5.7	Increase of the flow resistance induced by the sickle blood flow for both granular (a) and sickle (b) shapes. The inset plot shows a snapshot of the sickle cells in the tube flow. . . . .	110

5.8	Cell orientation angle distribution $f(\theta)$ for healthy, sickle and granular cells in pipe flow. The cell orientation is defined by the angle $\theta$ between the flow direction ( $x$ ) and the eigenvector $V1$ of the gyration tensor, as shown in the inset plot. The dash lines represent the fitted curves to the simulated results by superimposed gaussian wave functions. For the healthy cell, $f(\theta) = a\theta e^{-b\theta^p} + c$ , where $a = 0.014, b = 0.047, p = 1.4, c = 0.002$ . For the granular cell, $f(\theta) = a_1 e^{-c_1(\theta-b_1)^2} + a_2 e^{-c_2(\theta-b_2)^2}$ , where $a_1 = 0.0315, b_1 = 29.42, c_1 = 0.012, a_2 = 0.033, b_2 = 44.75, c_2 = 0.018$ . For the elongated cell, $f(\theta) = a_1 e^{-c_1(\theta-b_1)^2} + a_2 e^{-c_2(\theta-b_2)^2} + a_3(90 - \theta)e^{-c_3(90-\theta)}$ , where $a_1 = 0.024, b_1 = 53.2, c_1 = 0.021, a_2 = 0.015, b_2 = 70.3, c_2 = 0.015, a_3 = 0.025, c_3 = 0.2$ . The fitting parameters are subject to the constraint $\int f(\theta)d\theta = 1$ . . . . .	111
5.9	Sickle blood flow with adhesive dynamics. The green dots represent the ligands coated on the vessel wall. The blue cells represent the “active” group of sickle cell exhibiting adhesive interaction with the coated ligands. The red cells represent the “non-active” group of cells. Upper: a snapshot showing “active” group of cells flowing into the region coated with “ligands”. Lower: a snapshot of the SS-RBCs with local occlusion state. . . . .	113
5.10	Mean velocity of the sickle blood at different stages of the adhesive dynamics. The red and blue curve correspond to different pressure drop of $8.3 \times 10^4 Pa/m$ and $1.35 \times 10^5 Pa/m$ respectively. . . . .	115

6.1	Sketches of typical cell shapes for deoxygenated SS-RBCs observed in experiments [24]. From left to right, the three sketches represent the “sickle”, “holly leaf” and “granular” shape of SS-RBCs. The various cell morphologic states are mainly determined by the specific intracellular aligned hemoglobin polymer configurations, represented by the solid lines. The dots represent the post-homogeneous nucleus.	121
6.2	$\partial^2 V_{bond}/\partial r^2$ near the equilibrium length $l_0$ .	128
6.3	Upper: successive snapshots of the sickle cell membrane in the different development stages of the intracellular aligned hemoglobin polymer domain with “linear” growth in x-direction. The left sketch demonstrates the coarse-grained model for the aligned hemoglobin polymer domain development: free sickle hemoglobin monomers (green color), represented by the DPD particles, can potentially join with the pre-existed polymers (red color) with probability defined by Eq. (6.4). A linear polymer configuration is adopted in the current case to represent the specific growth direction. Different polymer configurations are adopted to represent the various aligned hemoglobin polymer domains, as shown in Fig. 6.4 and Fig. 6.5. Lower: successive snapshots of the sickle cell with growing aligned hemoglobin polymer domain deflected in the z-direction (normal to the cell), resulting in the classical “sickle” shape.	131
6.4	Successive snapshots of a SS-RBC with intracellular aligned hemoglobin polymer domain of finite angular width. Two polymer branches are used to represent the angular spanning during the domain development. The final cell morphology resembles a “holly leaf” shape.	132

6.5	Successive snapshots of a SS-RBC with intracellular aligned hemoglobin polymer domain of spherulite configuration, where the full domain is filled with sickle hemoglobin polymers due to the high heterogeneous nucleation rate during the growth procedure. The final cell morphology resembles a “granular” shape. . . . .	134
6.6	Final morphologies of the “sickle” (top) and “holly leaf” (bottom) shape of deoxygenated SS-RBC for different values of cell membrane shear modulus. The “sickle” shape of SS-RBC corresponds to low mean corpuscular hemoglobin concentration value (32 g/dL) and the shear modulus of the cells shown above is set to $20\mu_0$ , $40\mu_0$ and $70\mu_0$ according to experimental measurements [76]. The “holly leaf” shape of SS-RBC corresponds to medium mean corpuscular hemoglobin concentration and the shear modulus is set to $30\mu_0$ , $60\mu_0$ and $120\mu_0$ . We have also included a non-symmetric case in the fourth plot representing a cell morphology with the post-homogeneous nucleus off the cell center with shear modulus $60\mu_0$ . . . . .	136
6.7	Instantaneous values of the Asphericity (solid lines) and Elliptical shape factor (dash lines) of the “sickle” SS-RBC as the aligned hemoglobin polymer domain develops. The red curves correspond to SS-RBC with membrane shear modulus $\mu = 30\mu_0$ and deflection angle $\theta_0 = 179^\circ$ . The blue curves represent the SS-RBC with shear modulus $\mu = 60\mu_0$ and $\theta_0 = 178.5^\circ$ . . . . .	137
6.8	ASF and ESF for the various cell morphologies obtained. The label “B”, “G”, “S”, “H” and “E” represents the biconcave, granular, sickle, holly leaf and elongated shape, respectively. The snapshots show the typical cell shapes for each type of SS-RBC morphology obtained in the present study. . . . .	139

6.9	Circular (CSF) and 2D elliptical shape factors (ELSF) for different cell morphologies obtained from both medical image process [73] (red) and present simulations (blue). The circle and square symbols represent the shape factors of the granular and holly leaf SS-RBC. The red inverted triangle symbols represent both the “sickle” and the “elongated” SS-RBC obtained from experiment as they are unclassified in the experiment. The blue inverted triangle symbols represent the simulated “elongated” cells while the blue triangle symbols represent the simulated “sickle” cells. . . . .	141
6.10	Elongated shapes: with further aligned polymerization along the specific direction, the granular cell (left) transforms into an “elongated” cell with the cell center keeping the granular shape (upper right), resembling the non-traditional “elongated” cell observed in Ref. [24]. The lower right plot represents the final cell morphology with the high growth rate imposed only on the upper right direction. . . . .	144
7.1	Successive snapshots of sickle red blood cells in shear flow. Labels (a), (b) and (c) represent a deformable SS2 cell, rigid SS3 cell and ISC, respectively. The arrow represents the flow direction. . . . .	153
7.2	Instantaneous velocity (left) and contact area (right) for the sickle cells in shear flow conditions. Labels (a), (b) and (c) represent the simulation results of deformable discocyte, rigid discocyte and ISC cell, respectively. . . . .	157
7.3	Instantaneous contact area between the sickle cell and the plate coated with adhesive ligands. Labels (a), (b) and (c) represent the simulation results of discocyte with shear modulus $\mu_0$ , $4.0\mu_0$ and $10.0\mu_0$ , respectively. Label (d) represents the case of ISC with shear modulus of $10.0\mu_0$ . . . . .	159

7.4	Adhesive force between a sickle cells and the wall as a function of the membrane rigidity for two cell morphologies. The subplot shows a sketch of the simulation set up, where a uniform lift force is applied on the upper part of an ISC. . . . .	162
7.5	Snapshots of blood cells in a cylinder tube of $D = 10\mu m$ with $H_t = 30\%$ . The blue and red cells represent the SS2 cells and the ISCs, respectively. The subplot (a) represents the steady flow state free of adhesive interaction. Subplots (b-d) represent the snapshots of the blood flow where adhesive interaction is applied to both the SS2 cells and the ISCs. Specifically, (b) represents a snapshot where one SS2 cell adhere to the tube wall; (c) represents a snapshot where more cells adhere to the tube wall; (d) represents a snapshot of the blood occlusion state at the final stage of the simulation. The subplots (e-g) represent the snapshots of the blood flow where adhesive interaction is only applied to the ISCs. The subplot (f) shows a transient adhesion between ISC and the tube wall. Steady flow is recovered as the cell detaches from the tube wall, as shown in (g). . . . .	165
7.6	Instantaneous mean velocity of the blood flow in a cylinder tube of $D = 10\mu m$ containing SS2 cells and ISCs. Adhesive interaction is applied to both cell groups. The inset plots show several snapshots of the blood flow in the simulation. . . . .	166
7.7	Instantaneous mean velocity of the blood flow in a cylinder tube of $D = 10\mu m$ containing SS2 cells and ISCs. Adhesive interaction is only applied to the ISC group. The inset plots show two snapshots of the blood flow in the simulation. . . . .	167

7.8	Snapshots of the red blood cells in a cylinder tube of $D = 10\mu m$ with $H_t = 30\%$ . The blue and red cells represent the SS2 cells and healthy cells, respectively. The subplot (a) represents the steady flow state free of adhesive interaction. The subplots (b-d) represent snapshots of the blood flow where adhesive interaction is applied to the SS2 cell group. The SS2 cells adhere to the tube wall, as shown in the (b) and (c). Healthy cells can squeeze through the adherent sites as shown in (d). . . . .	167
7.9	Instantaneous mean velocity of the blood flow in a cylinder tube of $D = 10\mu m$ containing SS2 and healthy cells. Adhesive interaction is applied to the SS2 cell group. The inset plots show several snapshots of the blood flow in the simulation. . . . .	168
7.10	Instantaneous mean velocity of the blood flow in a cylinder tube of $D = 12\mu m$ , $H_t = 30\%$ . Simulation parameters are similar to the case shown in Fig. 7.6. . . . .	169
7.11	(a) Instantaneous mean velocity of the blood flow in a cylinder tube of $D = 12\mu m$ , $H_t = 45\%$ . Simulation parameters are similar to the case shown in Fig. 7.10. (b) a snapshot of the blood occlusion at the final stage of the simulation. . . . .	170
7.12	(a) Instantaneous mean velocity of the blood flow in a cylinder tube of $D = 13.4\mu m$ , $H_t = 45\%$ . Simulation parameters are similar to the case shown in Fig. 7.10. (b) a snapshot of the blood flow at the final stage of the simulation. . . . .	171
7.13	Instantaneous velocity of a single leukocyte with adhesive bond coefficient $k_s = 100$ (a), $300$ (b), and $1000$ (c), respectively. . . . .	173
7.14	(a) Instantaneous mean velocity of the blood flow in a cylinder tube of $D = 13.4\mu m$ with one leukocyte. (b-d) represent the blood cells in free motion, firm adhesion and flow occlusion states, respectively. . .	175

7.15 (a) Instantaneous mean velocity of the blood flow in a cylinder tube of  $D = 20.2\mu m$  with three leukocytes. (b-d) represent the blood cells in free motion, firm adhesion and flow occlusion states, respectively. . 176

# Chapter 1

## Introduction

### 1.1 Overview of Dissipative Particle Dynamics

The development of numerical modeling and simulation has greatly facilitated our understanding of matter in condensed state. By imposing the “dummy” interaction principles and conservation laws within *local* particles/elements, numerical simulation provides us a convenient tool to probe the evolution of the physical system with microscopic details as well as extract the macroscopic properties of the systems on *global* length scale. Different numerical simulation methods have been developed and applied to study the various physical systems on different length scales. At the atomistic level, the density functional theory (DFT), developed in 1960’s [70, 92] and improved in 1990’s [15], can accurately calculate the ground state of solid matter and has been widely used to study the catalyst effect in material sciences. At the molecular level, the molecular dynamics (MD) method, based on the empirical interaction potential between the atomistic particles, can successfully capture the nucleation process and the following phase transition of super-cooled water system [109]. In the continuum region, numerical methods such as the finite element, spectral element [79] and force coupling method [103, 110] have been widely implemented in the study of solid, fluid and solid/fluid coupled systems.

Besides the physical systems discussed above, many interesting phenomena of condensed matter occur in physical and biological systems on the mesoscopic level, where both the atomistic and continuum methods show limitation on numerical modeling of these systems. On one hand, continuum approximation in general breaks down on this length scale as it fails to capture the anisotropic feature of the local mass and momentum transportation in such systems. On the other hand, full representation of such systems on atomistic level is prohibitively expensive due to the short time scale and large number of the microscopic particles. While the typical time step in atomistic simulation is  $O(1)$  *fs*, many physical processes on this level occur within the time scale  $O(1)$  *s*. Alternatively, several mesoscopic simulation methods such as Brownian Dynamics (BD), Smooth Particle Hydrodynamics (SPH) and Dissipative Particle Dynamics (DPD) have been developed to study the systems on this level. This thesis work mainly focuses on the theory and numerical applications of the DPD method.

Dissipative Particle Dynamics is a Lagrangian based particle method proposed by Hoogerbrugge and Koelman [71] to simulate the complex hydrodynamic processes of isothermal fluid systems. In this method, each DPD particle represents a coarse-grained (CG) virtual cluster of multiple atomistic particles where the particle motion is governed by the soft potential imposed between the DPD particles. Compared with the classical MD method, the computational cost of the DPD simulation is greatly reduced due to the smaller number of simulation particles and the larger computational time step. Moreover, the particle based framework enables us to easily incorporate additional physical features into the systems and extend its application to complex fluid systems such as polymer solutions [43], colloid suspensions [16] and blood flow systems [125, 46], etc.

Different from the classical MD simulation, two additional force terms (dissipative force and random force) appear in the governing equation of the DPD method. The magnitude of the dissipative force between two DPD particles is proportional to their

relative velocities. It represents the energy dissipation from a single DPD particle to its neighbor particles. The random force term, on the contrary, represents the thermal perturbation on a single DPD particle from the surrounding environment. Although the coupling of these two force terms determine the thermal temperature of the fluid systems (following the fluctuation-dissipation theorem), we note that they are not merely the thermostat forces as the ones introduced in the Nose-Hoover thermostat. Instead, theoretical work shows that these two force terms originate from the eliminated atomistic degrees of freedom during the coarse-graining process, see Ref. [115, 153, 90]. Following these studies, one question arises naturally: does there exist a direct mapping between an atomistic system and a DPD system through the coarse-graining process? We address this issue in the first part of the thesis. Starting from an atomistic system, we construct a CG system within the framework of the Mori-Zwanzig theory [115, 153]. Simplification of the CG equations with Markovian approximation results in a force field similar to the DPD formulation. Physical similarities and differences between two systems with different length scales are identified.

Although the DPD systems show intrinsic relationship with the atomistic systems as discussed above, we note that there is no unique relationship between the physical units of the two systems [88, 97]. In practice, the parameters of the DPD force terms are usually chosen such that the fundamental properties (compressibility, kinematic viscosity, *etc.*) of the DPD systems match with the simulated systems. By properly choosing the simulation parameters and imposing correct no-slip boundary conditions [126], the DPD simulations show consistent results with the atomistic/continuum simulations in both periodic and wall bounded systems, *e.g.*, see Ref. [88]. Following this work, in the second part of this thesis, we aim to develop a novel outflow boundary conditions which enables us to simulate fluid systems of multiple outlets with different flow rates.

The third part of this thesis mainly focuses on the development of a multi-scale

model of the sickle red blood cell, which is then used to study the morphological transition of the single cells as well as the abnormal rheology and hemodynamics of the sickle blood flow. Remarkably, sickle cell anemia originates from an abnormal amino acid in the hemoglobin molecule within the erythrocyte, which is on the length scale of  $O(1)$   $nm$ ; on the contrary, the hematological disorder of sickle blood such as vaso-occlusion often occurs on the length scale of  $O(10)$   $\mu m$ . Due to the large span of the length scale, MD simulation would be extremely expensive or even beyond computation capacity for this system. Alternatively, the mesoscale DPD method provides us a convenient tool to probe the biophysical characteristics of this disease with reasonable computational complexity. We present some background information of the sickle cell anemia in the next section.

## 1.2 Background information of sickle cell anemia

Sickle cell anemia is a genetic disease which can cause several types of blood disorder such as vaso-occlusive crisis, splenic sequestration crisis, hemolytic crisis, *etc.* In the United States, this disease mainly affects the Americans of Sub-Saharan African descent with the prevalence of 1 in 500 in the African-American children. According to the National Institutes of Health [1], the average life expectancy of the patients with sickle cell anemia is round 50 years or beyond.

This disease is named by the special “elongated, sickled-shape” cells identified in the blood sample of an American-African patient, as first described by James B. Herrick [67] in 1910. In 1949, Linus Pauling and his colleagues, for the first time, proposed that this disease is attributed to the abnormal hemoglobin molecules within the erythrocyte [123]. Subsequent studies [75] reveal that in the sickle hemoglobin molecule (HbS), the hydrophilic amino acid glutamic acid is substituted by the hydrophobic amino acid valine at the  $\beta - 6$  chain site. In hypoxia conditions, the HbS molecules aggregate into polymerized state, resulting in the distortion of the

cell membranes. This process is well characterized by the double nucleation model proposed by Ferrone *et al.* [51, 52]. According to this model, the formation of a HbS polymer domain is triggered by the homogeneous nucleation of the HbS molecules in bulk solution and proceeds with the explosive growth via polymer elongation and heterogeneous nucleation on the pre-existing HbS polymers. Both the homogeneous and the heterogeneous nucleation rates show extremely high concentration dependence (with power between 40 and 100). Therefore, the intracellular HbS concentration plays a predominant role in determining the final configuration of polymer domain, and therefore has a profound influence on the cell morphology in the deoxygenated state.

Besides the abnormal cell morphology, sickle cell also exhibits elevated cell rigidity due to the intracellular polymerization. This results in the abnormal rheology and hemodynamics of the sickle blood flow. Experimental investigations show that sickle cell suspensions exhibit larger shear viscosity in bulk shear flow systems and elevated apparent viscosity in *ex vivo* microvascular systems.

Remarkably, one of the most important clinical feature of the sickle cell anemia is the vaso-occlusive crisis, as this is the major cause of the morbidity and mortality of the SCD patients. Early studies suspect that the pathophysiology of this crisis is the sickling process of a single cell during the circulation in capillaries. However, subsequent studies indicate that the vaso-occlusion crisis is a far more complicated process incorporating multiple inter-related factors [83, 147].

In this thesis, we develop a multi-scale model of the sickle red blood cell within the framework of the DPD method and use this model to investigate the cell morphological transition, the abnormal rheology as well as the vaso-occlusion crisis introduced above.

## 1.3 Outline

The thesis is organized as follows. In the first two chapters, we discuss the new capabilities of the DPD method. In the third chapter, we use the DPD method to identify the non-Newtonian to Newtonian transition for blood flow. The rest of this thesis is devoted to construct a multi-scale model of the sickle red blood cell and use this model to quantify the biophysical characteristics of the sickle cell anemia.

In chapter 2, we review the DPD method as a coarse-grained (CG) analogue of Molecular Dynamics (MD) and investigate the intrinsic relationship between the MD and DPD method by constructing a mesoscopic system directly from a microscopic system. The dissipative and random force terms are computed using the Markovian approximation. The many-body effect on the coarse-grained force field is identified and discussed.

In chapter 3, we develop a no-slip boundary condition for the wall-bounded DPD fluid systems and an outflow boundary condition for open fluid systems with multiple outlets. The boundary methods are validated by comparing the DPD simulation results with the continuum (Navier-Stokes equation) results.

In chapter 4, we present an application of the DPD method in simulating the blood flow in small vessels. By analyzing the micro-structures and local viscosities of the blood flow, we identify a non-continuum to continuum transition as the tube diameter increases to above  $100\mu m$ .

In chapter 5, we develop a multi-scale model of the sickle red blood cell basing on Dissipative Particle Dynamics, where different cell morphology and membrane properties can be incorporated. We implement this model to study the rheology and hemodynamics of the sickle blood in both shear and tube flow systems.

In chapter 6, we develop a coarse-grained model of the intracellular aligned hemoglobin polymer. We use this model to investigate the morphological transition process of the sickle red blood cells. The heterogeneous cell morphologies are compared with the experimental data using different structural factors (circular shape

factor, elliptical shape factor, *etc.*).

In chapter 7, we use the sickle red blood cell model developed in Chap. 4 to study the vaso-occlusion crisis in sickle cell anemia. By investigating the adhesive capabilities among the heterogeneous cell groups, we identify the specific hemodynamical conditions that trigger the vaso-occlusion conditions. We compare the simulation results with the *ex vivo* experimental observations.

We conclude in chapter 8 with a brief discussion about the future work.

# Chapter 2

## Direct construction of Dissipative Particle Dynamics system from microscopic system

### 2.1 Introduction

Many of the macroscopic phenomena observed for soft matter, such as liquid crystals, polymers, and colloids are consequences of physical processes at the microscopic level. It is usually extremely difficult and even beyond computational capacity to describe these systems at the microscopic level due to the short time scale and the large number of microscopic particles. Alternatively, many coarse-grained methods such as Langevin Dynamics [135], Smooth Particle Hydrodynamics (SPH) [106, 58], and Dissipative Particle Dynamics (DPD) [71] have been proposed to describe systems at mesoscopic scales, in which the force parameters are chosen to match some macroscopic properties, e.g., compressibility [60] or diffusivity [117, 95, 101]. Physically, any system at a certain level of interest can be described by its Hamiltonian, its governing equations and interaction parameters, all deduced from a more fundamental description. At the microscopic level, the long-range term of the Lennard-Jones

potential can be derived from a two-body renormalized dipole-dipole interaction in quantum electrodynamics. Similarly, the coarse-grained (CG) description at the mesoscale level employs a procedure for eliminating the fast microscopic variables of atoms or molecules and deducing the evolution of mesoscopic variables with slower dynamic modes [37]. Therefore, it is of great interest to explore if the parameters of the *effective* forces of the mesoscopic models can be directly evaluated from the microscopic level by a general method.

From the classical Liouville equation, Zwanzig [153] and Mori [115] introduced the projector operator method, which provides the theoretical basis for the coarse-graining procedure. Several studies have been reported on the application of this method to different systems, e.g., the one-dimensional harmonic chain [37], the single tagged particle [149, 138], and the polymer chain [3]. Recently, a more generalized equation of motion for coarse-grained many-body systems was proposed by Kinjo and Hyodo [90], which describes the dynamics of the mesoscopic variables with an explicit relationship to the microscopic description. It can be viewed as a “*priori*” CG equation from which the Langevin Dynamics and Dissipative Particle Dynamics can be derived from different assumptions. The generalized equation of motion consists of three types of forces: the ensemble average *conservative* force, the *random* force reflecting the microscopic fluctuations around the ensemble average force, and the *friction* force determined from the time correlation of the random force. The latter two are the dissipation and noise terms originating from the eliminated degrees of freedom as a consequence of the coarse graining [37].

The *static* properties of the CG system are closely related to the average force field. Extensive studies on this relation have been reported for many different systems [39, 91, 105, 89, 4, 63, 56]. Espanol [39] modeled the DPD particles by grouping several LJ particles into clusters, and derived the conservative force field from the radial distribution function of the clusters. Akkermans and Briels [4] computed the effective force field by minimizing the free energy difference between the CG and

MD systems. Harmandaris *et al.* [63] and Fukunaga *et al.* [56] extracted the effective force field for complex polymers from the distribution functions of the bond length, bending angle and torsion angle. However, much less work has focused on the *dissipative* and *random* forces of the coarse-grained systems, which play a crucial role in determining the dynamic properties of the CG system. To this end, Akkermans and Briels [3] computed the Langevin-type friction force for a single tagged chain. Eriksson *et al.* [35] estimated the dissipative force term of DPD system by the force covariance function. The absence of the dissipation and random terms introduces an ambiguity on the time scale of the CG system, which is typically resolved by matching the diffusivities of the two systems. However, for complex fluid problems such simple matching may not be applicable as more than one dynamic property are involved.

The aim of this chapter is to construct a mesoscopic system of clusters of microscopic particles governed by the Lennard-Jones potential and investigate its behavior. The dissipative and random force as well as the effective mean force are evaluated directly from the microscopic system. Both static and dynamic properties are evaluated in terms of the *reduced* LJ units without re-scaling the time unit between the two systems. Both Langevin and DPD simulations are performed separately depending on the different random force models we choose. In this respect, we expect similar results for both static and dynamic properties between the CG and microscopic simulation results. By such comparisons we expect to gain some insight into the relationship between the two levels of description.

The chapter is organized as follows. In Sec. 2.2, we review the general CG equation proposed by Kinjo and Hyodo, and simplify it with further approximations. In Sec. 2.3, we construct a microscopic model from which we extract the force field for the CG model of the system. In Sec. 2.4, we investigate the CG system governed by the Langevin and the DPD equations of motion and compare the results with MD simulations. In Sec. 2.5, we discuss the effect of different types of CG force fields.

We conclude in Sec. 2.6 with a brief discussion.

## 2.2 Theoretical background

Let us consider a microscopic system with  $N$  particles, each with mass  $m$ . The Hamiltonian of the system is

$$H = \sum_{i=1}^N \frac{\mathbf{p}_i^2}{2m} + \sum_{i<j}^N v(|\mathbf{r}_i - \mathbf{r}_j|), \quad (2.1)$$

where  $\mathbf{p}$  is the particle momentum and  $v(\mathbf{r})$  stands for the potential energy between two atomistic particles. If we divide the system into  $K$  groups with  $N_\mu$  particles in each group, then the Hamiltonian can be rewritten with respect to the coordinate of center of mass (COM) of each group and relative positions of each particle to its group, i.e.,

$$\begin{aligned} H = & \sum_{\mu=1}^K \frac{\mathbf{P}_\mu^2}{2M_\mu} + \sum_{\mu=1}^K \sum_{\mu_i=1}^{N_\mu} \frac{\mathbf{p}'_{\mu_i}{}^2}{2m_{\mu_i}} + \sum_{\mu<\nu}^K V(|\mathbf{R}_\mu - \mathbf{R}_\nu|) \\ & + \sum_{\mu=1}^K \sum_{\mu_i<\mu_j}^{N_\mu} v(|\mathbf{r}'_{\mu_i} - \mathbf{r}'_{\mu_j}|), \end{aligned} \quad (2.2)$$

where  $M_\mu$  is the mass of group  $\mu$ , and  $m_{\mu_i}$  is the mass of  $i$ th particle in group  $\mu$ .  $\mathbf{R}_\mu$  and  $\mathbf{P}_\mu$  denote the position of the COM and the total momentum of the group  $\mu$ , respectively, while  $V(\mathbf{R})$  is the interaction potential between two groups  $\mu$  and  $\nu$ . Also,  $\mathbf{r}'_{\mu_i}$  and  $\mathbf{p}'_{\mu_i}$  are the relative position and momentum, respectively, of  $i$ th particle with respect to the COM of group  $\mu$ , where

$$\mathbf{p}'_{\mu_i} = \mathbf{p}_{\mu_i} - \frac{m_{\mu_i}}{M_\mu} \mathbf{P}_\mu. \quad (2.3)$$

If the system is in the NVT ensemble, Eq. (2.1) and Eq. (2.2) reveal that the atomistic particles and the clusters are coupled with a thermostat at the same temperature.

This is based on the equi-partition theorem, as shown below in Eq. (2.4), noting that the added K quadratic terms in Eq. (2.2) are eliminated by the K constraints implied by Eq. (2.3).

$$\left\langle \frac{\mathbf{P}_i^2}{2m_i} \right\rangle = \left\langle \frac{\mathbf{P}_\mu^2}{2M_\mu} \right\rangle = \frac{3}{2}k_B T. \quad (2.4)$$

Therefore, if we coarse grain the original atomistic system into K clusters, the resulting system will be thermodynamically consistent.

The equation of motion of the CG groups in this system, derived by Kinjo and Hyodo [90], can be approximated by

$$\begin{aligned} \dot{\mathbf{P}}_\mu &= \frac{1}{\beta} \frac{\partial}{\partial \mathbf{R}_\mu} \ln \omega(\mathbf{R}) - \beta \sum_{\nu=1}^K \int_0^t ds \langle [\delta \mathbf{F}_\mu^{\mathcal{Q}}(t-s)] \\ &\quad \otimes [\delta \mathbf{F}_\nu^{\mathcal{Q}}(0)]^T \rangle \frac{\mathbf{P}_\nu(s)}{M_\nu} + \delta \mathbf{F}_\mu^{\mathcal{Q}}(t), \end{aligned} \quad (2.5)$$

where  $\beta = 1/k_B T$  and  $\mathbf{R} \in \mathbb{R}^{3K}$  is a point in the phase space of the CG groups<sup>1</sup>. The three terms on the right-hand-side of Eq. (2.5) represent the average conservative, dissipative, and random forces, respectively. Our objective is to evaluate the three terms directly from a specific microscopic model with further approximations, as discussed below.

Here,  $\omega(\mathbf{R})$  in the first term can be viewed as a normalized partition function of all the microscopic configurations corresponding to point  $\mathbf{R}$  in the CG phase space defined by:

$$\omega(\mathbf{R}) = \frac{\int d^N \hat{\mathbf{r}} \delta(\hat{\mathbf{R}} - \mathbf{R}) e^{-\beta U}}{\int d^N \hat{\mathbf{r}} e^{-\beta U}}, \quad (2.6)$$

where  $U$  is the potential energy of the atomistic system. Therefore, the first term is the ensemble average force on group  $\mu$  over all the microscopic phase points corresponding to a specific CG phase point  $\mathbf{R}$ , denoted as  $\langle \mathbf{F}_\mu \rangle_{\Gamma_S}$ .

---

<sup>1</sup>A point in phase space is  $(\mathbf{R}, \mathbf{P}) \in \mathbb{R}^{6K}$ , but here we neglect the momentum part.

The last term  $\delta\mathbf{F}_\mu^{\mathcal{Q}}(t)$  is the fluctuating force on group  $\mu$ . The second term is the dissipative force, which contains an integral of the memory kernel of the random force. A direct computation of this term is very difficult, even for the 1D harmonic chain [37]. In practice, if the typical time scale of the momentum and random force correlation of the CG cluster is *separable* (e.g., if the correlation function of the velocity decays much more slowly than the correlation function of the random force, as we will show in Sec. 2.4), we can make a Markovian approximation as

$$\left\langle [\delta\mathbf{F}_\mu^{\mathcal{Q}}(t-s)] [\delta\mathbf{F}_\nu^{\mathcal{Q}}(0)]^T \right\rangle = 2\Gamma_{\mu\nu}\delta(t-s), \quad (2.7)$$

$$\int_0^t ds \left\langle [\delta\mathbf{F}_\mu^{\mathcal{Q}}(t-s)] [\delta\mathbf{F}_\nu^{\mathcal{Q}}(0)]^T \right\rangle \frac{\mathbf{P}_\nu(s)}{M_\nu} = \Gamma_{\mu\nu} \frac{\mathbf{P}_\nu(t)}{M_\nu}, \quad (2.8)$$

where the factor 2 in Eq. (2.7) comes from the integration over the delta function from 0, and  $\Gamma_{\mu\nu}$  is the friction matrix defined by

$$\Gamma_{\mu\nu} \equiv \int_0^\infty dt \left\langle [\delta\mathbf{F}_\mu^{\mathcal{Q}}(t)] [\delta\mathbf{F}_\nu^{\mathcal{Q}}(0)]^T \right\rangle. \quad (2.9)$$

Given Eq. (2.7) and (2.8), the general CG Eq. (2.5) can be approximated as a real time equation, i.e, it does not depend on the time history. Hence, each term can be evaluated by microscopic simulation methods, as shown in the next section.

## 2.3 Microscopic model

### 2.3.1 Lennard-Jones system

We employ molecular dynamics (MD) simulation in a  $20 \times 20 \times 20$  box with periodic boundary conditions. We run several different cases but the largest size is 6400 particles governed by the Lennard-Jones (LJ) potential, adjusted to vanish at the

cutoff radius  $r_c$ ,

$$\begin{aligned} v(r) &= v_{\text{LJ}}(r) - v_{\text{LJ}}(r_c), \\ v_{\text{LJ}}(r) &= 4\epsilon \left[ \left(\frac{\sigma}{r}\right)^{12} - \left(\frac{\sigma}{r}\right)^6 \right], \end{aligned} \quad (2.10)$$

where  $r_c$  is  $2.5\sigma$ . All the quantities in this and the following sections are evaluated in the *reduced* LJ units (e.g., the length, mass and energy units are  $\sigma$ , 1,  $\epsilon$  respectively). The particles are grouped into  $K$  clusters with  $N_c$  particles per cluster. The cluster number density is defined as

$$\rho_c = \rho/N_c, \quad (2.11)$$

where  $\rho$  is the number density of the LJ system. For each cluster, the LJ particles are subject to the constraint of constant radius of gyration ( $R_g$ ), i.e.,

$$\frac{1}{N_c} \sum_{i=1}^{N_c} (\mathbf{r}_i^\mu - \mathbf{R}_\mu)^2 = R_g^2 = \text{constant}, \quad (2.12)$$

where  $\mathbf{R}_\mu$  is the COM of the cluster  $\mu$ , as shown in Fig. 2.1. The radius of gyration  $R_g$  is a natural measure of the cluster size. Although the LJ particles may wander across the cluster surfaces, the constraint associates the constituent particles with a specific cluster so that the dynamic properties of the clusters can be evaluated [89]. It defines the inner number density of the atomistic particles inside each cluster

$$\rho_{\text{inner}} = N_c / \frac{4}{3}\pi R_g^3. \quad (2.13)$$

The system was simulated in a NVT ensemble with the Nose-Hoover thermostat and the RATTLE algorithm to deal with the constraints [108, 6]. The time step was varied from  $5 \times 10^{-4}$  to  $10^{-3}$ .

Theoretically, the coarse-grained potential field of the clusters  $U_{CG}(\mathbf{R})$  depends on the  $K$ -body configuration  $\{\mathbf{R}\} \equiv (\mathbf{R}_1, \mathbf{R}_2, \dots, \mathbf{R}_K, \rho_c, T)$ , as does the average force

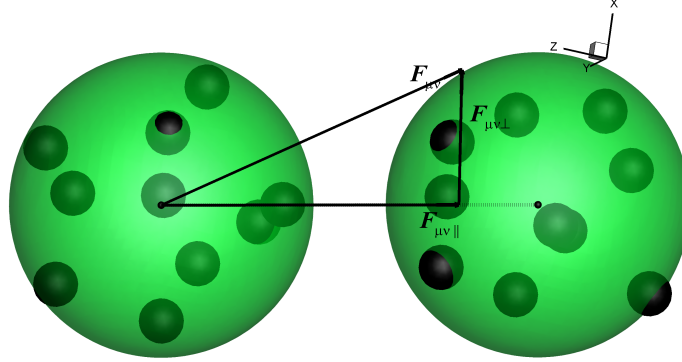


Figure 2.1: A sketch of the force between two clusters. Small spheres represent atomistic particles while shells represent CG particles. The force vectors drawn in the figure correspond to the instantaneous forces obtained from the MD simulation. The total force  $\mathbf{F}_{\mu\nu}$  between two clusters is generally not parallel to the radial vector  $\mathbf{e}_{\mu\nu}$ .

$\langle \mathbf{F}_{\mu} \rangle_{\Gamma_S}$  on cluster  $\mu$ , which is difficult to evaluate directly. If we approximate the mean field force on a single cluster by pair-wise forces with respect to other clusters [89],  $\langle \mathbf{F}_{\mu} \rangle_{\Gamma_S}$  can be simplified as  $\sum_{\nu \neq \mu} \langle f(R_{\mu\nu}) \rangle$ , where  $\langle f(r) \rangle$  is the average pair force between two clusters and can be obtained by the MD simulation with specific cluster density  $\rho_c$  and temperature  $k_B T$ . (We note, however, that this assumption may lead to erroneous results at high densities, as we will discuss later in Sec. 2.4.) To compute the average pair force  $\langle f(r) \rangle$ , we divide the distance between two clusters into several bins with  $dr$  the distance between each bin. Then,  $\langle f(r) \rangle$  is obtained by taking the ensemble average of the radial component of the instantaneous force  $\mathbf{f}_{\mu\nu}$  between two clusters  $\mu$  and  $\nu$ , over all microscopic configurations with the pair distance between  $r - dr/2$  and  $r + dr/2$ , i.e.,

$$\langle f(r) \rangle = \left\langle \mathbf{f}_{\mu\nu} \cdot \frac{\mathbf{R}_{\mu\nu}}{R_{\mu\nu}} \right\rangle_{r-dr/2 < R_{\mu\nu} < r+dr/2}. \quad (2.14)$$

We also introduce the corresponding pair potential of mean force  $\langle V(r) \rangle$  as the spatial

integration of  $\langle f(r) \rangle$ , i.e.,

$$\langle V(r) \rangle = \int_r^\infty \langle f(r') \rangle dr'. \quad (2.15)$$

From the simulations, we found that the average force (potential) field depends on the temperature  $k_B T$ , the radius of gyration  $R_g$ , the number of particle within each cluster  $N_c$ , and the number density of the clusters  $\rho_c$ . We discuss our findings in detail below.

### 2.3.2 Simulation Results

We examine the average pair force  $\langle f(r) \rangle$  for two different values  $R_g = 0.95$  and  $R_g = 1.4397$  (the latter value is chosen so that  $\rho_{inner} \equiv \rho = 0.8$ ). Fig. 2.2 shows the temperature-scaled pair potential  $\beta \langle V(r) \rangle$  for  $\rho_c = 0.08$  and  $N_c = 10$ . Compared to the LJ system, the CG potential field for both  $R_g$  values show softer and temperature-dependent properties. For  $R_g = 1.4397$ , the potential field is similar to the Gaussian chain model [105]. For  $R_g = 0.95$ , the clusters behave more like a “single” LJ particle and therefore the force field is stiffer with a stronger repulsive force and deeper attractive well. With temperature between 2.0 and 5.0, both force fields collapse approximately onto a single curve; this property will be discussed further in conjunction with the results of static properties later in this section.

We also examine the potential field with different number of particle per cluster  $N_c$ , whereas the inner density  $\rho_{inner}$  is the same that at  $N_c = 10$  by choosing the proper value of  $R_g$ . Similar temperature dependence is observed. Moreover, if we scale the potential by  $N_c$  and the distance by  $R_g$ , the potential functions approximately collapse into a single curve, as shown in Fig. 2.3. Based on the results we obtained, we can propose the following scaling:

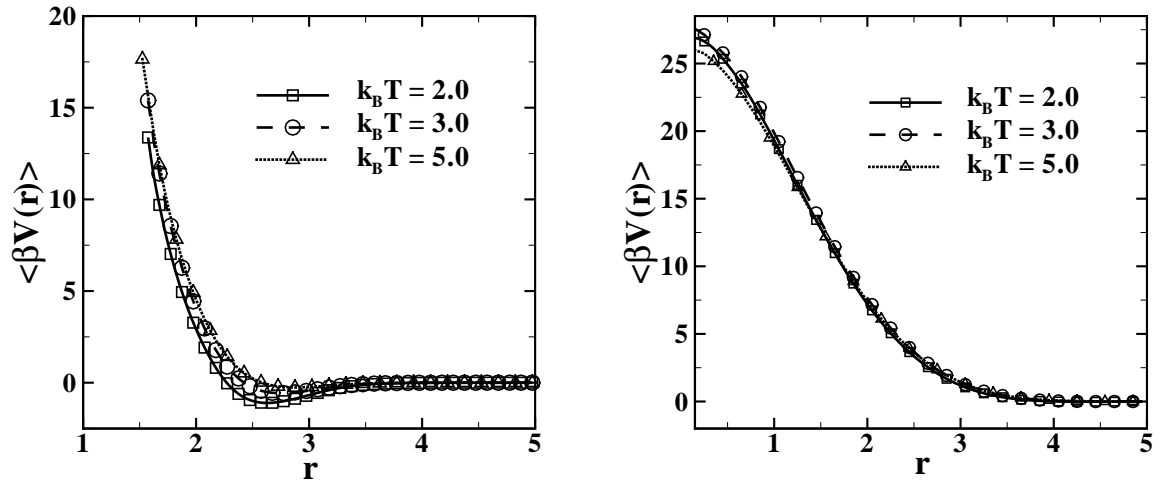


Figure 2.2: Potential of the average pair force scaled by temperature, with  $\rho = 0.8$ ,  $N_c = 10$ ,  $R_g = 0.95$  (left) and  $R_g = 1.4397$  (right).

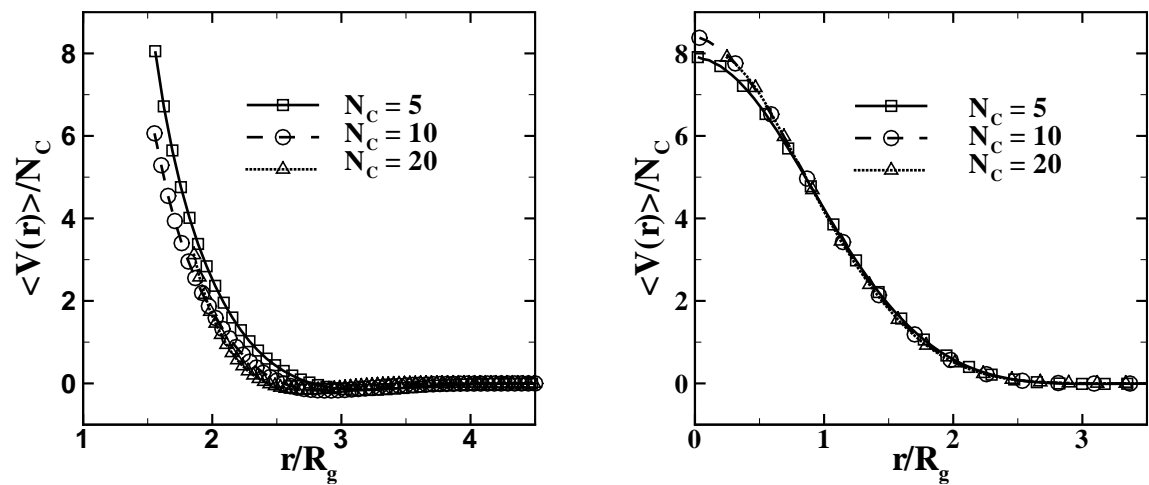


Figure 2.3: Potential of the average pair force scaled by  $N_c$  with  $k_B T = 3.0$ ,  $\rho = 0.8$ ,  $N_c = 10$ ,  $R_g = 0.95$  (left) and  $R_g = 1.4397$  (right).

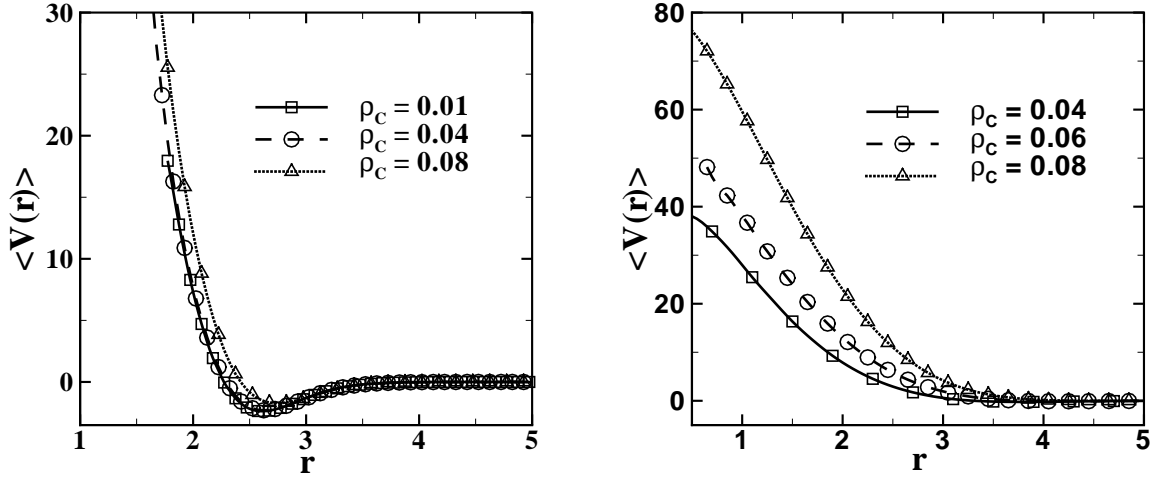


Figure 2.4: Potential of the average pair force for different densities with  $N_c = 10$ ,  $k_B T = 3.0$ ,  $R_g = 0.95$  (left) and  $R_g = 1.4397$  (right).

$$\begin{aligned} \langle f(r) \rangle &\sim \frac{N_c k_B T}{R_g} h(r/R_g) \\ \langle V(r) \rangle &\sim N_c k_B T g(r/R_g), \end{aligned} \quad (2.16)$$

where  $h(r) = -dg(r)/dr$  and  $g(r)$  are dimensionless functions depending on  $\rho_c$  and  $\rho_{inner}$ . Note that these simulation results are similar to the scaling relationship for an unconstrained DPD system as derived in [55].

Fig. 2.4 shows  $\langle f(r) \rangle$  for different number densities  $\rho_c$  at fixed temperature  $k_B T = 3.0$ . Compared with the  $R_g = 0.95$  case,  $\langle f(r) \rangle$  for  $R_g = 1.4397$  depends strongly on  $\rho_c$ , indicating a significant many-body effect, which may affect the properties of the coarse-grained system, as discussed in Sec. 2.4.

Having obtained the CG force field, we now turn to the *static* and *dynamic* properties of the system. Fig. 2.5 shows the radial distribution function  $g(r)$  of the clusters at different temperatures. For  $R_g = 1.4397$ ,  $g(r)$  is flat and similar to the standard DPD result, while for  $R_g = 0.95$ ,  $g(r)$  is much sharper, similar to the

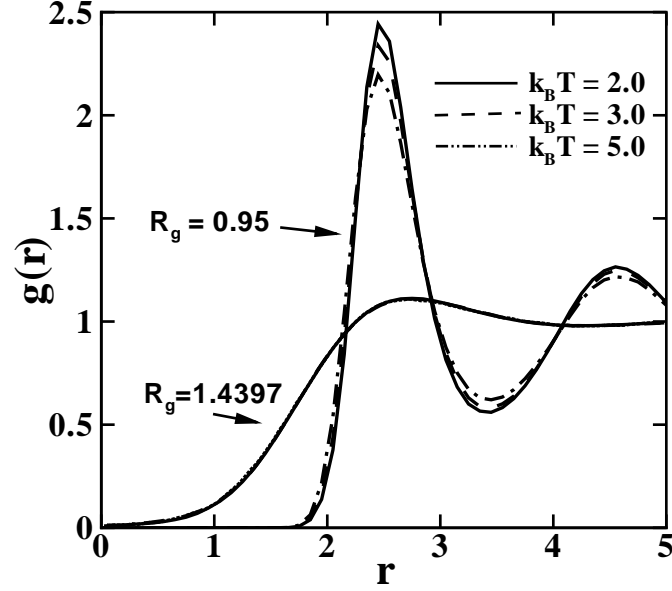


Figure 2.5: Radial distribution function  $g(r)$  computed for different temperatures, with  $\rho = 0.8$ ,  $N_c = 10$ ,  $R_g = 0.95$  and  $R_g = 1.4397$ . For the latter case, the three curves coincide.

“single” LJ particle result as expected. Unlike the simple fluid system, the radial distribution function shows very weak dependence on temperature between 2.0 and 5.0. This result can be readily understood from the weak temperature-dependence of  $\langle V(r) \rangle$  shown in Fig. 2.2.

For *dynamic* properties, we determine the self-diffusivity of the clusters in the MD system by the Einstein relationship

$$D = \lim_{t \rightarrow \infty} \frac{1}{6t} \langle |\mathbf{R}_\mu(t) - \mathbf{R}_\mu(0)|^2 \rangle . \quad (2.17)$$

We determine the viscosity of the MD system by the periodic Poiseuille flow method [10] and Lees-Edwards Couette flow. The velocity profile obtained for the periodic Poiseuille flow is shown in Fig. 2.6. For simulation details, we refer to [10]. The dynamic properties are listed in table 2.1.

$\rho$	$R_g$	D	$\eta$	$S_c$
0.8	0.95	0.0234	7.41	395
0.4	0.95	0.271	1.05	9.69
0.8	1.4397	0.0255	7.08	347
0.4	1.4397	0.141	1.66	29.4

Table 2.1: Dynamic properties for the MD system with  $k_B T = 3.0$ ,  $N_c = 10$ ;  $D$ ,  $\eta$  and  $S_c$  stand for diffusivity, dynamic viscosity, and Schmidt number, respectively.

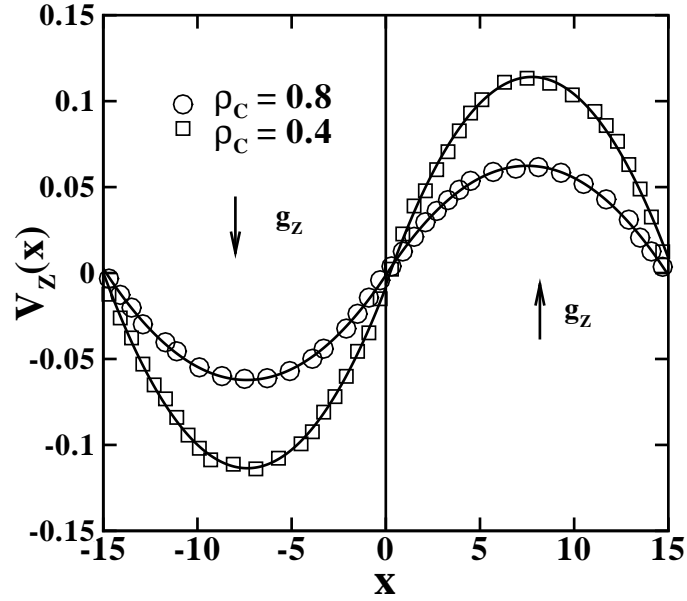


Figure 2.6: Velocity profiles obtained using the periodic Poiseuille flow method. The square and circle symbols represent velocity profiles for  $\rho = 0.8$  and  $\rho = 0.4$ , respectively. The lines are quadratic fit curves for each case. The body force  $g_z$  is added on each atomistic particle;  $g_z$  is chosen as 0.02 and 0.005 for  $\rho = 0.8$  and  $\rho = 0.4$ , respectively. The box size is changed to  $30 \times 15 \times 15$  in this test and the temperature is  $k_B T = 3.0$ .

## 2.4 Coarse Grained Models

To investigate the relationship between the two different scales we construct different *mesoscale* models based on the microscopic results in previous section. Specifically, we construct CG clusters whose mass is the sum of the mass of MD particles within each cluster. The CG system remains in the canonical ensemble at the same temperature  $k_B T$ .

### 2.4.1 Mean force field approach

We start with a very simple model where we employ only the average force field, i.e., the first term in Eq. (2.5). The static properties are determined by this term. Fig. 2.7 compares the Equation of State (EOS) of the CG system with the MD system. The results are close to the MD results with a difference less than 2%. Fig. 2.8 compares the radial distribution function of the system. For  $R_g = 0.95$ , the results of the MD and CG systems match well over the entire density regime. However, for  $R_g = 1.4397$  and  $\rho_c = 0.08$ , the CG result shows a sharper peak than the MD result. Similar differences have been reported for flexible polymer chains in [56, 4]. In contrast, Akkermans and Briels [5] proposed a structure-based effective potential which reproduces the radial distribution of coarse-grained polymer system over the entire density regime. However, it generates a pressure much lower than the MD system. These differences are primarily due to the approximation of the clusters as point particles and the absence of the full many-body interaction, which plays an important role at high density and larger  $R_g$ .

In general, the mean field by itself cannot reproduce the correct dynamic properties of the CG system. As an illustration, we calculate the self-diffusion coefficient and the dynamic viscosity for CG system of  $R_g = 1.4397$  with  $\rho_c = 0.08$  and  $k_B T = 3.0$ . The results are  $D_{MF} = 0.53$  and  $\eta_{MF} = 0.74$  respectively, indicating a larger mass transport and smaller momentum transport, compared with the MD

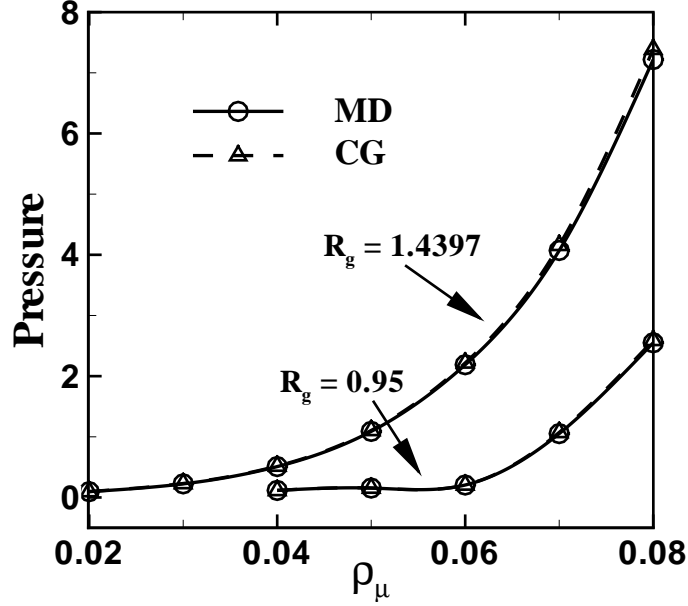


Figure 2.7: Pressure computed by MD and CG simulations for  $N_c = 10$ ,  $k_B T = 3.0$  with  $R_g = 0.95$  and  $R_g = 1.4397$ .

system ( $D_{MD} = 0.0255$ ,  $\eta_{MD} = 7.08$ ). Moreover, this discrepancy cannot be eliminated by simply re-scaling the units of the CG system. Specifically, if we artificially match the diffusivity of two system by re-scaling the time unit of the CG system while keeping the length and mass units fixed, the scaled time unit of CG system is  $[t]_{MF} = 20.78[t]_{MD}$ . Consequently, the dynamic viscosity of the CG system, by the mean field model, should be  $0.74[M]/[L][t]_{MF} = 0.0356[M]/[L][t]_{MD}$ , which is different from the MD result  $\eta_{MD} = 7.08$ . In particular, the dimensionless Schmidt number is different in the two systems. In the MD system,  $Sc_{MD}$  is around 347 (see table I) while in the mean field  $Sc_{MF}$  is around 1. Therefore, the dissipative and random force terms in Eq. (2.5) cannot be neglected, if the dynamic properties are considered.

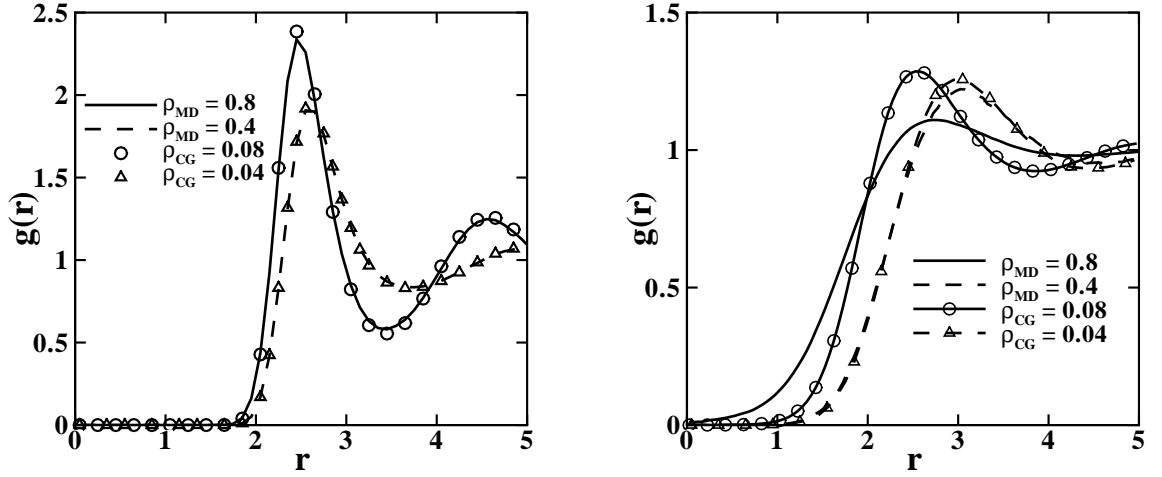


Figure 2.8: Radial distribution function of the coarse-grained particles for  $\rho_c = 0.08$  and  $\rho_c = 0.04$ , with  $R_g = 0.95$  (left) and  $1.4397$  (right). The lines denote the MD simulation results. The symbols correspond to MD simulations.

## 2.4.2 Langevin thermostat approach

Next, we discuss a model including the dissipative and random force terms. We assume that the random force of each component on each CG particle is an identical independently distributed (i.i.d.) variable and hence Eq. (2.8) and Eq. (2.7) are simplified, respectively, as

$$\beta \int_0^t ds \left\langle [\delta \mathbf{F}_\mu^Q(t-s)] \otimes [\delta \mathbf{F}_\nu^Q(0)]^T \right\rangle = \frac{1}{2} \beta \sigma^2 \delta_{\mu\nu} I, \quad (2.18)$$

$$\langle \delta F_{\mu x}^Q(0) \cdot \delta F_{\nu y}^Q(t) \rangle = \sigma^2 \delta_{\mu\nu} \delta_{xy} \delta(t), \quad (2.19)$$

where  $I$  is the identity matrix, and we define  $\gamma = 0.5\beta\sigma^2$  as the friction coefficient. The fluctuation-dissipation theorem is satisfied, and Eq. (2.5) simplifies to:

$$\dot{\mathbf{P}}_\mu = \sum_{\nu \neq \mu} \langle f(r_{\mu\nu}) \rangle \mathbf{e}_{\mu\nu} - \gamma \mathbf{V}_\mu + \delta \mathbf{F}_\mu^Q, \quad (2.20)$$

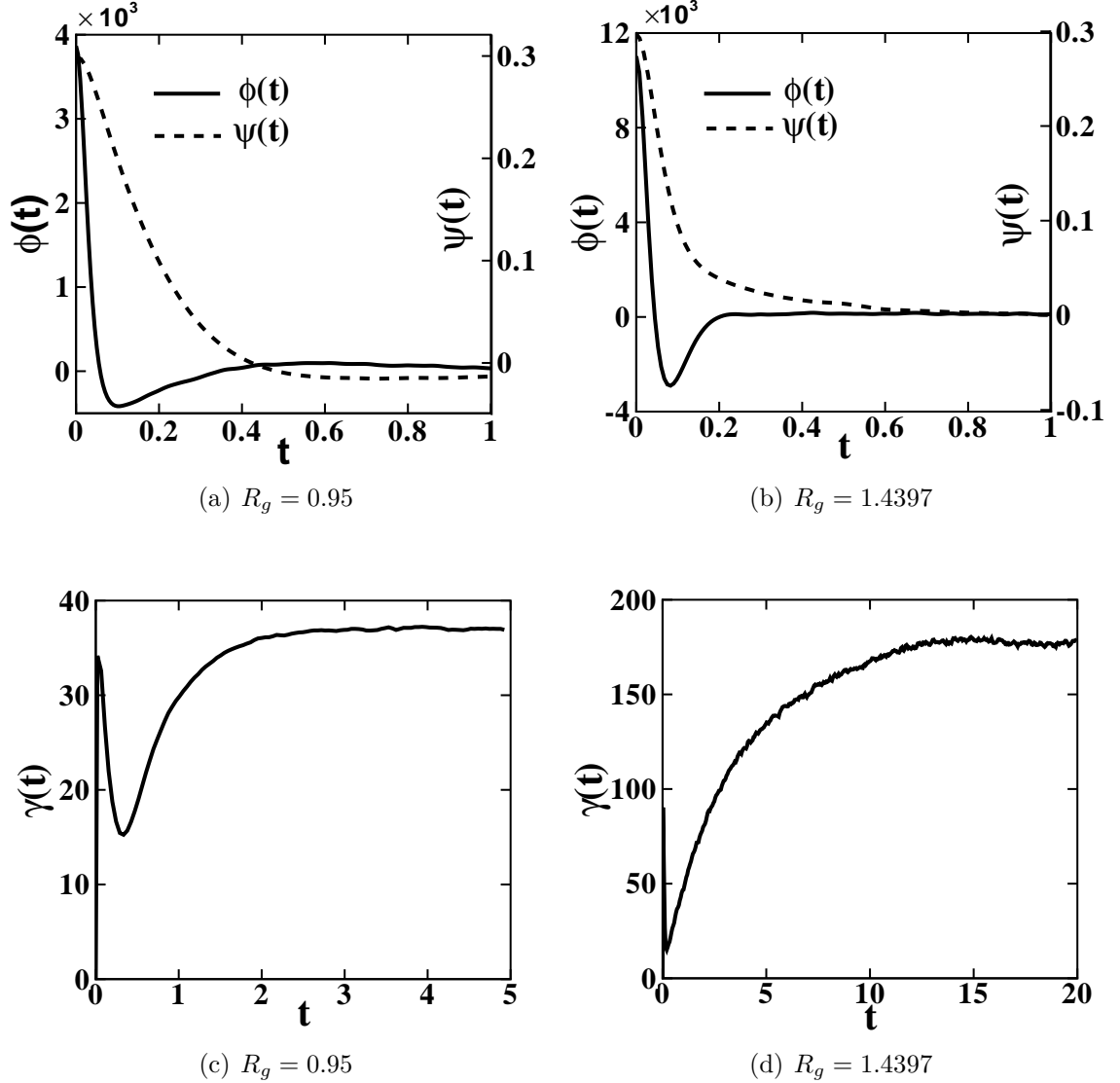


Figure 2.9: Computation of the Langevin thermostat coefficient. (a-b): Time correlation of the velocity and random force on each cluster for  $\rho = 0.8$ ,  $N_c = 10$ ,  $k_B T = 3.0$ . The solid line denotes ensemble correlation of the x-component of total random force on a cluster. The dashed line denotes the velocity correlation of the x-component. (c-d): Time integration of correlation defined by  $\gamma(t) = \beta \int_0^t \langle \delta F_{\mu x}^Q(0) \delta F_{\mu x}^Q(t-s) \rangle ds$ . The result converges when  $t \approx 3.0$  for  $R_g = 0.95$  and  $t \approx 15.0$  for  $R_g = 1.4397$ .

where  $\mathbf{V}_\mu$  is the velocity of the CG particle. This model states that the motion of the CG particles is coupled with the standard Langevin thermostat [135, 93], as implemented in the coarse-grained polymer melts [117]. Note that the friction coefficient  $\gamma$  is not casually chosen but computed by Eq. (2.18).

The instantaneous random force term on a single cluster  $\mu$  is  $\delta\mathbf{F}_\mu^\mathcal{Q} = \mathbf{F}_\mu - \langle\mathbf{F}_\mu\rangle$ , where  $\langle\mathbf{F}_\mu\rangle$  is a function depending on  $K$ -body configurations of the system, which is difficult to evaluate directly. In practice, we approximate  $\langle\mathbf{F}_\mu\rangle$  by decomposing it into pairwise functions as discussed in Sec. 2.3.1. Accordingly, we approximate  $\delta\mathbf{F}_\mu^\mathcal{Q}$  as

$$\delta\mathbf{F}_\mu^\mathcal{Q} \approx \sum_{\nu \neq \mu} \delta\mathbf{f}_{\mu\nu}^\mathcal{Q}, \quad (2.21)$$

where  $\delta\mathbf{f}_{\mu\nu}^\mathcal{Q}$  is the pairwise random force between cluster  $\mu$  and  $\nu$ , defined as

$$\delta\mathbf{f}_{\mu\nu}^\mathcal{Q} = \mathbf{f}_{\mu\nu} - \langle f(r) \rangle \mathbf{e}_{\mu\nu}, \quad (2.22)$$

where  $\mathbf{f}_{\mu\nu}$  is the instantaneous force between the two clusters.

Fig. 2.9 shows the correlation function of the random force on a single cluster. It also verifies the Markovian approximation in Eq. (2.8) since the autocorrelation of velocity decays slower than the random force correlation. The friction coefficient is obtained by taking the long-time integration of the random force correlation function until a converged value is obtained.

Having obtained the friction coefficient, we are ready to simulate the CG system by Eq. (2.20) using the standard algorithm [6]. The temperature is kept constant by the Langevin thermostat and the static properties are determined by the mean force term as shown in the previous section. For  $R_g = 0.95$  and  $\rho_c = 0.08$  ( $\rho = 0.8$ ), the self-diffusion coefficient determined by this method is  $D_{LD} = 0.0063$ , which is approximately four times smaller than the MD result ( $D_{MD} = 0.0234$ ), see table I.

Moreover, this CG system does not capture the correct hydrodynamics. This result originates from Eq. (2.19), which assumes that the random force on each CG

particle is independent and therefore cannot be represented in a pairwise fashion. Physically, it appears that each CG particle is surrounded by some heat bath particles [32], and the random force on each particle arises from thermal collisions with heat bath particles. Therefore, the momentum transport between two clusters in the MD system is modeled in two parts: the pairwise interaction between the two CG particles through the mean force field, and the thermal collisions with the heat bath particles represented as the i.i.d. force  $\delta\mathbf{F}^{\mathcal{Q}}$  on each particle. Specifically, if the conservative interaction is much larger than the thermal collision effect, the system approaches the Newtonian regime [122]. However, if the friction and random forces become comparable with the conservative force (as in the case of this study), the Langevin thermostat significantly damps the hydrodynamic correlation [32] between the particles, and the system cannot reproduce the correct hydrodynamics [122, 142]. In this study, the loss of momentum transport between the CG particles in the random force field eliminates the information needed for the calculation of viscosity.

### 2.4.3 Dissipative Particle Dynamics (DPD)

To establish the correlation of the random force between different CG clusters, we decompose the random force into additive pairwise components between different particles. Generally, the random force  $\delta\mathbf{f}_{\mu\nu}^{\mathcal{Q}}$  defined by Eq. (2.22) is not along the radial direction  $\mathbf{e}_{\mu\nu}$ , as shown in Fig. 2.1. Therefore, we decompose  $\delta\mathbf{f}_{\mu\nu}^{\mathcal{Q}}$  into two parts: the radial force along  $\mathbf{e}_{\mu\nu}$  and the perpendicular part, e.g.,

$$\begin{aligned}\delta\mathbf{f}_{\mu\nu}^{\mathcal{Q}} &= \mathbf{e}_{\mu\nu}\mathbf{e}_{\mu\nu}^T\delta\mathbf{f}_{\mu\nu}^{\mathcal{Q}} + (\mathbf{I} - \mathbf{e}_{\mu\nu}\mathbf{e}_{\mu\nu}^T)\delta\mathbf{f}_{\mu\nu}^{\mathcal{Q}} \\ &= \delta f_{\mu\nu,\parallel}^{\mathcal{Q}}\mathbf{e}_{\mu\nu} + \delta\mathbf{f}_{\mu\nu,\perp}^{\mathcal{Q}},\end{aligned}\tag{2.23}$$

where  $\delta\mathbf{f}_{\mu\nu,\perp}^{\mathcal{Q}}$  is the perpendicular part of the random force. We assume that the random force pairs are independent and uncorrelated in time, i.e.,

$$\begin{aligned}\langle \delta f_{\mu\nu,\parallel}^{\mathcal{Q}}(0) \delta f_{\epsilon\eta,\parallel}^{\mathcal{Q}}(t) \rangle &= [\sigma_{\parallel} w_{\parallel}(R)]^2 \mathcal{K}(t) \\ \langle \delta\mathbf{f}_{\mu\nu,\perp}^{\mathcal{Q}}(0) \cdot \delta\mathbf{f}_{\epsilon\eta,\perp}^{\mathcal{Q}}(t) \rangle &= 2 [\sigma_{\perp} w_{\perp}(R)]^2 \mathcal{K}(t),\end{aligned}\quad (2.24)$$

where  $\sigma_{\parallel} w_{\parallel}(R)$  and  $\sigma_{\perp} w_{\perp}(R)$  are the variances of the random force depending on the distance  $R$ , and

$$\mathcal{K}(t) = (\delta_{\mu\epsilon}\delta_{\nu\eta} + \delta_{\mu\eta}\delta_{\nu\epsilon}) \delta(t). \quad (2.25)$$

These assumptions lead to

$$\begin{aligned}\langle \delta\mathbf{f}_{\mu\nu}^{\mathcal{Q}}(0) \delta\mathbf{f}_{\epsilon\eta}^{\mathcal{Q}}(t)^T \rangle &= (\delta_{\mu\epsilon}\delta_{\nu\eta} - \delta_{\mu\eta}\delta_{\nu\epsilon}) \\ &\times \langle \delta\mathbf{f}_{\mu\nu}^{\mathcal{Q}}(0) \delta\mathbf{f}_{\mu\nu}^{\mathcal{Q}}(t)^T \rangle.\end{aligned}\quad (2.26)$$

In addition, the memory kernel  $\int_0^{\infty} \langle \delta\mathbf{f}_{\mu\nu}^{\mathcal{Q}}(0) \delta\mathbf{f}_{\mu\nu}^{\mathcal{Q}}(t)^T \rangle dt$  is isotropic in planes perpendicular to  $\mathbf{e}_{\mu\nu}$ . Therefore, we decompose the matrix as

$$\begin{aligned}\gamma_{\mu\nu} &= \beta \int_0^{\infty} \langle \delta\mathbf{f}_{\mu\nu}^{\mathcal{Q}}(0) \delta\mathbf{f}_{\mu\nu}^{\mathcal{Q}}(t)^T \rangle dt \\ &= \gamma_{\parallel}(R_{\mu\nu}) \mathbf{e}_{\mu\nu} \mathbf{e}_{\mu\nu}^T + \gamma_{\perp}(R_{\mu\nu}) (\mathbf{I} - \mathbf{e}_{\mu\nu} \mathbf{e}_{\mu\nu}^T),\end{aligned}\quad (2.27)$$

where  $\gamma_{\parallel}$  and  $\gamma_{\perp}$  are scalars depending on  $R_{\mu\nu}$ . Using Eq. (2.24), they are determined by

$$\begin{aligned}\gamma_{\parallel}(R_{\mu\nu}) &= \mathbf{e}_{\mu\nu}^T \gamma_{\mu\nu} \mathbf{e}_{\mu\nu} \\ &= \beta \int_0^{\infty} dt \langle \delta f_{\mu\nu,\parallel}^{\mathcal{Q}}(0) \delta f_{\mu\nu,\parallel}^{\mathcal{Q}}(t) \rangle \\ &= \frac{1}{2} \beta [\sigma_{\parallel} w_{\parallel}(R_{\mu\nu})]^2\end{aligned}\quad (2.28)$$

$$\begin{aligned}
\gamma_{\perp}(R_{\mu\nu}) &= \frac{1}{2}\text{Tr} [(\mathbf{I} - \mathbf{e}_{\mu\nu}\mathbf{e}_{\mu\nu}^T) \gamma_{\mu\nu} (\mathbf{I} - \mathbf{e}_{\mu\nu}\mathbf{e}_{\mu\nu}^T)] \\
&= \frac{1}{2}\beta\text{Tr} \left[ \int_0^{\infty} \langle (\mathbf{I} - \mathbf{e}_{\mu\nu}\mathbf{e}_{\mu\nu}^T) \delta\mathbf{f}_{\mu\nu}^{\mathcal{Q}}(0) \delta\mathbf{f}_{\mu\nu}^{\mathcal{Q}}(t)^T \right. \\
&\quad \left. \otimes (\mathbf{I} - \mathbf{e}_{\mu\nu}\mathbf{e}_{\mu\nu}^T) \rangle dt \right] \\
&= \frac{1}{2}\beta \int_0^{\infty} \langle \delta\mathbf{f}_{\mu\nu,\perp}^{\mathcal{Q}}(0) \cdot \delta\mathbf{f}_{\mu\nu,\perp}^{\mathcal{Q}}(t) \rangle dt \\
&= \frac{1}{2}\beta [\sigma_{\perp} w_{\perp}(R_{\mu\nu})]^2. \tag{2.29}
\end{aligned}$$

The dissipative force on a single cluster  $\mu$  is then obtained from:

$$\begin{aligned}
&\beta \sum_{\eta} \int_0^{\infty} \langle \mathbf{F}_{\mu}^{\mathcal{Q}}(s) \mathbf{F}_{\eta}^{\mathcal{Q}}(0)^T \rangle ds \mathbf{V}_{\eta} \\
&= \beta \sum_{\eta} \sum_{\nu \neq \mu} \sum_{\epsilon \neq \eta} \int_0^{\infty} \langle \mathbf{f}_{\mu\nu}^{\mathcal{Q}}(s) \mathbf{f}_{\eta\epsilon}^{\mathcal{Q}}(0)^T \rangle ds \mathbf{V}_{\eta} \\
&= \sum_{\eta} \sum_{\nu \neq \mu} \sum_{\epsilon \neq \eta} (\delta_{\mu\eta} \delta_{\nu\epsilon} - \delta_{\mu\epsilon} \delta_{\nu\eta}) [\gamma_{\parallel}(R_{\mu\nu}) \mathbf{e}_{\mu\nu} \mathbf{e}_{\mu\nu}^T + \gamma_{\perp}(R_{\mu\nu}) (\mathbf{I} - \mathbf{e}_{\mu\nu} \mathbf{e}_{\mu\nu}^T)] \mathbf{V}_{\eta} \\
&= \sum_{\nu \neq \mu} \gamma_{\parallel}(R_{\mu\nu}) \mathbf{e}_{\mu\nu} \mathbf{e}_{\mu\nu}^T (\mathbf{V}_{\mu} - \mathbf{V}_{\nu}) + \sum_{\nu \neq \mu} \gamma_{\perp}(R_{\mu\nu}) (\mathbf{I} - \mathbf{e}_{\mu\nu} \mathbf{e}_{\mu\nu}^T) (\mathbf{V}_{\mu} - \mathbf{V}_{\nu}) \\
&= \sum_{\nu \neq \mu} \gamma_{\parallel}(R_{\mu\nu}) (\mathbf{e}_{\mu\nu} \cdot \mathbf{V}_{\mu\nu}) \mathbf{e}_{\mu\nu} + \sum_{\nu \neq \mu} \gamma_{\perp}(R_{\mu\nu}) (\mathbf{V}_{\mu\nu} - (\mathbf{e}_{\mu\nu} \cdot \mathbf{V}_{\mu\nu}) \mathbf{e}_{\mu\nu}). \tag{2.30}
\end{aligned}$$

Similar to Eq. (2.8), the above approximation replaces the continuously varying impulses on a CG particle by discrete time-independent values, along both the radial and perpendicular directions for each pair. The first term on the right hand side of the above equation is the dissipative force of standard DPD [60, 90, 40]. The second term represents the friction between two CG particles along the perpendicular directions. This is exactly the dissipative force for the ‘‘transverse DPD thermostat’’, recently proposed by Junghans *et al.* [78]. Putting the three terms together, we obtain the *generalized DPD equation*:

$$\begin{aligned}
\dot{\mathbf{P}}_\mu &= \sum_{\nu \neq \mu} \langle f(r_{\mu\nu}) \rangle \mathbf{e}_{\mu\nu} - \sum_{\nu \neq \mu} \gamma_{\parallel}(R_{\mu\nu}) (\mathbf{e}_{\mu\nu} \cdot \mathbf{V}_{\mu\nu}) \mathbf{e}_{\mu\nu} \\
&+ \sum_{\nu \neq \mu} \gamma_{\perp}(R_{\mu\nu}) (\mathbf{V}_{\mu\nu} - (\mathbf{e}_{\mu\nu} \cdot \mathbf{V}_{\mu\nu}) \mathbf{e}_{\mu\nu}) + \sum_{\nu} \delta \mathbf{f}_{\mu\nu}^{\mathcal{Q}},
\end{aligned} \tag{2.31}$$

Specifically, we use Eq. (2.28) and Eq. (2.29) to calculate the friction coefficient in the radial and perpendicular directions, with  $\delta f_{\mu\nu,\parallel}^{\mathcal{Q}}$  and  $\delta \mathbf{f}_{\mu\nu,\perp}^{\mathcal{Q}}$  defined by Eq. (2.23). Noting that the radial vector  $\mathbf{e}_{\mu\nu}$  changes with time, the random force terms  $\delta f_{\mu\nu,\parallel}^{\mathcal{Q}}(t)$  and  $\delta \mathbf{f}_{\mu\nu,\perp}^{\mathcal{Q}}(t)$  are defined by projecting  $\delta \mathbf{F}_{\mu\nu}^{\mathcal{Q}}(t)$  onto the vector  $\mathbf{e}_{\mu\nu}$  at time zero. Fig. 2.10(a) and Fig. 2.10(b) show the random force correlation along both the parallel and perpendicular direction. For  $R_g = 0.95$ , the clusters behave like the “single” particles, and the radial part of random force dominates for most distances. However, for the larger  $R_g = 1.4397$ , the shearing part becomes comparable to the radial part, and the integration converges for longer times, as shown in Fig. 2.10(d).

Fig. 2.11 shows the friction coefficients for different distances with  $R_g = 0.95$ ,  $k_B T = 3.0$ . We fit the  $\gamma_{\parallel}$  and  $\gamma_{\perp}$  by polynomials  $a(1.0 - r/b)^n$ , where  $n$  is 4.0 and 3.0, respectively. Using the fitted function form of  $\gamma$ , we simulate the CG system by DPD using both the radial and the shear thermostat [78]. In Fig. 2.12 and Fig. 2.13, we show the mean square displacement of the CG system in the long-time region and the velocity correlations in short-time region. The difference in the results obtained with the best fit and the original points is less than 5%. Fig. 2.14 shows velocity profiles from both the MD and DPD systems obtained by the periodic Poiseuille flow method. As the momentum transport between clusters is represented by pairwise forces, the simulation results recover Newtonian flow behavior in this model, as expected. The dynamic properties of the DPD system are listed in table 2.2.

The DPD results show smaller diffusivities and larger viscosities compared with the MD results, the deviations being different for the four cases. For  $R_g = 0.95$ , the difference of the diffusivity is about 16% and 1.2% for DPD densities  $\rho_c =$

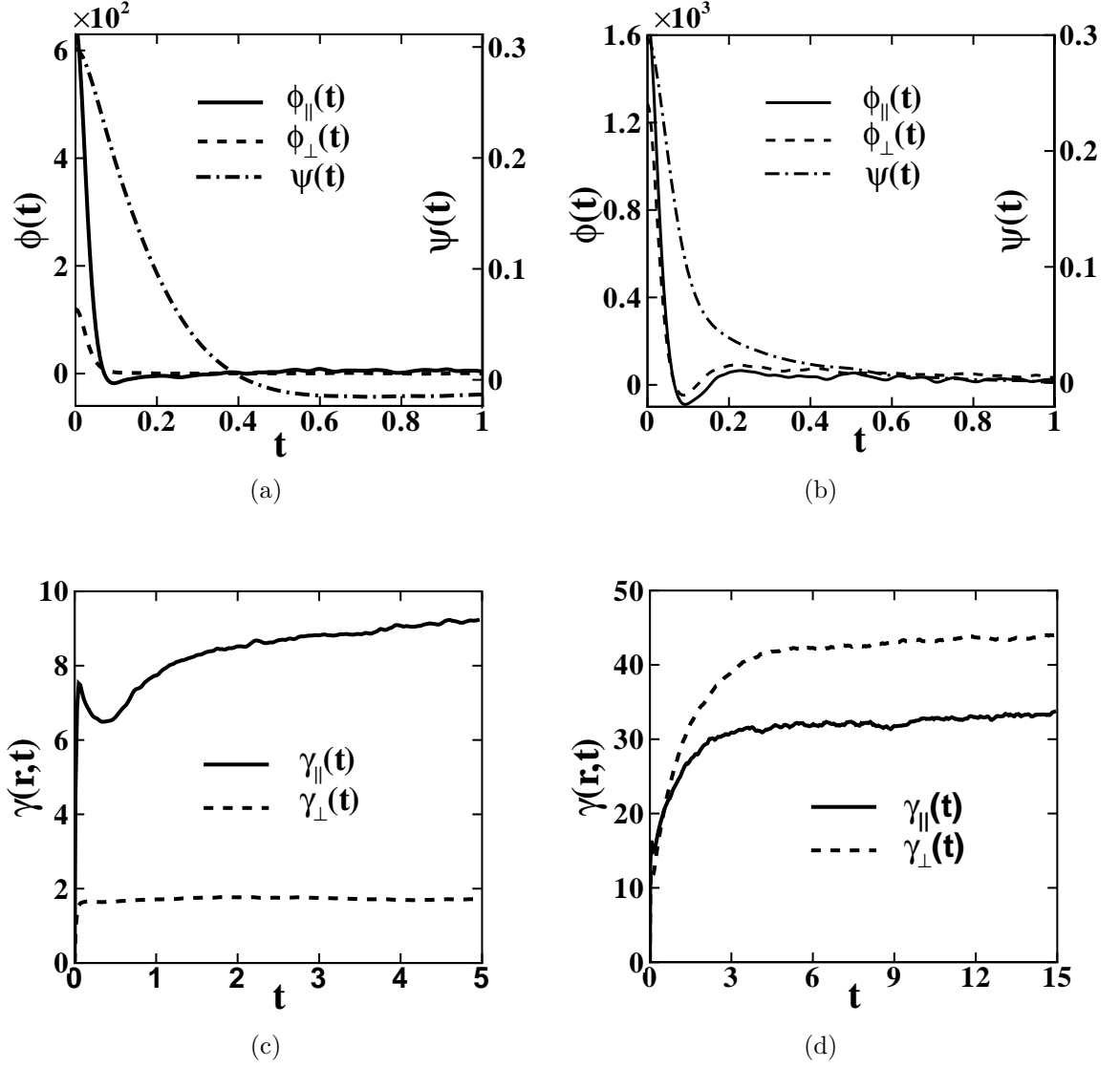


Figure 2.10: Upper: Time correlation of the pairwise random force between two clusters for  $\rho = 0.8$ ,  $N_c = 10$ ,  $k_B T = 3.0$ , with (a)  $R_g = 0.95, r = 2.65$  and (b)  $R_g = 1.4397, r = 2.25$ . The solid line is the radial part and the dash line is the perpendicular part. The velocity correlation function decays slower than the random force as shown. Lower: time integration of the correlation function with (c)  $R_g = 0.95, r = 2.65$  and (d)  $R_g = 1.4397, r = 2.25$ .

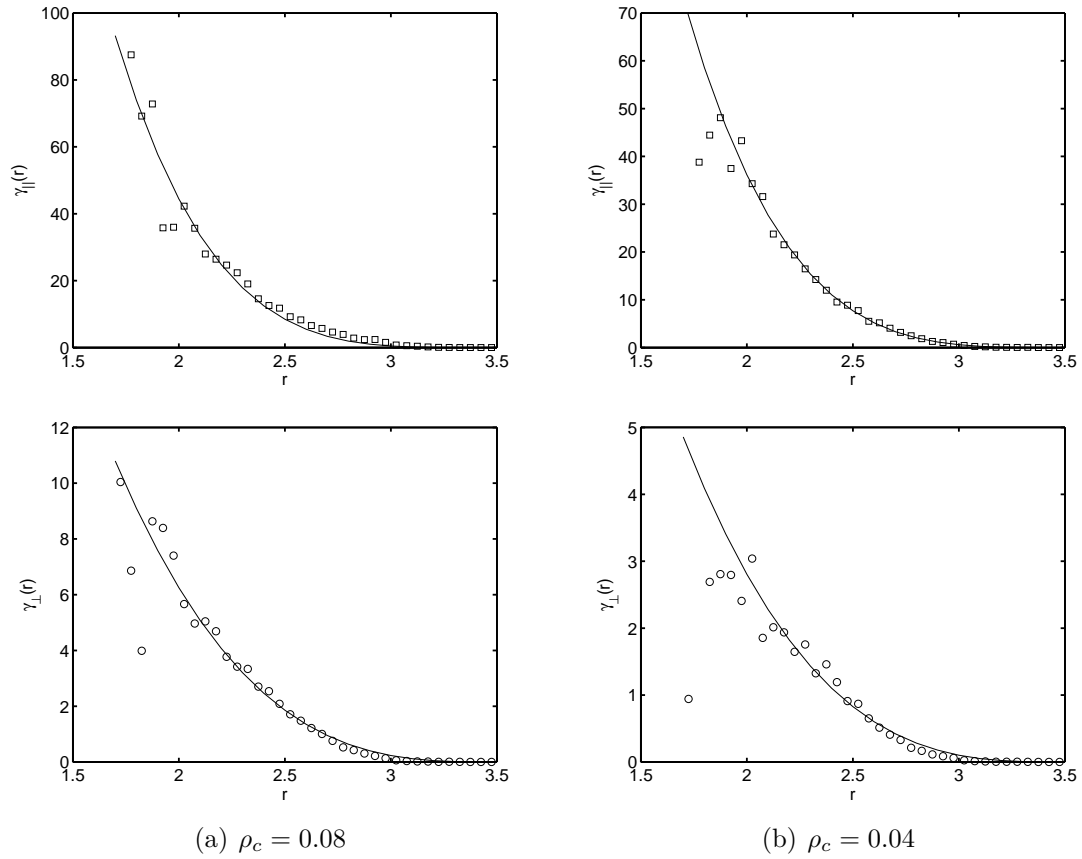


Figure 2.11: Radial and shear friction coefficients for  $R_g = 0.95$ ; the solid line is a fit to: (a)  $\rho_c = 0.08$ ,  $\gamma_{\parallel}(r) = a(1 - r/b)^4$ , where  $a = 1.06 \times 10^3$ ,  $b = 3.6$ ;  $\gamma_{\perp}(r) = a(1 - r/b)^3$ , where  $a = 80.1$ ,  $b = 3.5$  (b)  $\rho_c = 0.08$ ;  $\gamma_{\parallel}(r) = a(1 - r/b)^4$ , where  $a = 0.97 \times 10^3$ ,  $b = 3.6$ ,  $\rho = 0.4$ ;  $\gamma_{\perp}(r) = a(1 - r/b)^3$ , where  $a = 35.6$ ,  $b = 3.5$ .

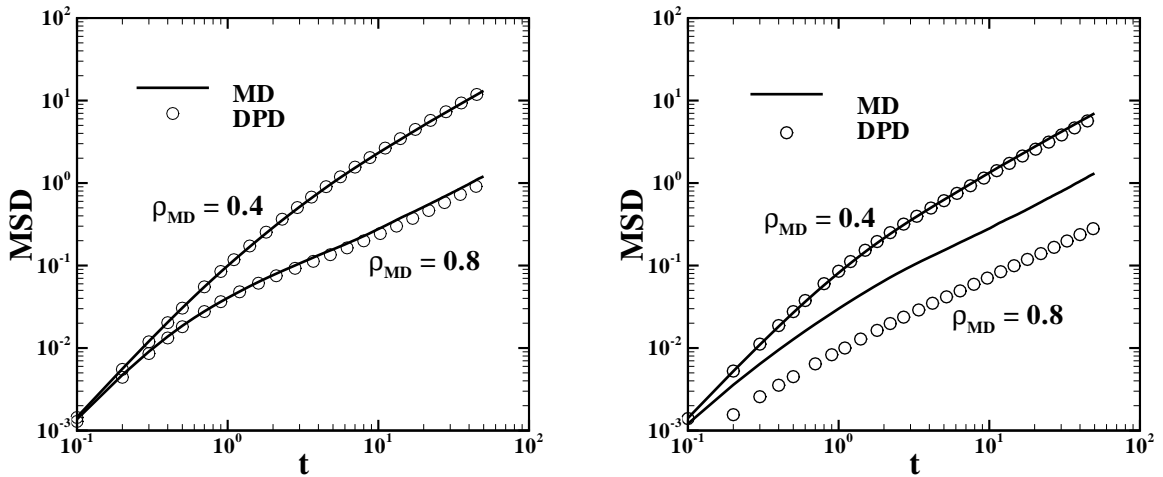


Figure 2.12: Mean square displacement of the clusters and CG particles for different densities with  $R_g = 0.95$  (left) and  $R_g = 1.4397$  (right);  $N_c = 10$ ,  $k_B T = 3.0$ .

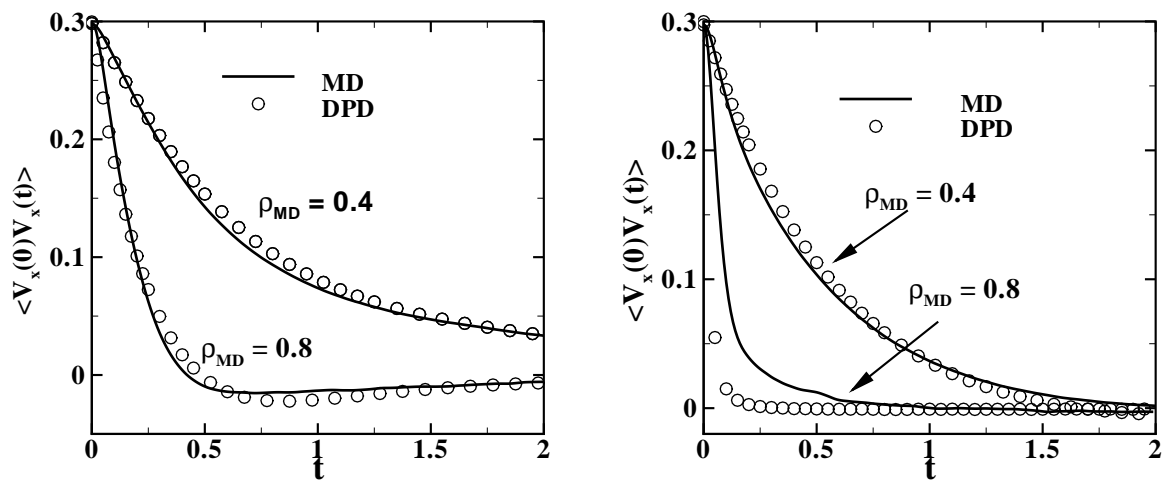


Figure 2.13: Velocity correlation function of the clusters and CG particles for different densities with  $R_g = 0.95$  (left) and  $R_g = 1.4397$  (right);  $N_c = 10$ ,  $k_B T = 3.0$ .

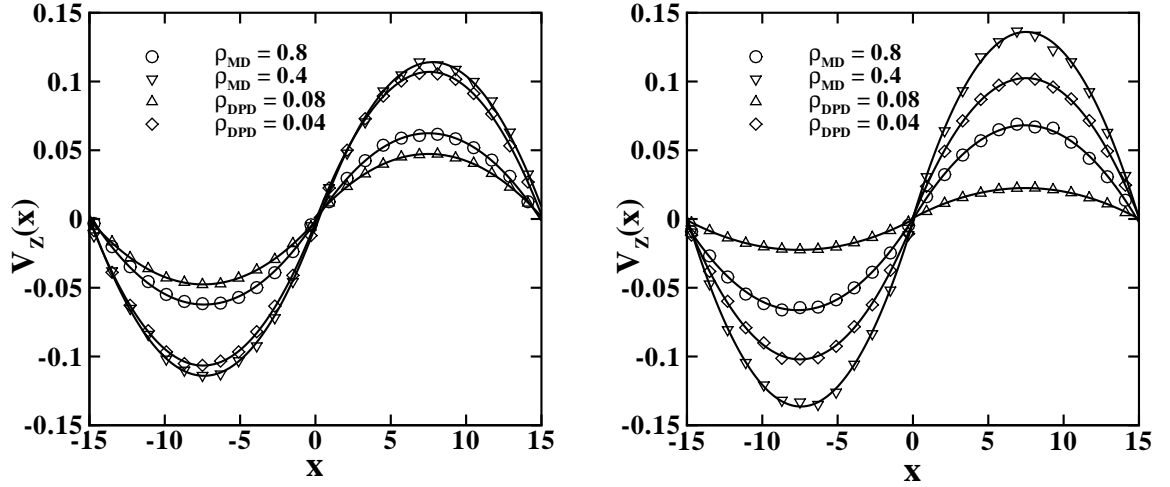


Figure 2.14: Velocity profile for periodic Poiseuille flow method for MD and DPD model. Body forces  $f_{MD}$  and  $f_{CG}$  are applied on each MD and CG particle, respectively. Upper:  $R_g = 0.95$ ,  $\rho = 0.4$ ,  $f_{MD} = 0.005$ ,  $f_{CG} = 0.05$ ;  $R_g = 0.95$ ,  $\rho = 0.8$ ,  $f_{MD} = 0.02$ ,  $f_{CG} = 0.2$ . Lower:  $R_g = 1.4397$ ,  $\rho = 0.4$ ,  $f_{MD} = 0.01$ ,  $f_{CG} = 0.1$ ;  $R_g = 1.4397$ ,  $\rho = 0.8$ ,  $f_{MD} = 0.02$ ,  $f_{CG} = 0.4$

0.08 and 0.04, respectively. For  $R_g = 1.4397$ , the difference is about 80% and 25%, respectively. The differences are due mainly to two factors: the *Markovian approximation* and the *overestimation* of the friction coefficient. Firstly, the DPD model we have derived is based on the assumption that the velocity correlation of the CG particles decays more slowly than the random force correlation. When the density is high and the velocity correlation is comparable to the random force correlation, the DPD particles would be overdamped (see, ref [3]), which explains why we get better results in the semi-dilute regime. Secondly, the friction coefficient we use is overestimated since we lack the “full” information of the force field for the CG system [19]. Physically, the many-body potential field  $U_{CG}(\mathbf{R}^K)$  is the mean field which *minimizes* the random force covariance. It depends on the entire particle configuration of the CG system. Therefore, the pairwise mean force field implemented in this study would always lead to overestimated friction coefficients. In this study, when the many-body effect is important (e.g.,  $R_g = 1.4397$ ,  $\rho = 0.8$ ,

	$R_g$	D	$\eta$	$S_c$
$\rho = 0.8$	0.95	0.0234	7.41	395
$\rho_{DPD} = 0.08$	0.95	0.0195	9.69	621
$\rho = 0.4$	0.95	0.271	1.05	9.69
$\rho_{DPD} = 0.04$	0.95	0.269	1.075	9.98
$\rho = 0.8$	1.4397	0.0255	7.08	347
$\rho_{DPD} = 0.08$	1.4397	0.00525	41.23	$9.81 \times 10^3$
$\rho = 0.4$	1.4397	0.141	1.66	29.4
$\rho_{DPD} = 0.04$	1.4397	0.133	2.26	42.47

Table 2.2: Dynamic properties for MD and CG system with  $k_B T = 3.0$ ,  $N_c = 10$

see Fig. 2.4),  $\gamma(r)$  is largely overestimated in this pairwise style and the diffusivity of the DPD system is only 20% of the MD results. For the other three cases, the many-body effect is less important and the pairwise mean field we use can approximate  $U_{CG}(\mathbf{R}^K)$ . The friction coefficient can be accurately estimated and therefore the DPD results match reasonably well with the MD results.

## 2.5 Other potentials

As shown in the previous sections, while the mean force field  $\langle f(r) \rangle$  we chose reproduces the EOS in a wide density range, it does not reproduce the structure properties of the MD system in the high density regime when  $R_g$  is large. On the other hand, several methods [105, 5, 143, 107] have been proposed for obtaining a structure-based effective potential  $V_{eff}(r)$ , which reproduces the pair distribution function of the MD system. Therefore, it is worthwhile exploring if a structure-based force field can improve the dynamic property predictions.

For demonstration, we compute the pair distribution function by MD simulation with  $R_g = 1.2$  and  $\rho = 0.8$ . An iterative method [143] is used to obtain  $V_{eff}(r)$ , where  $\langle V(r) \rangle$  is used as the initial guess. As shown in Fig. 2.15,  $V_{eff}(r)$  shows a longer attractive tail compared with the mean field result, and it reproduces the pair

distribution function. However, the pressure obtained is 5.37, which is approximately 18% lower than the MD result. In contrast, with our approach EOS is reproduced very accurately.

Next,  $V_{eff}(r)$  is used as the input for Eq. (2.28) and Eq. (2.29) to compute the dissipative force term and the dynamic properties of the CG system are revisited. As shown in Fig. 2.16, both the velocity correlation and mean square displacement obtained from  $V_{eff}(r)$  show smaller values than the MD results. No obvious improvement is observed compared with the mean field results. This result is reasonable and consistent with what we expect. Although the pairwise effective potential  $V_{eff}(r)$  can *mimic* the *higher order* interactions of the MD system and can reproduce the *second* order correlation (radial distribution function) (as shown in Fig. 2.15), the higher order correlations of the MD system may not be reproduced. The instantaneous random force  $\delta f_{\mu\nu,\parallel}^{\mathcal{Q}}(t)$  and  $\delta f_{\mu\nu,\perp}^{\mathcal{Q}}(t)$  in Eq. (2.28) and Eq. (2.29) may still be far from the real value, depending on the strength of the higher order correlation of the MD system.

Finally, we also checked the coarse-graining results with the Weeks-Chandler-Andersen (WCA) potential as the input interaction between the MD particles. Both static and dynamic properties show qualitatively similar results with the previous sections, e.g., we can represent the MD clusters by DPD particles and predict the friction coefficient reasonably well in semi-dilute regime or  $R_g$  relatively small, which indicates that the approach we use is quite general and may be extended to many other systems.

## 2.6 Summary and Discussion

Starting from a microscopic simulation of LJ clusters in a canonical ensemble, we conducted mesoscopic simulations of the system by coarse-graining clusters that we constructed with fixed radius of gyration and represented them as point particles.

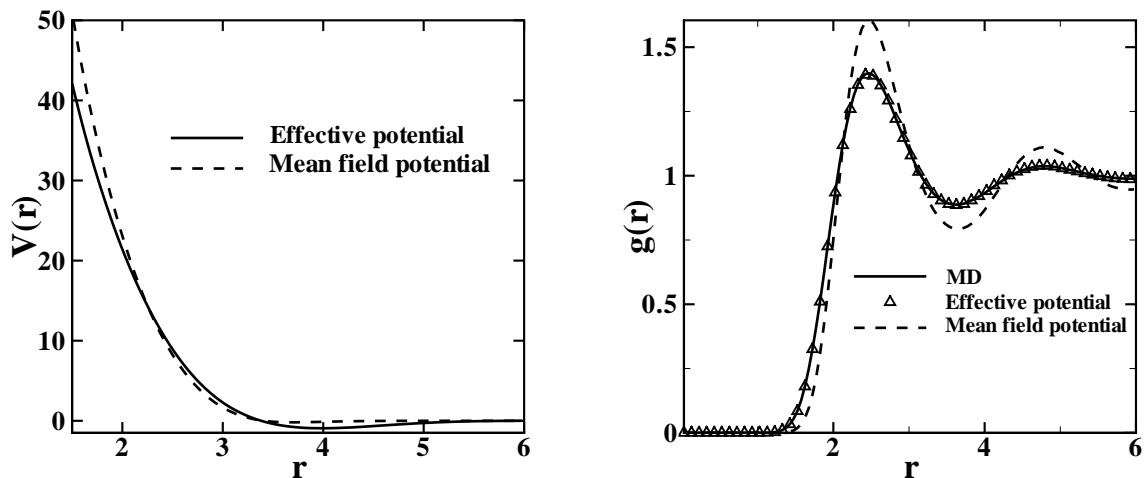


Figure 2.15: Left: Effective potential  $V_{eff}(r)$  obtained from the pair distribution function of MD simulation and mean field potential  $\langle V(r) \rangle$  obtained from Eq. 2.14 with  $R_g = 1.2$ ,  $k_B T = 3.0$ ,  $N_c = 10$  and  $\rho = 0.8$ .  $V_{eff}(r)$  shows an artificially longer tail compared with  $\langle V(r) \rangle$ . Right: Pair distribution function measured by MD,  $V_{eff}(r)$  and  $\langle V(r) \rangle$ .

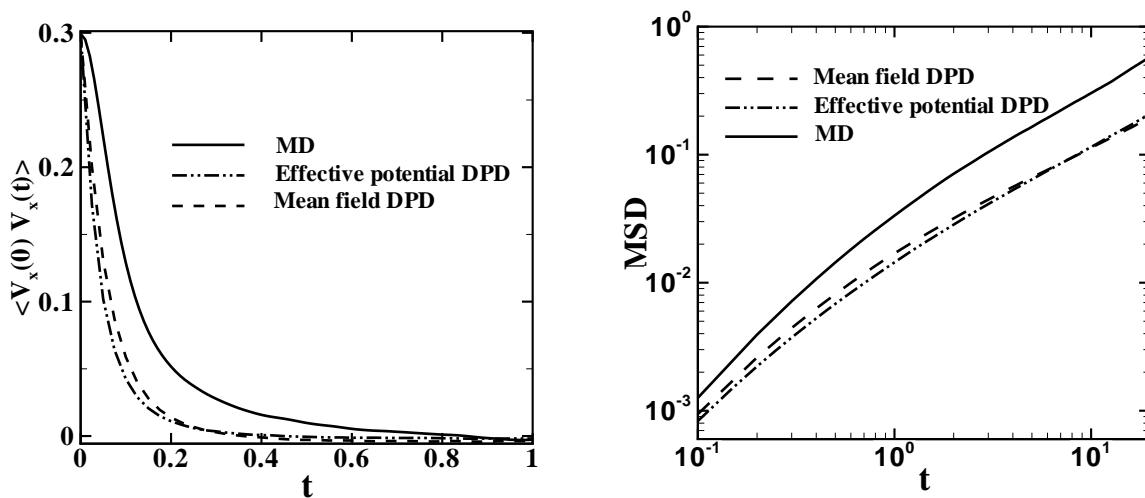


Figure 2.16: Velocity correlation function (left) and mean square displacement (right) measured by MD, effective potential  $V_{eff}(r)$  and mean field potential  $\langle V(r) \rangle$  for  $R_g = 1.2$ ,  $k_B T = 3.0$ ,  $N_c = 10$  and  $\rho = 0.8$ .

The mean, dissipative and random forces needed for the motion of the CG particles are extracted from the microscopic simulation. In particular, the mean force field is approximated by the ensemble average of the pairwise atomistic force between two clusters, and we find that its corresponding potential is proportional to the number of particles per cluster. We also approximated the memory kernel of the dissipative force with two different assumptions, leading to Langevin Dynamics and Dissipative Particle Dynamics (DPD), the latter endowed with two thermostats. While both models produce the same static properties, the Langevin model requires extra hydrodynamic information as input to produce the correct dynamic properties. On the other hand, DPD seems to be a good candidate for reproducing the correct mass and momentum transport properties. Compared to the MD results, the DPD results can approximate the dynamic properties reasonably well when the many-body effect of microscopic system is not too strong (e.g., for small  $R_g$  or semi-dilute system). However, the DPD model is not so successful when the many-body effect is very strong, i.e., for large density and  $R_g$ . We note that we also tested DPD with a single thermostat, i.e. neglecting the perpendicular contribution as it is typically done in standard DPD simulations. In that case, we did not achieve as good in accuracy for the dynamic properties for the small  $R_g$  cases as we did with the two-thermostat DPD but the results for the high  $R_g$  cases were slightly better.

This work provides a general framework for constructing a “bottom-up” mesoscopic simulation directly from the microscopic level, with explicit relationships between the two hierarchies. It can be extended to the mesoscopic description of complex fluid systems in the dilute and semi-dilute regime, e.g., star polymers, flexible polymer chains and mixture of polymer and colloid systems. The friction coefficients can be extracted from microscopic *sample* systems in pilot simulations within affordable computation time. Hence, coarse-grained simulation of a large system at the mesoscopic level can be conducted with the various dynamic properties evaluated directly, i.e., without any scaling ambiguities.

We note, however, that in the present study the friction coefficient was computed with data from *equilibrium* MD simulations and this may affect the computation of the dynamic viscosity, which was obtained here based on CG simulations of a periodic Poiseuille or Couette flow. It will be interesting in the future to investigate whether improved predictions of the dynamic viscosity can be achieved if the friction coefficients are based on non-equilibrium MD simulations. We also note the similarity of the “parallel-normal” thermostat in the current work with a similar thermostat employed in the single-particle DPD version in [120, 38] where a shear drag coefficient is imposed explicitly.

Another natural extension of this work is to construct friction force models, where a more sophisticated mean force field is implemented in the coarse-grained system. In the high density regime, the pairwise mean field in this study may not be adequate to describe the full coarse-grained potential field  $U_{CG}(\mathbf{R}^K)$ , leading to the overestimation of the memory kernel of the dissipative term. In these cases, a mean field that incorporates the “many-body” information may lead to a more accurate dissipative force and therefore more accurate prediction of the dynamic properties.

Finally, rather than a constrained microscopic system, it would be interesting to coarse grain the unconstrained LJ fluid by the DPD model of this study, especially with regards to the computation of the dissipative force term. In this direction, some work has been done in this direction is by Eriksson *et al.* [35], and also Flekkoy *et al.* [53]. It would be interesting to directly compute the dissipative force term of the coarse-grained LJ fluid by the method of this study and compare the DPD predictions of dynamic properties with those of the LJ fluid.

# Chapter 3

## No-slip and outflow boundary conditions for Dissipative Particle Dynamics

### 3.1 Introduction

As discussed in Chap. 2, Dissipative Particle Dynamics (DPD) is mesoscopic simulation method stemming from the coarse-graining (CG) procedure of the atomistic system. Compared with the MD method, the computation advantages of the DPD simulation originate from the soft potential field and the reduced number of simulation particles. Due to these features, the DPD method is an effective approach to simulate the hydrodynamics of the simple and complex fluid systems [60, 144, 43, 146, 129, 46] at the mesoscopic level. In contrast to MD, the larger spatial and time scales enable the DPD method to be used successfully in simulations of various soft matter systems, such as the polymer and DNA suspensions [144, 43, 146], platelet aggregation [129], and red blood cells in shear flow [128, 46] and in tube flow [44].

One of the fundamental problems for these hydrodynamic systems is how to impose proper boundary conditions (BCs) on non-periodic domains, e.g., on the fluid-

wall and outflow boundaries. For bulk systems, the Lees-Edwards boundary method [96] and the reverse Poiseuille flow method [10] have been proposed to simulate shear and Poiseuille flows, respectively. These methods employ periodic BCs in order to avoid explicit modeling of solid walls and to eliminate artificial density fluctuations. For non-periodic systems, where solid boundaries play an important role, several attempts have been made to simulate the wall-fluid interface. In general, there exist two main approaches. The first approach is based on the representation of a wall by frozen particles while the fluid-wall interactions are prescribed by the conservative and dissipative forces between the fluid and the wall particles, e.g., simple fluid [126], colloidal suspension [16] and a polymer solution between bounded walls [45]. In the second approach, the fluid-wall interactions are represented by certain effective forces with the combination of proper reflections to prevent particle penetration. In Ref. [130], a continuum-based approximation of the uniformly distributed wall particles is employed and combined with the bounce-back reflection to enforce no-slip BCs. In Refs. [127] and [49] a boundary force is computed adaptively to eliminate density fluctuations and excessive slip velocity near a solid wall, respectively.

However, to the best of our knowledge, little work has been done for the following two boundary problems. The first problem is how to impose no-slip BCs for time-dependent fluid flows using proper effective boundary forces rather than the wall particle representation. An oscillatory Stokes flow was simulated in [126] using the wall particle representation with adjusted force parameters. In Ref. [152], Couette flow with a transient start-up was simulated by creating a dynamic wall layer, where images of the DPD particles from the fluid layer next to the wall are inserted into the wall layer with a random shift. Both methods explicitly employ wall particles introducing additional computational cost and complexity. The second problem we would like to address is how to impose the outflow BCs for a fully developed fluid flow. Werder et al. [151] proposed an algorithm based on particle insertion/deletion, which relies on the knowledge of the velocity profile at the outflow. However, as we

know from continuum CFD, the outflow profiles are rarely known.

In this chapter, we focus on the two problems: (i) the no-slip BCs for unsteady flows, and (ii) the outflow BCs. In Section 3.2 we briefly describe the DPD method. In Section 3.3, we derive an effective boundary force from the total dissipative force on a single DPD particle in homogeneous shear flow. We show that the effective force can be implemented as the boundary force in the vicinity of the wall and is sufficient to impose no-slip BCs for unsteady flows while maintaining thermodynamic consistency near the boundary in contrast to an abnormal temperature profile in [131]. We validate the method by comparing the numerical results of transient Couette and oscillatory Stokes and Womersley flows with the corresponding analytical solutions. In Section 3.4, we propose the outflow boundary method which is similar to the Neumann BCs in CFD for fully developed flows. We validate this method through simulations of the backward facing step and arterial bifurcation flows in combination with the no-slip BCs introduced in Section 3.3. Furthermore, we test the outflow method for the case of a time-dependent flow system by considering the unsteady Womersley flow. We conclude with a brief summary in Section 3.5.

## 3.2 DPD method

In this chapter, we develop the boundary method within the framework of standard DPD system [71, 61]. In practice, different DPD force terms can be adopted depending on the individual physical systems, e.g., see Ref. [119] and Chap. 2. Nevertheless, the boundary method developed in the this chapter can be extended to those systems governed by different potential fields. In standard DPD system, the motion of each particle is governed by

$$\begin{aligned} d\mathbf{r}_i &= \mathbf{v}_i dt \\ d\mathbf{v}_i &= (\mathbf{F}_i^C dt + \mathbf{F}_i^D dt + \mathbf{F}_i^R \sqrt{dt})/m, \end{aligned} \tag{3.1}$$

where  $\mathbf{r}_i$ ,  $\mathbf{v}_i$ ,  $m$  are the position, velocity, and mass of the particle  $i$ , and  $\mathbf{F}_i^C$ ,  $\mathbf{F}_i^D$ ,  $\mathbf{F}_i^R$  are the total conservative, dissipative and random forces acting on the particle  $i$ , respectively. Under the assumption of pairwise interactions the DPD forces are given by the sum of the pair interactions with the surrounding particles as follows

$$\mathbf{F}_{ij}^C = \begin{cases} a(1.0 - r_{ij}/r_c)\mathbf{e}_{ij}, & r_{ij} < r_c \\ 0, & r_{ij} > r_c \end{cases} \quad (3.2)$$

$$\begin{aligned} \mathbf{F}_{ij}^D &= -\gamma w^D(r_{ij})(\mathbf{v}_{ij} \cdot \mathbf{e}_{ij})\mathbf{e}_{ij}, \\ \mathbf{F}_{ij}^R &= \sigma w^R(r_{ij})\xi_{ij}\mathbf{e}_{ij}, \end{aligned} \quad (3.3)$$

where  $\mathbf{r}_{ij} = \mathbf{r}_i - \mathbf{r}_j$ ,  $r_{ij} = |\mathbf{r}_{ij}|$ ,  $\mathbf{e}_{ij} = \mathbf{r}_{ij}/r_{ij}$ , and  $\mathbf{v}_{ij} = \mathbf{v}_i - \mathbf{v}_j$ .  $r_c$  is the cut-off radius beyond which all interactions vanish. The coefficients  $a$ ,  $\gamma$  and  $\sigma$  represent the strength of the conservative, dissipative and random force, respectively. The last two coefficients are coupled with the temperature of the system by the fluctuation-dissipation theorem [40] as  $\sigma^2 = 2\gamma k_B T$ . Here,  $\xi_{ij}$  are independent identically distributed (i.i.d.) Gaussian random variables with zero mean and unit variance. The weight functions  $w^D(r)$  and  $w^R(r)$  are defined by

$$\begin{aligned} w^D(r_{ij}) &= [w^R(r_{ij})]^2 \\ w^R(r_{ij}) &= (1.0 - r_{ij}/r_c)^k, \end{aligned} \quad (3.4)$$

where  $k = 1.0$  in the standard DPD method; however, other values of  $k$  have been used to increase the viscosity of the DPD fluid [43, 49]. In the current work we chose  $k = 0.25$ ,  $a = 25.0$ ,  $\sigma = 3.0$ ,  $\gamma = 4.5$ , and  $k_B T = 1.0$ . The number density of the fluid is  $n = 3.0$ .

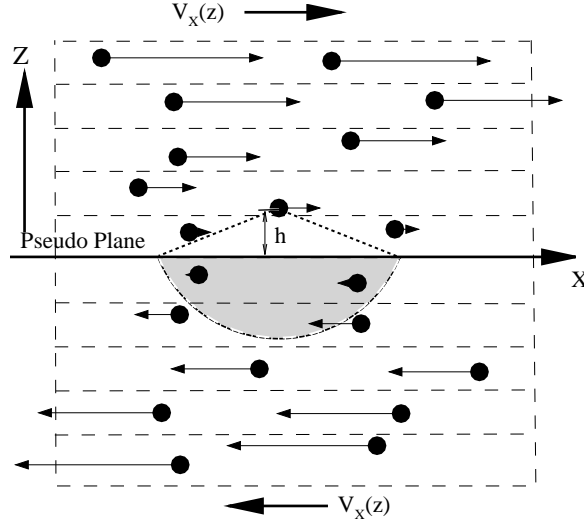


Figure 3.1: A sketch of the shear flow illustrated by DPD particles. The arrows represent the magnitude and direction of the particles' average velocities. The solid line represents a reference plane for the target particle while the total interaction of the target particle with the DPD particles below the reference plane (the gray area) is calculated using Eq. (3.8).

### 3.3 No-slip boundary conditions

#### 3.3.1 Boundary method

Generally, we need to impose a certain boundary force on the particles near the solid wall to impose the no-slip boundary condition. In Ref. [68], the boundary force is extracted from the fluid-solid interaction for Smoothed Particle Hydrodynamics (SPH). Similarly, we use an effective force to represent the presence of solid-wall next to DPD fluid. Rather than computing the force contribution from the wall directly, let us start with a DPD particle in shear flow. We define the flow direction  $\hat{x}$  in Fig. 3.1, and the shear rate  $\dot{\gamma} = du(z)/dz$ , where  $u(z) = \langle v_x \rangle$ . We calculate the force on the particle  $i$  exerted by the particles in the semi-spherical region satisfying  $(z_j - z_i) > h$ , i.e, the particles in the gray area drawn in Fig. 3.1. Using the continuum

approximation the total conservative force on the particle  $i$  can be evaluated as

$$\begin{aligned}
 \mathbf{F}_c(h) &= \sum_j f^C(r_{ij}) \mathbf{e}_{ij} \\
 &\sim n \int_{V_s/V_{ex}(h)} f^C(r) \hat{\mathbf{e}}(r) g(r) dV \\
 &= f_p(h) \hat{z},
 \end{aligned} \tag{3.5}$$

where  $g(r)$  is the radial distribution function of DPD particles,  $V_s/V_{ex}(h)$  represents the spatial part of the fluid domain shown by the gray area in Fig. 3.1. The  $x$  and  $y$  components of  $\mathbf{F}_c(h)$  vanish due to spherical symmetry. We note that the  $z$  component  $f_p(h)$  is exactly the pressure force proposed in [151] to eliminate density fluctuations in the vicinity of the wall boundary.

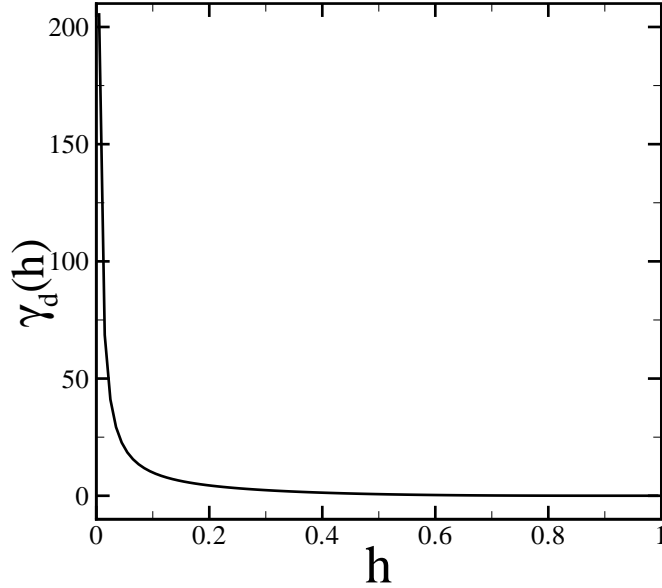


Figure 3.2: The dissipative force coefficient for a single DPD particle in shear flow with respect to the distance to the reference plane calculated by Eq. (3.10).

Next, we calculate the total dissipative force on the particle  $i$  as follows

$$\mathbf{F}_D(h) = - \sum_j \gamma(\Delta \mathbf{v}_{ij} \cdot \mathbf{e}_{ij}) \mathbf{e}_{ij}. \quad (3.6)$$

This force depends on the instantaneous velocity difference between particle  $i$  and  $j$ , but we notice that in the bulk shear flow the velocity difference satisfies  $\langle \Delta \mathbf{v}_{ij} \rangle = (\Delta v_x, 0, 0) = (\dot{\gamma} h \frac{r \cos \theta}{h}, 0, 0)$ . Thus, we can calculate the ensemble average of  $\mathbf{F}_D(h)$  as

$$\langle \mathbf{F}_D(h) \rangle = - \sum_j \gamma(\Delta v_x \hat{x} \cdot \mathbf{e}_{ij}) w^R(r_{ij}) \mathbf{e}_{ij}. \quad (3.7)$$

We further simplify this term by taking the continuum limit of the force as follows

$$\begin{aligned} \langle \mathbf{F}_D(h) \rangle &= - \int_{V_s / V_{ex}(h)} \gamma(\Delta v_x \hat{x} \cdot \hat{\mathbf{e}}(r)) w^R(r) \hat{\mathbf{e}}(r) dV \\ &= F_d(h) \hat{x}, \end{aligned} \quad (3.8)$$

where the  $y$  and  $z$  components vanish due to spherical symmetry. After the integration over the angles in the spherical coordinates the x-component is simplified as

$$\begin{aligned} F_d(h) &= - \frac{\pi n \gamma \Delta v_0}{4h} \int_h^{r_c} r^3 g(r) w^R(r) \left[ 1 - \left( \frac{h}{r} \right)^2 \right]^2 dr \\ &= -\gamma_d(h) \Delta v_0, \end{aligned} \quad (3.9)$$

where  $\gamma_d(h)$  is a function of the height from the particle  $i$  to the reference plane and  $\Delta v_0 = -\dot{\gamma} h$  corresponds to the average velocity difference between the particle  $i$  and the reference plane. The function  $\gamma_d(h)$  is shown in Fig. 3.2 and a best fit is given by

$$\gamma_d(h) = C_1(h + \delta h)^{-1} + C_2(h + \delta h)^{-2} + C_3(h + \delta h)^{-3}, \quad (3.10)$$

where  $C_1 = 0.8504$ ,  $C_2 = 9.6 \times 10^{-3}$ ,  $C_3 = 4.0 \times 10^{-4}$  and  $\delta h = 0.01$ .

Now we consider fluid flow above the reference plane replaced by a solid wall. Each fluid particle within the distance  $h < r_c$  from the solid wall is subject to the effective forces which compensate for the interactions with the “missing” particles under the reference plane (solid wall). A natural choice of the effective shear force is the ensemble average of the dissipative force as follows

$$f_{eff} = -\gamma_d(h)\dot{\gamma}h = -\gamma_d(h)(v_x - U) \quad (3.11)$$

where  $v_x$  and  $U$  are the velocities of the particle and the wall along the flow direction. *The main approximation we rely on is that the velocity profile near the solid boundary remains linear with a quasi-constant shear rate  $\dot{\gamma}$ .* In addition, for thermodynamic consistency a thermal random force is required to represent the fluctuation part of interactions with the “missing” particles, i.e.,

$$f_{rand} = \sigma_d(h)\xi, \quad (3.12)$$

where  $\xi$  is an i.i.d random variable with the Gaussian distribution and  $\sigma_d(h)^2 = 2k_B T \gamma_d(h)$ . We note that the analytical solution of the effective force shown in Eq. (3.9) and Eq. (3.11) applies only to the fluid near a planar surface, as these equations are not valid for a fluid system with arbitrary curvilinear boundary geometry. In principle, Eq. (3.9) should be replaced with integration over the corresponding curvilinear boundary. However, for simplicity, we can still use a “piecewise-plane” approximation even for complex geometries. The major assumption is that the near-wall profile can be approximated linearly. The corresponding force equation is not going to be “exact” for cases with arbitrary geometries, but it can be a very good approximation as shown in our numerical tests.

In summary, under the assumption of the *linear velocity profile* near the solid wall, no-slip BCs can be enforced through the three effective forces: the pressure force defined in Eq. (3.5) acting in the normal direction to the wall, and the dissipative

and random forces defined in Eqs. (3.11) and (3.12) acting along the flow direction. Thus, we define the boundary force  $f_{noslip}$  for the no-slip BCs as follows

$$\mathbf{f}_{noslip} = f_p \hat{z} + f_{eff} \hat{x} + f_{rand} \hat{x}, \quad (3.13)$$

where  $\hat{x}$  corresponds to the shear direction. Finally, to prevent penetration of the solid wall by fluid particles, specular reflection [151] is imposed for each DPD particle on the fluid-solid interface.

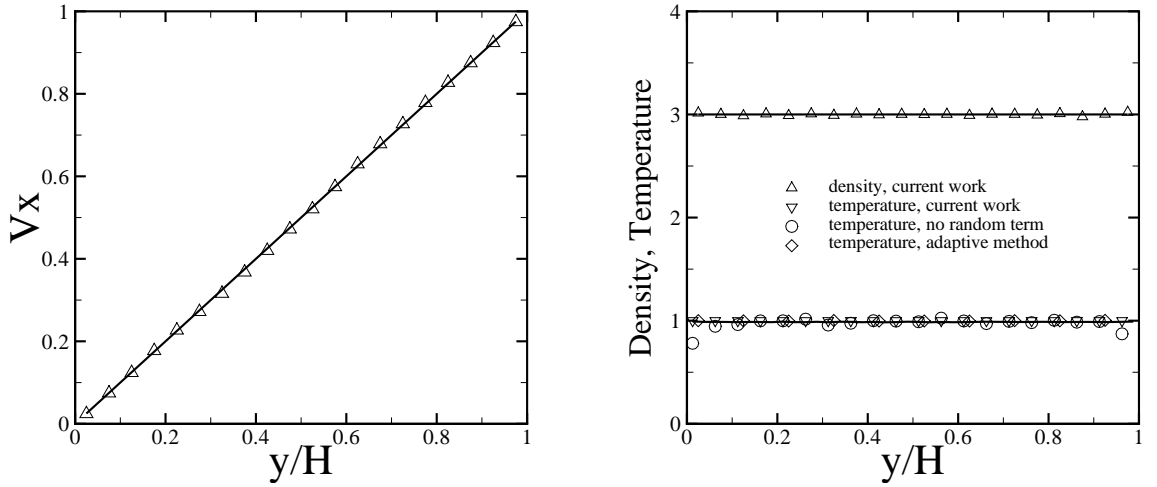


Figure 3.3: Left: velocity profile of the plane Couette flow. Right: density and temperature profiles. The triangle symbols represent the numerical results by DPD using Eq. (3.13). The circle symbols correspond to the numerical results by Eq. (3.13) without the random force term. The diamond symbols show the numerical results by the adaptive boundary method used in [49]. The solid lines are the analytical solution.

### 3.3.2 Numerical verification

The proposed boundary method is verified through simulations of different prototype flows. The first test is the steady plane Couette flow. The DPD fluid is confined between two parallel plates placed at  $y = 0$  and  $y = 10$  with periodic BCs imposed

along the other two directions. The velocity of the upper plate is  $U = 1.0$  and that of the lower plate is  $U = 0.0$ . The parameters of the DPD fluid are specified in section 3.2. Fluid particles near the two boundaries are subject to the velocity-dependent force  $f_{eff}(v_x - U)$  described in the previous section. The system is integrated over  $5 \times 10^4$  time steps with the time step  $dt = 5 \times 10^{-3}$ . Statistical averaging is performed over the second half of the simulation. Fig. 3.3 shows the velocity, density and temperature profiles across the flow. The no-slip BCs are satisfied and the velocity profile is in excellent agreement with the analytical solution. Moreover, the density and temperature profiles are uniform across the computational domain showing no density fluctuations and verifying the thermodynamic consistency of the boundary method. The effective boundary forces mimic a system which can be viewed as a part of the unbounded shear flow whose bulk properties are successfully recovered. The boundary method was also tested for the case of steady Poiseuille flow, and the numerical results agree well with the corresponding analytical solution.

Next, the no-slip BCs are tested for the three unsteady flows: (i) sudden start-up of the Couette flow; (ii) Stokes flow over an oscillating plate; (iii) plane Womersley flow. For the first test the DPD fluid is confined between two parallel plates placed at  $y = 0$  and  $y = 20$ . The size of the computational domain is  $20 \times 20 \times 40$  with periodic BCs along the  $x$  and  $z$  directions. The viscosity of the DPD fluid is equal to  $\nu = 0.54$  measured by the periodic Poiseuille flow method [10]. To improve the statistical averages of the DPD results we run ten independent replicas of the DPD system with different initial conditions. The initial state of each replica is obtained by running them independently for several hundred time steps with the velocity of both the upper and lower plates set to zero. Then, the velocity of the upper plate is set to  $U = 1.0$  at the time  $t = 0$ , while the velocity of the lower plane is kept at  $U = 0.0$ . The velocity profile of each replica is recorded as a function of time and the final result is obtained by taking the ensemble average of all replicas. Figure 3.4 shows the simulation results and the corresponding analytical solution for

the transient Couette flow at various times. The DPD results agree well with the analytical solution for different times. As time increases the flow converges to the steady case shown in Fig. 3.3. Note that the fluid velocity near the upper plate ( $y = 20$ ) is very sensitive to the BCs. Thus, even a small slip at the upper plate would greatly affect the velocity profiles.

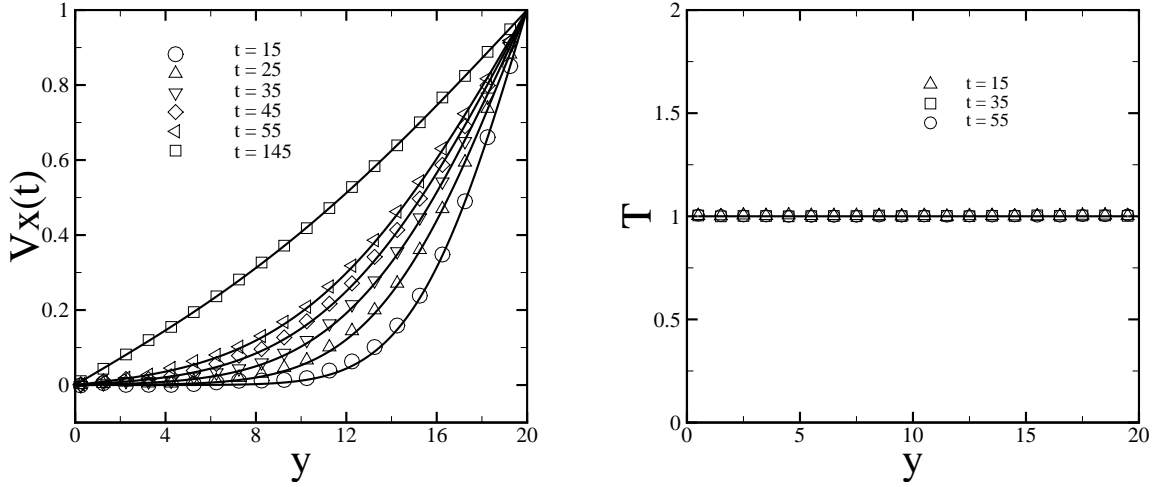


Figure 3.4: Left: velocity profiles of the sudden start-up of Couette flow at different times. The symbols correspond to the simulation results, while the solid lines represent the analytical solution of the Navier-Stokes equation. Right: instantaneous temperature of the system at different times.

The second test case is the oscillatory Stokes flow over a flat plate, where the velocity of the lower plate changes according to the time-dependent function  $U(t) = \sin(\Omega t)$  with  $\Omega = 2\pi/40$ . The upper plate has velocity  $U(t) = 0$  and is placed at  $y = 20$  which is far enough from the lower plate to yield a good approximation for the semi-bounded oscillatory Stokes flow. The DPD simulations are run over 80 periods and the statistical average of velocity is accumulated over the last 40 periods at different times. In Fig. 3.5 the simulation results are compared with the analytical solution [121] given by

$$U = \exp(-Y/\sqrt{2}) \sin\left(T - \frac{Y}{\sqrt{2}}\right), \quad (3.14)$$

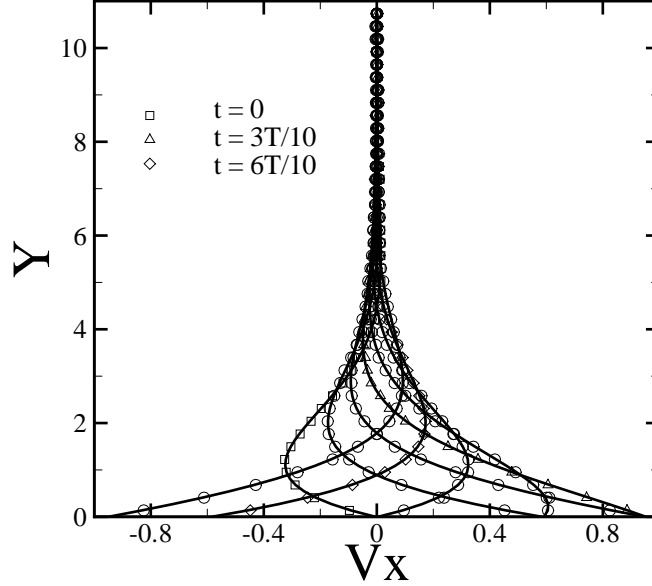


Figure 3.5: Velocity profiles of the oscillatory Stokes flow at times  $t = \frac{k}{10}T$ , where  $k = 0, 1, 2, \dots, 7$  and  $T$  is the oscillation period. The symbols are the numerical results, while the solid lines represent the analytical solution given in Eq. (3.14).

where  $Y = y(\nu/\Omega)^{-1/2}$  is the dimensionless distance, and  $T = \Omega t$  is the oscillation period. Note that Eq. (3.14) is derived for a semi-infinite system, however the dimensionless height of the upper plate in simulations is  $H = 10.87$  which is sufficient to recover the analytical solution as illustrated in Fig. 3.5.

Finally, we apply the proposed boundary method to a time-dependent pressure-driven flow. The computational domain assumes the same size as the plane Couette flow, where DPD particles are confined between two plates placed at  $y = 0$  and  $y = 20$  with periodic BCs imposed along the  $x$  and  $z$  directions. The flow is driven by a time-dependent body force on each particle in the  $x$ -direction  $f_{body} = f_0 + f \cos(\Omega t)$ , which is equivalent to a pressure gradient  $dP/dx = n f_{body}$ , where  $n$  is the density of the DPD fluid. The no-slip BCs are imposed on both plates. In the continuum

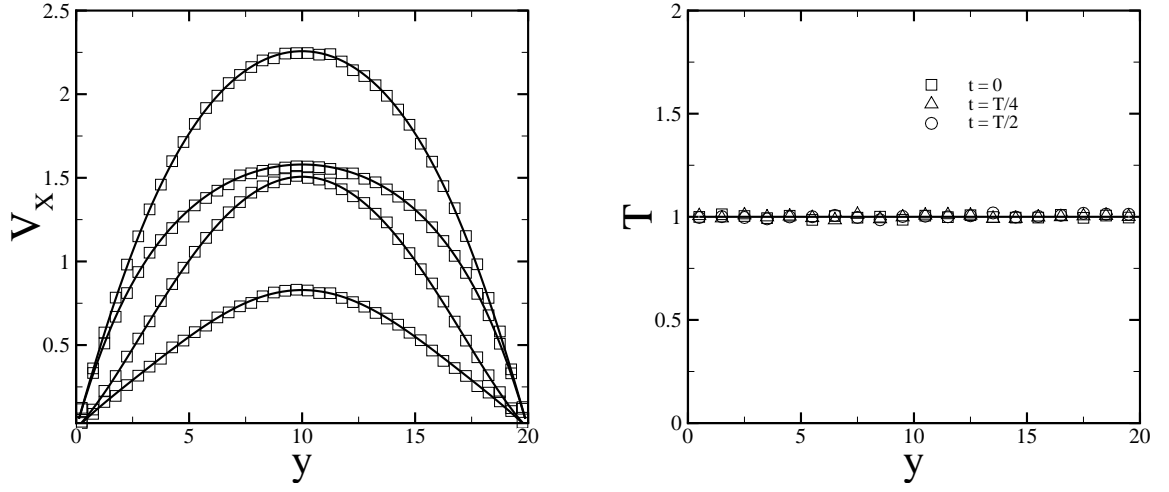


Figure 3.6: Left: velocity profiles of the flow driven by an oscillating pressure gradient. The symbols, from the bottom to the top, correspond to the simulation results obtained at  $t = \frac{k}{4}T$ , where  $k$  equals to 1, 0, 2, 3. The solid lines represent the exact solution for the Womersley flow given in Eq. (3.15). Right: instantaneous temperature of the DPD system at different times.

limit, this flow is called the Womersley flow with the analytical solution given by

$$\begin{aligned}
 u(h, t) = & \frac{p_0 h^2}{2\mu} + \frac{p^*}{\Omega n} \sin(\Omega t) - \frac{p^*}{\Omega n} \frac{1}{x_1^2 + x_2^2} \times \\
 & \{ [x_1 \cos(\alpha h) \cosh(\alpha h) + x_2 \sin(\alpha h) \sinh(\alpha h)] \sin(\Omega t) \\
 & - [x_2 \cos(\alpha h) \cosh(\alpha h) - x_1 \sin(\alpha h) \sinh(\alpha h)] \cos(\Omega t) \},
 \end{aligned} \tag{3.15}$$

where  $p_0 = f_0 n$ ,  $p^* = f n$  are the amplitude of the steady and oscillating pressure gradient respectively;  $h$ ,  $\alpha$ ,  $x_1$  and  $x_2$  are defined by  $h = \frac{2y}{H} - 1$ ,  $\alpha = \frac{H\sqrt{\Omega/\nu}}{2\sqrt{2}}$ ,  $x_1 = \cos \alpha \cosh \alpha$  and  $x_2 = \sin \alpha \sinh \alpha$ . For the DPD simulations we choose  $f_0 = 0.0167$ ,  $f = 0.05$  and  $\Omega = 2\pi/80$ , and the statistical average is collected over the last 40 periods. Figure 3.6 shows the velocity and temperature profiles of the Womersley flow at different times. The numerical results are in good agreement with the analytical solution.

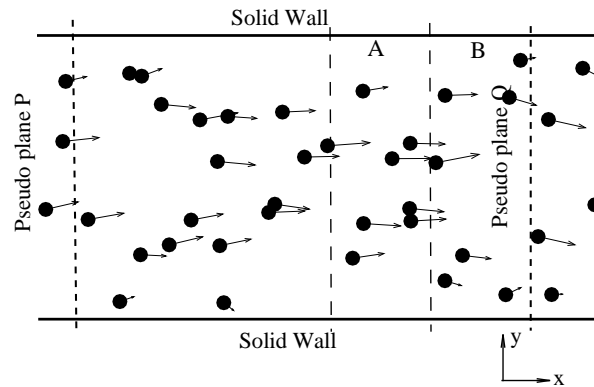


Figure 3.7: A sketch of the domain of an open flow system. The solid lines are the wall boundaries. The plane P represents the inlet through which DPD particles enter the domain with a specified velocity profile. The plane Q represents a pseudo-plane where the flow is fully developed. A and B correspond to two regions adjacent to the plane Q, where the flow is also fully developed.

## 3.4 Outflow boundary conditions

In this section, we consider different flow systems with non-periodic BCs, where inflow and outflow boundary conditions have to be imposed. Rather than imposing the strong Dirichlet BCs with a velocity profile explicitly specified at the outflow boundary [151], we explore the weak condition as in the standard CFD methods, where the BCs are implicitly imposed under the assumption that the flow is fully developed. Unlike the CFD methods, in DPD it is not straightforward to impose explicitly pressure values at the outflow boundary. Instead, if the pressure value and the flowrate at the outflow are approximately in-phase, we can impose the flowrate at the outflow boundary.

### 3.4.1 Boundary method

For a particle fluid system with non-periodic open boundaries the two physical properties need to be controlled are: the flow rate at the inflow/outflow boundaries and the velocity gradient at the outflow similarly to the fully developed condition in CFD. Let us consider the open fluid system shown in Fig. 3.7. We place a pseudo-plane  $P$  perpendicular to the flow direction. From the macroscopic perspective the flow flux through the plane is determined by the velocity profile at the plane  $P$ . In practice, this plane can be modeled as an inflow with a specified velocity profile. Inflow at the plane  $P$  can be simulated by inserting DPD particles into a near boundary layer according to the local particle flux. Without loss of generality, we consider a local area  $dA$  on the plane, and define  $N_A$  as the number of DPD particles to be inserted into the plane  $P$  at the area  $dA$  according to the following equation:

$$N_A^i = N_A^{i-1} + n\delta t dA v_n, \quad (3.16a)$$

$$N_A^i = N_A^i - 1, \text{ if } N_A^i \geq 1, \quad (3.16b)$$

where  $i$  is the timestep of the simulation,  $n$  is the number density of the DPD fluid, and  $v_n$  is the local normal velocity at the inflow plane. When Eq. (3.16b) is executed (it can be executed several times if  $N_A^i > 1$ ), one DPD particle will be inserted next to the plane  $P$  at the local area  $dA$ . The velocity of the inserted particle is generated according to the Maxwellian distribution with known temperature of the system and local boundary velocity. In general, the position of the inserted particle at  $dA$  has to be generated by the USHER algorithm [28] to minimize the local thermal disturbance due to the inserted DPD particle. However, we omit this procedure in practice since we found that the system remains stable with random insertions due to the soft interactions between DPD particles. The disturbances on the local number density due to insertions is on the order of 5%.

Next, we consider the region of the fluid system where the flow is fully developed. Let us place another plane  $Q$  in this region and consider the two regions  $A$  and  $B$  adjacent to the plane, as shown in Fig. 3.7. Physically, there should be no macroscopic difference between  $A$  and  $B$  since the flow is fully developed in this region, i.e., the macroscopic velocity should be identical in the two regions. In practice, we model this pseudo-plane as the outflow BCs. The DPD particles which pass through this outflow plane are deleted from the system. To control the flow rate at the outflow and eliminate any velocity differences between the two regions ( $A$  and  $B$ ) we apply an *adaptive* force on the DPD particles near the outflow as follows

$$f_{out}^k(h) = \beta^k(1 - h/r_0)^p + \gamma^k f_{press}(h), \quad (3.17a)$$

$$\beta^{k+1} = \sum_{\sigma=0}^q \beta^{k-\sigma} + \xi(v_A^k - v_B^k), \quad (3.17b)$$

$$\gamma^{k+1} = \gamma^k + \kappa(\phi^k - \phi_0), \quad (3.17c)$$

where the first term of the adaptive force eliminates the velocity difference between the two regions and the second term imposes proper flow rate at the outflow bound-

ary. The parameters  $k$ ,  $\xi$ , and  $\beta^k$  are the iteration number, the relaxation parameter, and the adaptive coefficient, respectively. Also  $h$  is the distance from a particle to the outflow plane, and  $r_0$  defines the total width of regions  $A$  and  $B$  together. In this work,  $r_0$  is chosen to be the cutoff radius of the DPD particle interactions if not specified otherwise;  $p$  defines the stiffness of the adaptive force and  $p$  is equal to 6. We choose this value by considering a static single DPD particle in uniform flow with the average velocity of  $u\hat{n}$ . We compute the dissipative force  $f_{norm}(h)$  on the target particle from the particles located in a semi-spherical region behind the pseudo-plane. The dissipative force scales as  $f_{norm} \sim f_n u$ , where  $f_n$  is best fitted by  $(1.0 - h/r_c)^6$ . Moreover,  $v_A^k$  and  $v_B^k$  in equation above are the average normal velocities in the regions  $A$  and  $B$  during the time between the  $(k - 1)$ th and  $k$ th iterations. Also,  $q$  is the total number of the under-relaxation steps, which is coupled to the number density of the system as follows

$$q^{k+1} = \begin{cases} q^k + 1, & \text{if } n^k < n - \delta n \\ q^k, & \text{if } n - \delta n < n < n + \delta n \\ q^k - 1, & \text{if } n^k > n + \delta n \end{cases} \quad (3.18)$$

where  $n^k$  is the average number density during the  $k$ th iteration, and  $\delta n$  is the accepted deviation of the system's number density.

The second adaptive force term in Eq. (3.17a) controls the flow rate at the outflow, where  $\phi^k$  represents the instantaneous flux at the outflow and  $\phi_0$  corresponds to the desired flux value;  $f_{press}(h)$  is the pressure force defined in Eq. (3.5). We note that for fluid systems with a single outflow boundary, this term can be neglected. However, for flows with multiple outflows (e.g., arterial bifurcations), this term is necessary to impose the desired flux value at each outflow boundary. In addition to  $f_{out}$  the pressure force defined in Eq. (3.5) is applied on fluid particles near the inflow and outflow planes, which compensates for the “missing” fluid part outside

the computational domain.

We note that our method of inserting particles is different from that in [151], where each particle that left the system is re-inserted at the inflow boundary, and hence the number density of the system is strictly conserved. In this work DPD particles are inserted at the inflow plane with no dependence on the number of particles removed. For the insertion method of [151] we found that the desired flux prescribed by the velocity profile at the inflow depends strongly on the number of particles leaving the system, and therefore the numerical system may be unstable. In the current method the instantaneous number density is not strictly conserved, however the converged density remains within the pre-specified tolerance ( $\delta n = 0.002n$ ) as shown in the next section.

### 3.4.2 Simulation results

The first test of the described method is the plane Poiseuille flow in combination with the no-slip method proposed in section 3.3.1. The computational domain is similar to that shown in Fig. 3.7 with periodic BCs in the  $z$  direction. The fluid is confined between two walls placed at  $y = 0$  and  $y = 10$  and the inflow and outflow planes are placed at  $x = 0$  and  $x = 20$ , respectively. DPD particles are inserted at the inflow according to the parabolic velocity profile given by

$$v_x(y) = v_0 \left[ 1.0 - \left( \frac{2y}{H} - 1 \right)^2 \right], \quad (3.19)$$

where  $v_0 = 1.0$  and  $H = 10$ . To impose the no-slip BCs at the walls particles near the walls are subject to the no-slip force defined in Eq. (3.13). In addition, particles near the outflow plane ( $x = 20$ ) are subjected to the adaptive outflow boundary force. Specifically, the outflow region was divided into 20 bins across the flow in the  $y$ -direction and each bin was further divided into two sub-volumes, labeled as  $A$  and  $B$ . The velocity in each sub-volume  $v_A$  and  $v_B$ , as well as the number density of the

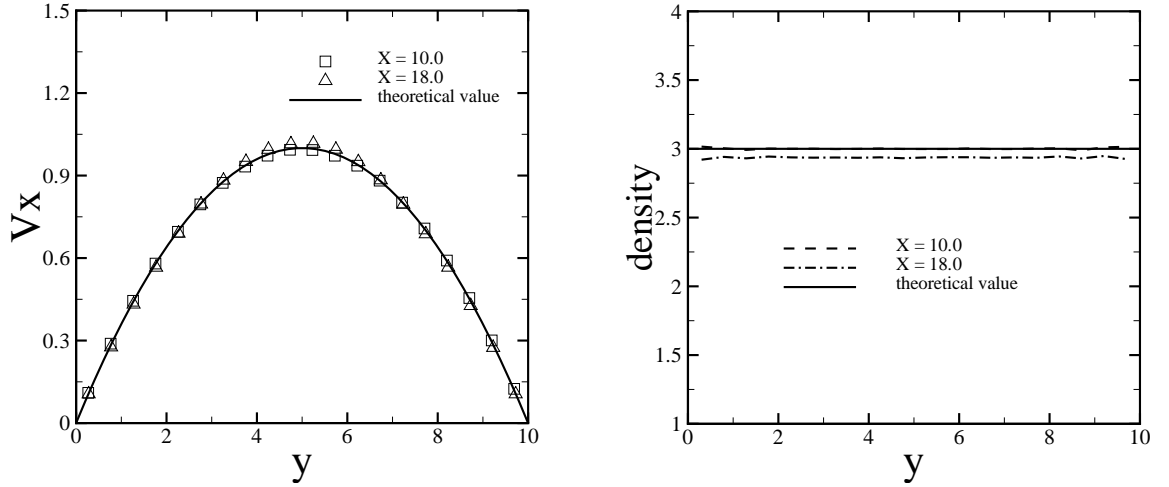


Figure 3.8: Velocity profiles (left) and density profiles (right) of the fully developed Poiseuille flow. The DPD results are shown for the planes  $x = 10.0$  and  $x = 18.0$ . The solid lines correspond to the analytical solution.

system, are sampled during the time between two consecutive iterations. The flow converges within approximately 100 iterations, where one iteration corresponds to 100 time steps. Statistical averaging is performed during  $1 \times 10^4$  time steps after steady state is achieved.

Physically, this system represents a part of the fully developed Poiseuille flow given by Eq. (3.19). Therefore, a parabolic velocity profile is expected in the downstream region as in upstream. Fig. 3.8 shows velocity and density profiles obtained at the planes in the middle of the system at  $x = 10.0$  and in the outflow region at  $x = 18.0$ . The simulation results agree well with the prescribed inflow profile. The fluid density at the outflow ( $x = 18.0$ ) is slightly lower ( $\rho = 2.94$ ) than the exact number density due to a finite compressibility of the DPD fluid.

For a more quantitative analysis, we compute the pressure profile along the flow direction shown in Fig. 3.9. The DPD results agree well with the analytical prediction given by

$$v_{max} = \frac{H^2}{8\mu} \frac{dP}{dx}, \quad (3.20)$$

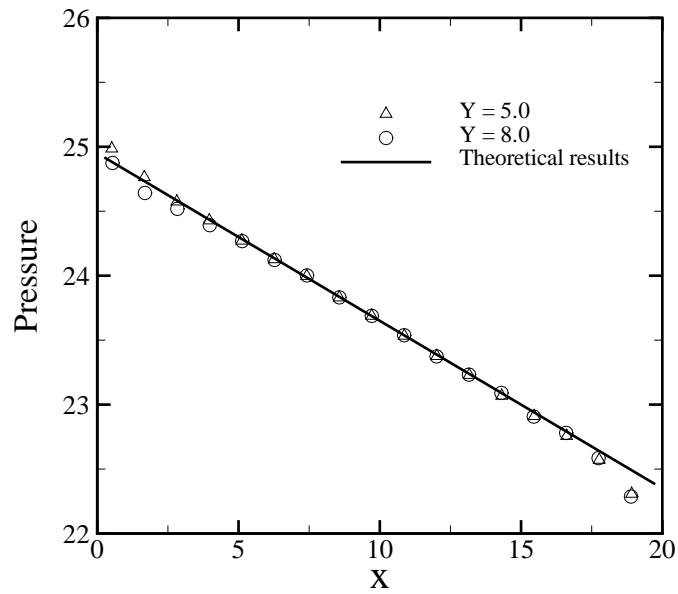


Figure 3.9: Pressure profile for the Poiseuille flow along the x direction. The symbols represent the numerical results by DPD extracted at  $y = 5$  and  $y = 8$ , and the solid line represents the analytical solution.

where  $H = 10$ ,  $\mu = 1.62$ , and  $v_{max} = 1.0$ . The small fluctuation at the inlet/outlet boundary is mainly due to the particle insertion and the superposition of the boundary force.

The compressibility of the DPD fluid can be approximated [60] as follows

$$dP/d\rho = k_B T + 2\alpha a\rho, \quad (3.21)$$

where  $\alpha = 0.101$  and therefore  $dP/d\rho = 16$ . The density difference between  $x = 10$  and  $x = 18$  predicted by Eq. (3.21) is approximately  $\Delta\rho = d\rho/dP\Delta P = 0.065$ , which agrees well with the simulation results. Moreover, the adaptive force  $f_{out}$  applied at the outflow serves as a perturbation term on the pressure force  $f_p$  defined in Eq. (3.5), which also contributes to the density fluctuations. Therefore, the proposed boundary method is valid for nearly incompressible fluid flows since the boundary forces are based on the global number density of a simulated system. Large density fluctuations due to finite compressibility are likely to void the method's applicability.

For the second test we consider the backward-facing step flow at different values of Reynolds number ( $Re$ ). The computational domain is illustrated in Fig. 3.10 where  $Re$  is defined as  $v_{max}H/\nu$ . A parabolic velocity profile defined by Eq. (3.19) is imposed at the inflow with  $v_{max} = 1.08$  and the height of the inlet channel is  $H = 10$ , while the step height is chosen to be  $S = \frac{H}{2}$ . For different  $Re$  numbers the height of the inlet and the size of step is scaled accordingly while  $v_{max}$  is fixed. The no-slip boundary condition is imposed by the dissipative force for all the DPD particles near the solid wall defined by Eq. (3.10). We compare DPD results with Navier-Stokes results obtained by the spectral element simulation solver NEKTAR [79].

Fig. 3.10 presents the simulation results obtained with DPD and with the spectral element method for  $Re = 20, 40$  and  $60$ . The streamlines agree well for the two methods. In addition, we extract several velocity and pressure profiles at different heights for a more detailed comparison with the NS solution shown in Figs. 3.10

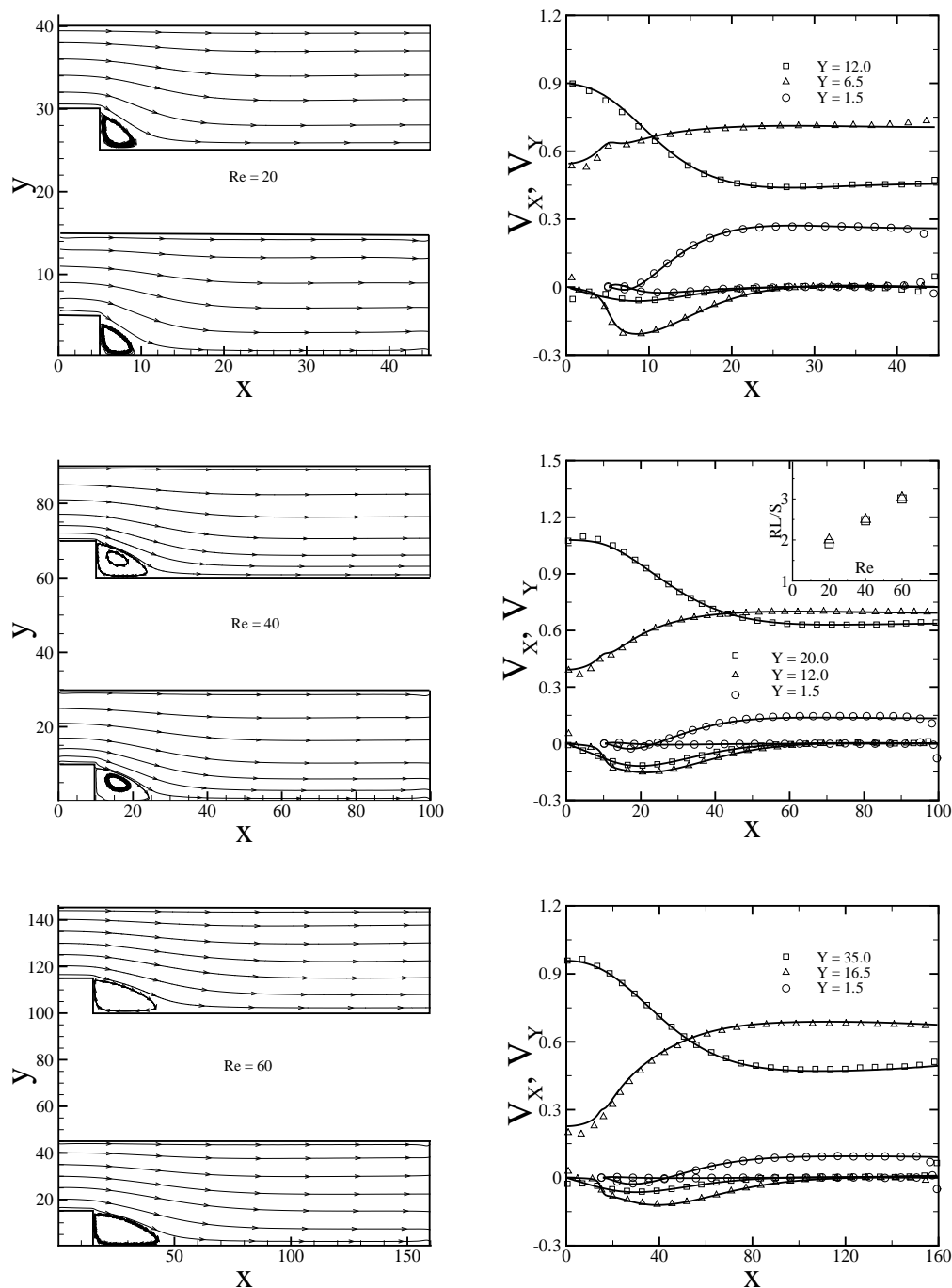


Figure 3.10: Streamlines (left) and velocity profiles (right) for backward facing step flow at  $Re = 20, 40$  and  $60$ . The velocity profiles are extracted at different planes as labeled in the plots. The symbols correspond to the DPD results and the solid lines represent the numerical solution of NS equation. The inset plot in the velocity plot of  $Re = 40$  shows normalized recirculation lengths of the step flow as a function of  $Re$  number. The square symbols correspond to the DPD results and the triangle symbols are the NS results.

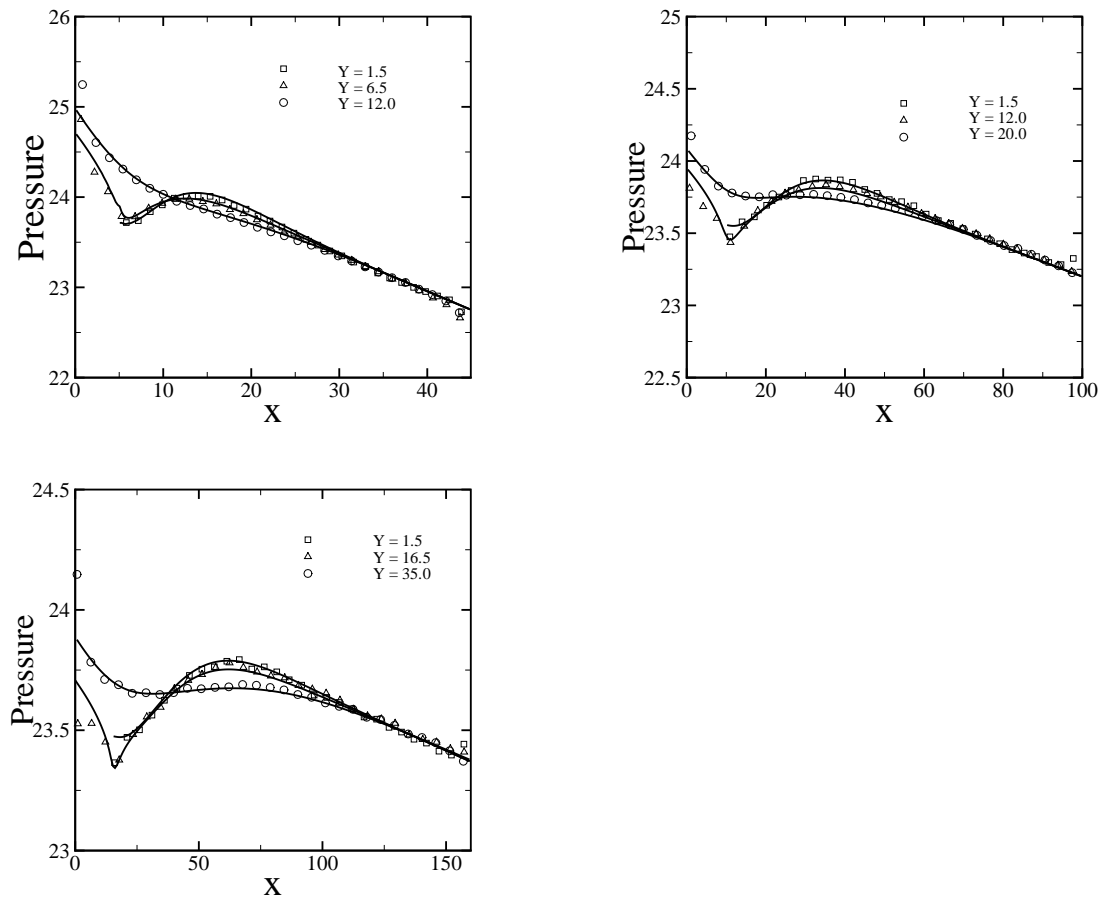


Figure 3.11: Pressure profiles for the step flow for Reynolds numbers  $Re = 20, 40, 60$ . The symbols represent DPD simulations, while the solid lines correspond to the NS results.

and 3.11. The DPD results are in good agreement with the NS solution with slight deviations near the inlet and outflow boundaries within the distance of  $4r_c$ . This appears to be due to the density fluctuations near those boundaries. At the inlet the number density is approximately 5% larger than the global density due to particle insertions. At the outflow region additional density fluctuations are introduced due to the adaptive force serving as a perturbation term to the pressure force term. We note that the velocity deviations at the outflow will not propagate upstream due to a finite speed of sound [36] in the DPD system. Therefore, the outflow region can be treated as a “buffer layer” region with perturbed number density, where the results may not be accurate. Moreover, we note that the shear rate varies (even changes sign) along the lower wall, which defines the recirculation length. In the inset plot of Fig. 3.10 we show the recirculation length of the step flow normalized by the step height  $S$  as a function of the Reynolds number. The values of the normalized recirculation lengths scale linearly with  $Re$  number showing good agreement with the spectral element method results. This further verifies that no-slip BCs are well imposed locally for different shear rates.

Next, we consider several flow systems with multiple outflow boundaries such as those encountered in the human arterial tree. Fig. 3.12 shows a bifurcated channel flow with two symmetric outflow boundaries. The channel is divided into two branches at  $L = 30$  with the branch angle  $\theta = \pi/3$ . The parabolic velocity profile defined in Eq. (3.19) is imposed at the inlet with  $v_0 = 0.72$  and  $H = 20$  and periodic BCs are imposed along the  $z$  direction. The outflow BCs are imposed separately at the two outflow boundaries with the adaptive force updated according to Eq. (3.17a). Fig. 3.12 shows velocity contours in both  $x$  and  $y$  directions. For comparison we also plot the numerical results of the NS equation with identical pressure values imposed at the two outflow boundaries. The DPD results show good agreement with the continuum results apart from the regions near the outflow boundaries and near the bifurcation point due to the density fluctuations. The fluctuations near the

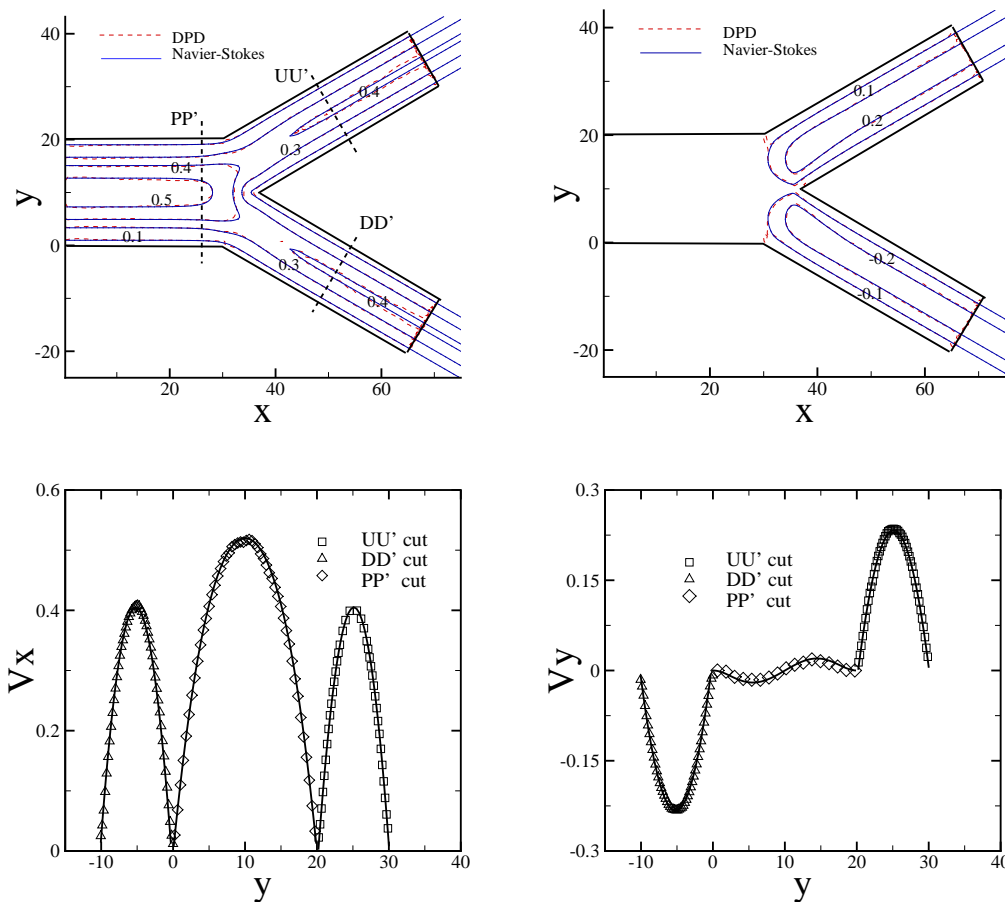


Figure 3.12: Top: 2D contour plot of velocity for both x (left) and y (right) directions for a symmetrically bifurcated channel flow obtained by DPD and NS equation. Bottom: 1D plot of the velocity profile at PP', DD', and UU' cuts. The symbols are the DPD results and the solid lines represent the NS results.

outflow are due to the adaptive force as discussed previously. The fluctuations near the bifurcation point are mainly due to finite compressibility of the DPD fluid.

Furthermore, we consider a bifurcated system with prescribed flow rate at each boundary as shown in Fig. 3.13. The planar channel is divided into two non-symmetric channels at  $L = 30$  with the bifurcation angle  $\theta = \pi/2$ . The widths of the two sub-channels scale as  $1 : \sqrt{3}$ . A parabolic velocity profile defined in Eq. (3.19) is imposed at the inlet with  $v_0 = 0.54$  and  $H = 20$ . This flow system resembles a small part of the arterial network, where additional information downstream may be unknown. To this end, we can prescribe the ratio of flow rates between the two outlets. The specified flow rate at each of the outlet is imposed through the force defined in Eq. (3.17a). The different ratio value corresponds to the different pressure values imposed on the outlets. On the other hand, the total flow rate of the two outlets is equal to the inflow rate to ensure mass conservation of the system. We consider two cases where the flow rates at the two outflow boundaries are 1:2 and 1:3, respectively. For the reference Navier-Stokes results, we use the method described in Ref. [59]. In both cases, the DPD results are in good agreement with the corresponding Navier-Stokes results as shown in Figs. 3.13 and 3.14.

The different flow rates controlled by our method correspond to different pressure values at the outflow boundaries. Therefore, we also look at the pressure distribution for different flow ratios. Fig. 3.15 presents the pressure distributions along the centerline of the channel marked as CC' in Fig. 3.13. The pressure difference between the two outflow boundaries is larger for the flow ratio of 1:2, since a larger flow rate for the upper branch corresponds to a larger pressure drop along the branch. For both cases the DPD results agree well with the NS solutions. The flow examples used in this study show that the outflow boundary method usually converges within a few thousand time steps. Therefore, we can extend this method to unsteady flows with a time-dependent inflow velocity profile. For a test we consider the pulsatile flow, where the fluid is confined between the plates at  $y = 0$  and  $y = 20$ , and the

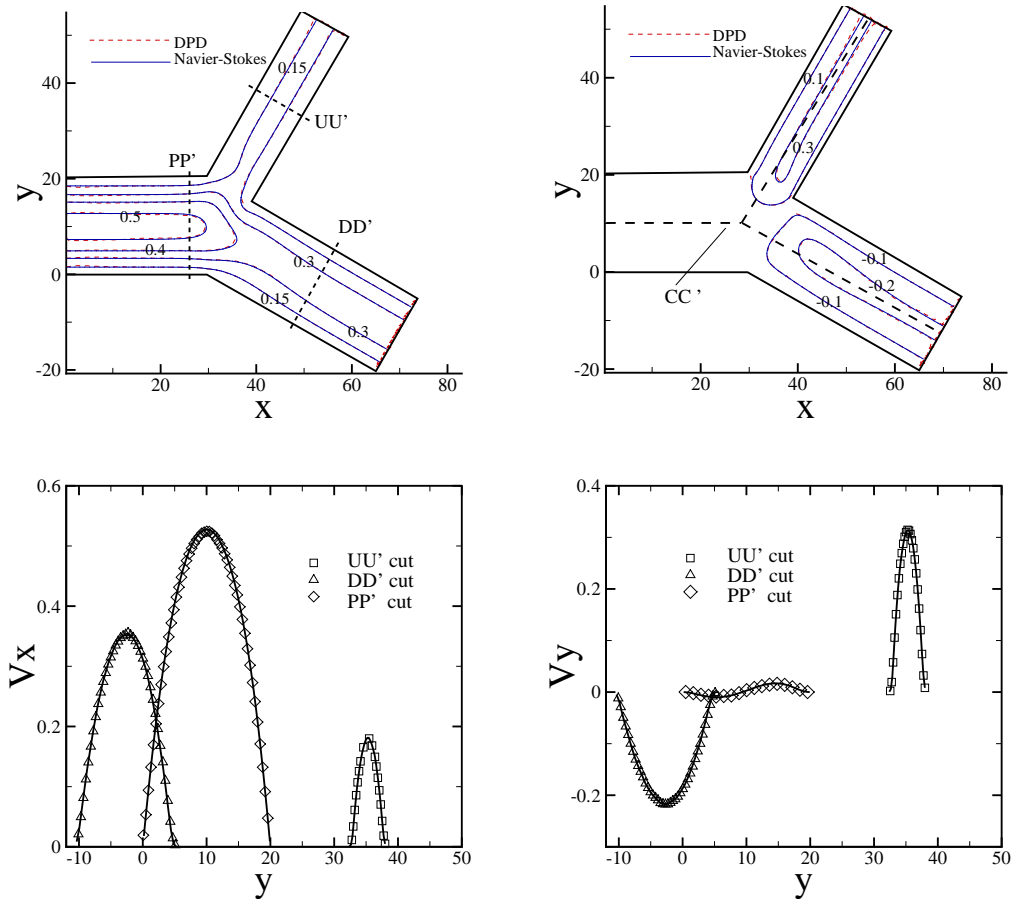


Figure 3.13: Top: 2D contour plot of velocity for both x (left) and y (right) directions for a non-symmetrically bifurcated channel flow obtained by DPD and NS equation. The flow rates of the two outflow boundaries scale as 1 : 2. Bottom: 1D plot of the velocity profile at PP', DD', and UU' cuts. The symbols are the DPD results and the solid lines represent the NS results.

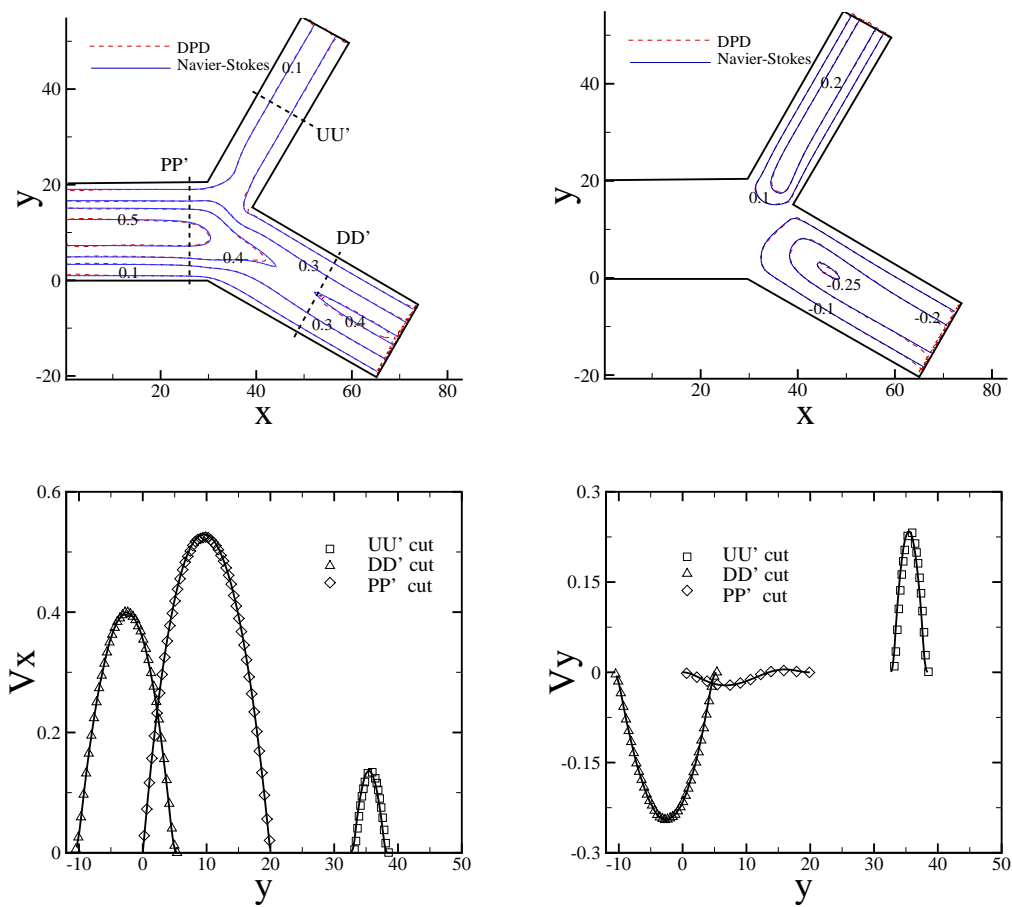


Figure 3.14: Top: 2D contour plot of velocity for both x (left) and y (right) directions for an non-symmetrically bifurcated channel flow obtained by DPD and NS equation. The flow rates of the two outflow boundaries scale as 1 : 3. Bottom: 1D plot of the velocity profile at PP', DD', and UU' cuts. The symbols are the DPD results and the solid lines represent the NS results.

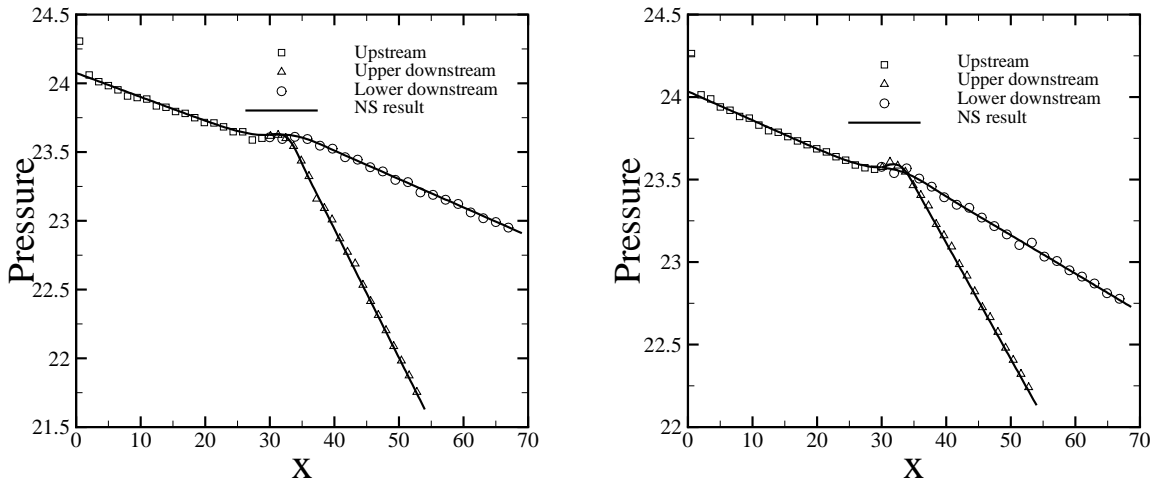


Figure 3.15: Pressure distribution along the centerline  $CC'$  of the channel shown in Fig. 3.13. The flow rate ratio at the outflow boundaries scales as 1 : 2 (left) and 1 : 3 (right). The solid line corresponds to the NS results.

inflow and outflow planes are placed at  $x = 0$  and  $x = 20$ , respectively. The inflow velocity profile is given by Eq. (3.15) with  $f_0 = 0.06$ ,  $f = 0.03$  and  $\Omega = 2\pi/200$ . The corresponding Womersley number  $\alpha$  is equal to 1.71, which is a typical value for biological flow systems [104]. The DPD particles are inserted next to the inflow plane using the instantaneous inflow velocity profile and the boundary force is updated according to Eq. (3.17a). Statistical average is taken over the last four periods. Fig. 3.16 (left) shows velocity profiles extracted at  $x = 10$  and  $x = 18$  at different times. The DPD results are in good agreement with the theoretical predictions. However, for flows with a higher Womersley number, the current method may not be sufficient to track instantaneous velocity profile. As shown in Fig. 3.16 (right) for the higher frequency  $\Omega = 2\pi/50$  ( $\alpha = 3.42$ ), the DPD results begin to deviate from the theoretical predictions. This appears to be due to a finite compressibility of the DPD fluid. Thus, the boundary information is not able to propagate through the computational domain with such high frequency.

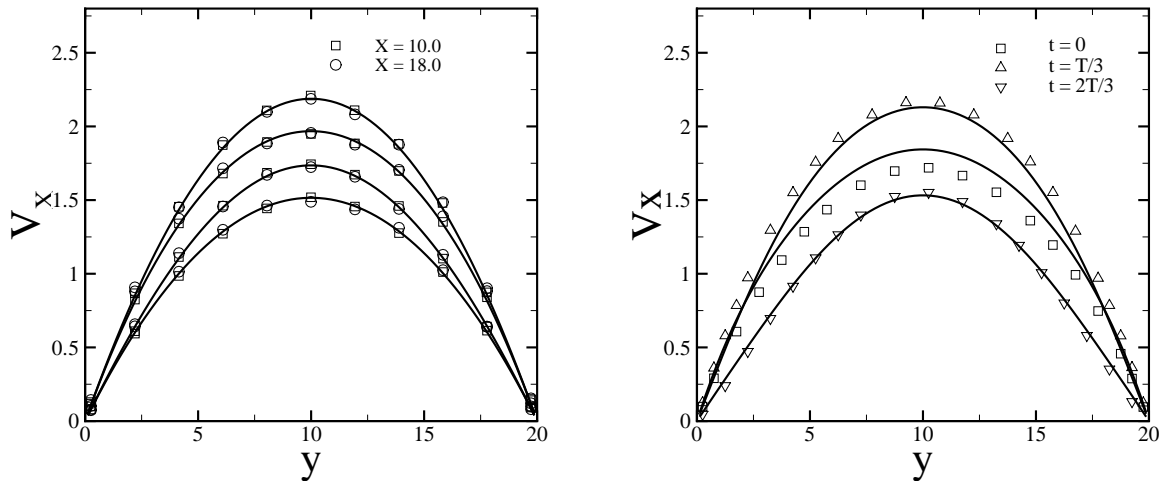


Figure 3.16: The velocity profiles extracted from the Womersley flow with  $\Omega = 2\pi/200$  (left) and  $\Omega = 2\pi/50$  (right). Left: the solid lines, from top to bottom, represent the theoretical predictions at  $t = T/4, 0, 2T/4$  and  $3T/4$ . The square and circle symbols represent the numerical results extracted at  $x = 10$  and  $x = 18$ . Right: the solid lines, from top to bottom, represent the theoretical predictions at  $t = T/3, 0, 2T/3$ , the symbols represent the DPD results extracted at  $x = 10$ .

### 3.5 Summary and Discussion

In this chapter two important issues on boundary conditions for particle simulations of fluid systems have been addressed: the no-slip BCs at a wall-fluid interface and the outflow BCs for non-periodic flow systems. We introduced two boundary methods validated for various flow problems. Starting from a single DPD particle in shear flow we computed the total dissipative interaction of this particle with surrounding particles. The dissipative interaction is computed as a function of the distance from the target particle to the pseudo-plane placed at different positions. For wall bounded systems, no-slip BCs are modeled by imposing the effective boundary forces (Eq. (3.13)) on DPD particles near the walls. Originated from the bulk shear flow, this boundary method can effectively impose no-slip BCs without artificial density and thermal fluctuations near the walls. The tested unsteady flows of the sudden start-up Couette, oscillatory Stokes and Womersley flows further validate the proposed

no-slip boundary method. The backward-facing step flow verifies that the method works well locally for different shear rates. Moreover, this method is free of boundary particles, and therefore it is more efficient in comparison with the method in [152].

We developed the outflow boundary method by considering a fully developed flow region of the bulk system. The BCs are weakly imposed under the assumption of the translational invariance of the velocity profile along the flow direction. In a non-periodic system the outflow boundary is modeled by the boundary force, which consists of two adaptive terms that control the flow rate at the boundary and eliminate the velocity difference in the region adjacent to the outflow boundary. Combined with the no-slip boundary method for fluid-wall interactions, the outflow boundary method is verified for the backward-facing step flow at different Reynolds numbers and for the bifurcated flow with different flow rates, which correspond to different pressure values at the outlets. The simulation results show good agreement with the corresponding analytical or reference solutions apart from the narrow regions near the outflow boundaries, where the velocity fluctuations of maximum 10% are observed due to the perturbation of the boundary force in that region. For quasi-steady flows where the pressure value and flow rate on the outlet boundary are approximately in-phase, the prescribed flow rate corresponds to specified pressure value on the outlet. This is obvious for a fluid system with a single outlet since the flow rate at the outlet equals to the inflow rate for mass conservation. However, for a fluid system with multiple outlets, the different flow ratio prescribed on the outlets corresponds to the different pressure values imposed on the outlets since the information farther downstream is unknown. Moreover, we test the current method for a time-dependent non-periodic flow system. The simulation results agree well with the analytical solution for the flow with Womersley number on the order  $O(1)$ , which is in the range of typical biological arterial flows [104]. The numerical results begin to deviate from the analytical solution for higher Womersley number due to finite compressibility (sound speed) *as well as* the out-of-phase condition between

the pressure value and the outflow rate.

As a conclusion, this chapter provides a general framework to impose different BCs. Even though we test the method for Newtonian fluids, our future goal is to apply such BCs to complex fluid systems such as blood flow. In the practice, the human blood vessels are far more complicated than a straight channel. Typical models for a part of the blood vessels usually contains complex topological structures such as bifurcations, which contains multiple outlets. To investigate these systems, more sophisticated methods for inserting molecules or cells have to be developed. Some related work has already been done in [14, 140]. It would be interesting to further explore how to impose proper BCs for these systems such that the dynamic flow and rheological properties can be correctly predicted.

# Chapter 4

## Mesosopic simulation of blood flow in small tubes

In Chap. 2, we discuss the intrinsic relationship between the DPD and the MD method by constructing a mesoscopic system from the microscopic system. In this chapter, we explore the application of the DPD method on the length scale near the mesoscopic-macroscopic transition. By simulating the red blood cell (RBC) suspensions in different tube systems, we identify a non-continuum to continuum transition as the tube diameter increases to above  $100\mu m$ .

### 4.1 Introduction

Due to the visco-elastic properties of the RBC membranes, blood suspensions exhibit non-Newtonian behaviors under physiological conditions. In homogeneous shear flow systems, blood suspensions show apparent shear thinning effect, which is well characterized by Chien [111, 22, 139] *et al.*. In Poiseuille flow systems, the cross-stream stress gradient drives the cells to migrate toward the centerline of the tube, leading to the inhomogeneous cell density distribution. In blood rheology, this effect results in the formation of a cell free layer (CFL) near wall, the Fahraeus-Lindquist ef-

fect with respect to different tube diameters, the inhomogeneous cell transportation (blood plasma skimming) at vessel junctions, *etc.*. Therefore, numerical modeling of blood flow requires proper incorporation of these non-Newtonian characteristics. Practically, this is often achieved by *explicitly* modeling of the RBCs as individual “capsules”, where proper visco-elastic properties are imposed on individual cell membranes. Using this approach, the major rheological properties of blood suspensions such as the bulk viscosity in shear flow, the apparent viscosity and CFL region in tube flow can be accurately captured, see Ref. [54, 48, 50, 33]. However, we note the scale of these simulation systems is often limited to  $O(10^3)$  RBCs. This is mainly due to the expensive modeling of the individual cells. Remarkably, Freund *et al.* [54] use a spectral boundary integral method to model the blood flow in a tube with diameter  $D = 11.3\mu m$ . Dupin *et al.* [33] construct a RBC model by Lattice Boltzman method and use this model to study blood flow of  $O(10^2)$  RBCs. Fedosov and Karniadakis [48] study the blood flow in tubes with diameter  $10 - 40\mu m$  using a multi-scale RBC model by DPD method.

Alternatively, other theoretical approaches have modeled the blood flow in large vessels by continuum methods [136, 116]. In these models, the blood flow is represented by separate cell-rich region and cell-depleted region, where different fluid properties are imposed through the continuous equations for each region. While it is widely believed that the blood flow can be treated by continuum Newtonian fluid in tube flow with diameter larger than  $200\mu m$ , the fidelity of the continuum approximation for smaller tube system is unclear. A question arises naturally: *is the homogeneous continuum approximation just a simplification for continuum modeling, or it is a natural result stemming from the length scale (macroscopic) limit of the mesoscopic blood flow system.* We address this issue in this chapter. In particular, we investigate whether the continuum assumptions built into such models are supported by results from the our mesoscopic simulations of blood suspensions, where individual RBCs are explicitly modeled. The tube flows of blood suspensions

[48] are expensive to simulate, and therefore it is desirable to know when simplified approaches are feasible. As the tube size is reduced toward the RBC diameter the CFL becomes the dominant feature, and the assumption of a core of homogeneous flow will become increasingly tenuous. Hence our goal is to determine the effective range of such approximations.

This chapter is organized as follows. In section 4.2 we analyze the micro-structures of the blood flow in different tube diameters. In section 4.3 we measure the local viscosity of the blood flow to uncover the way in which these suspension flows change as the tube diameter decreases. Using a continuum model with slip boundary velocity, we explore the possibility to model the blood systems with continuum approximation. We conclude in section 4.4.

## 4.2 Microstructure of blood flow

In this section, we investigate the micro-structure of healthy blood flow in tube systems with diameter ranging from  $20\mu m$  to  $150\mu m$ . The blood flow is modeled as a suspension of the individual red blood cells (RBCs) in blood plasma solution, whereas other components such as leukocytes and platelets are omitted in the present studies. The RBCs are represented by the multi-scale model developed by Pivkin *et al.* [125] and Fedosov *et al.* [46]. The blood plasma is modeled by a simple DPD fluid with dynamic viscosity  $\mu_p = 1.2 \times 10^{-3} P_a \cdot s$ .

### 4.2.1 Velocity and shear rate distribution

Fig. 4.1 shows the velocity distribution  $u(r)$  of the blood flow for tube flow with  $D = 20\mu m$  and  $D = 100\mu m$ . The dash lines represent the quadratic fitting of the numerical results. For  $D = 20\mu m$ , the velocity profile exhibits apparent deviation from the quadratic fitting. However, the velocity profile for the case of  $D = 100\mu m$  fits well with the parabolic profiles, except for the region of the cell-free layer near

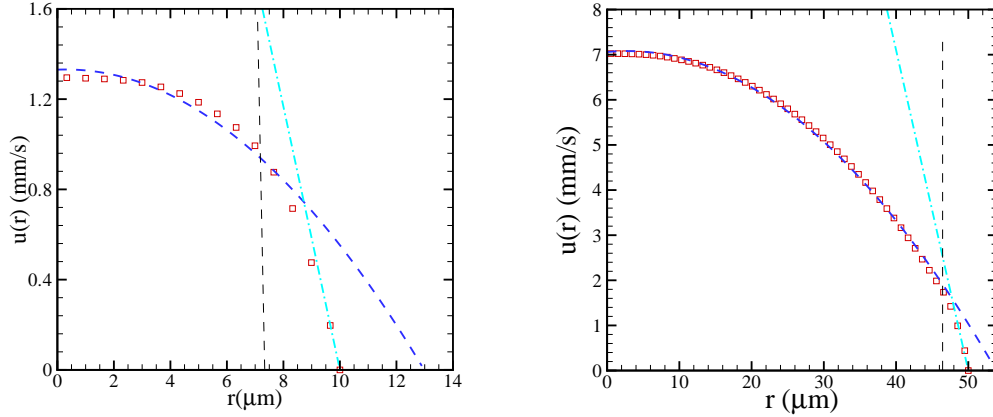


Figure 4.1: Velocity profiles for  $D = 20$  (left) and  $100\mu m$  (right) with  $H^T = 0.3$ . The blue dash curves represent the parabolic fitting to the simulation results. The data is also fitted with parabolic curves (blue dashed lines) and the tangent lines at the wall with slopes  $\tau_w/\mu$ , while the vertical dashed line indicates the cell-free layer thickness.

the blood channel where the blood plasma dominates. In this region, the velocity profile agrees well with the linear approximation  $du/dr = \tau_w/\mu$ , where  $\tau_w$  is the wall shear stress.

Using the velocity profiles, we compute the shear rate distribution of the blood flow for  $D = 20\mu m$  and  $D = 100\mu m$ , as shown in Fig. 4.2. Similar to the velocity profiles, the two systems exhibit different properties. For  $D = 20\mu m$ , the system can be roughly divided into two regions: a nonlinear region representing the blood core near the centerline and a linear region representing the cell free layer near the tube wall. On the other hand, for large tube size ( $D = 100\mu m$ ), the system exhibits three different regions: (i) the non-Newtonian flow region with shear rate smaller than  $60s^{-1}$ , (ii) the linear region between the centerline and the CFL with shear rate between  $60s^{-1}$  and  $250s^{-1}$ , and (iii) a linear region representing the CFL region. The inset plot shows two snapshots of blood flow obtained at  $r/R = 0.1$  and  $r/R = 0.85$  for  $D = 100\mu m$ , respectively. Due to the different local shear rates, the two snapshots exhibit different local configurations. For  $r/R = 0.1$ , the RBCs

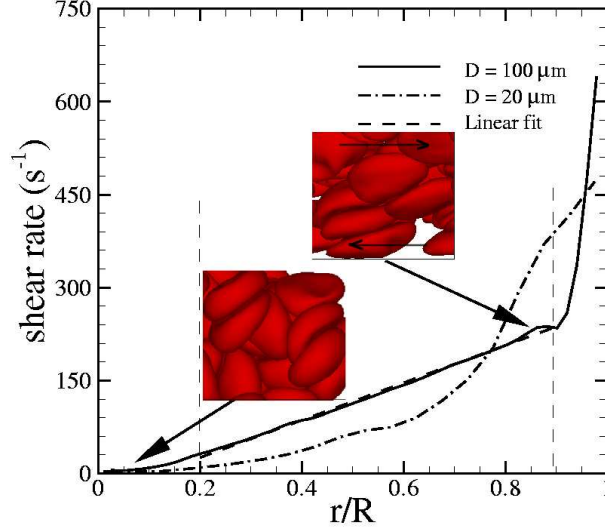


Figure 4.2: Shear rate distributions for blood flow in tubes of various diameters at  $H^T = 0.3$ . For  $D = 100 \mu m$  the vertical dashed lines indicate: the CFL thickness near the wall, and the limit of the linear portion of the distribution near the centerline.

exhibit close-packing state with near-spherical shape. For  $r/R = 0.85$ , the RBCs exhibit large deformation due to the high shear rate near the CFL region. We systematically investigate this issue in next section.

#### 4.2.2 Cell density and local hematocrit distribution

Due to the hydrodynamic interaction, the deformable RBCs tend to migrate towards the centerline of the channel, resulting in an inhomogeneous cell distribution along the radial direction as well as a cell depletion layer near the tube wall. Fig. 4.3 shows the snapshots of the blood flow cut through the center of the tube for  $D = 40 \mu m$  and  $D = 100 \mu m$  with  $H^T = 0.3$ . For both systems, the RBCs show close packing state with parachute shape near the tube center. On the contrary, the RBCs align with the flow direction at high shear rate region, followed by the CFL region near the tube wall.

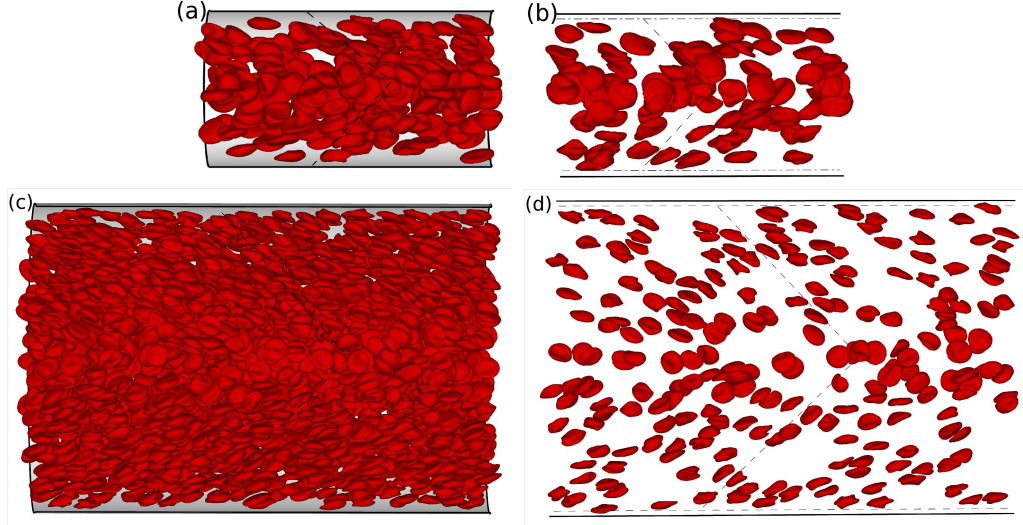


Figure 4.3: Central cut-plane snapshots along the tube axis for  $D = 40 \mu m$  ((a) and (b)), and  $100 \mu m$  ((c) and (d)) at  $H^T = 0.3$ . (a) and (c) are the half-tube images, while (b) and (d) are thin slices across the cut. CFL thickness is shown by dashed lines parallel to the walls.

To quantify these local variations, we measure the normalized RBC center distribution along the radial direction, as shown in Fig. 4.4. Three interesting points appear in this result. First, the cell densities exhibit maximum values near the tube center, which is consistent with the flat plug-like velocity profile near the tube center in Fig. 4.1. This feature is mainly due to the small local shear rate in that region, resulting in a better close packing of the RBCs. As  $r$  increases, these quasi-steady structures are gradually destroyed due to the stronger cell mixing effect induced by the larger local shear rate, accompanied with a lower local cell density. Second, the inhomogeneous distribution is more pronounced for small tubes ( $D = 20, 40 \mu m$ ): the cell density exhibits nearly monotonic decrease along the radial direction. On the contrary, a homogeneous region appears in large tube systems, which is reflected by the flat cell density value as shown in Fig. 4.4. We note that this result is also consistent with the linear shear rate distribution for  $D = 100 \mu m$  as shown in Fig. 4.2. Both results indicate that the blood flow exhibits isotropic properties in this region.

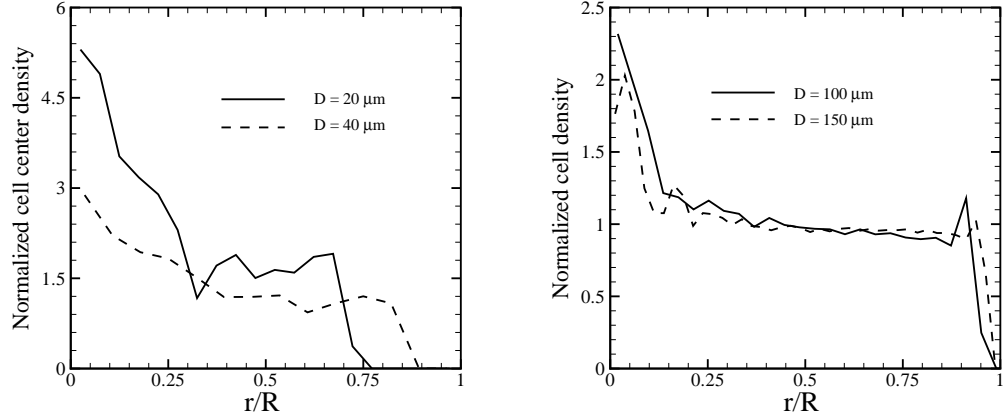


Figure 4.4: Radial RBC-density distributions normalized by the mean prescribed density for  $D = 20, 40 \mu m$  (left) and  $D = 100, 150 \mu m$  (right) for  $H^T = 0.3$ .

Finally, we note that the cell center distributions show limitation to characterize the local density. This is because the local cell volume contribution is not counted in the sampling process. This limitation is especially pronounced for small tubes with diameters comparable to the size of individual RBC (see the abnormal high value of the cell center density near  $r = 0$  for  $D = 20 \mu m$ .) .

To incorporate the local cell volume contribution, we define the local hematocrit  $H(r)$  by

$$H(r) = \frac{1}{2\pi L} \int_0^L \int_0^{2\pi} g(r, \theta, x) dx d\theta, \quad (4.1)$$

where  $g(r, \theta, x)$  is defined by

$$g(r, \theta, x) = \begin{cases} 1, & \text{if point}(r, \theta, x) \text{ is inside of a RBC,} \\ 0, & \text{if point}(r, \theta, x) \text{ is outside of RBCs.} \end{cases} \quad (4.2)$$

Following this definition, we directly measure the local blood volume fraction  $H(r)$  for the different tube flow systems, as shown in Fig. 4.5. For small tube diameters,  $H(r)$  shows similar tendency with cell center distribution as  $r$  increases.

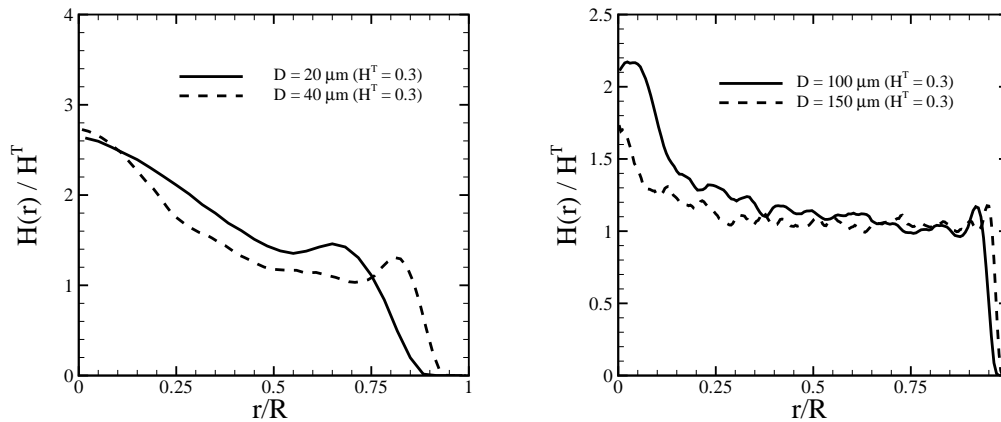


Figure 4.5: Local hematocrit distributions normalized by  $H^T$  for  $D = 20, 40 \mu m$  (left) and  $D = 100, 150 \mu m$  (right) for  $H^T = 0.3$ .

However, the artificial peak near the tube center is absent in the  $H(r)$  distribution. For large tube diameters, the variations between the  $H(r)$  and cell center distribution become small, both featured by a wide range of homogeneous distribution. This result is not surprising, since the RBC size effect becomes less important in the large tube systems.

### 4.2.3 Cell deformation and orientation

Due to the different local shear rates, the RBCs undergo various stretching and deformation along the flow direction. This is characterized by the different cell shapes shown in Fig. 4.3. To quantify this effect, we analyze the gyration tensor of the individual RBCs and compute the asphericity distributions (see Sec. 5.3.1 for detail definition) along the radial direction, as shown in Fig. 4.6. The horizontal dash line represents the asphericity value for the equilibrium biconcave shape. In the blood core region, the asphericity values are smaller than the equilibrium value, indicating that the RBCs in close packing structures keep a more spherical shape. This result is also consistent with numerical simulations of single RBC in Poiseuille

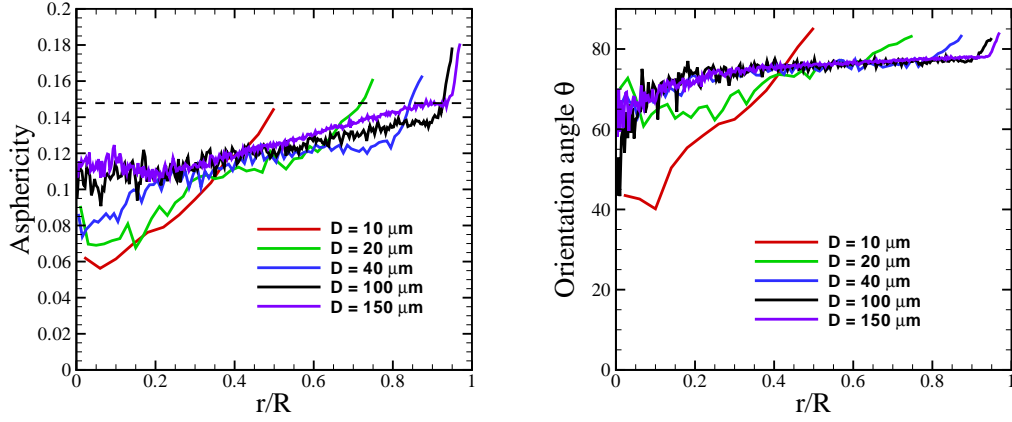


Figure 4.6: Asphericity (left) and cell orientation angle (right) distributions for different tube diameters with  $H^T = 0.3$ . The horizontal dashed line denotes the equilibrium RBC asphericity equal to approximately 0.15.

flow by Fedosov and Karniadakis [46]. In that simulation, the smallest eigenvalue of the cell gyration tensor undergoes a positive shift along the flow direction, resulting in a transition into parachute shape with smaller asphericity.

As  $r$  increases, the RBC asphericity increases due to the larger local shear rate. For large tube with  $D = 100\mu m$  and  $D = 150\mu m$ , the asphericity values show linear increase in the homogeneous flow region  $0.22 < r/R < 0.85$ , where the slope is weakly dependent on the tube diameter. This is followed by a sharp increase near the CFL region, where the RBCs are subjected to the largest shear rate, as shown in Fig. 4.2.

To quantify the cell orientation distribution along the radial direction, we compute the eigenvector  $V1$  for the smallest eigenvalue of the cell gyration tensor. The orientation angle  $\theta$  is defined by the angle between the flow direction and  $V1$  (see Sec. 5.3.3 for details). Fig. 4.6 shows the cell orientation angle distribution for different tube diameters. Similar to the asphericity distribution, the blood flow systems can be roughly divided into three regions. (i) In the blood core region, the orientation angle shows small, scattered values, representing the “random” orientated cells near

the tube center. (ii) In the region between the blood core and the CFL, the cell orientation angles keep a near-constant value with very slow increase. We note that the typical value is very close to the swinging angle for a single RBC in tank-treading motion in shear flow system [2]. (iii) Near the CFL region, the cell orientation angles increase sharply due to the abrupt increase of the local shear rate. As the tube size increases to above  $100\mu m$ , the orientation distributions converge into a single curve, which is independent of the tube diameters. On the contrary, the cell orientation distribution for  $D = 10\mu m$  differs from the other cases, indicating that blood core region dominates for the small tube systems.

### 4.3 Continuum approximation

In Sec. 4.2, we demonstrate that the tube blood flow systems exhibit inhomogeneous micro-structures for small tube diameters. As the tube diameter increase to above  $100\mu m$ , the various micro-structures gradually converge into single states, indicating the homogeneous flow region plays a dominant role. In this section, we further explore the possibility to model the blood system using continuum approximation.

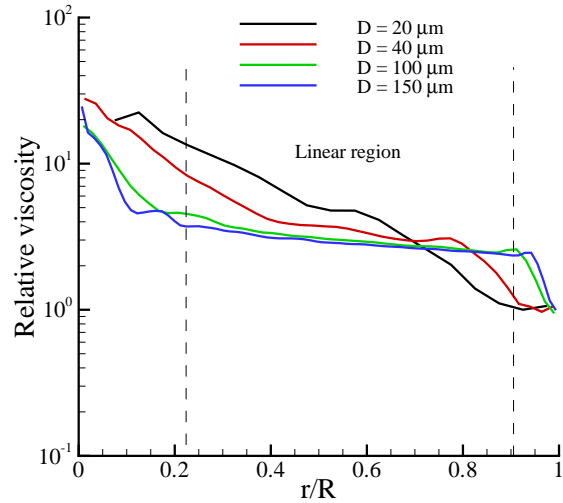
#### 4.3.1 Local shear viscosity

For blood suspensions in shear flow, the local shear stress  $\tau$  and shear rate  $\dot{\gamma}$  are homogeneous through the domain. Therefore, the shear viscosity of the blood flow only depends on the  $\dot{\gamma}$  and cell volume fraction  $H$ . However, for the blood suspensions in Poiseuille flow, both  $\tau$  and  $\dot{\gamma}$  are inhomogeneous along the radial direction, where the dependence of the shear viscosity on the local hematocrit  $H(r)$  is unknown. To explore the continuum limit of the blood system, we compute the local shear viscosity as a function of  $r$  for the different tube diameters, as shown in Fig. 4.7 (a).

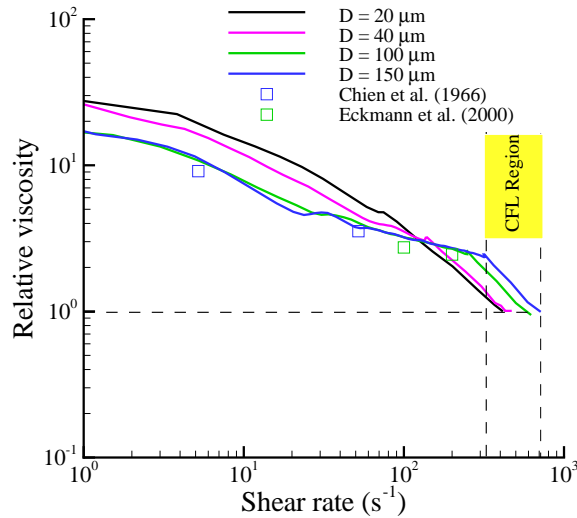
Unlike the homogeneous shear flow, the blood viscosity in tube flow shows a general decrease along the radial direction. Near the tube center, the blood core

is characterized by the largest viscosity values. As  $r$  increases, the blood viscosity gradually decreases and jumps to the value of blood plasma within the CFL region. Moreover, the viscosity distribution also depends on the tube size. For small tube systems, the blood viscosity shows monotonic decrease across the tube. However, for large tube systems, a homogeneous region characterized by near constant viscosity appears. Recalling the linear shear rate and homogeneous cell density distribution in this region (see Fig. 4.5), we suspect that this region resembles to the homogeneous shear flow of blood suspension under high shear rate, where the individual RBCs become largely deformed and the suspensions exhibit near constant, low viscosity value. To verify this postulation, we plot the blood viscosity as a function of the local shear rate, as shown in Fig. 4.7 (b). The large drop of the viscosity across the whole domain is counter-intuitive in view of the homogeneous region in Fig. 4.7 (a). However, we note that the main drop occurs within shear rate less than  $60s^{-1}$ , e.g., the blood core near the tube center. For shear rate larger than  $60s^{-1}$ , blood viscosity keeps a near constant value.

In Fig. 4.7 (b), we also plot the blood viscosities measured by Chien *et al.* [22] and Eckmann *et al.* [34] in shear flow systems. The experimental data is represented by symbols at constant shear rate  $5.2s^{-1}$ ,  $52s^{-1}$ ,  $100s^{-1}$ ,  $200s^{-1}$ . From the shear rate and blood density distribution, the two lowest shear rates correspond to the blood core region with  $H \approx 0.5$ ,  $H \approx 0.4$ , respectively. The two larger shear rates lie the linear shear rate region with  $H \approx 0.34$ . For large tube diameters, the simulation results agree well with the experimental measurement, which suggests that the local shear viscosity in Poiseuille flow is well characterized by the momentum transportation properties of the blood suspensions in homogeneous shear flow. However, the deviation from the experimental measurements for small tubes indicates that the continuum assumption may not be valid for tube diameter smaller than  $100 \mu m$ . Therefore, by varying the tube diameters, we identify a transition from non-continuum to continuum description for the blood systems. We quantify this



(a)



(b)

Figure 4.7: (a): relative viscosity (the cell suspension viscosity normalized by the solvent viscosity) distribution along the radial direction for  $D = 20, 40, 100,$  and  $150\mu m$  at  $H^T = 0.3$ . The dash line represents the separation of the “blood core”, “linear” and the blood plasma region for  $D = 150\mu m$ . (b): relative viscosity from the shear-rates distribution For reference the horizontal dashed line is the plasma viscosity. The vertical dashed line gives the position of the CFL for  $D = 150\mu m$ . Experimental values are shown as points.

effect by applying a continuum model to describe the blood systems, as discussed in next subsection.

### 4.3.2 Continuum approximation with slip boundary velocity

For both shear rate and relative viscosity, we notice that the inhomogeneous “blood core” region becomes small (within 5%) for large tube size. Therefore, we further approximate the system into two regions: the linear shear rate region of blood flow with relative constant value of viscosity with  $0 < r < R_A$  and Newtonian flow region of blood plasma for  $R_A < r < R$ . The viscosities for the two regions are  $\mu_c = \mu\mu_p$  and  $\mu_p$ , respectively. The  $R_A$  defines the separation of the two phase flow and is defined by  $R_A = (1 - \delta_1)R$ , where  $\delta_1$  is determined by the value of cell free layer. With pressure drop  $\Delta P/\Delta x$ , the velocity profiles are

$$\begin{aligned} U_c(r) &= \frac{\Delta P}{\Delta x} \frac{1}{4\mu_c} (-r^2 + \mu(R^2 - R_A^2) + R_A^2) \\ U_p(r) &= \frac{\Delta P}{\Delta x} \frac{1}{4\mu_p} (-r^2 + R^2), \end{aligned} \quad (4.3)$$

where  $U_c(r)$  and  $U_p(r)$  represent the velocity profiles in  $0 < r < R_A$  and  $R_A < r < R$ , respectively. In general, the blood viscosity is larger than plasma viscosity ( $\mu > 1$ ). If we extend the velocity profile of blood flow  $U_c(r)$  to  $r = R$ , finite slip velocity appears on the wall boundary. Therefore, there exists certain value  $R_B$  between  $R_A$  and  $R$  such that the flow rate of blood plasma can be represented by the extension of the velocity profile  $U_c(r)$  within  $R_A < r < R_B$ , e.g.,

$$\int_{R_A}^R 2\pi r U_p(r) dr = \int_{R_A}^{R_B} 2\pi r U_c(r) dr, \quad (4.4)$$

The Left-hand-side (LHS) and right-hand-side (RHS) of Eq. (4.4) is given by

$$\begin{aligned} \int_{R_A}^{R_B} 2\pi r U_c(r) dr &= \frac{\Delta P}{\Delta x} \frac{2\pi}{4\mu_c} \left\{ [\mu(R^2 - R_A^2) + R_A^2] \frac{R_B^2 - R_A^2}{2} - \frac{R_B^4 - R_A^4}{4} \right\} \\ \int_{R_A}^R 2\pi r U_p(r) dr &= \frac{\Delta P}{\Delta x} \frac{2\pi}{4\mu_p} \frac{(R^2 - R_A^2)^2}{4}. \end{aligned} \quad (4.5)$$

For simplicity, we define  $R_B = (1 - \delta_2)R$ . With  $R_A = (1 - \delta_1)R$ , Eq. (4.4) can be simplified as

$$2[(4\mu - 2)\delta_1 + 2\delta_2](\delta_1 - \delta_2) = \mu\delta_1^2(4 - 4\delta_1), \quad (4.6)$$

where the high order terms  $O(\delta_1^3)$ ,  $O(\delta_2^3)$  have been neglected since  $\delta_1, \delta_2 \ll 1$  for cases of large tube diameter. Solving the above equation yields the result  $\delta = \delta_2/\delta_1$  given by

$$\begin{aligned} \delta &= -(\mu - 1) + \sqrt{\mu^2 - \mu} \\ R_B &= (1 - \delta\delta_1)R \end{aligned} \quad (4.7)$$

With  $\mu \geq 1$ ,  $\delta$  falls between 0 and 0.5. Specifically,  $\mu = 1$  leads to  $\delta = 0$  since the blood flow and plasma have the same viscosity in this case, e.g.,  $R_B = R$  without any slip length. On the other limit case,  $\mu \rightarrow \infty$  leads to  $\delta = 0.5$  since the extension of  $U_c(r)$  can be treated as flat line compared with  $U_p(r)$ . Numerically,  $\delta$  approaches 0.5 given  $\mu > 3.0$ .

With the continuum model given by Eq. (4.3) and Eq. (4.7), the velocity profile has finite non-zero value at the boundary  $r = R_B$ . The slip value is given by  $U_c(r = R_B)$

$$\begin{aligned} U_{slip} &= \frac{\Delta P}{\Delta x} \frac{1}{4\mu_c} (-R_B^2 + \mu(R^2 - R_A^2) + R_A^2) \\ &= \frac{\Delta P}{\Delta x} \frac{R^2}{4\mu_c} (1 - (1 - \delta_2)^2 + 2\mu\delta_1 - 2\delta_1) \\ &\approx \frac{\Delta P}{\Delta x} \frac{R^2}{2\mu_c} \delta_1 \sqrt{\mu^2 - \mu}. \end{aligned} \quad (4.8)$$

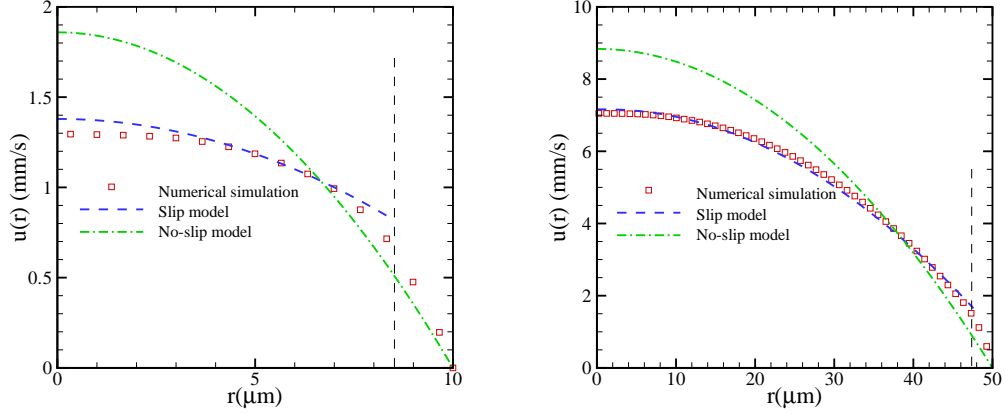


Figure 4.8: The velocity profile of the blood flow for  $D = 20, 100\mu m$ . The symbols represent the numerical results obtained by the numerical simulation from the DPD simulation. The dash lines represent the results from the continuum model with slip boundary condition defined by Eq. (4.3) and Eq. (4.7). The dash dot lines represent the results from the continuum model with no-slip boundary condition defined by Eq. (4.11). The vertical dash line represents the position of the slip boundary  $R_B = (1 - \delta_2)R$ , where  $\delta_2$  defined by Eq. (4.7).

Therefore, the continuum model can viewed as a pressure driven flow with specific slip velocity as defined above, e.g.,

$$U(r) = \frac{\Delta P}{\Delta x} \frac{1}{4\mu_c} (-r^2 + R_B^2) + U_{slip}, \quad (4.9)$$

and the corresponding flow rate is given by

$$Q = \frac{\pi}{8\mu_c} \frac{\Delta P}{\Delta x} R_B^4 + \pi R_B^2 U_{slip}. \quad (4.10)$$

Given the value of  $\mu$  and  $\delta_1$ , the continuum system is fully determined for the pressure drop  $\Delta P/\Delta x$  by Eq. (4.8 - 4.10).  $\mu_c$  is the characteristic value of the relative viscosity in the linear shear region as the value. For smaller tube systems, Eq. (4.8 - 4.10) may not be valid due to the dominance of the blood core region. Nevertheless, their continuum approximations are also computed for comparison reason.

model	D ( $\mu\text{m}$ )	$\Delta P/\Delta x(P_a/m)$	$U_{slip}(mm/s)$	Q ( $mm^3/s$ )	$U(0)(mm/s)$
DPD	20	$1.31 \times 10^5$	N/A	$2.92 \times 10^{-4}$	1.32
<i>Newtonian</i> <sup>S</sup>	20	$1.31 \times 10^5$	0.89	$3.62 \times 10^{-4}$	1.37
<i>Newtonian</i> <sup>N</sup>	20	$1.31 \times 10^5$	N/A	$2.92 \times 10^{-4}$	1.859
DPD	40	$6.78 \times 10^4$	N/A	$1.97 \times 10^{-3}$	2.41
<i>Newtonian</i> <sup>S</sup>	40	$6.78 \times 10^4$	1.07	$2.08 \times 10^{-3}$	2.48
<i>Newtonian</i> <sup>N</sup>	40	$6.78 \times 10^4$	N/A	$1.97 \times 10^{-3}$	3.15
DPD	100	$3.41 \times 10^4$	N/A	$3.24 \times 10^{-2}$	7.03
<i>Newtonian</i> <sup>S</sup>	100	$3.41 \times 10^4$	1.51	$3.31 \times 10^{-2}$	7.08
<i>Newtonian</i> <sup>N</sup>	100	$3.41 \times 10^4$	N/A	$3.24 \times 10^{-2}$	8.83
DPD	150	$2.65 \times 10^4$	N/A	0.124	12.44
<i>Newtonian</i> <sup>S</sup>	150	$2.65 \times 10^4$	1.71	0.126	12.55
<i>Newtonian</i> <sup>N</sup>	150	$2.65 \times 10^4$	N/A	0.124	14.18

Table 4.1: Flow rate  $Q$  and maximum flow velocity  $U_m$  calculated in DPD simulations and with the *Newtonian*<sup>S</sup> and *Newtonian*<sup>N</sup> models at  $H^T = 0.3$ . The slip velocity  $U_{slip}$  for the *Newtonian*<sup>S</sup> model is also shown. For each tube size  $D$  the pressure gradient  $\Delta P/\Delta x$  is fixed. The tabulated values for  $D = 20$  and  $100 \mu\text{m}$  correspond to the velocity profiles of figure 4.8.

Fig. 4.8 and Tab. 4.1 present the velocity profiles and flow rates  $Q$  obtained from the slip-velocity model as well as the DPD simulation. The continuum results in general agree well with the DPD simulation. The discrepancy near the center line of the blood channel is mainly due to the non-Newtonian blood core near the centerline of the channel. The errors in  $Q$  and  $U_m$  range from about 2% to 10% as the diameter decreases. When only flow rate is considered, a no-slip boundary approximation will yield the correct results. The velocity profile is defined by

$$U_{ns}(r) = \frac{\Delta P}{\Delta x} \frac{1}{4\mu_{app}} (-r^2 + R^2), \quad (4.11)$$

where  $\mu_{app}$  is the apparent viscosity of the blood system. However, this approximation results in large over-estimation of  $U_m$ , as shown in Fig. 4.8. For small tube systems, improved accuracy calls for the incorporation of the inhomogeneous local information, which is omitted in the continuum approximation.

## 4.4 Conclusion

In this chapter, we present the DPD simulation results of blood suspensions in different tubes with size-range  $20 - 150 \mu m$ . Different from the homogeneous shear flow, the blood suspensions in Poiseuille flow exhibit inhomogeneous shear stress across the tube, resulting in the heterogeneous micro-structures along the radial directions. This effect is especially pronounced in small tubes, where the blood flow can be roughly divided into two regions: the non-Newtonian blood core and the Newtonian blood plasma layer. The inhomogeneous cross stream stress gradient is reflected by the cell density peak and flat plug-like velocity profile near the tube center. On the contrary, in large tube systems, a homogeneous cell suspension region appears between the blood core and the plasma layer, where the cell density distribution keeps a near constant value. Analysis of the velocity profiles reveals that the large tubes show a linear shear rate distribution in this region, whereas for the smaller tubes, the shear rate profiles are non-linear over the whole domain. The response of the suspended cells to the varying shear rates cross the tube is derived from the gyration tensors of the individual cells, where the cell asphericity and orientation angle are quantified for different tube systems. As the tube diameter increases to above  $100\mu m$ , the simulation results converge to single profiles.

The appearance of the homogeneous cell suspension region indicates that the blood system approaches the continuum region as the tube diameter increases. This postulation is investigated by measuring the local viscosity across the tube. In large tube systems, the local viscosity of the blood flow approaches the value measured in homogeneous shear flow systems, indicating the local properties can be described by the shear viscosity defined on the macroscopic scale. As tube diameter decreases, the local viscosity shows apparent deviation from the homogeneous value, indicating the break down of the continuum approximation. Therefore, using the mesoscopic DPD method, the present work identifies a non-continuum to continuum transition for blood flow systems. For tube flow of  $D \geq 100\mu m$ , the blood velocity profiles can

be well characterized by a continuum description with slip velocity at the boundary. However, this description shows poor approximation for smaller tube systems, where the inhomogeneous local properties need to be specified.

# Chapter 5

## A multi-scale model for sickle red blood cell

### 5.1 Introduction

Sickle cell anemia has been identified as the first “molecular disease” [123] where the hemoglobin molecules inside the sickle red blood cell (SS-RBC) are different from the healthy ones. Specifically, the difference results from the substitution of a single amino acid in the  $\beta$ -chain of hemoglobin. In a deoxygenated state, the sickle hemoglobin (HbS) molecules exhibit low solubility and tend to aggregate and form a polymerized state [133] characterized by the double nucleation mechanism [52]. Due to the polymerized HbS, the SS-RBCs undergo various morphological changes depending on the mean corpuscular hemoglobin concentration (MCHC) and the deoxygenation procedure [84, 23]. With a slow deoxygenation procedure and low MCHC value, the SS-RBCs tend to form into a classical sickle shape, where HbS inside a single sickle cell tends to form into a single aligned polymerized domain. On the other hand, fast deoxygenation and high MCHC conditions favor the mosaic or granular shapes, where *multiple* polymerized domains are typically found inside the cell.

In addition to the various cell morphologies, the membrane mechanics of a SS-RBC also exhibits different properties in both oxygenated and deoxygenated states. In full oxygenated state, measurements of the effective cell membrane elasticity by optical tweezers [17] reported 50% increase compared with the healthy cells. Measurements by micropipette [41] reported that the effective shear modulus of the sickle cell membrane is about two to three times the value of the healthy cell. On the contrary, the shear modulus of the SS-RBC increases sharply as the oxygen tension is decreased below 60 mmHg [76]. Moreover, the rigidity of the full deoxygenated cell depends on the MCHC value for each single cell. For a sickle cell with low value of MCHC (e.g., 25.5 g/dL), the effective cell rigidity is about 100 times larger than the healthy value, while for cells with higher value of MCHC ( $> 35$  g/dL), the cell rigidity shows further increases and could be even larger than the upper limit of the instrument used in the experiment.

The intracellular polymerization and the stiffened cell membrane lead to an elevation in flow resistance of SS-RBC suspensions. Extensive experimental studies on the dynamics of SS-RBC suspensions have been reported for both shear flow and isolated vascular systems [148, 84, 87, 86]. Usami et al. measured the shear viscosity of HbS cell suspensions in a Ringer's solution with Hematocrit (Hct) 45%. While the viscosity of the normal blood exhibits the shear-thinning behavior, the behavior of the full-deoxygenated HbS blood is similar to Newtonian flow as the viscosity value is nearly shear-independent. Kaul et al. [84, 87, 86] investigated the rheological and hemodynamic properties of SS-RBC suspensions with various cell morphologies obtained at different MCHC values and deoxygenation rates. It was found that the dynamics of SS-RBC suspensions is heterogeneous with the various cell morphologies. More recently, Higgins et al. [69] studied SS-RBC suspensions in a microfluidic network where the oxygen tension of the environment could be controlled. Vaso-occlusion was observed as the oxygen was gradually removed while blood flow could be resumed as the oxygen was refilled into the microfluidic device. The basis of

the occlusion phenomenon was attributed to the stiffened cell membrane in deoxygenated state while the detailed biophysical mechanism for the occlusion event was not explained.

Numerical simulations can be used for qualitative and quantitative understanding of the behavior of blood flow with sickle cell anemia although much less numerical work has been reported, probably due to the complexity of the sickling process and also the *heterogeneous* characteristics of SS-RBCs. To this end, Dong et al. [30] studied the effect of cell deformability and cytosol polymerization by a 2D model of sickle cell in capillaries where a RBC was represented as a 2D cylinder shape. The blood flow resistance for different values of the cell membrane shear modulus and cytosol viscosity were investigated. Dupin et al. [33] studied a collection of SS-RBCs passing through an aperture of diameter less than the size of a single cell.

To quantify the hemodynamics of blood flow with sickle cell anemia under various physiological conditions, we employed a multiscale model [125, 46] to simulate healthy RBCs and SS-RBCs. A RBC is modeled as a network of viscoelastic bonds combined with bending energy and constraints for surface area and volume constraints. The mechanical properties of the cell membrane are fully determined by the microscopic parameters such that various cell membrane mechanical states can be imposed without changing the model's parameters. Different realistic 3D cell morphologies are constructed according to the typical shapes observed in experiments by SEM [84, 87]. Quantitative shape characteristics are analyzed by introducing the asphericity and elliptical shape factors. The corresponding shear viscosity and peripheral resistance are computed in shear and tube flow systems. Comparison with experiment results is made where it is possible and physical mechanisms are discussed. We show that the model can capture the *heterogeneous* hemodynamics of SS-RBC suspensions with different cell morphologies. We also discuss the physiological conditions for the occurrence of vaso-occlusion. Although the flow resistance of diseased blood exhibits an apparent elevation compared with healthy blood, no

occlusion events occur until proper adhesive interactions are introduced into the system. Our simulation results indicate that the adhesive interactions between the sickle cells and the vascular endothelium play a key role for the triggering of the vaso-occlusion phenomenon in *straight* vessels.

The chapter is organized as follows. In Sec. 5.2, we explain the details of the multiscale RBC model and the method of constructing SS-RBCs. In Sec. 5.3, SS-RBCs with various 3D morphological states are constructed and quantified by the asphericity and elliptical shape factors. The dynamic properties of SS-RBC suspensions are studied in shear flow and tube flow with diameter of  $9\mu m$ . The shear viscosity and tube flow resistance are computed and compared with the available experimental results. The effect of the blood cell-endothelium interaction on the hemodynamics of SS-RBCs is further examined. We conclude in Sec. 5.4 with a brief summary.

## 5.2 Multiscale model

### 5.2.1 RBC membrane

The sickle red blood cell model is based on a multi-scale model of healthy red blood cell developed by Pivkin *et al.* [125] and Fedosov *et al.* [46]. Here we briefly review this model. We refer to Ref. [44] for the details of this model.

In the equilibrium state, the RBC keeps a biconcave shape as described by [42]. In the present model, the RBC membrane is represented by a two-dimensional triangulated network with  $N_v$  vertices where each vertex is represented by a DPD particle. The vertices are connected by  $N_s$  visco-elastic bonds to impose proper membrane mechanics [29, 46]. Specifically, the elastic part of bond is represented by the potential

$$V_s = \sum_{j \in 1 \dots N_s} \left[ \frac{k_B T l_m (3x_j^2 - 2x_j^3)}{4p(1 - x_j)} + \frac{k_p}{(n - 1)l_j^{n-1}} \right], \quad (5.1)$$

where  $l_j$  is the length of the spring  $j$ ,  $l_m$  is the maximum spring extension,  $x_j = l_j/l_m$ ,  $p$  is the persistence length,  $k_B T$  is the energy unit,  $k_p$  is the spring constant, and  $n$  is a power. Physically, the above two terms represent the wormlike chain potential and a repulsive potential, respectively.

The membrane viscosity is imposed by introducing a viscous force on each spring. Following the general framework of the fluid particle model [38], we can define the dissipative force  $\mathbf{F}_{ij}^D$  and random force  $\mathbf{F}_{ij}^R$  given by

$$\mathbf{F}_{ij}^D = -\gamma^T \mathbf{v}_{ij} - \gamma^C (\mathbf{v}_{ij} \cdot \mathbf{e}_{ij}) \mathbf{e}_{ij}, \quad (5.2)$$

$$\mathbf{F}_{ij}^R dt = \sqrt{2k_B T} \left( \sqrt{2\gamma^T} d\overline{\mathbf{W}}_{ij}^S + \sqrt{3\gamma^C - \gamma^T} \frac{tr[d\mathbf{W}_{ij}]}{3} \mathbf{1} \right) \cdot \mathbf{e}_{ij}, \quad (5.3)$$

where  $\gamma^T$  and  $\gamma^C$  are dissipative parameters,  $\mathbf{v}_{ij}$  is the relative velocity of spring ends,  $tr[d\mathbf{W}_{ij}]$  is the trace of a random matrix of independent Wiener increments  $d\mathbf{W}_{ij}$ , and  $d\overline{\mathbf{W}}_{ij}^S = d\mathbf{W}_{ij}^S - tr[d\mathbf{W}_{ij}^S] \mathbf{1}/3$  is the traceless symmetric part.

To uniquely relate the model parameters and elastic properties of the cell membrane, we extend the linear analysis of [27] for a regular hexagonal network [46]; the derived shear modulus of the membrane  $\mu_0$  is given by

$$\mu_0 = \frac{\sqrt{3}k_B T}{4pl_m x_0} \left( \frac{x_0}{2(1-x_0)^3} - \frac{1}{4(1-x_0)^2} + \frac{1}{4} \right) + \frac{\sqrt{3}k_p(n+1)}{4l_0^{n+1}}, \quad (5.4)$$

where  $l_0$  is the equilibrium spring length and  $x_0 = l_0/l_m$ .

The bending resistance of the RBC membrane is modeled by the potential

$$V_b = \sum_{j \in 1 \dots N_s} k_b [1 - \cos(\theta_j - \theta_0)], \quad (5.5)$$

where  $k_b$  is the bending constant,  $\theta_j$  is the instantaneous angle between two adjacent triangles having the common edge  $j$ , and  $\theta_0$  is the spontaneous angle. The relation between the model bending coefficient  $k_b$  and the macroscopic bending rigidity  $k_c$  of the Helfrich model [66] can be derived as  $k_b = 2k_c/\sqrt{3}$  for a spherical membrane

[46].

In addition, the RBC model includes the area and volume conservation constraints, which mimic the area-incompressibility of the lipid bilayer and the incompressibility of the interior fluid, respectively. The corresponding energy is given by

$$V_{a+v} = \sum_{j \in 1 \dots N_t} \frac{k_d(A_j - A_0)^2}{2A_0} + \frac{k_a(A - A_0^{tot})^2}{2A_0^{tot}} + \frac{k_v(V - V_0^{tot})^2}{2V_0^{tot}}, \quad (5.6)$$

where  $N_t$  is the number of triangles in the membrane network,  $A_0$  is the triangle area, and  $k_d$ ,  $k_a$  and  $k_v$  are the local area, global area and volume constraint coefficients, respectively. The terms  $A$  and  $V$  are the total RBC area and volume, while  $A_0^{tot}$  and  $V_0^{tot}$  are the specified total area and volume, respectively.

### 5.2.2 Sick cell membrane

Different from normal RBCs, the sickle cells exhibit various morphological states due to the presence of the polymerized HbS inside the cell. In deoxygenated state, the HbS molecules polymerize and grow into bundles of fiber. Consequently, the sickle cell undergoes various degrees of distortion due to the interaction between the growing fiber and the cell membrane. The final shape of the sickle cell depends on the intracellular HbS polymer configuration. In general, classical “sickle” and “holly leaf” shapes originate from a single HbS polymer domain growing along one direction; granular and near biconcave shapes originate from multiple domains with homogeneous growth directions. The configuration of the HbS polymer is determined by several physiological conditions: the MCHC of the sickle cell, the rate of the deoxygenation process, the final gas tension, temperature, PH level, *etc.* (see Chap. 6 for further discussion on the effect of the HbS polymer configuration on the sickle cell morphology.)

In this chapter, we directly consider the surface tension applied on the cell membrane exerted by the growing HbS fibers, similar to the systems discussed in Ref.

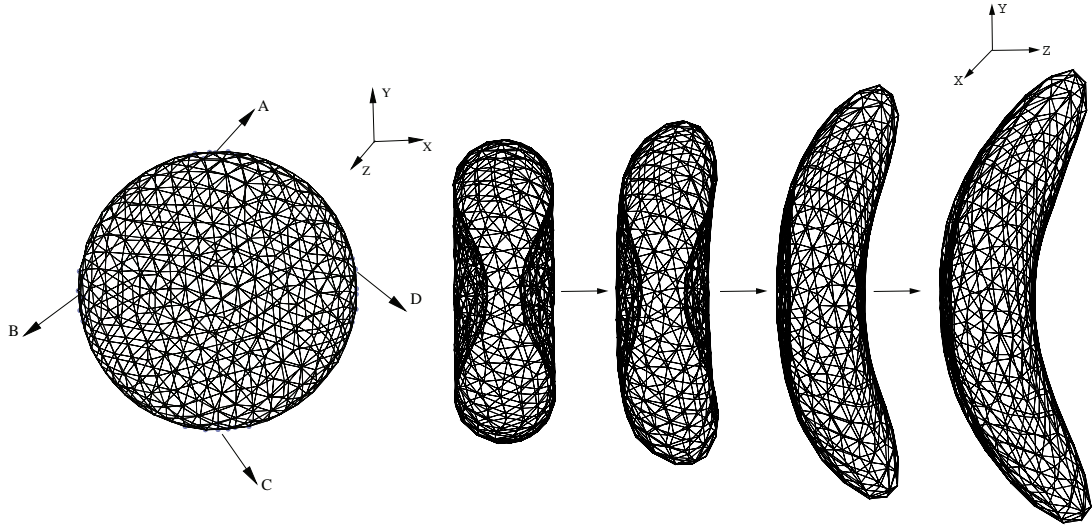


Figure 5.1: Left: triangulated mesh of the RBC membrane. The label “A”, “B”, “C” and “D” represents the four anchor points where the stretching force is applied. Right: Successive snapshots of a RBC during the morphological transition to the “sickle” shape.

[25]. Fig. 5.1 shows the triangulated mesh of a healthy RBC with biconcave shape. We define the direction along the thickness of RBC as z-direction while the plane determined by the two long axes is defined as the x-y plane. The letters “A”, “B”, “C” and “D” are the four points with the maximum/minimum values in the x/y directions, representing the four anchor points where the intracellular growing fibers can potentially approach the cell membrane. Each anchor point is represented by  $\epsilon N_v$  vertices, where  $\epsilon = 0.016$ . Different surface tension is exerted on the cell membrane depending on the configuration of the HbS fibers. For deoxygenated SS-RBCs with low MCHC, the intracellular HbS polymer tend to grow into single domain whereas the angular width is relatively small due to the limited heterogeneous nucleation and branching rates, resulting to the classical sickle shape. Accordingly, the surface tension is applied only on points “A” and “C” to represent the specific direction of the polymer growth. For SS-RBCs with high MCHC, the intracellular HbS polymers tend to form spherulitic configurations due to the explosive growth via the high heterogeneous nucleation rate on the pre-existed HbS polymers, resulting

in the granular shape. In this case, the growing HbS fibers may approach the cell membrane from multiple directions. Therefore, the surface tension is applied on all the four anchor points for this case. We note that the HbS polymer may interact with the cell membrane at more than four positions, resulting in the multiple spicules distributed in the cell membranes. However, this type of cells exhibits similar granular shape. Therefore, we use four anchor points in the current study to represent the positions where the growing HbS fibers interact with the cell membrane.

Starting from the original biconcave shape, the cell membrane undergoes various deformations until a certain new shape is achieved. We define the new shape as the equilibrium state of the sickle cell and remove the surface tension applied at the anchor points. To define the distorted shape as the stable state of the sickle cell with minimum free energy, the local stress on the cell membrane generated by the distortion has to be eliminated. To achieve this, we employ a “stress-free” model to the new state of the sickle cell. The equilibrium length of  $l_0^i$  of each bond is set to the edge length of the new state for  $i = 1, \dots, N_s$ . This leads to individual maximum extension for each bond as  $l_0^i/x_0$ , where  $x_0$  is a constant less than 1. This *annealing procedure* provides a bond network free of local stress abnormalities. Finally, the bond parameters are adjusted according to the shear modulus of the sickle cell.

### 5.2.3 Adhesion model

Besides the abnormal cell morphologies, the SS-RBCs also exhibit adhesive behavior with the blood vessel wall as well as with leukocytes present in the blood systems; in this chapter we omit the different cell adhesive dynamics among the various cell fractions. (see Chap. 7 for detail discussion on this issue.) To investigate the effect of the SS-RBC/wall adhesive mechanism on the hemodynamics of the sickle blood, we employ a simple stochastic model [62, 47] to represent the multi-functional interactions. Specifically, we assume that the sickle cell vertices can interact with the endothelial ligands within interaction distance  $d_{on}$ . For each time step  $\Delta t$ , transient

bonds can be formed between the cell vertices and the endothelial ligands with probability  $P_{on} = 1 - e^{-k_{on}\Delta t}$ , while the existing bonds can be ruptured with probability  $P_{off} = 1 - e^{-k_{off}\Delta t}$ , where  $k_{on}, k_{off}$  are the reaction rates defined by

$$\begin{aligned} k_{on} &= k_{on}^0 \exp\left(-\frac{\sigma_{on}(l-l_0)^2}{2k_B T}\right) \\ k_{off} &= k_{off}^0 \exp\left(\frac{\sigma_{off}(l-l_0)^2}{2k_B T}\right), \end{aligned} \quad (5.7)$$

where  $\sigma_{on}$  and  $\sigma_{off}$  are the effective formation/rupture strengths. For existing bonds, the force between the receptors and ligands is defined by  $F(l) = 2k_s(l-l_0)$ , where  $k_s$  is the spring constant and  $l_0$  is the equilibrium length.

During the simulation, the above stochastic process is executed at each time step. First, all existing bonds between cell vertices and ligands are checked for a potential dissociation. A bond is ruptured if the bond length is larger than  $d_{off}$ , otherwise it is determined according to the probability  $P_{off}$ . Second, a bond formation procedure is looped through all the free ligands. For each free ligand, all the cell vertices within the distance  $d_{on}$  are examined, and bond formation is accepted in a stochastic way according to the probability  $P_{on}$ . Finally, the forces of all existing bonds are calculated and applied.

## 5.2.4 Scaling of model and physical units

In the present work, the scaling between DPD model units ( $M$ ) and physical units ( $P$ ) adopts the following length and time scales

$$r^M = \frac{D_0^P}{D_0^M} m, \quad \tau = \left(\frac{D_0^P}{D_0^M} \frac{\eta^P}{\eta^M} \frac{Y^M}{Y^P}\right) s, \quad (5.8)$$

where  $r^M$  is the model unit of length,  $D_0$  is the cell diameter,  $m$  stands for meters,  $\eta$  is the characteristic viscosity (e.g., solvent viscosity) and  $Y^P$  is the Young's modulus of the red blood cell. Moreover, we can define the scaling of the energy per unit mass

$(k_B T)$  and of the force unit (“ $N$ ” denotes Newton) as follows

$$\begin{aligned} (k_B T)^M &= \frac{Y^P}{Y^M} \left( \frac{D_0^P}{D_0^M} \right)^2 (k_B T)^P, \\ N^M &= \frac{Y^P}{Y^M} \frac{D_0^P}{D_0^M} N^P. \end{aligned} \tag{5.9}$$

## 5.3 Results

In this section, three different types of sickle cell membranes typically observed in experiments [87] are constructed. The various morphologies are further quantified by the asphericity and ellipticity factors to represent the degree of distortion of the cell membrane. The shear viscosity of SS-RBC suspensions with different morphologies and hematocrit values are investigated and compared with experiment results. The hemodynamics of SS-RBC suspensions is studied in a tube with diameter of  $9.0\mu m$ . Finally, we investigate the effect of the adhesive interaction between the SS-RBCs and a modeled vascular endothelium on the vaso-occlusion phenomenon.

### 5.3.1 Morphology of sickle red blood cell

Kaul et al. studied the morphologic characteristics of sickle cells by SEM for different intracellular MCHC values [84] and deoxygenation rates [87]. Sickle cells with medium MCHC values exhibit sickle shape while cells with high MCHC values exhibit granular shape. Similarly, slow deoxygenation rate results in sickle shape while the fast deoxygenation rate favors granular shape. Remarkably, a third type of sickle red blood cell is observed with prolonged 30-min incubation of the granular cell in the deoxygenated condition. Different from the sickle and granular shape, the cell exhibits extremely elongated shape in one direction with projection much longer than the diameter of the cell. This type of cell is probably originated from further polymerization of HbS in a certain direction during the prolonged deoxygenated condition.

	A	B	C	D
S	(0.0, 55, 54)	(0.0, 0.0, 0.0)	(0.0, -55, 54)	(0.0, 0.0, 0.0)
G	(0.0, 23, 31)	(-23, 0.0, 31)	(0.0 - 23, 31)	(23, 0.0, 31)
E	(0, 55, 11)	(0, 0, 0)	(0, -55, -11)	(0, 0, 0)

Table 5.1: Stretching force (pN) applied on the anchor points for each type of the cell morphology.

To mimic the various distortion effects on the cell membrane, different forces are applied at the anchor points as discussed in Sec. 5.2.2 and shown in Fig. 5.1. An opposite force is applied uniformly on the rest of the vertices to keep the total force on the cell as zero. The sickle shape is obtained from the aligned HbS polymer growing along one direction. The stretching force is only applied on the anchor points “A” and “C”. The z-component of the forces represent the deflection of the HbS fiber widely observed in the experiment. The successive snapshots in Fig. 5.1 show the shape transition of a SS-RBC from the biconcave to the classical sickle shape. Similarly, the granular shape is constructed by applying the stretching force on all of the four anchor points. Detailed information of the stretching force is presented in Tab. 5.1.

The distorted shape of the cell is defined as the equilibrium state for the sickle cell through the procedure explained in Sec. 5.2.2. The degree of distortion can be identified by eigenvalue analysis of the gyration tensor defined by

$$G_{mn} = \frac{1}{N_v} \sum_i (r_m^i - r_m^C)(r_n^i - r_n^C), \quad (5.10)$$

where  $r^i$  are the RBC vertex coordinates,  $r^C$  is the center-of-mass, and  $m, n$  can be  $x, y$ , or  $z$ . The three eigenvalues obtained from the gyration tensor are denoted by  $\lambda_1, \lambda_2$  and  $\lambda_3$ , where  $\lambda_1 < \lambda_2 < \lambda_3$ . The asphericity and elliptical shape factors are

defined by

$$\begin{aligned} ASF &= ((\lambda_1 - \lambda_2)^2 + (\lambda_2 - \lambda_3)^2 + (\lambda_3 - \lambda_1)^2)/2R_g^4, \\ ESF &= \lambda_3/\lambda_2, \end{aligned} \quad (5.11)$$

where  $R_g$  is the radius of gyration defined by  $R_g^2 = \lambda_1 + \lambda_2 + \lambda_3$ .

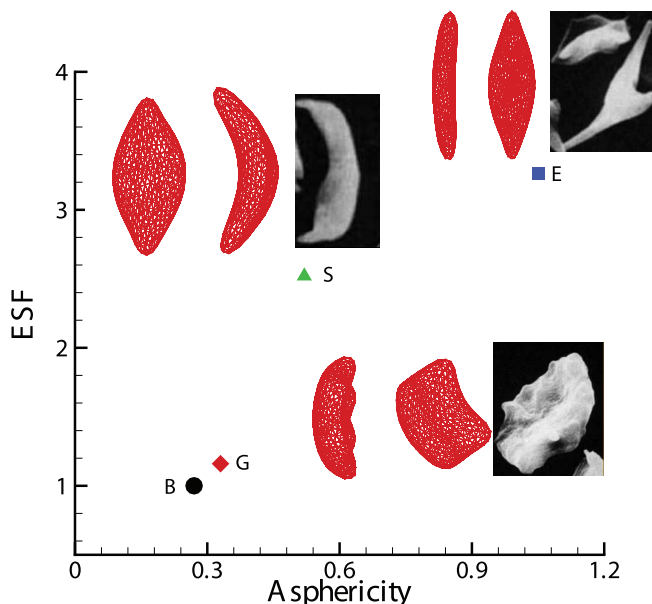


Figure 5.2: Asphericity and elliptical shape factors for the different shapes of the sickle cells. The label “G”, “S” and “E” represents the granular, sickle and elongated shape of the sickle cells respectively, and the inset sketches represent their morphologic projections on the x-z and x-y planes; the inset images represent the experimental observations on different morphologic states of deoxygenated SS-RBC by scanning electron microscopy, reproduced from DK Kaul and H Xue, *Blood*, 1991 77:1353-1361, by permission. The label “B” corresponds to the original biconcave shape, whose morphological projection is shown in Fig. 5.1.

The *asphericity* shape factor (ASF) measures the deviation of the RBC from a perfect sphere shape while the *elliptical* shape factor (ESF) measures the degree of distortion on the x-y plane as shown in Fig. 5.1. Fig. 5.2 plots both ASF and ESF for the three types of cell constructed above. The granular cell shows similar characteristics with a healthy cell while the elongated cell exhibits the largest

deviation from the perfect biconcave shape. Similar morphological analysis has been conducted on the medical image of different sickle cells on 2D plane, where the circular and elliptical shape factors are computed for the granular and the sickle shape cells [73, 9]. The different morphologies constructed by the present work show consistent agreement with the results from medical image analysis [73, 9].

Besides the structural factors defined above, we also use a polynomial function  $z = f(x, y)$  to fit the surface of the cell membrane for all the three types of cells, similar to the approach in Ref. [42]. The polynomial function is defined by

$$f(x, y) = \alpha_0 + \alpha_1 x^2 + \alpha_2 y^2 + \alpha_3 x^4 + \alpha_4 y^4 + \alpha_5 x^2 y^2, \quad (5.12)$$

where  $\alpha_0, \alpha_1, \dots, \alpha_5$  are fitting coefficients determined by the specific shape of the cell and the boundary of the cell on the x-y plane is defined by

$$(x/b_1)^p + (y/b_2)^p = 1, \quad (5.13)$$

where  $b_1, b_2$  and  $p$  vary for different cell morphologies. Remarkably, we note that  $b_1$  and  $b_2$  defines the maximum extension along the x and y direction, which determines the length and width of the cells respectively. The mean curvature  $C_H$  of the fitting surface is determined by  $\alpha_1, \dots, \alpha_5$  and given by

$$C_H(x, y) = \frac{\left(1 + \left(\frac{\partial f}{\partial x}\right)^2\right) \frac{\partial^2 f}{\partial y^2} - 2 \frac{\partial f}{\partial x} \frac{\partial f}{\partial y} \frac{\partial^2 f}{\partial x \partial y} + \left(1 + \left(\frac{\partial f}{\partial y}\right)^2\right) \frac{\partial^2 f}{\partial x^2}}{2 \left(1 + \left(\frac{\partial f}{\partial x}\right)^2 + \left(\frac{\partial f}{\partial y}\right)^2\right)^{3/2}}. \quad (5.14)$$

Analytical solution can be obtained as  $f(x, y)$  defined by the polynomial function.

The  $L_2$  error of the polynomial fitting is defined by

$$\epsilon = \frac{1}{N_v} \sqrt{\sum_{i=1}^{N_v} (f(x_i, y_i) - z_i)^2 / Z^T}, \quad (5.15)$$

where  $x_i$ ,  $y_i$  and  $z_i$  are the coordinates of a discrete cell vertex,  $N_v$  is the total number of vertices considered.

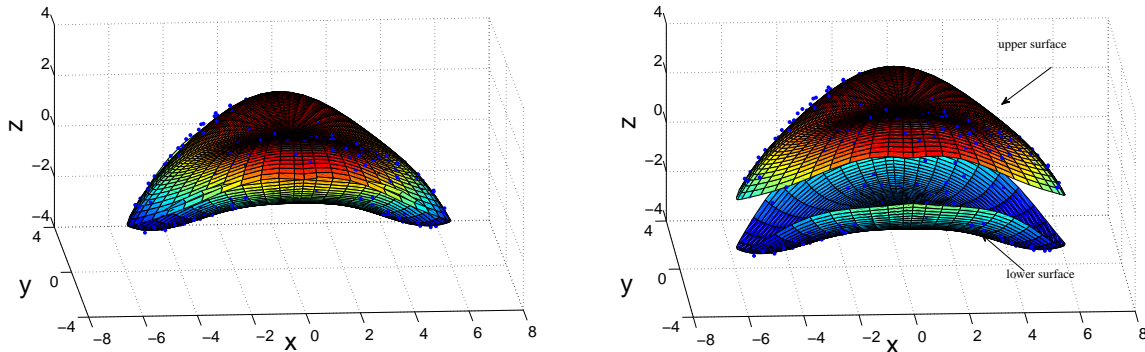


Figure 5.3: Upper: fitted surface of cell membrane for the sickle shape of SS-RBC. Lower: For illustration purposes, the upper and lower surface is shifted by 1 and  $-1$  in the  $z$  direction respectively. The blue dots represent the cell vertices obtained from the procedure described in the current work.

For each cell, the membrane is divided into two parts according to the dual values in  $z$  direction; each part is fitted by Eq. (5.12) separately as shown in Fig. 5.3. Similarly, the elongated and granular shape of cell membranes are fitted and plotted in and Fig. 5.3.

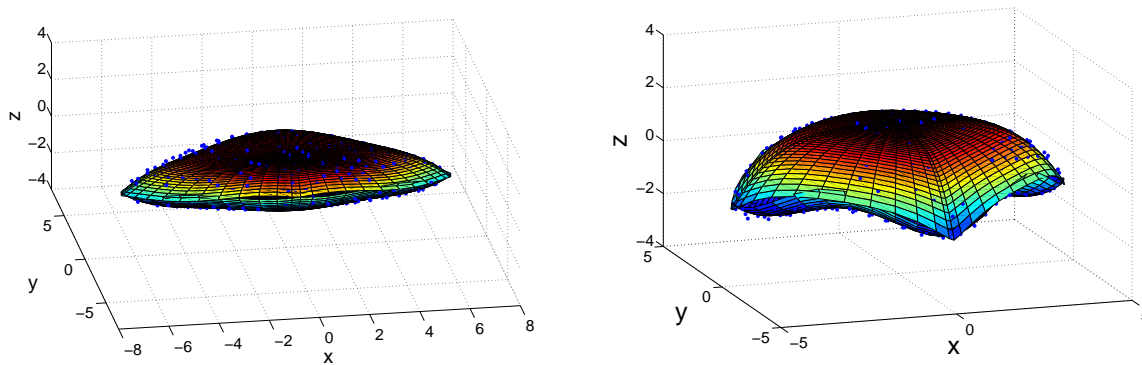


Figure 5.4: Cell vertices (blue dots) and the fitted surface of the cell membrane for the *elongated* (upper) and *granular* (lower) shape of SS-RBC.

The fitting parameters and the basic cell morphological properties (length, width, thickness, etc.) for each cell type are shown in Tab. 5.2 and Tab. 5.3.

	$\alpha_0$	$\alpha_1$	$\alpha_2$	$\alpha_3$	$\alpha_4$	$\alpha_5$
$S^l$	-0.806	-0.1141	-0.00678	$2.12 \times 10^{-3}$	$2.01 \times 10^{-2}$	$2.84 \times 10^{-2}$
$S^u$	1.36	-0.0403	0.306	$-1.69 \times 10^{-3}$	$-3.60 \times 10^{-2}$	$-2.77 \times 10^{-2}$
$E^l$	-0.995	-0.0361	-0.092	$1.11 \times 10^{-3}$	$2.21 \times 10^{-2}$	$2.17 \times 10^{-2}$
$E^u$	1.04	0.00836	0.203	$-1.09 \times 10^{-3}$	$-2.89 \times 10^{-2}$	$-2.22 \times 10^{-2}$
$G^l$	-0.237	-0.171	-0.180	$6.35 \times 10^{-3}$	$6.84 \times 10^{-3}$	$4.40 \times 10^{-2}$
$G^u$	1.701	-0.0123	-0.0245	$-5.06 \times 10^{-3}$	$-4.86 \times 10^{-3}$	$-1.85 \times 10^{-2}$

Table 5.2: The fitting parameters for the cell membranes with different morphologies. The label “S”, “E” and “G” represent the sickle, elongated and granular shape respectively. The upper label “u” and “l” represent the upper and lower part of the cell surface. The unit of  $x$ ,  $y$  and  $z$  is in micrometer.

	$b_1$	$b_2$	$p$	$Z^T$	$Z^m$	$\langle C_H \rangle$	$\epsilon$
S	5.80	3.05	1.54	1.58	3.87	0.22	0.0748
E	6.40	3.1	1.45	1.56	2.37	0.25	0.0581
G	4.58	4.58	1.25	1.52	2.75	0.21	0.0607

Table 5.3: The parameters of Eq. (5.13) representing the boundary of cell on the x-y plane, where the surface of the cell membrane is defined. The label “S”, “E” and “G” represent the sickle, elongated and granular shape, respectively.  $Z^T$  and  $Z^m$  are the average/maximum cell thickness.  $\langle C_H \rangle$  is the average value of the mean curvature over the cell surface.  $\epsilon$  is the  $L_2$  error of the polynomial fitting.

### 5.3.2 Shear viscosity of SS-RBC suspensions

The abnormal rheological properties of SS-RBCs are correlated with the stiffened cell membrane, which was measured by micropipette experiments in [76] at different deoxygenated stages. The shear modulus of the full deoxygenated sickle cell falls within a wide range of values depending on the intracellular HbS polymerization. For the SS-RBC with low MCHC value (25.5 g/dL), the shear modulus is about 100 times the value of healthy cells. However, for the SS-RBC with high MCHC value ( $> 35$  g/dL), the ratio between the sickle and healthy cell varies from 300 to  $\infty$ , where  $\infty$  represents a certain high value beyond the instrument measurement range. For SS-RBCs studied in rheological experiments, the typical MCHC value reported is between 32.2 g/dL and 41 g/dL. Therefore, the shear modulus of the full deoxygenated sickle cell is chosen to be 2000 times the value of the healthy cells in

the present study. The bending rigidity of sickle cell under different deoxygenated stages is unknown. We set its value to be 200 times the value of the healthy RBC in the present studies. With respect to the specific value of the shear modulus we used, sensitivity studies reveal that the shear viscosities of SS-RBC suspensions show weak dependence on shear rate until the ratio of SS-RBC shear modulus to the value of healthy cell is on order of 1000; similarly, for bending rigidity, weak dependence on shear rate is achieved with the value of SS-RBC about 200 times the value of healthy cell.

Blood flow with sickle cell anemia is modeled by a suspension of SS-RBCs in a solvent, which is represented by a collection of coarse-grained particles with DPD interactions. The dissipative force coefficient  $\gamma$  for the vertex-solvent interaction defines the RBC-solvent boundary conditions [46]. A short-range Lennard-Jones repulsive interaction is imposed between the membrane vertices of different (both healthy and diseased) cells for volume exclusion between the cells. The Lennard-Jones potential is defined by

$$U_{LJ}(r) = \begin{cases} 4\epsilon [(\sigma_{LJ}/r)^{12} - (\sigma_{LJ}/r)^6], & \text{if } r \leq r_{cut} \\ U_{LJ}(r_{cut}), & \text{if } r > r_{cut} \end{cases} \quad (5.16)$$

where  $\sigma_{LJ} = 0.42$ ,  $\epsilon = 1.0$ ,  $r_{cut} = 2^{1/6}\sigma_{LJ}$  in the DPD unit. The repulsive interaction vanishes for  $r > r_{cut}$ .

With the SS-RBC suspension defined above, we first consider the shear flow system with Hct = 45% following the experiment of Ref. [148]. The viscosity of the solvent is chosen to be  $\eta_0 = 1.2$  cp. The specific morphological characteristics of the SS-RBCs were not specified in the experiment. However, we note that the reported MCHC value of the sickle cell is relatively high (37.7g/dL). Therefore, the *granular shape* is adopted for the current simulation. Periodic Lees-Edwards boundary [96] conditions are imposed on the fluid system where different shear rates

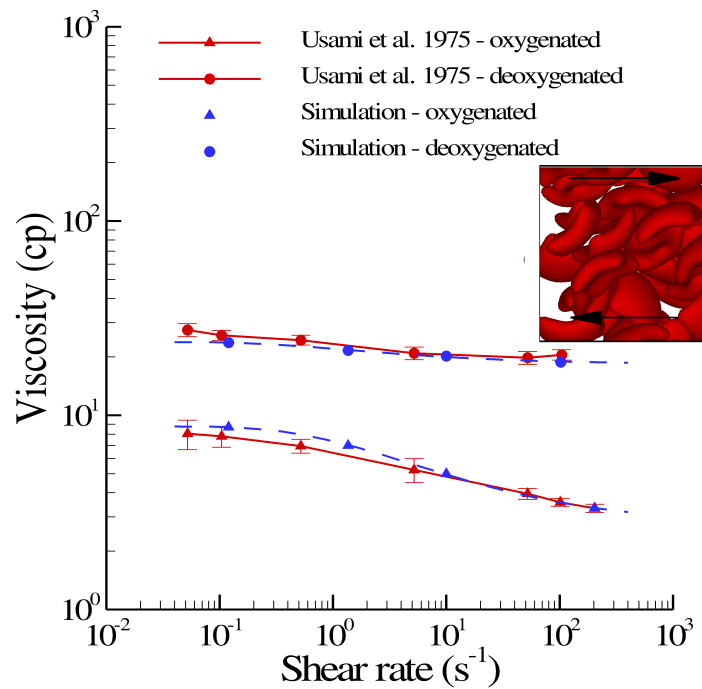


Figure 5.5: Shear viscosity of the healthy blood and SS-RBC suspensions with Hct = 45%. The dash lines represent the fitted curve to the simulation result by  $\eta = be^{-a/\gamma^{0.5}} + c$ , where  $\gamma$  is the shear rate.  $a$ ,  $b$  and  $c$  equal to 1.43,  $-6.04$ ,  $8.78$  for healthy blood and 1.08,  $-5.5$ ,  $23.9$  for deoxygenated SS-RBC suspension. The inset plot shows a snapshot of the “granular” SS-RBCs in shear flow.

can be obtained. The simulation domain has the size of  $40 \times 38 \times 28$  in DPD units, with 182 cells placed in the system. Fig. 5.5 shows the viscosity computed for both healthy and diseased blood with different shear rates. The dash lines are the simulation results fitted by  $\eta = be^{-a/\gamma^{0.5}} + c$ , where  $\gamma$  is the shear rate while  $a$ ,  $b$  and  $c$  are fitting parameters specified in Fig. 5.5. Good agreement with the experimental results is obtained for both types of blood. Healthy blood behaves as a non-Newtonian fluid under normal conditions with a shear-dependent viscosity [50]. The blood cells are less deformed at low shear rate conditions and exhibit “solid” like properties with relatively high viscosity. On the other hand, the blood cells can be substantially deformed at high shear rate conditions with the fluid properties more pronounced. Therefore, the viscosity of healthy blood decreases as the shear rate increases as shown in Fig. 5.5. Different from the healthy RBC suspension, the deoxygenated SS-RBC suspension shows elevated viscosity values nearly independent of the shear rate. This difference arises from the significantly stiffened sickle cell membrane, which is so rigid that the cell cannot be deformed even with the high shear rate employed in the experiment [148]. Therefore, the sickle cell exhibits “solid” behavior throughout the entire region of shear rate conducted in the present study. The present model, consisting of only SS-RBCs in suspension, clearly captures this transition from non-Newtonian to Newtonian flow.

To investigate the relationship between the rate of deoxygenation effect and the rheology of SS-RBC suspensions, Kaul et al. examined the shear viscosity of SS-RBC suspensions subjected to both fast and gradual deoxygenation procedures [87]. SS-RBC suspensions subjected to gradual deoxygenation procedure showed monotonic elevation of shear viscosity and the formation of the sickle shape of blood cells over a period of 30 mins until the full deoxygenated state was achieved. On the contrary, SS-RBC suspensions subjected to the fast deoxygenation procedure exhibits two distinct phases. The shear viscosity of the SS-RBC suspensions showed fast elevation within the first 7 mins of deoxygenation accompanied with the cell morphology

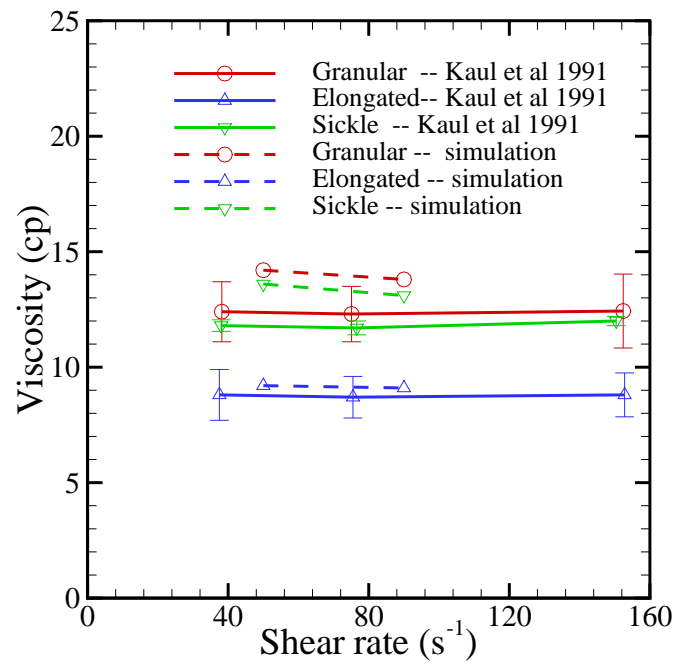


Figure 5.6: Shear viscosity of the sickle blood flow with different cell morphologies reported in Ref. [87], Hct = 40%.

transition to granular shape. However, the shear viscosity decreased gradually during further deoxygenation. A large portion of cells appears extremely elongated with the intracellular HbS fibers aligned in one direction. To study the morphology effect on the rheological behavior of the SS-RBC, we simulate the shear flow of SS-RBC suspensions with the three distinct types of sickle cell reported in the experiment (Hct = 40%). Fig. 5.6 plots the shear viscosity with shear rate from 25 to  $75s^{-1}$ ; the shear modulus of the cell membrane is the same for all the three types. Similar to Fig. 5.5, the SS-RBC suspension shows elevated and shear-independent viscosity values for all three types. Moreover, the SS-RBC suspensions exhibit different viscosity values for the different cell shapes. Within the shear rate of the current simulation, the viscosity of SS-RBC suspensions with granular, sickle and elongated shape is about 13.5, 12.2 and 9.4 cp, respectively. This result explains the progressive decrease of the viscosity value with further deoxygenation, since a large portion of granular cell transforms into the elongated shape during the procedure. This result is probably due to the different effective volume for each type of the SS-RBC in the shear flow system [87], which affects the momentum transport ability between the cells.

### 5.3.3 SS-RBC suspensions in tube flow

The hemodynamics of SS-RBCs was studied in an isolated vasculature in [84] with subpopulations of different MCHC values. While the oxygenated SS-RBCs exhibit hemodynamics similar to healthy blood flow, the deoxygenated SS-RBCs show distinctive dynamic properties for each type of subpopulation. In the simulation, we consider SS-RBC suspensions in a tube flow system with Hct = 30% similar to the experiment. However, the detailed size and topology information of the microvasculature for the experiment is unknown. To this end, we set the diameter of the tube to be  $9.0\mu m$ , which is a typical size for capillary flow. In this sense, we do not expect the apparent viscosity obtained from the simulation to match exactly with the experiment results. Instead, we explore the effect of different types of SS-RBCs

on the flow resistance in the microcirculation.

Deoxygenated blood flow is represented by a suspension of RBCs with sickle and granular shapes. The membrane shear modulus and bending rigidity are similar with the values adopted in the simulation of shear flow system. Blood plasma and cytosol are explicitly represented by DPD, and they are separated by the cell membrane through the bounce-back reflection on membrane surface. The viscosity of the cytosol is set to  $4\eta_0$  and  $50\eta_0$  for the healthy and deoxygenated blood flow, where  $\eta_0$  is the viscosity of the blood plasma <sup>1</sup>.

Fig. 5.7 plots the increase of the flow resistance with different oxygen tension for the sickle and granular shapes. While both types of blood flow show further increase in flow resistance at deoxygenated state, the granular type of blood flow shows a more pronounced elevation compared with the sickle shape. One possible explanation proposed by the Kaul et al. is the different distribution of SS-RBCs in the capillary. The inset plot of Fig. 5.7 shows the snapshots of the sickle and granular cells in the tube flow. The cells of sickle shape tend to flow along the axis of the tube as observed by La Celle et al. in experimental studies in [94]. To quantify this phenomenon, we computed the *cell orientation angle distribution* in the tube flow, as shown in Fig. 5.8. The cell orientation is defined by the angle  $\theta$  between the flow direction and the eigenvector  $V_1$  of the gyration tensor defined by Eq. (5.10). For each type of the cell, the simulated orientation angle distribution  $f(\theta)$  is fitted by superimposed gaussian wave functions. Detailed fitted functions and parameters are presented in the Fig. 5.8. Compared with the granular cells, the orientation angle of the sickle shape blood shows a wider distribution for large value of  $\theta$ , indicating that the sickle shape SS-RBCs are more likely to orient along the flow direction <sup>2</sup>. This configuration results in a lower flow resistance as compared with the granular

---

<sup>1</sup>We note that the viscosity of the cytosol under deoxygenated conditions could be much larger than  $50\eta_0$ . On the other hand, a sensitivity study we performed with cytosol viscosity  $\eta_{inner} = 100\eta_0$  shows that the blood dynamics is nearly independent of  $\eta_{inner}$  with  $\eta_{inner} > 50\eta_0$ .

<sup>2</sup>This is also supported by unpublished data at MIT. (Ming Dao and Sarah E Du, private communication.)

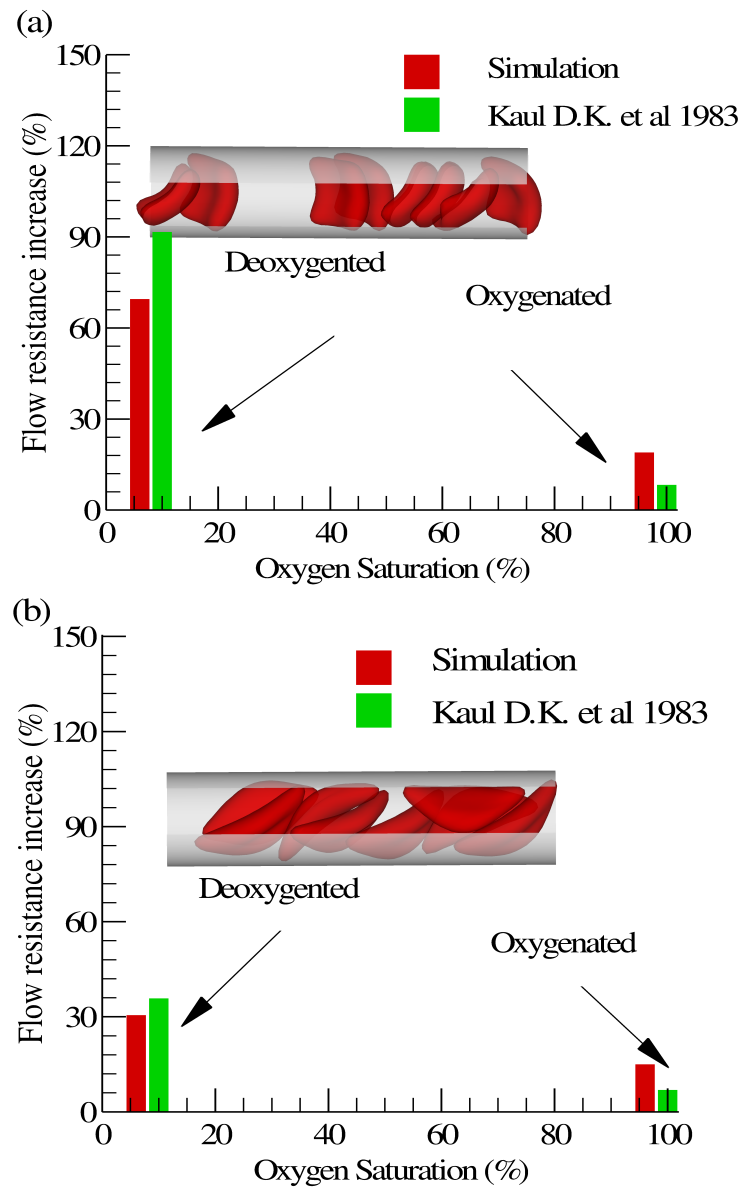


Figure 5.7: Increase of the flow resistance induced by the sickle blood flow for both granular (a) and sickle (b) shapes. The inset plot shows a snapshot of the sickle cells in the tube flow.

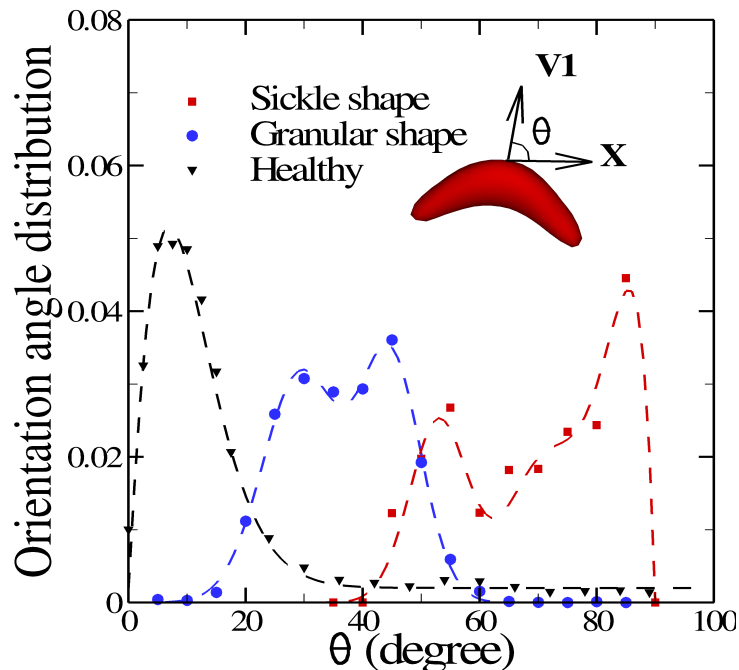


Figure 5.8: Cell orientation angle distribution  $f(\theta)$  for healthy, sickle and granular cells in pipe flow. The cell orientation is defined by the angle  $\theta$  between the flow direction ( $x$ ) and the eigenvector  $V1$  of the gyration tensor, as shown in the inset plot. The dash lines represent the fitted curves to the simulated results by superimposed gaussian wave functions. For the healthy cell,  $f(\theta) = a\theta e^{-b\theta^p} + c$ , where  $a = 0.014$ ,  $b = 0.047$ ,  $p = 1.4$ ,  $c = 0.002$ . For the granular cell,  $f(\theta) = a_1 e^{-c_1(\theta-b_1)^2} + a_2 e^{-c_2(\theta-b_2)^2}$ , where  $a_1 = 0.0315$ ,  $b_1 = 29.42$ ,  $c_1 = 0.012$ ,  $a_2 = 0.033$ ,  $b_2 = 44.75$ ,  $c_2 = 0.018$ . For the elongated cell,  $f(\theta) = a_1 e^{-c_1(\theta-b_1)^2} + a_2 e^{-c_2(\theta-b_2)^2} + a_3(90 - \theta)e^{-c_3(90-\theta)}$ , where  $a_1 = 0.024$ ,  $b_1 = 53.2$ ,  $c_1 = 0.021$ ,  $a_2 = 0.015$ ,  $b_2 = 70.3$ ,  $c_2 = 0.015$ ,  $a_3 = 0.025$ ,  $c_3 = 0.2$ . The fitting parameters are subject to the constraint  $\int f(\theta)d\theta = 1$ .

cells, which exhibit scattered distribution near the centerline of the tube. Finally, we note that the elevation of the flow resistance is underestimated by the simulation as compared with the experiment results. This discrepancy is probably due to the entrapment of certain cells to the microvascular endothelium, which may further increase the flow resistance of the blood flow. We discuss this mechanism in the following section.

### 5.3.4 Effect of the adhesive interaction: a simplified example

The hemodynamic results presented in Sec. 5.3.3 show elevated flow resistance for deoxygenated SS-RBC suspensions. However, no full flow occlusion was observed in the present study with a straight tube of diameter  $D = 9\mu\text{m}$  under different parametric variations<sup>3</sup>. This result is in contrast with the *in vitro* experimental results reported by Higgins et al. [69], where it is reported that SS-RBC suspensions may result in full flow occlusion in microchannels under deoxygenated conditions, i.e., without any adhesion with the wall. We suspect that the occlusion reported in the experiment is due to the complex geometry of the microchannel used in the experiment. Some deoxygenated cells with stiffened membrane may get stuck at the corner of certain channels with size smaller than a single cell, which is similar to microchannel experiment with malaria-infected RBC reported in [137].

Alternatively, recent studies on the SS-RBC occlusion indicate that the adhesive interaction between SS-RBCs and vascular endothelium plays a key role in the vicious “occlusion-and-sickle” cycle [81, 13]. The mechanism of the adhesive interaction is relatively complicated with several inter-related factors playing important role during the procedure. In addition to the interactions between SS-RBC and endothelium, an *in vivo* experiment indicates that SS-RBCs can also interact with the leukocytes adherent to inflamed postcapillaries [147].

---

<sup>3</sup>We performed 16 sets of simulations with different combinations of cell membrane rigidities and inner viscosity; however, no full occlusion was observed in any of these simulations.

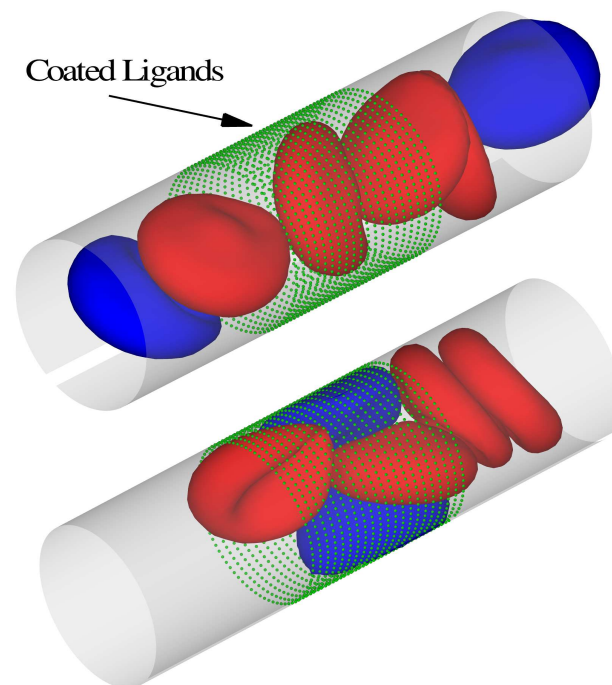


Figure 5.9: Sickle blood flow with adhesive dynamics. The green dots represent the ligands coated on the vessel wall. The blue cells represent the “active” group of sickle cell exhibiting adhesive interaction with the coated ligands. The red cells represent the “non-active” group of cells. Upper: a snapshot showing “active” group of cells flowing into the region coated with “ligands”. Lower: a snapshot of the SS-RBCs with local occlusion state.

Parameters	Simulations	Physical
spring constant ( $k_s$ )	400	$1.85 \times 10^{-5} \text{ N/m}$
equilibrium spring length ( $l_0$ )	0.0	$0.0 \text{ m}$
reactive distance ( $d_{on}$ )	0.5	$4.8 \times 10^{-7} \text{ m}$
rupture distance ( $d_{off}$ )	0.5	$4.8 \times 10^{-7} \text{ m}$
on strength ( $\sigma_{on}$ )	0.22	$1.02 \times 10^{-8} \text{ N/m}$
off strength ( $\sigma_{off}$ )	0.33	$1.52 \times 10^{-8} \text{ N/m}$
unstressed on rate ( $k_{on}^0$ )	600.0	$6.0 \times 10^5 \text{ s}^{-1}$
unstressed off rate ( $k_{off}^0$ )	0.25	$250 \text{ s}^{-1}$

Table 5.4: Simulation (in DPD units) and physical (in SI units) parameters for blood flow with adhesive interaction with vascular endothelium.

In this chapter, we present a simple toy example to highlight the effect of the adhesive interaction on the hemodynamics of sickle blood flow. *The stiff bioconcave* shape is adopted in this example. A systematically investigation of the cell adhesive interaction among the different cell groups is presented in Chap. 7. In this work, we simply assume that there exist certain types of endothelial ligands coated on the wall of the tube referring to the relevant adhesive proteins that we model indirectly, as shown in Fig. 5.9. The ligands are uniformly distributed with density  $4\mu\text{m}^{-2}$ . Bond interaction can be formed and ruptured between the cell vertices and the ligands with a stochastic model described in Sec. 5.2.3, where the simulation parameters are presented in Tab. 5.4.

With the simplified adhesive model defined above, we reconsider blood flow in a tube similar to Sec. 5.3.3. For comparison study, steady flow is first achieved with the adhesive interaction being turned off. The measured relative apparent viscosity is about 1.52 and no blood occlusion is observed in the simulation. Next, we consider blood flow with the adhesive interaction incorporated. As shown in Fig. 5.9, the blood cells are divided into two groups. Each SS-RBC in the “active” group (labeled by blue) expresses the adhesive receptors with the average adherent force about  $68pN$ , whereas the “non-active” group (labeled by red) does not interact with the ligands. The “active” group of cells, once it flows into the region coated with the

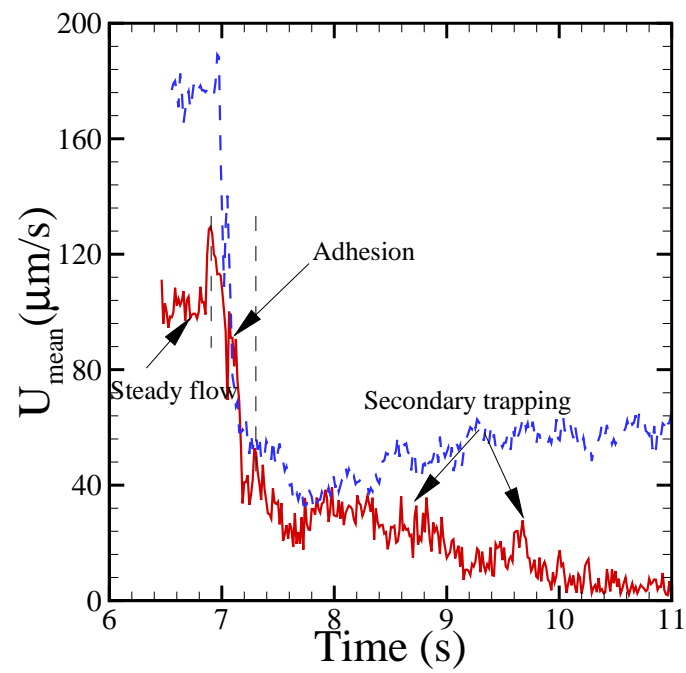


Figure 5.10: Mean velocity of the sickle blood at different stages of the adhesive dynamics. The red and blue curve correspond to different pressure drop of  $8.3 \times 10^4 Pa/m$  and  $1.35 \times 10^5 Pa/m$  respectively.

ligands, shows firm attachment to the wall of the channel, which results in substantial decrease in the effective tube diameter and the shear rate near the trapped cells. Moreover, the entrapped cells result in a secondary trapping of the “non-active” cells in the adhesion area due to the largely increased membrane stiffness. This procedure is accompanied with further decrease of the shear rate, which eventually leads to the partial or full occlusion of the tube flow.

Fig. 5.10 presents the mean velocity of the blood flow as a function of time corresponding to the procedure described above. For the case without adhesion, the steady flow state is reached with average velocity about  $180\mu\text{m}/\text{s}$  and  $115\mu\text{m}/\text{s}$ , respectively. With the adhesive dynamics turned on, blood flow exhibits a transition from steady flow to partial/full occluded state, which can be roughly divided into three stages according to the velocity values shown in Fig. 5.10. The first stage ( $t < 6.9\text{s}$ ) represents the steady flow state before the “active” cells arriving at the region coated with ligands. The velocity value is similar to the case without adhesion. However, the average velocity undergoes a sharp decrease to  $40\mu\text{m}/\text{s}$  during the second stage ( $6.9\text{s} < t < 7.3\text{s}$ ), representing the adhesion procedure between the “active” cells and the coated ligands with decreased effective tube diameter. In the third stage, the blood flow (blue curve) with larger pressure drop exhibits a partial occluded state with average velocity of  $50\mu\text{m}/\text{s}$  due to persistently adherent cells on the wall of channel. Moreover, the velocity of the blood flow with smaller pressure drop (red curve) decreases slowly to about  $10\mu\text{m}/\text{s}$ , representing the secondary entrapment of the “non-active” cells and the full occluded state.

## 5.4 Discussion

A validated multiscale model is employed to quantify the morphology and dynamic properties of sickle red blood cells. To the best of our knowledge, this is the first work on *multiscale 3D* modeling of sickle red blood cell which captures the heterogeneous

nature of both realistic single cell shape and corresponding collective hemodynamics. Specifically, three typical shapes of distorted sickle cell are constructed according to the experimental observations by SEM with different deoxygenation rates and MCHC values. The different degrees of distortion are quantified by the asphericity and the elliptical shape factors of each different cell shape, and our results are consistent with the medical image observations. We note that the modeling procedure provides a general framework to link the experimental results in macro-scale with the numerical modeling of blood cells at the meso-scale level, which can be further extended to general modeling of diseased cells with other specific shapes characterized by optical techniques.

With regards to the rheological properties, the simulated results are in good agreement with the experimental results for both healthy and deoxygenated SS-RBC suspensions. Compared with the healthy blood, the shear viscosity of the deoxygenated SS-RBC suspensions shows a general elevation for different shear rate conditions. Two main points emerge from the shear viscosity results of SS-RBC suspensions. First, the transition from the shear-thinning flow to the shear-independent flow reveals the profound effect of the cell membrane stiffening during the deoxygenation procedure as reported by Ref. [76]. Second, the simulated results of shear flow with different cell shapes indicate that the cell morphology further influences the shear viscosity values. While the blood with granular shape exhibits the largest viscosity, the elongated shape originated from the granular cell with further deoxygenation results in the least viscous state. Our simulation results further validate the dependence of SS-RBC rheology on the cell morphology as reported by Ref. [87].

Besides the shear flow system, the heterogeneous nature of the SS-RBC is also observed in the microtube flow system. The change of the flow resistance induced by granular RBCs shows a greater increase than the resistance of blood with sickle shape RBCs as the latter may align along the flow directions resulting in a wider plasma layer. Compared with the experiments conducted in isolated micro-vasculature, our

simulations indicate a general underestimation of the blood flow resistance induced by SS-RBC. This discrepancy is mainly due to the two simplifications in the current model: (i) the isolated vasculature is modeled as a simple tube flow, whereas the detailed wall topological information is omitted. (ii) The erythrocyte-endothelium interaction is not considered. Remarkably, the perfusion of the Ringer's solution after the deoxygenated SS-RBC suspensions only results in partial recovery of pressure and flow rate [84], indicating persistent adhesion events and local vascular obstruction.

Using a toy example, we show that the adhesive interactions have a profound effect on the hemodynamics of the sickle blood flow. The adhesive cells attaching to the vessel wall reduce the effective diameter of blood vessel, which results in further elevation of the flow resistance. Moreover, the adhesive cells attached on the vessel wall can further entrap those non-adhesive, less-deformable cells, leading to a secondary elevation of the flow resistance, or even the full occlusion of the channel. The “adhesion - trapping” procedure predicted by the present work resembles the essential stages of the “two-step” model for SS-RBC occlusion in the postcapillary venules proposed by Kaul et al. [81, 82]. However, we note that the present toy example fails to capture the heterogeneous adhesive capabilities among the different cell groups. In fact, recent experimental studies show the various cell fractions exhibit different adhesive dynamics under similar physiological conditions. These discrepancies are mainly due to the different *cell morphologies* and *membrane rigidities* among the different cell groups. Therefore, numerical characterization of the heterogeneous *cell morphologies* and *adhesive responses* would be of great interest. We address these two issues in Chap. 6 and Chap. 7, respectively.

## Chapter 6

# Predicting the heterogeneous morphologies of sickle red blood cells

In chapter 5, we constructed three typical cell morphological states for sickle red blood cells by applying artificial stretching forces at the selected anchor points on cell membrane. The stretching forces represent the surface tension exerted on the cell membrane due to the growth of intracellular sickle hemoglobin (HbS) polymers. In this chapter, we conduct a systematical investigation on the sickle cell morphological transition process by *explicitly* using a coarse-grained (CG) model of intracellular aligned hemoglobin polymers. It is found that the final shape of SS-RBCs is primarily determined by the angular width of the aligned hemoglobin polymer domain, but it also depends, to a lesser degree, on the polymer growth rate and the cell membrane rigidity. The heterogeneous sickle cell morphologies observed in experiments are successfully predicted without introducing any further *ad hoc* assumptions.

## 6.1 Introduction

Sickle red blood cells (SS-RBCs) exhibit heterogeneous morphological states under hypoxia conditions. This is mainly due to the polymerization of the abnormal sickle hemoglobin molecules inside the erythrocyte membranes. Specifically, the glutamic acid residues at the sixth position of the two  $\beta$ -subchains are replaced by valine in sickle hemoglobin, which results in low solubility in hypoxic conditions. As the oxygen of a SS-RBC is removed, sickle hemoglobin tends to aggregate in the bulk solution through a homogeneous nucleation and further grows into polymer states via a heterogeneous nucleation on the surface of the pre-existed polymers, according to the double nucleation model [51, 52]. Due to the intracellular sickle hemoglobin polymers, SS-RBCs exhibit substantial increase in the cell rigidity [76], elevating the blood flow resistance and potentially triggering vaso-occlusion in the microcirculation. Besides altering the cell rigidity, the growing sickle hemoglobin polymers domain inside the SS-RBC can potentially distort (“sickle”) the cell membrane, and therefore change the cell morphology under certain conditions.

However, unlike the elevation of cell rigidity, only some types of the deoxygenated SS-RBCs undergo apparent morphologic changes. Kaul et al. [84] investigated the deoxygenated SS-RBC morphology by categorizing the SS-RBCs into four groups according to the mean corpuscular hemoglobin concentration values. While the cell groups with medium mean corpuscular hemoglobin concentration ( $< 35$  g/dL) exhibit apparent cell deformation in deoxygenated conditions, most of the cells with high mean corpuscular hemoglobin concentration values exhibit granular or near biconcave shapes. Moreover, it is found that the SS-RBC morphology also depends on the rate of the deoxygenation procedure [87, 86]. SS-RBC suspensions following fast deoxygenation exhibit a large portion of cells with granular shape. In contrast, most of the SS-RBCs undergo large shape transition to “sickle” or “holly leaf” cells after gradual deoxygenation, see Fig. 6.1. To explore the mechanism of the cell distortion, the intracellular sickle hemoglobin polymers configuration were visualized

by optical birefringence [23] and differential polarization microscopy [24] with different cell morphologies and mean corpuscular hemoglobin concentration. It was revealed that the wide variety of SS-RBC morphologies has a close relationship with the intracellular aligned hemoglobin polymer. Although the aligned hemoglobin polymer occupies only about 5% of the total sickle hemoglobin polymer [112], the cell morphology is mainly determined by the total number of the aligned hemoglobin polymer domains and the configuration of each domain in the cell [23, 24].

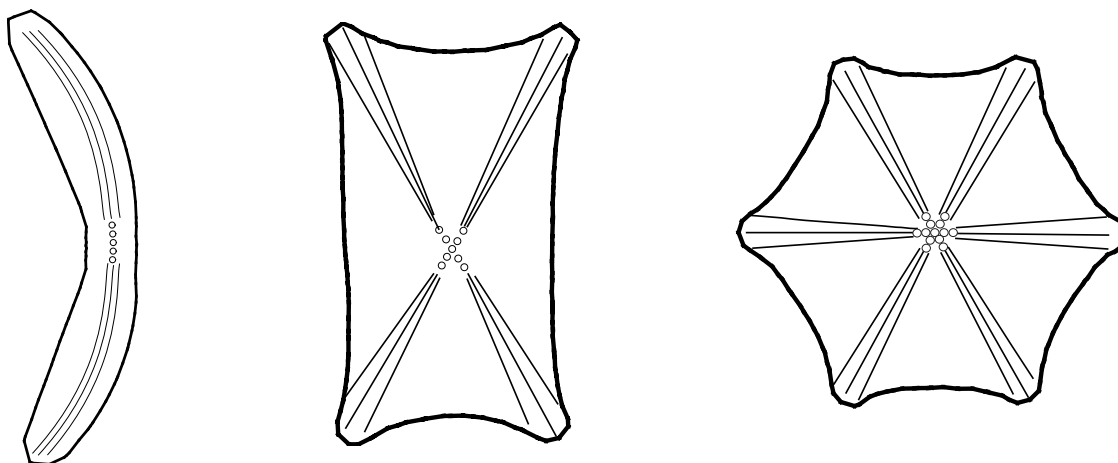


Figure 6.1: Sketches of typical cell shapes for deoxygenated SS-RBCs observed in experiments [24]. From left to right, the three sketches represent the “sickle”, “holly leaf” and “granular” shape of SS-RBCs. The various cell morphologic states are mainly determined by the specific intracellular aligned hemoglobin polymer configurations, represented by the solid lines. The dots represent the post-homogeneous nucleus.

According to the double nucleation theory [51, 52], the formation of a single polymer domain is initialized by the homogeneous nucleation of the sickle hemoglobin molecules in bulk solution and proceeds with explosive growth via polymer elongation and heterogeneous nucleation on the pre-existed polymers. The homogeneous nucleation rate is reported to be concentration dependent with power of  $60 \pm 10$  [77]. Such extremely high concentration dependence explains the prevalence of sin-

gle polymer domains in low mean corpuscular hemoglobin concentration cells, and that multiple sickle hemoglobin domains are usually found in high mean corpuscular hemoglobin concentration cells. On the other hand, the structure and amount of aligned hemoglobin polymer for individual domains are mainly controlled by the heterogeneous nucleation and the fiber growth rates [132, 57, 18]. With high concentration and fast growth rate, a post-nucleation aggregate of twofold symmetry develops into spherulitic domain through the growth of heterogeneously nucleated fibers and further deflection from the parent fibers. On the contrary, the angular widening of the polymer domain, originated from the fiber branching, is largely suppressed for smaller heterogeneous nucleation rate as observed in both experiments [18] and numerical simulations [31]. Remarkably, this tendency is also consistent with the inverse relationship between the amount of intracellular aligned hemoglobin polymer and the mean corpuscular hemoglobin concentration values for each class of cells (categorized by the total number of polymer domains) reported in Ref. [24].

To study the physical basis of the various SS-RBC shapes observed in experiment, we conducted numerical simulations to systematically investigate the effect of the sickle hemoglobin polymer configurations and SS-RBC membrane rigidity on the final morphologic states. The *primary* goal of this work is to examine if the various types of distorted cell shapes can be obtained from the different intracellular aligned hemoglobin polymer configurations determined by the different cell mean corpuscular hemoglobin concentration values and deoxygenation rates observed in experiments. Specifically, we employed a previously developed RBC model [46] in combination with a new coarse-grained (CG) stochastic model to represent the growth of the aligned hemoglobin polymer domain inside the cells. We studied the distortion of the cell membrane with aligned hemoglobin polymer domains of different angular width. The classical elongated cell with “sickle” and “holly leaf” shapes appear to be originated from the single aligned hemoglobin polymer domain with relatively limited angular width, whereas the “mosaic” or the near-biconcave shapes are favored

with the near spherulitic configurations. Moreover, for each type of the cell shapes, individual SS-RBCs exhibit various morphologic states as shown in Ref. [73, 9]. Therefore, the *second* goal of this work is to examine if, for each type of the SS-RBC (elongated, sickle, holly leaf, *etc.*), the various degrees of membrane distortion observed in experiments [73] can be obtained as a result of the typical intracellular sickle hemoglobin growth rates and the cell rigidities without introducing any further *ad hoc* assumptions. We note that the heterogeneous nucleation events are not explicitly modeled in the present work; instead, we directly consider the different aligned hemoglobin polymers originated from the various heterogeneous nucleation conditions and we investigate the subsequent cell morphological transition with those typical aligned hemoglobin polymer configurations observed in Ref. [24, 112]. We note that the current CG modeling may yield limited new physical insight into the details of sickle hemoglobin polymerization; however, it allows us to quantify the complex relationships among the fiber growth rate, cell membrane-polymer interaction and aligned hemoglobin polymer configurations, and identify their effects on the distortion of cell membranes.

This chapter is organized as follows. In Sec. 6.2, we explain the details of the intracellular aligned hemoglobin polymer. In Sec. 6.3, we study the final shapes of SS-RBC with different intracellular aligned hemoglobin polymer configurations. For each type of the SS-RBC, we study the effect of the cell rigidity on the final morphologic states. Moreover, the various cell morphologies are quantified by both 3D and 2D structure factors and compared with the results obtained from medical images. We conclude in Sec. 6.4 with a brief discussion.

## 6.2 Numerical model

The physical model for the red blood cell (RBC) membrane and the aligned hemoglobin polymer is developed in the framework of the Dissipative Particle Dynamics (DPD)

method [71, 40]. As discussed in Chap. 2, it is a particle-based method widely used for simulation of soft matter systems such as polymer solutions [100] and red blood cell suspensions [118]. We refer to Sec. 3.2 for details of the DPD method and Sec. 5.2.1 for the model of the RBC membrane.

### 6.2.1 Aligned Hemoglobin Polymer

In the deoxygenated state, the post-homogeneous aggregates grow into polymer state and further form into bundles of sickle hemoglobin fibers and cross-linked gel through heterogeneous nucleation and branching. A single sickle hemoglobin fiber is composed of seven double strands in the style of twisted rope with diameter of about  $d_0 = 21$  nm; fully representing the detailed structure of a single sickle hemoglobin fiber is too expensive in the scale of a single RBC ( $\sim 10\mu m$ ). Instead, we employ a CG model to represent a bundle of sickle hemoglobin fibers where the detailed structure of a single fiber is omitted. Each bundle is represented by single DPD particles connected by elastic bond interactions defined by

$$V_{bond} = \frac{k_b(3x_{ij}^2 - 2x_{ij}^3)}{(1 - x_{ij})} + \frac{k_p}{l_{ij}}, \quad (6.1)$$

where  $x_{ij} = l_{ij}/l_m$ ,  $l_{ij}$  is the bond length between particle  $i$  and  $j$ ,  $l_m$  is the maximum extension of the bond.  $k_b$  and  $k_p$  are the spring constants of the attractive and repulsive terms, respectively. The coupling of the two terms determines the equilibrium length  $l_0$ .

The bending rigidity of the aligned hemoglobin polymer bundle is modeled by

$$V_{angle} = k_a(\theta - \theta_0)^2, \quad (6.2)$$

where  $k_a$  is the bending coefficient and  $\theta_0$  is the spontaneous angle representing the deflection of the aligned hemoglobin polymer. Finally, the aligned hemoglobin polymer model includes an in-plane dihedral potential to represent the fixed growth

direction in global scale; the corresponding potential is given by

$$V_{dihedral} = k_d [1 + \cos(\phi_{ijkl})], \quad (6.3)$$

where  $i, j, k$  and  $l$  are four adjacent DPD particles on the modeled aligned hemoglobin polymer,  $\phi_{ijkl}$  is the instantaneous angle between the triangle  $\Delta_{ijk}$  and  $\Delta_{lkj}$ , and  $k_d$  is the constraint coefficient such that the growing fiber is in the same plane.

The development of the aligned hemoglobin polymer domain is modeled by the addition of single beads to the end of the polymer as ‘‘Brownian Ratchets’’ [124]. The growth rate  $k_t$  is represented by

$$k_t = k_{on} e^{-(\mathbf{f}_s \cdot \hat{\mathbf{e}})\delta/k_B T} - k_{off}, \quad (6.4)$$

where  $k_{on}$ ,  $k_{off}$  are the polymerization and depolymerization rate, respectively,  $\mathbf{f}_s$  is the instantaneous stall force exerted on the end of the polymer bead, and  $\hat{\mathbf{e}}$  is the polymer growth direction. We emphasize that  $\delta$  represents the unit length increase upon the addition of a single sickle hemoglobin monomer rather than the equilibrium length between the CG beads, which is *independent* of the length scale of the CG model. This is because the sickle hemoglobin polymer growth is driven by monomer addition rather than oligomer addition. A single sickle hemoglobin monomer can join the pre-existing polymers when the energy cost of this reaction overwhelms the energy gain due to the entropy loss. This result is also validated by experimental measurements [8]. On the other hand,  $k_{on}$  and  $k_{off}$  represent the growth and dissociation rates in terms of the CG polymer beads and should be adjusted according to the choice of the length scale of the CG model, as discussed in the following section. For each time step  $\Delta t$ , a single DPD particle is added to the polymer end according to the probability  $P_t = 1 - e^{-k_t \Delta t}$ . Specifically, a random number  $\eta$  is generated between  $[0, 1]$ , and a DPD particle is added if  $\eta < P_t$ . Details on the choice of the model parameters are discussed in the next section.

### 6.2.2 Simulation setup and physical parameters

The unperturbed RBC membrane keeping the biconcave shape in equilibrium is represented by a stress-free triangulated mesh [46] composed of  $N_v = 1000$  vertices. The shear modulus of the healthy RBC membrane is  $\mu_0 = 6.8\mu N/m$  and the bending rigidity is  $k_c = 3.7 \times 10^{-19} J$  according to the experimental measurements [42, 74, 113]. On the contrary, the membrane shear modulus of SS-RBC increases sharply in deoxygenated states. Experimental measurements by micropipette [76] revealed that the cell rigidity depends on the mean corpuscular hemoglobin concentration values. For SS-RBC with low value of mean corpuscular hemoglobin concentration, the effective cell rigidity is between  $20\mu_0$  and  $100\mu_0$ , while for cells with higher value of mean corpuscular hemoglobin concentration ( $> 35$  g/dL), the cell rigidity is on order of  $O(10^2)\mu_0$ . In the current work, we choose the cell shear modulus as described above. Values of the bending rigidity of SS-RBC under different deoxygenated states are unknown; we set its value to be  $20k_c$  in the current study. Sensitivity studies show that the final cell morphologies depend weakly on the bending rigidity within the range from  $10k_c$  to  $30k_c$ .

The growth rate of the sickle hemoglobin polymer was measured by Aprelev et al. in Ref. [8] as a function of monomer activity in bulk solution, given by

$$J = k_+\gamma_c c - k_-, \quad (6.5)$$

where  $\gamma_c$  is the activity coefficient, and  $c$  is the monomer concentration;  $k_+$  and  $k_-$  are the monomer addition and subtraction rate. The linear relationship between  $J$  and  $\gamma_c c$  reveals that the growth occurs by monomer addition instead of obligomer addition. While  $k_+$  and  $k_-$  are nearly constant for different sickle hemoglobin solution,  $\gamma_c c$  depends strongly on the intracellular mean corpuscular hemoglobin concentration value. On the other hand, the development of the aligned hemoglobin polymer domain is modeled in a coarse-grained manner in the this work, where each single

DPD particle is added to the end of the sickle hemoglobin polymer, forming elastic bonds with its adjacent particles with equilibrium length  $l_0 = 0.15\mu m$ . Moreover, the modeled polymer represents an aligned hemoglobin polymer bundle composed of multiple sickle hemoglobin fibers. Therefore, the unit increase length per bundle  $\delta$  scales as

$$\delta = \delta_0/N_f, \quad (6.6)$$

where  $\delta_0 \approx 0.45$  nm is a unit increase length per single fiber, and  $N_f$  is number of the sickle hemoglobin fiber of the bundle. In the present coarse-grained model, we consider the interaction between the aligned polymer and a local area of cell membrane with finite size. The polymer beads interact with the cell membrane vertices within a range of  $0.2 \sim 0.4\mu m$ . Accordingly, it models a bundle of aligned polymers on the order of  $O(10^2)$ . To this end, we choose  $N_f = 100$ , and the effective fiber bundle radius scales as  $\frac{1}{2}\sqrt{N_f} \times 21$  nm  $\approx l_0$ . Accordingly, the polymerization and depolymerization rates scale as

$$k_{on} = \frac{N_f k_+ \gamma_c c \delta}{l_0}; \quad k_{off} = \frac{N_f k_- \delta}{l_0}. \quad (6.7)$$

The bending rigidity and Young's modulus of the aligned hemoglobin polymer bundle scale as  $\kappa = N_f^2 \kappa_0$  and  $Y = Y_0$ , where  $\kappa_0$  and  $Y_0$  are the bending modulus and the Young's modulus of a single sickle hemoglobin fiber. According to the measurements in Ref. [150], we choose  $\kappa_0 = 1.0 \times 10^{-24} Nm^2$  and  $Y_0 = 0.1 GPa$ . In the present model, the parameters of elastic bond interaction  $V_{bond}$  between the CG polymer beads is determined by

$$Y = \frac{4l_0}{N_f \pi d_0^2} \left. \frac{\partial^2 V_{bond}}{\partial r^2} \right|_{r=l_0}, \quad (6.8)$$

to match the experimental value of Young's modulus. Fig. 6.2 shows the  $\partial^2 V_{bond}/\partial r^2$  near the equilibrium length  $l_0$  for the bond interaction. The effective Young's mod-

ulus is approximately  $21.1N/m \times 0.15 \times 10^{-6}m/100 \times \pi \times (10 \times 10^{-9}m)^2 \approx 0.1$  GPa. Similarly, the parameters of the angle potential  $V_{angle}$  are determined by matching the bending rigidities of the aligned hemoglobin polymer bundle using the thermal fluctuation method discussed in Ref. [150, 99].

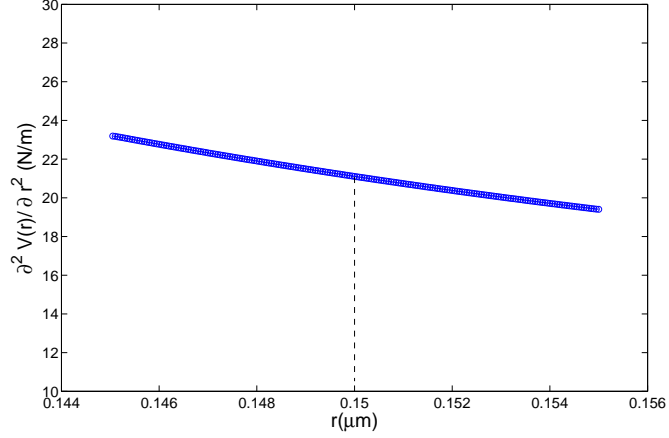


Figure 6.2:  $\partial^2 V_{bond}/\partial r^2$  near the equilibrium length  $l_0$ .

Starting from an intracellular homogeneous nucleation, the sickle hemoglobin polymers grow toward the cell membrane with growth rate determined by Eq. (6.4) and Eq. (6.7). As the polymer approaches the cell membrane, the polymer end undergoes a repulsive force exerted by the cell membrane, originated from the entropy loss of the cell membrane due to the presence of the underneath polymer end. To model this effect, we employ a short range repulsive interaction between the polymer end and the cell vertex, as defined by

$$U_{LJ}(r) = 4 \left[ \left( \frac{\sigma_{LJ}}{r} \right)^{12} - \left( \frac{\sigma_{LJ}}{r} \right)^6 \right], \quad (6.9)$$

where  $\sigma_{LJ} = 0.4\mu m$  and the repulsive interaction vanishes for  $r > 2^{1/6}\sigma_{LJ}$ . This repulsive force, in turn, results in various distorted cell membranes, as we discussed in the following section.

## 6.3 Results

### 6.3.1 Sickle cell morphology

Sickle red blood cells exhibit heterogeneous shapes in deoxygenated conditions due to the variable stress exerted by the growing sickle hemoglobin polymer on the cell membrane. The final cell shape is mainly determined by two factors: (i) the effective sickle hemoglobin polymer growth rate  $k_t$  (ii) the intracellular aligned hemoglobin polymer domain configuration.

The sickle hemoglobin polymer growth rate in bulk solution  $J$  depends mainly on the sickle hemoglobin concentrations as shown in Eq. (6.5). In the present work, we consider the polymer growth of SS-RBCs with typical mean corpuscular hemoglobin concentration value from 32 g/dL to 38 g/dL. The corresponding bulk growth rates vary from  $1.2 \times 10^4$  molecules/s to  $5.3 \times 10^4$  molecules/s. However, the effective growth rate  $k_t$ , different from the bulk value, also depends on the stall force  $\mathbf{f}_s$  exerted on the polymer ends according to Eq. (6.4). Since  $\mathbf{f}_s$  depends on the cell membrane rigidity, the effective growth rate  $k_t$  is determined by both the cell membrane rigidity and the mean corpuscular hemoglobin concentration values. As the growing fibers approach and distort the cell membrane,  $k_t$  decreases due to the increasing stall force. For individual SS-RBCs with specific mean corpuscular hemoglobin concentration value, we can define a threshold for the coarse-grained polymer bead number  $N_m$  such that the effective growth rate  $k_t$  vanishes as the number of polymer beads exceeds  $N_m$ , whereas  $N_m$ , in turn, depends on the cell rigidity and the intracellular polymer configuration.

Different from the effective sickle hemoglobin polymer growth rate, the intracellular aligned hemoglobin polymer configuration depends on several inter-related conditions: the mean corpuscular hemoglobin concentration of the sickle cell, the rate of the deoxygenation process, the final gas tension, temperature, *etc.*, which are difficult to be explicitly incorporated into the current model. Instead, we construct

four different types of post-homogeneous nucleation in cell populations of different mean corpuscular hemoglobin concentration values, from which the various aligned hemoglobin polymer configurations typically observed in experiment can be obtained [24]. In the current section, the SS-RBC morphology is investigated for a specific value of  $N_m$  (determined by a specific cell membrane shear modulus) for each type of SS-RBC. The influence of the cell rigidity on  $N_m$  and final cell morphology will be discussed in Sec. 6.3.2

First, we consider a post-homogeneous nucleation in linear style, where the free monomers can only be added to the “active” beads at both ends of the polymer, as shown in Fig. 6.3. This configuration implies that the polymer domain develops along a specific direction in the x-y plane as represented by the growth of a single polymer branch, whereas the angular span of the aligned hemoglobin polymer domain is relatively small. This configuration prevails with the physiological conditions of low mean corpuscular hemoglobin concentration value and slow deoxygenation rate, where the sickle hemoglobin heterogeneous nucleation is largely suppressed, as observed in experiments [24] and predicted by simulations [31]. Accordingly, we choose the mean corpuscular hemoglobin concentration value as 32 g/dL, where the bulk growth rate is  $1.2 \times 10^4$  molecules/s. Moreover, we note that the aligned hemoglobin polymer domain may deflect along the z direction due to the heterogeneous growth [31]. To incorporate this effect, we set the polymer spontaneous angle  $\theta_0$  to be  $179^\circ$  and  $180^\circ$  respectively, where the former represents a deflection and the latter corresponds to a straight bundle.

Fig. 6.3 shows successive snapshots of the cell morphology at different stages of the aligned hemoglobin polymer development. The polymer growth threshold  $N_m$  is 80 and 93, respectively. Starting from the post-homogeneous nucleation, the aligned hemoglobin polymer domain develops towards the cell membrane. As the sickle hemoglobin polymer approaches the membrane, two spicules appear on the cell membrane near the interaction points. Moreover, as the length of the aligned

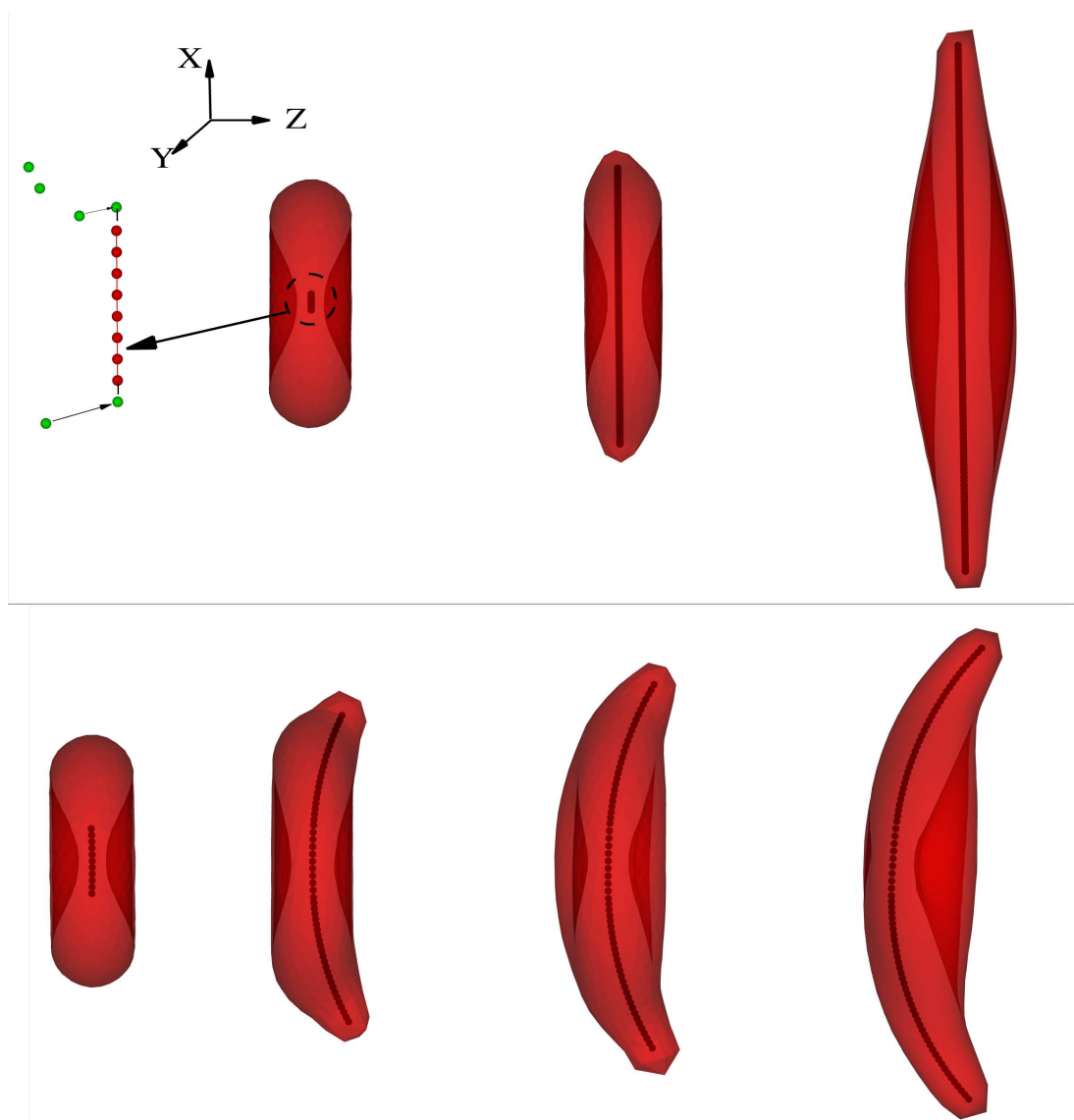


Figure 6.3: Upper: successive snapshots of the sickle cell membrane in the different development stages of the intracellular aligned hemoglobin polymer domain with “linear” growth in x-direction. The left sketch demonstrates the coarse-grained model for the aligned hemoglobin polymer domain development: free sickle hemoglobin monomers (green color), represented by the DPD particles, can potentially join with the pre-existed polymers (red color) with probability defined by Eq. (6.4). A linear polymer configuration is adopted in the current case to represent the specific growth direction. Different polymer configurations are adopted to represent the various aligned hemoglobin polymer domains, as shown in Fig. 6.4 and Fig. 6.5. Lower: successive snapshots of the sickle cell with growing aligned hemoglobin polymer domain deflected in the z-direction (normal to the cell), resulting in the classical “sickle” shape.

hemoglobin polymer domain continuously increases and exceeds the size of the original cell, the cell membrane undergoes subsequent distortion. For a straight sickle hemoglobin bundle free of deflection in the  $z$  direction, the distorted membrane exhibits largely distortion along the growth direction. In the  $x$ - $y$  plane, the original “discocyte” shape transits into the oval shape where the prolonged diameter is almost twice the value of the original cell. This configuration resembles the sickle cells widely observed in deoxygenated SS-RBCs with low mean corpuscular hemoglobin concentration values [9]. Moreover, for a polymer model with spontaneous angle  $\theta_0 = 179^\circ$ , the developed sickle hemoglobin fibers exhibit skewed morphology in the  $y$ - $z$  plane as well as an elongated state in the  $x$ - $y$  plane. Accordingly, the elongated cell membrane follows the spontaneous curvature of the aligned hemoglobin polymer domain, resulting in the classical “sickle” shape of SS-RBC as widely observed under slow deoxygenation.

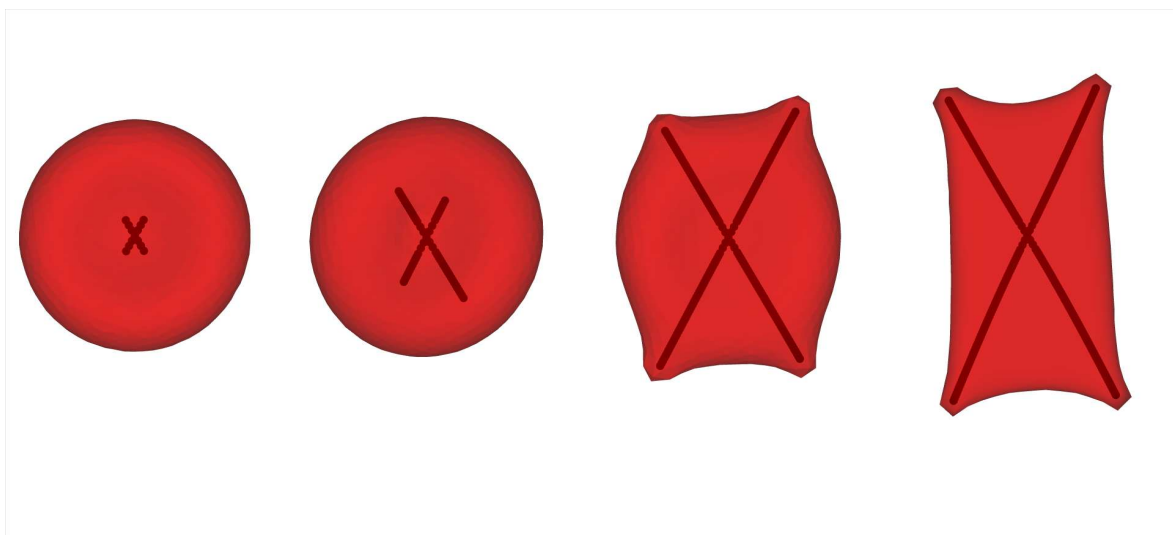


Figure 6.4: Successive snapshots of a SS-RBC with intracellular aligned hemoglobin polymer domain of finite angular width. Two polymer branches are used to represent the angular spanning during the domain development. The final cell morphology resembles a “holly leaf” shape.

Next, we consider the aligned hemoglobin polymer domain with finite angular span in the  $x$ - $y$  plane. This configuration can be derived from post-homogeneous

nucleation composed of multiple sickle hemoglobin fiber branches, as shown in Fig. 6.4. The angular width of the aligned hemoglobin polymer domain quantified by the angle between the two main polymer branches, varies from  $45^\circ$  to  $60^\circ$ . Free sickle hemoglobin monomers can join the aligned hemoglobin polymer domain at each of the four polymer ends. This configuration corresponds to another type of widely observed aligned hemoglobin polymer domain in SS-RBCs named “central-constriction” according to Ref. [24]. The polymer domain resembles a dumbbell shape; limited amount of aligned hemoglobin polymer is observed *near the center* of the nucleation while large amount of aligned hemoglobin polymer is found in the outer regions. As this type of aligned hemoglobin polymer domain is widely found in SS-RBC with medium mean corpuscular hemoglobin concentration value, we choose the mean corpuscular hemoglobin concentration value as 34 g/dL in the present work, and the corresponding bulk growth rate is  $1.97 \times 10^4$  molecules/s. Successive snapshots of a SS-RBC with this type of aligned hemoglobin polymer domain are shown in Fig. 6.4, where the polymer growth threshold  $N_m$  and the value of the spontaneous angle  $\theta_0$  are set to 120 and  $180^\circ$ , respectively. The growing sickle hemoglobin fiber not only expands the cell along the growth direction but also results in multiple spicules on the cell membrane. The final cell morphology resembles the “holly leaf” shape as widely observed in the SS-RBC with low/medium mean corpuscular hemoglobin concentration value [84, 87, 73].

Finally, we consider SS-RBCs with spherulite shape of the aligned hemoglobin polymer domain with the corresponding homogeneous nucleation shown in Fig. 6.5. In the present work, this configuration represents the polymer domain with spherulite configuration, similar to the polymer configuration observed in sickle hemoglobin solution (Ref. [18]), individual cells (Ref. [24]), and through simulation (Ref. [31]). It can be viewed as an extreme case of the four arm structure: for a sickle cell with high value of mean corpuscular hemoglobin concentration, the heterogeneous nucleation rate is large and the polymer domain can transform into spherulite configuration

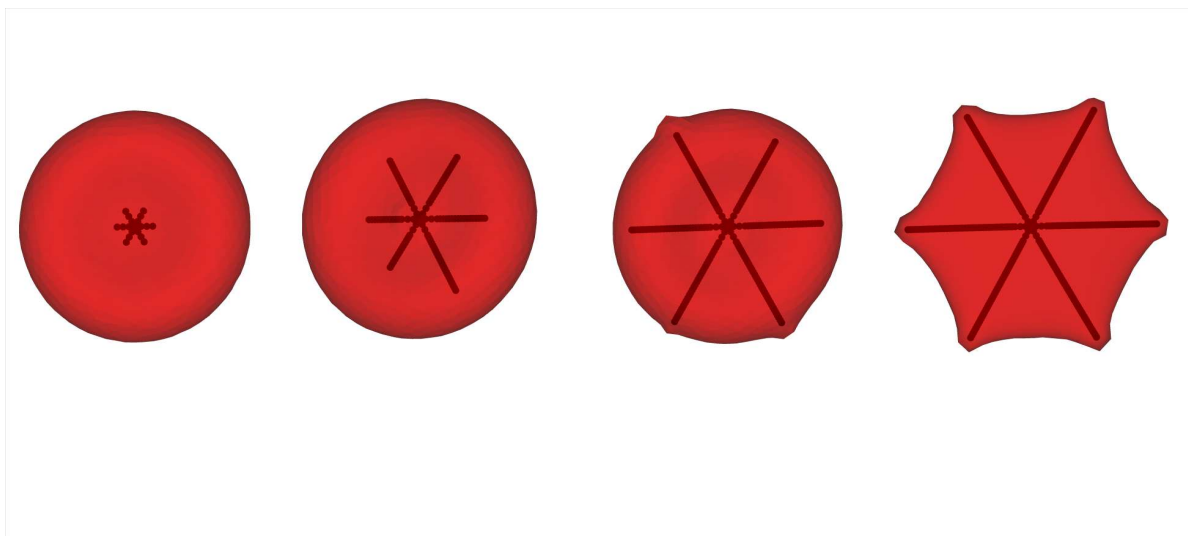


Figure 6.5: Successive snapshots of a SS-RBC with intracellular aligned hemoglobin polymer domain of spherulite configuration, where the full domain is filled with sickle hemoglobin polymers due to the high heterogeneous nucleation rate during the growth procedure. The final cell morphology resembles a “granular” shape.

and subsequently develop a radial symmetry. We note that this “radial symmetry” configuration is not the initial configuration of homogeneous nucleus, but results from the subsequent heterogeneous nucleation events. The development of the polymer network topologies is not considered in the present model. To incorporate the properties of this polymer domain, we start with the post-homogeneous state where the spherulite configuration has already formed, and we study the subsequent development of the polymer domain to explore the effect of the polymer domain on the cell morphologies. The value of “six” arm is kind of arbitrary. This value represents the number of sites where the Hbs polymer can potentially interact with the cell membrane where multiple “spicules” formed. We notice that this type of polymer configuration prevails in cells with high value of mean corpuscular hemoglobin concentration [24]. Accordingly, we choose the mean corpuscular hemoglobin concentration value as 38 g/dL with the bulk growth rate  $5.3 \times 10^4$  molecules/s. The polymer growth threshold  $N_m$  and the spontaneous angle  $\theta_0$  are 160 and  $180^\circ$ , respectively. With isotropic distribution of sickle hemoglobin polymer branches, free

sickle hemoglobin monomers are added to the aligned hemoglobin polymer domain with full angular symmetry. As the sickle hemoglobin fiber approaches the cell membrane, multiple spicules appear on the cell membrane. However, different from the “sickle” and “holly leaf” cells, this type of SS-RBC does not bear further distortion. This is mainly due to two reasons: i) the growth of the individual sickle hemoglobin arm can be limited due to the depletion of the free sickle hemoglobin monomers. For the spherulite polymer domain, the inner polymer density is relatively high due to the large heterogeneous rate. The polymer domain may run out of free sickle hemoglobin monomer as the domain develops towards the cell membrane. ii) For deoxygenated SS-RBCs with high mean corpuscular hemoglobin concentration value, the membrane shear modulus exhibits much larger value than the cells with low mean corpuscular hemoglobin concentration, resulting in much larger stall force on the growing polymer ends. Moreover, the growth of the spherulite sickle hemoglobin domain expands the cell membrane isotropically. However, the total area of the cell membrane is constrained due to the incompressibility of the lipid bilayer. Therefore, the effective growth rate of the individual sickle hemoglobin fiber is largely suppressed due to the large force exerted on the polymer end. The final stage of the cell resembles the near-biconcave shape with multiple spicules on the cell surface, which corresponds to the granular shape of deoxygenated SS-RBC widely observed in the cells of high mean corpuscular hemoglobin concentration value or with fast deoxygenation procedure.

### 6.3.2 Quantifying the cell membrane distortion

In the previous section, the final morphology of the sickle cell is obtained for a specific threshold value  $N_m$  for the growth of each aligned hemoglobin polymer domain to represent the effect of the stall force exerted on the polymer ends as shown in Eq. (6.4). However, we note that the stall forces on the polymer end depend on the specific cell rigidity, which varies for individual deoxygenated SS-RBCs [76]. For each

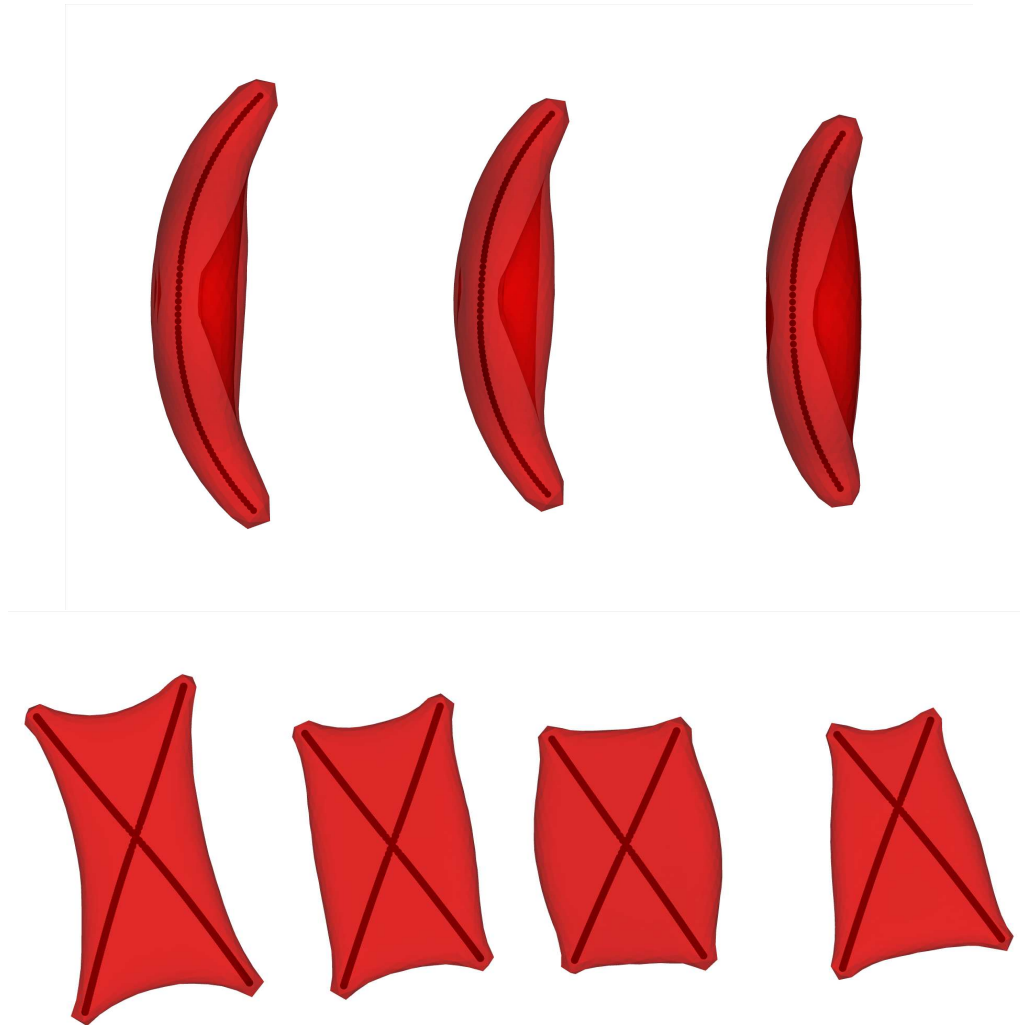


Figure 6.6: Final morphologies of the “sickle” (top) and “holly leaf” (bottom) shape of deoxygenated SS-RBC for different values of cell membrane shear modulus. The “sickle” shape of SS-RBC corresponds to low mean corpuscular hemoglobin concentration value (32 g/dL) and the shear modulus of the cells shown above is set to  $20\mu_0$ ,  $40\mu_0$  and  $70\mu_0$  according to experimental measurements [76]. The “holly leaf” shape of SS-RBC corresponds to medium mean corpuscular hemoglobin concentration and the shear modulus is set to  $30\mu_0$ ,  $60\mu_0$  and  $120\mu_0$ . We have also included a non-symmetric case in the fourth plot representing a cell morphology with the post-homogeneous nucleus off the cell center with shear modulus  $60\mu_0$ .

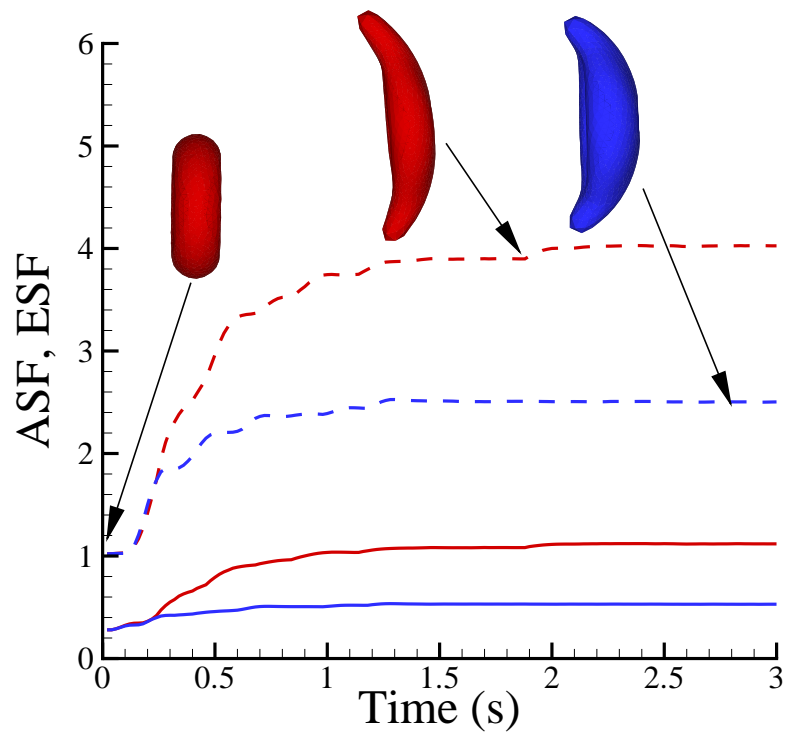


Figure 6.7: Instantaneous values of the Asphericity (solid lines) and Elliptical shape factor (dash lines) of the “sickle” SS-RBC as the aligned hemoglobin polymer domain develops. The red curves correspond to SS-RBC with membrane shear modulus  $\mu = 30\mu_0$  and deflection angle  $\theta_0 = 179^\circ$ . The blue curves represent the SS-RBC with shear modulus  $\mu = 60\mu_0$  and  $\theta_0 = 178.5^\circ$ .

type of the SS-RBC discussed above, the bulk growth rate of the intracellular sickle hemoglobin polymer is similar and is determined mainly by the mean corpuscular hemoglobin concentration values [8]. However, the deoxygenated cells with different cell rigidities may still end up with different extent of membrane distortion, where the growth rate  $k_t = k_{on}e^{-f\delta/k_B T} - k_{off}$  approaches zero. To investigate the effect of cell rigidity on the final cell morphology, we simulate the development of the intracellular aligned hemoglobin polymer domain with different cell membrane shear modulus according to the experimental measurements [76]. The detailed choices of the simulation parameters are shown in Tab. 6.1.

	MCHC	$\mu$	$\theta_0$	$w$
E	32 g/dL	$[20\mu_0, 80\mu_0]$	$180^\circ$	$0^\circ$
S	32 g/dL	$[20\mu_0, 80\mu_0]$	$[178.5^\circ, 179^\circ]$	$0^\circ$
H	34 g/dL	$[30\mu_0, 120\mu_0]$	$180^\circ$	$[45^\circ, 60^\circ]$
G	38 g/dL	$[40\mu_0, 2000\mu_0]$	$180^\circ$	$180^\circ$

Table 6.1: Simulation parameters for each type of SS-RBC. The symbol ‘‘MCHC’’ represents mean corpuscular hemoglobin concentration values. The symbol ‘‘E’’, ‘‘S’’, ‘‘H’’ and ‘‘G’’ represents the elongated, sickle, holly leaf and granular shape of the SS-RBC.  $\mu$  and  $\mu_0$  represent the shear modulus of the deoxygenated SS-RBC and healthy RBC respectively.  $\theta_0$  and  $w$  represent the spontaneous deflection angle and the angular width of the aligned hemoglobin polymer domains, respectively.

For each type of the post-homogeneous nucleus discussed above, the development of the aligned hemoglobin polymer domain is simulated with shear modulus shown in Tab. 6.1. *Instead of terminating the polymer growth with pre-determined threshold value  $N_m$ , the development of the aligned hemoglobin polymer domain is terminated automatically as the effective growth rate  $k_t$  approaches 0, therefore defining the final cell morphological states without any ad hoc threshold parameters.* Fig. 6.6 shows the final morphological state of the ‘‘sickle’’ and ‘‘holly leaf’’ cells with different shear modulus values. For low shear modulus value, both types of SS-RBCs exhibit large membrane distortion; however, the cell shape approaches the undisturbed state as the cell rigidity increases. Sensitivity studies have also been conducted on the elongated

and granular types of SS-RBCs, where similar tendency has been observed.

To further quantify the membrane distortion, we introduce both 3D and 2D structural factors to characterize the individual SS-RBC as discussed above. The 3D structural factors can be identified by the eigenvalue analysis of the gyration tensor defined by Eq. (5.10). Basing on the eigenvalues of the gyration tensor, we define the *asphericity* shape factor (ASF) and the *elliptical* shape factor (ESF) by Eq. (5.11).

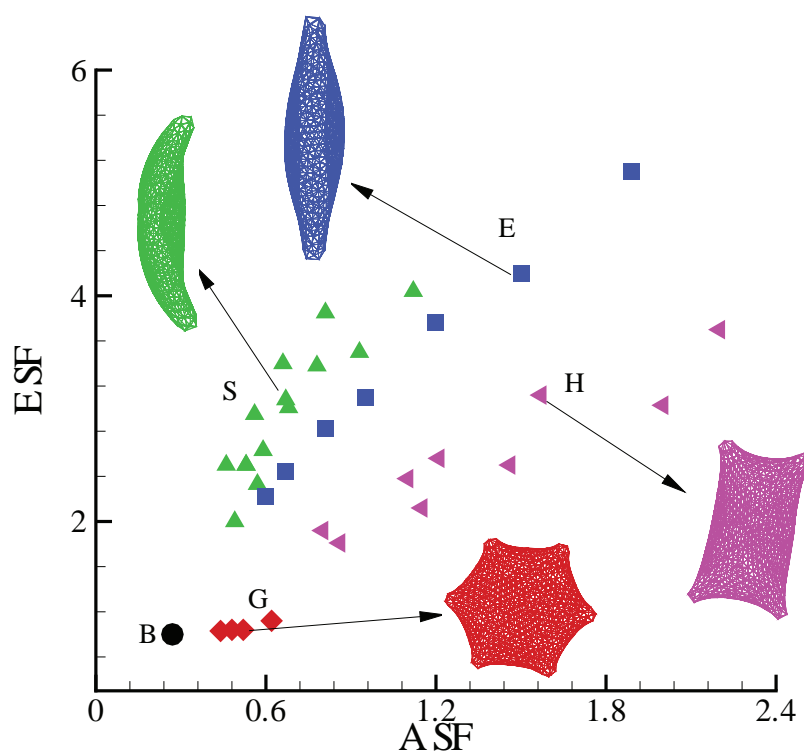


Figure 6.8: ASF and ESF for the various cell morphologies obtained. The label “B”, “G”, “S”, “H” and “E” represents the biconcave, granular, sickle, holly leaf and elongated shape, respectively. The snapshots show the typical cell shapes for each type of SS-RBC morphology obtained in the present study.

Fig. 6.7 shows the instantaneous ASF and ESF for the “sickle” SS-RBC as a function of the development of the aligned hemoglobin polymer domain for two different values of cell rigidity. Starting from the biconcave shape, the structural factors for both cases show rapid changes within the first  $0.4 \sim 0.5s$ , representing

the initial fast development of the aligned hemoglobin polymer domain. However, the structural factors show slower change after 0.5s and converge to specific values due to the decrease of the effective growth rate  $k_t$ . The more rigid the cell membrane, the sooner the structural factors begin to converge. Moreover, the asymptotic values of ASF and ESF are larger for less rigid cells. These results are consistent with the theoretical studies in Ref. [26] and can be understood by Eq. (6.4). For the same degree of cell distortion, the polymer ends approaching the cell membrane of larger rigidity bear with larger stall (entropy) force [26], resulting in faster decay of the growth rate  $k_t$ .

To systematically quantify the different cell distortions, the structural shape factors are evaluated for each type of SS-RBC within the physiological region of the cell shear modulus listed in Tab. 6.1. As shown in Fig. 6.8, the granular cells show similar characteristics with a healthy cell for both ASF and ESF. On the contrary, the elongated cells exhibit the largest deviation from the perfect biconcave shape. Compared with the elongated cells, the sickle cells exhibit smaller ASF due to the curvature membrane surface while the holly leaf cells exhibit smaller ESF due to the larger angular width of the intracellular aligned hemoglobin polymer domain.

Similar to the 3D structural shape factors, 2D morphological analysis has also been conducted on medical images of different sickle cells, where the circular shape factor (CSF) and 2D elliptical shape factors (ELSF) are used to quantify the various SS-RBC morphologies [73, 9]. Accordingly, we analyze the 2D structural properties of the SS-RBC by defining CSF and ELSF as

$$\begin{aligned} \text{CSF} &= 4\pi \textit{area}/(\textit{perimeter})^2 \\ \text{ELSF} &= D_b/D_a, \end{aligned} \tag{6.10}$$

where *area* and *perimeter* are the in-plane area and perimeter of the close curve defined by the cell.  $D_a$  and  $D_b$  are the long and short diameter, respectively. CSF and ELSF characterize the deviation of a curve from the circular shape. These two

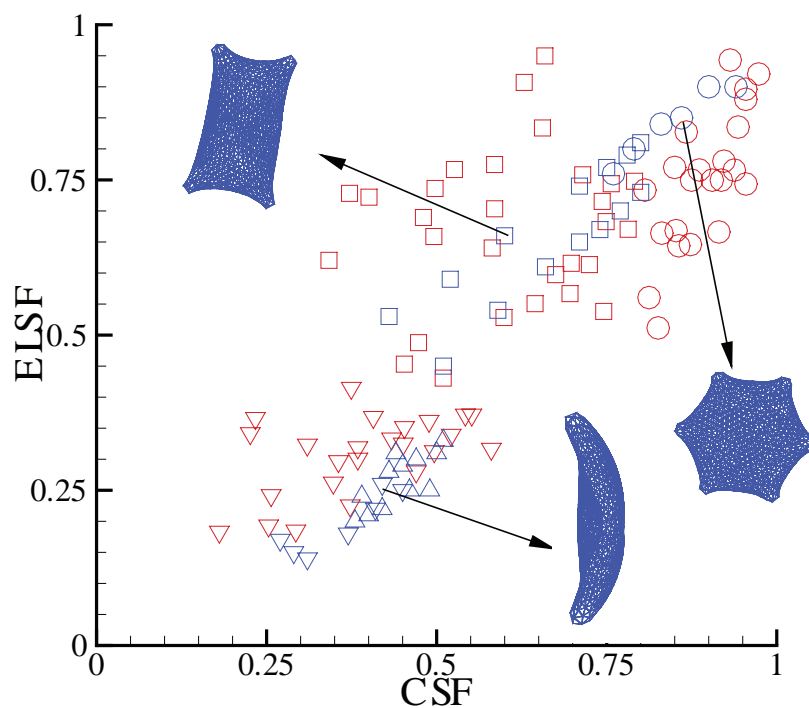


Figure 6.9: Circular (CSF) and 2D elliptical shape factors (ELSF) for different cell morphologies obtained from both medical image process [73] (red) and present simulations (blue). The circle and square symbols represent the shape factors of the granular and holly leaf SS-RBC. The red inverted triangle symbols represent both the “sickle” and the “elongated” SS-RBC obtained from experiment as they are unclassified in the experiment. The blue inverted triangle symbols represent the simulated “elongated” cells while the blue triangle symbols represent the simulated “sickle” cells.

factors are unit for a perfect circle and close to zero for a “line” shape. Similarly, the structural factors are analyzed for each type of the SS-RBC with shear modulus values shown in Tab. 6.1. Fig. 6.9 plots both CSF and ELSF for the various cell membranes obtained from the above simulations. As a comparison, we also show the experimental results of the sickle red blood cells from medical images [73]. The sickle red blood cells are classified into the “sickle”, “holly leaf” and “granular” types according to the cell morphologies under deoxygenated states [73]. As shown in Fig. 6.9, while the structural factors of sickle red blood cell obtained from the simulation fall within the region of the experimental observations, the simulated results do not cover the entire range of experimental results. The quantitative difference is probably due to the limited knowledge of the physiological conditions for the SS-RBCs in the experiment as the mean corpuscular hemoglobin concentration, rate of deoxygenation and cell membrane deformability are not specified for the individual cell groups of the experiments. Therefore, the physiological conditions specified in Tab. 6.1 may not cover the exact region of physiological values adopted in the experiment. This issue requires further experimental and numerical investigations.

## 6.4 Discussion

Starting from a single post-homogeneous nucleation proposed in Ref. [52], we investigated the effect of the intracellular growing sickle hemoglobin fiber on the final morphological properties of SS-RBCs. Based on the different sickle hemoglobin configurations typically observed by polarization imaging microscopy, the growth rate of sickle hemoglobin polymer and the mechanical properties of sickle hemoglobin fibers, we constructed a coarse-grained model for the development of the aligned hemoglobin polymer (aligned hemoglobin polymer). For individual SS-RBCs, the final morphological state is obtained through the following three steps:

- We choose a specific type of post-homogeneous nucleus according to experimental

observations.

- We simulate the development of the aligned hemoglobin polymer domain with the bulk growth rate of the sickle hemoglobin bundles determined by the intracellular mean corpuscular hemoglobin concentration value.
- As the sickle hemoglobin fibers approach the cell membrane, the effective growth rate of the aligned hemoglobin polymer domain decreases with the stall force depending on the cell membrane rigidities. The final morphological state is obtained when the effective growth rate tends to zero.

Using this model, we explored the extent to which the heterogeneous morphologies of deoxygenated SS-RBCs can be obtained without any further knowledge of the detailed structure of the polymer domain at the molecular level. Our simulation results indicate that the various shapes of deoxygenated SS-RBCs are mainly determined by the aligned hemoglobin polymer configuration, which is consistent with the results of Ref. [112]. Specifically, the polymer domain in SS-RBCs with low mean corpuscular hemoglobin concentration value tends to form aligned configuration with limited angular width, resulting in the typical “sickle” or “holly leaf” shape. On the other hand, the spherulite polymer domain is favored in SS-RBCs with high mean corpuscular hemoglobin concentration values, resulting in a near-biconcave shape with multiple spicules on the cell surface. This tendency is also consistent with the experimental observation on cell morphology in *in vitro* blood suspensions in Ref. [84, 87]. Within each type of SS-RBC, the cells further show scattered morphological states depending on the individual cell membrane rigidity. Given the membrane shear modulus in the range of physiologic values measured by micropipette [76], the simulated cell morphological states, quantified by the structural factors CSF and ELSF, fall within the range of the experimental results from medical images.

However, we note that several other physical conditions omitted in the current model can potentially also contribute to the heterogeneous distributions of cell morphologies. First, we have assumed that the bulk growth rate is the same at each

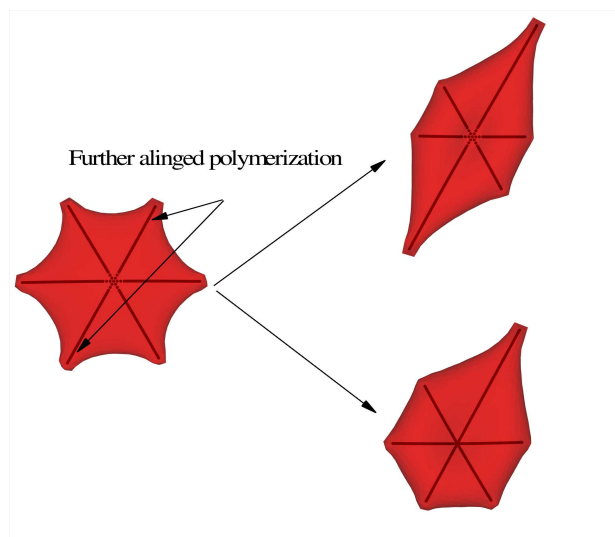


Figure 6.10: Elongated shapes: with further aligned polymerization along the specific direction, the granular cell (left) transforms into an “elongated” cell with the cell center keeping the granular shape (upper right), resembling the non-traditional “elongated” cell observed in Ref. [24]. The lower right plot represents the final cell morphology with the high growth rate imposed only on the upper right direction.

of the polymer ends. The implicit assumption here is that the rate-limiting process for the aligned hemoglobin polymer domain development is the stall force on the sickle hemoglobin polymers instead of sickle hemoglobin density changes during the polymerization process. Incorporation of the anisotropic/time-dependent fiber growth rates and time-dependent cell rigidity may result in further heterogeneous morphological states. In Ref. [87], a non-traditional type of “elongated” cells is obtained after further deoxygenation treatment on the granular cells. They are characterized by elongated projection along certain direction while the center part keeps the granular shape. It was postulated [87] that this type of “elongated” cell originates from the further growth of aligned polymer along the elongated direction during the prolonged deoxygenation process. In the present work, we test this idea by imposing anisotropic growth rate for intracellular polymer domain. Starting from a granular shape of cell, we impose the polymer growth rate twenty times the original value along the other direction. At the new equilibrium state, as shown in Fig.

6.10, the cell transforms into an “elongated” shape along that direction while the cell center keeps the granular shape, resembling the non-traditional “elongated” cell observed in Ref. [87]. We note that the high growth rate value along the specific direction is chosen arbitrarily in this simulation, representing the prolonged incubation of deoxygenation condition. A complete understanding of the above process requires further investigation. Second, the intracellular post-homogeneous nucleus is assumed to be near the center of the cell. Although this assumption is similar to the experimental observation in Ref. [24, 112] for the “central constriction” cells, the basis of the assumption needs further validation. As a sensitivity study, we have also considered one case for the “holly leaf” cell where the post-homogeneous nucleus is off the cell center, which results in further asymmetry and irregularity on the final cell morphology, as shown in Fig. 6.6. To the best of our knowledge, there are no experimental results reported on the spatial distribution of the intracellular post-homogeneous nucleus inside a sickle red blood cell. Therefore, it would be interesting to explore if there exist specific spatial preferences/distributions of the intracellular post-homogeneous nucleus by experimental measurements. This information would be important for further systematic exploration of the morphologic transition procedure discussed in the current work. Also, we have assumed that there is only one single post-homogeneous nucleation and polymer domain inside each cell in the present work. In reality, multiple sickle hemoglobin polymer domains can be formed in a single SS-RBC with high mean corpuscular hemoglobin concentration values [24, 23], resulting in multiple irregular spicules on the “granular” cell membrane. Moreover, we note that the intracellular CG polymer model in the present study represents bundles of aligned sickle hemoglobin polymers on length scale of  $O(1) \mu m$  whereas the detailed configuration of single sickle hemoglobin polymers, which may affect the local cell membrane distortion, is omitted. Finally, we note that the cell morphology transition is a complex procedure where many different physiological factors play important roles, resulting in the well-known “heterogeneous” properties

of the sickle cell morphology. While the cell deformability, intracellular polymer configuration and growth rate depend on the intracellular mean corpuscular hemoglobin concentration values, the cell preparation process such as deoxygenation rate can also affect the intracellular polymer configuration and therefore affect the cell morphologies. For the experimental data set used for comparison in the current work, the sickle cells are collected from blood suspension and classified by the different morphologic characteristics while the mean corpuscular hemoglobin concentration and deoxygenation rate for each cell type are not specified. In the present work, we studied sickle cells with different mean corpuscular hemoglobin concentration values and chose the polymer configuration according to experimental observation [24] that cells with low mean corpuscular hemoglobin concentration favor elongated type of polymer and low membrane rigidity while cells with high mean corpuscular hemoglobin concentration favor spherulite type of polymer and high membrane rigidity. There is no direct mapping between experimental data set and the simulation of the present work on the specific physiological conditions. This is a limitation of the present work. Systematic investigation with these effects incorporated would further help to elucidate the cell morphologic transition process.

The typical time scale of the aligned hemoglobin polymer domain formation in the present work is of the order  $O(1)s$ , consistent with the prediction in Ref. [8]. This process is relatively short as compared to the total time of the “sickling” procedure ( $O(10)$  to  $O(100)$  s). In microcirculation, we note that the typical time for cell transition in capillaries is around 1 – 2s [134]. The widespread blood vaso-occlusion originated from the distorted cell membrane is avoided in typical *in vivo* environments. This is mainly because the homogeneous nucleus formation is omitted in the current work. This procedure is well characterized by a “delay time” before which no sickle hemoglobin polymer can be detected [145]. On the other hand, deoxygenated SS-RBCs can get trapped in the post-capillaries due to adhesive interaction with the vessel endothelium [82]. This procedure may seriously increase the transit time for

a SS-RBC to get re-oxygenated, and result in the vaso-occlusion crisis. We discuss this process in Chap. 7.

# Chapter 7

## Effects of Adhesion

In the simplified example of Chap. 5 (see Sec. 5.3.4), we demonstrate that the vaso-occlusion crisis is initialized by the abnormal cell adhesion to the vessel wall. However, the heterogeneous cell morphologies and adhesive capabilities are not incorporated in that example. In this chapter, we conduct a systematic investigation on the vaso-occlusion crisis induced by the sickle red blood cells. The adhesive dynamics of different sickle cell groups are studied in a shear flow and their specific contribution to the vaso-occlusion crisis is identified.

### 7.1 Introduction

Sickle cell anemia is a genetic disease originating from the abnormal sickle hemoglobin molecules (HbS). In hypoxia conditions, the intracellular HbS solution transit into a polymerized state and results in a series of alterations in the cell membrane functions. Consequently, sickle cell exhibits heterogeneous properties on both cell morphology and membrane rigidity under different physiological conditions. According to the seminal study by Kaul [84], sickle blood suspensions contain heterogeneous cell density classes, which can be roughly divided into four groups by the intracellular mean corpuscular hemoglobin concentration (MCHC) values. Fraction I (SS1) and

II (SS2) are mainly composed of reticulocyte and discocytes with MCHC similar to the healthy cells (30 g/dL). On the other hand, the fraction IV (SS4) group is mainly composed of the irreversible sickle cells (ISC) with high MCHC ( $> 45$  g/dL). Micropipette experiments show that the cell rigidity of this fraction is six to ten times larger than the healthy cells in oxygenated conditions. Associated with the heterogeneous cell morphology is the abnormal rheology and hemodynamics of the sickle blood suspensions. Compared with the healthy blood, the sickle blood suspensions exhibit a general elevation in the flow resistance in shear flow [87, 86], micro-fluidic channel [69] and isolated vascular systems [83], where the hemodynamic properties further depend on the cell morphology, MCHC values, oxygen tension, *etc.*

Among the multiple hematologic disorders associated with this disease, one of the most important clinical features is the painful vaso-occlusive crisis, as this is the major cause of the morbidity in patients with sickle cell anemia. The mechanism of the vaso-occlusion crisis has been studied extensively for more than 30 years. Since this disease was first described and characterized by the “elongated sickle shape of cells” [67], early studies suspected that the major cause of the vaso-occlusive is the sickling process of the dense SS4 cells during their circulation in capillaries. However, subsequent studies show that vaso-occlusion mainly occurs in post-capillaries rather than in capillaries. Moreover, clinical investigations indicate that there is no direct correlation between the percentage of the dense SS-RBC with the disease severity [11]. An alternative pathology was proposed by Hebbel *etc.* [65] and Hoover *etc.* [72] in 1980’s. They revealed that there exist abnormal adhesive interactions between the sickle cells and cultivated endothelium cells and suspected that this abnormal interaction can potentially contribute to this crisis. This postulation was further investigated by Kaul [84] in the *ex vivo* microvasculatures. It is found that vaso-occlusion is a complex process triggered by multiple cell interactions in multiple steps [21]. While single SS4 cells do occasionally get stuck in the capillaries, most of the vaso-occlusion events are initialized by cell adhesion to the endothelium cells in

post-capillaries, and those adherent cells can further trap the other cells, resulting in transient or permanent vaso-occlusions. Moreover, further studies indicate that the heterogeneous cell groups contribute differently to the occlusion crisis. While the deformable SS2 cell group showed preferential adherence to the vascular wall, a large number of rigid and elongated ISCs accumulated at the occlusion sites, indicating a preferred pattern of SS-RBC suspension mixture for blood occlusion. In addition, it is found that the occlusion events exhibit a preferred distribution in post-capillaries with diameter between 7 and 10  $\mu\text{m}$ , where maximum adherent cells are found [83].

Currently hydroxyurea (HU) is the only FDA-approved drug used for patients with sickle cell anemia. The major mechanism of this drug is that it can induce the production of the fetal hemoglobin (HbF), which can effectively decrease the polymerization rate of HbS molecules and increase the delay time required for cell sickling under hypoxia conditions. However, the clinical observations discussed above indicate that the predominant stimuli for this type of disease in *in vivo* conditions is the vaso-occlusion crisis, which is a complex multi-step process involving multiple cell interactions. Therefore, quantitative investigation of this process may facilitate our understanding of this crisis and potentially provide new paradigm for the therapeutic treatments on this disease by targeting the individual physiological conditions that trigger the vaso-occlusion crisis.

To investigate the abnormal hemodynamic characteristics of the vaso-occlusion process under different physiological conditions, we employed a previously developed multi-scale model of sickle red blood cells [98] (see Chap. 5). That is based on a coarse-grained particle method [71, 40]. This model successfully captures the heterogeneous cell morphological and rheological properties. Using this model, adhesive dynamics of single sickle red blood cell was investigated in simple shear flow conditions. Our simulation results indicate that heterogeneous adhesive behaviors among the different cell groups are mainly due to the different cell morphologies and membrane properties. To further identify the specific contributions of the individ-

ual cell groups to the vaso-occlusion process, we investigate the hemodynamics of sickle blood suspensions mixed with different cell fractions. Our simulation results indicate that both SS2 and SS4 cell groups are the participants rather than the sole “causative” of the occlusive crisis. The interplay of the two cell groups results in the final occlusion events in a tube flow with diameter and shear rate similar to the blood flow in post-capillaries under physiological conditions.

This chapter is organized as follow. In the next section, the adhesive dynamics of single sickle red blood cell with different cell morphologies and membrane rigidities is investigated under shear flow condition. The effects of the cell morphology and membrane rigidity on shear flow responses are discussed. In section 7.3, the hemodynamics of the sickle blood flow is investigated in tube flow systems coated with adhesive ligand particles. Sickle cell mixtures with different cell groups are perfused into the tube and their contribution to the vaso-occlusion are identified. We conclude in section 7.4 with a brief discussion.

## **7.2 Adhesive dynamics of single sickle red blood cell**

### **7.2.1 Shear flow system**

Different from the healthy red blood cell, the sickle red blood cell membrane expresses multiple types of abnormal protein epitopes due to the membrane injury by the intracellular HbS polymerization. Moreover, the sickle red blood cell may damage the endothelium cells, resulting in the activation and up-regulation of the adhesive molecules expressed on the endothelium cells. As a result, the sickle red blood cells exhibit adhesive interaction with endothelium cells through multiple pathways. For example, the adhesive receptor VLA-4 expressed on the cell membrane can directly interact with the ligand VCAM-1 expressed on the endothelium. And

their interaction can be further elevated by cytokines in blood plasma such as tumor necrosis factor (TNF- $\alpha$ ), platelet activating factor (PAF) and interleukin-1(IL-1). In addition, other adhesive receptors such as CD36 expressed on the cell membrane can interact with endothelium ligands such as  $\alpha_v\beta_3$  through the extracellular matrix proteins such as TSP. A thorough review of the adhesive interaction mediated by the multiple proteins expressed on the cell membrane and their responses on the different inflammation level are discussed in Ref. [64].

Due to the physiological complexity and multiple-function characteristics of the adhesive interaction between the sickle red blood cell and the endothelium cell, explicit modeling of the individual receptor/ligand interactions is out of the scope of the current work. Instead, the adhesive proteins are represented by the effective receptor particles expressed on the cell membrane and the effective ligand particles on the vascular wall, respectively. The adhesive interaction is modeled by the transient bond formation and dissociation between the receptor and ligand particles in a stochastic way. This model can be viewed by a coarse-grained version of the adhesive model for leukocyte dynamics developed by Hammer *et al.* [62], where the multiple adhesive proteins are coarse-grained and represented by single DPD particles. We refer to Sec. 5.2.3 and Ref. [47] for details of the model and algorithms.

Adhesive dynamics of the individual sickle red cells was investigated in *in vitro* shear flow system by Barabino *et al.* [12] using a parallel-plate flow chamber. It was found that the SS-RBCs with different cell density show different dynamic responses under similar shear flow conditions. The cell fractions with the least MCHC value (SS1, SS2) exhibit the largest adhesion while the densest irreversible sickle cell (ISC) exhibits the least adhesion. Basing on this experimental observation, one question arises naturally: *is the different adhesive responses originated from the different adhesive proteins expressed on the cell membrane, or the different behavior is mainly due to the heterogeneous bio-mechanical properties among the cell subpopulations.* Numerical modeling and simulation provide a convenient tool to elucidate

this problem, as the different cell rigidity and morphologies can be easily imposed on individual cells.

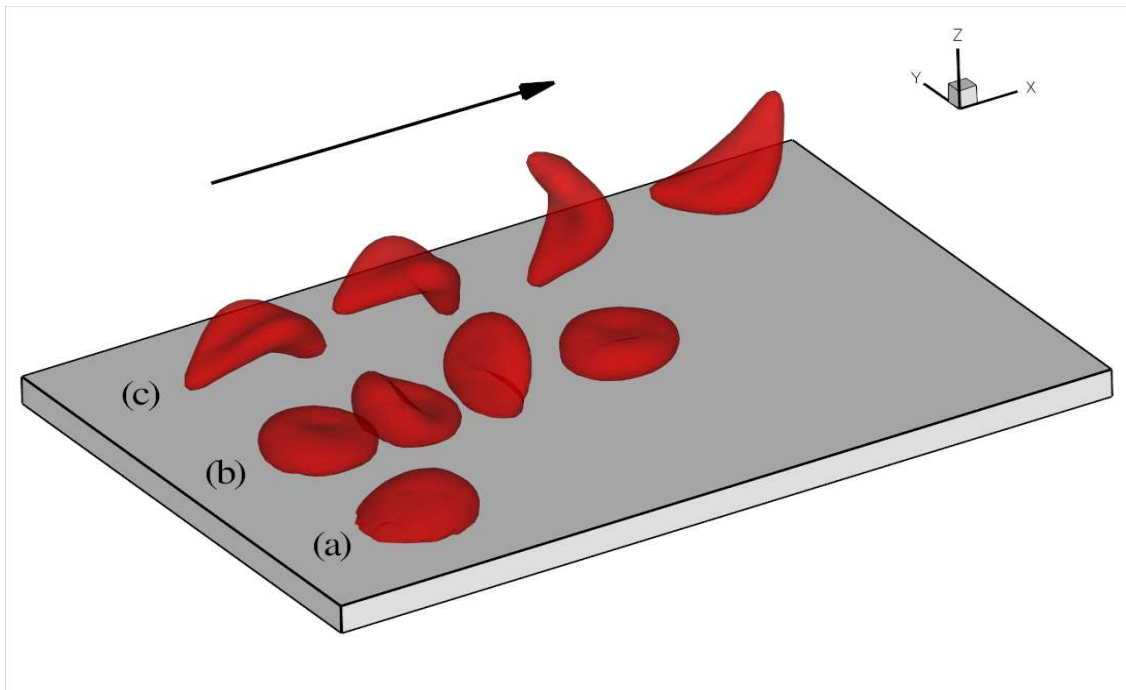


Figure 7.1: Successive snapshots of sickle red blood cells in shear flow. Labels (a), (b) and (c) represent a deformable SS2 cell, rigid SS3 cell and ISC, respectively. The arrow represents the flow direction.

As shown in Fig. 7.1, we consider three different types of the sickle red blood cells under shear flow conditions. The cell (a) represents a deformable discocyte cell from the SS2 subpopulation. The shear modulus  $\mu$  and bending rigidity  $k_c$  are similar to the value of healthy RBC. In the present work, we set the value  $\mu = \mu_0 = 6.8\mu N/m$  and  $k_c = k_{c0} = 3.7 \times 10^{-19} J$ , where  $\mu_0$  and  $k_{c0}$  represent the shear modulus and bending rigidity of the healthy red blood cell according to the experimental measurements [42, 74, 113]. The cell (c) represents a ISC from the densest SS4 cell group. (The “sickled” shape of cell is constructed by applying local stress - annealing process on the cell membrane. For details of the construction process, see Chap. 5 and Ref. [98].) Experimental measurements show scattered results on the cell rigidity of this cell type. Evans *et al.* reported that the ratio of the

cell rigidity between the densest sickle cell and healthy RBC varies from 4 to 11.5. Itoh *et al.* reported that this ratio is round 2.0 before the deoxygenation. However, the value increases up to 20 after one deoxygenation-reoxygenation cycle. These results indicate that the cell rigidity further depends on the cell sickling process since the cell membrane function can be altered during this procedure. To this end, we set the shear modulus  $\mu = 10\mu_0$  and  $k_c = 10k_{c0}$ . Finally, the cell (b) represent a rigid discocyte cell with medium MCHC value (SS3), the cell rigidity is between the SS2 and SS4 cell group. We set  $\mu = 3\mu_0$  and  $k_c = 3k_{c0}$  for the comparative study.

According to the experimental set up in Ref. [12], the three cells are placed between two parallel plates as show in Fig. 7.1. The simulation domain is  $60 \times 30 \times 15$  in DPD unit, and periodic boundary condition is imposed along the x and y direction. The lower plate is coated with effective ligand particles with density  $4\mu m^{-2}$ . *Same* adhesive interaction is applied between the ligand particles and the three types of sickle red blood cells. Detail simulation parameters are shown in Tab. 7.1.

Parameters	Simulations	Physical
spring constant ( $k_s$ )	50	$2.41 \times 10^{-5} N/m$
equilibrium spring length ( $l_0$ )	0.0	0.0 m
reactive distance ( $d_{on}$ )	0.15	$1.44 \times 10^{-7} m$
rupture distance ( $d_{off}$ )	0.15	$1.44 \times 10^{-7} m$
on strength ( $\sigma_{on}$ )	0.1	$4.83 \times 10^{-8} N/m$
off strength ( $\sigma_{off}$ )	0.033	$1.59 \times 10^{-8} N/m$
unstressed on rate ( $k_{on}^0$ )	100.0	$3.49 \times 10^5 s^{-1}$
unstressed off rate ( $k_{off}^0$ )	0.1	$349 s^{-1}$
shear rate ( $\dot{\gamma}$ )	0.067	$231 s^{-1}$

Table 7.1: Simulation (in DPD units) and physical (in SI units) parameters for blood flow with adhesive interaction with coated ligand particles.

Three cells are initially placed at a distance of  $0.12\mu m$  from the lower plate. Shear flow is generated by imposing constant moving velocity on the upper plate while the lower plate is kept stationary. Detail simulation parameters among the external solvent ( $S_o$ ), cell vertices ( $V$ ), cytosol ( $S_i$ ) and wall particles( $W$ ) is shown in Tab. 7.2.

Interaction	a	$\gamma$	$r_c$	$k$
$S_o - S_o, S_o - W$	2.5	30	1.0	0.25
$S_i - S_i$	2.0	30	1.2	0.25
$S_o - V, W - V$	0.5	10	1.0	0.25
$S_i - V$	0.5	25	1.0	0.25
$V - V$	20	30	0.5	0.25

Table 7.2: DPD simulation parameters for the adhesive dynamics of single sickle red blood cells.

Fig. 7.1 shows successive snapshots for each of the three sickle red blood cells along the flow direction. Starting from the similar initial conditions, the three cells exhibit different adhesive dynamics. The deformable discocyte cell (*a*) moves toward the lower plate due to the bond formation with the ligand particles and shows firm adhesion to lower plate thereafter. Similarly, the rigid discocyte cell (*b*) show transient adhesion to the lower plate initially. However, the cell shows periodic flip movement along the flow direction thereafter, indicating that the adhesive interaction is weaker than the case of cell (*a*), and the cell can overcome the adhesive constraint with certain probability. This result is similar to the adhesive behavior of another type of disease red blood cell named as malaria-infected RBC [47, 7], where the cell membrane is about 3 to 9 times more rigid than the healthy RBC depending on the parasite development stage. Different from cell (*a*) and (*b*), cell (*c*) does not show apparent firm/transient adhesion to the plate. Following the start of the shear flow, the cell shows direct attachment from the lower plate due to the hydrodynamic force and moves freely thereafter, indicating the least adhesive interaction between the cell and the plate.

To further quantify this heterogeneous adhesive behavior, we measure the instantaneous velocity and the contact area for the three different cells. The instantaneous velocity  $v_c^i$  is define by

$$v_c^i = (x^{i+1} - x^{i-1})/2\delta t, \quad (7.1)$$

where  $x^{i+1}$  and  $x^{i-1}$  represent the position of the cell center of mass at snapshot

$i + 1$  and  $i - 1$ .  $\delta t$  is the time interval between the two successive snapshots. The instantaneous contact area is evaluated as

$$a_c^i = \frac{A_0}{N_v} \sum_{j=1}^{N_v} A_j^i, \quad (7.2)$$

where  $N_v$  is the total number of the cell vertices.  $A_0$  is the total area of the cell.  $A_j^i$  is defined by

$$A_j^i = \begin{cases} 1, & \text{if } z_j^i < d_{on} \\ 0, & \text{if } z_j^i \geq d_{on}, \end{cases} \quad (7.3)$$

where  $z_j^i$  is the instantaneous position of cell vertex  $j$  on  $z$  direction at snapshot  $i$ ,  $d_{on}$  is the reactive distance defined in Tab. 7.1.

Fig. 7.2 shows the instantaneous cell velocity and the contact area for the three cells as a function of time. The subplot Fig. 7.2(a) corresponds to the simulation results of cell  $a$ . The initial peak value of the cell velocity is mainly due to the limited bond formation during the starting stage. At the later stage, more adhesive bonds are formed between the cell vertices and the ligand particles, the cell velocity decreases and fluctuates around zero, where the negative velocity values are mainly due to the thermal fluctuation. Accordingly, the contact area increases from zero to  $48\mu m^2$  at the later stage. Fig. 7.2(b) shows the simulation results for cell  $b$ . The occasional flip movement is characterized by the peak values of the instantaneous cell velocity at 0.38, 0.64, 1.12 s. Accordingly, the contact area shows minimum value at those times. The average velocity during the simulation period is  $46\mu m/s$ , which falls within the velocity region of the adherent SS-RBCs in Ref. [12]. Fig. 7.2(c) shows the simulation results for the ISC. In the initial stage, the small cell velocity and the peak value of the cell contact area represent the adhesive interaction during which the ISC undergoes one half cycle of flip movement on the plate. After that, the cell shows full detachment from the plate indicating that the adhesive constraint is not sufficient to counter the hydrodynamic force on the cell. The cell

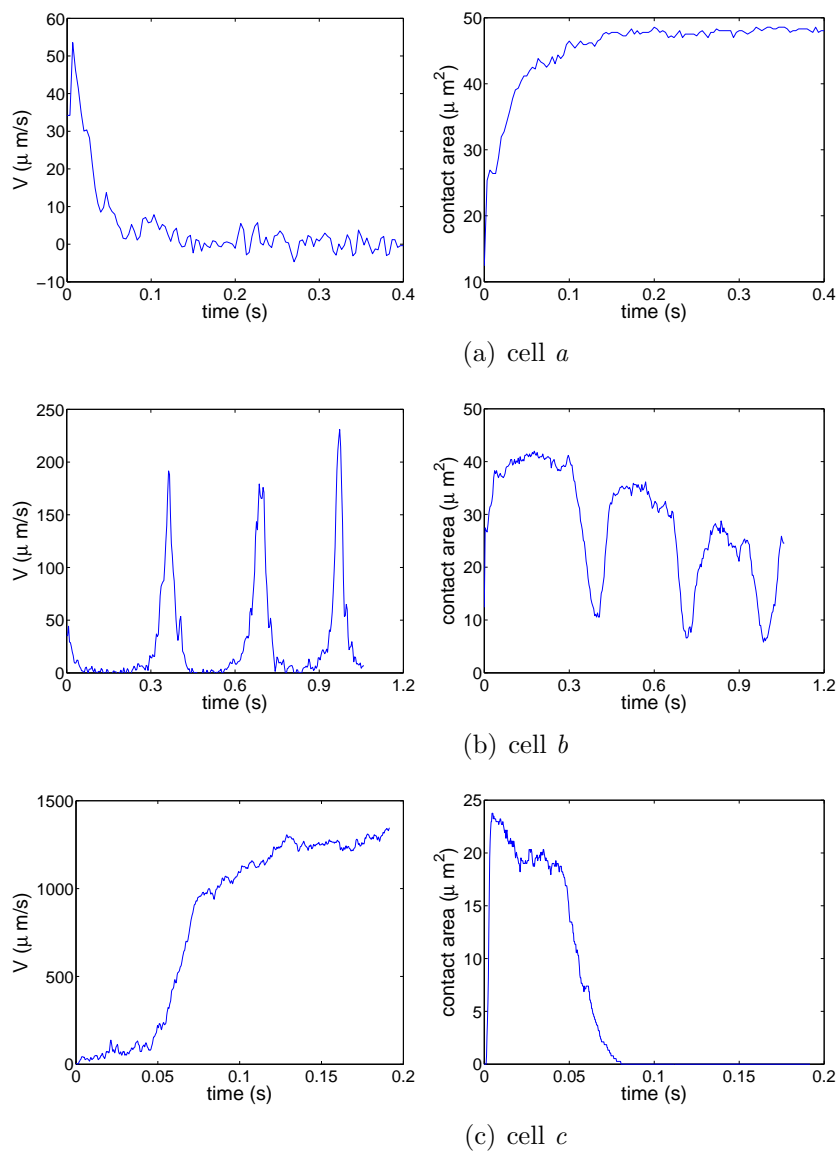


Figure 7.2: Instantaneous velocity (left) and contact area (right) for the sickle cells in shear flow conditions. Labels (a), (b) and (c) represent the simulation results of deformable discocyte, rigid discocyte and ISC cell, respectively.

moves freely thereafter with velocity on the order of  $O(10^3)\mu m/s$  and no adhesive bond is established during the later stage.

Besides the *in vitro* experiment by Barabino *et al.*, we note that the current simulation results are also consistent with several other experimental observations [141, 80]. In Ref. [141], the adhesive dynamics of a neutrophil and a rigid bead coated with same ligands are investigated under the similar shear flow conditions. It was reported that the neutrophil exhibits different shear responses from the rigid bead due to the cell deformation under shear flow condition. Similar experimental work is also conducted by Kaul *et al.* on the effect of dehydration/rehydration processes on the adhesive properties among the different cell populations [80]. Using the Nystatin-sucrose method, the cell rigidity and the MCHC value of the individual cells can be elevated/decreased through the dehydration/rehydration process. It was reported that the deformable discocyte group (SS2), after the dehydration procedure, results in larger flow resistance and less adherent sites, while those cell can completely recover the cell adhesive properties after the rehydration treatment. Similarly, the rehydration treatment on the densest cell group (SS4) can significantly improve the cell deformability, resulting in enhanced cell adhesion and elevated number of adherent SS4 cells in post-capillaries.

These experimental results indicate that the deformable SS2 cell group and the rigid SS4 cell group share similar adhesive attribute; the different adhesive dynamics exhibited in shear flow conditions is mainly due to the different cell rigidity. This result is also consistent with present work. Since the same adhesive parameters are adopted for the different cells, our simulation results suggest that the different mechanical properties of the individual cell groups impose a profound influence on adhesive properties. Moreover, in Ref. [80], it is reported that the different cell types among the rehydrated SS4 cell population also exhibit heterogeneous cell adhesion. Although the ISCs outnumber the rigid discocytes by 2 to 1 in the SS4 cell suspension, 80% of the adherent SS4 cells are the discocytes. This result indicates that the cell

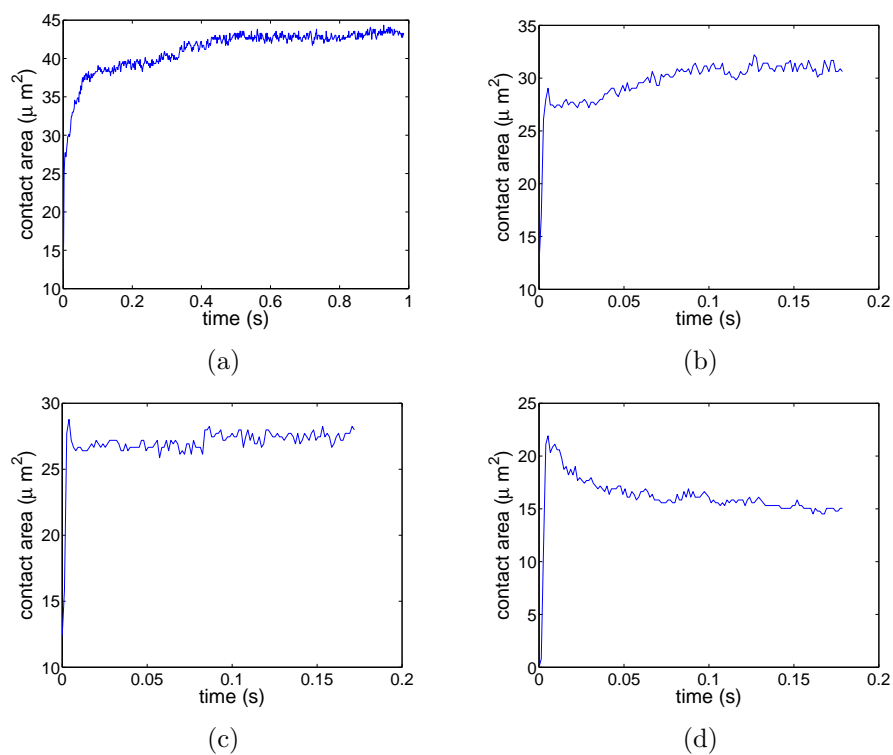


Figure 7.3: Instantaneous contact area between the sickle cell and the plate coated with adhesive ligands. Labels (a), (b) and (c) represent the simulation results of discocyte with shear modulus  $\mu_0$ ,  $4.0\mu_0$  and  $10.0\mu_0$ , respectively. Label (d) represents the case of ISC with shear modulus of  $10.0\mu_0$ .

morphological characteristics may also contribute to the cell adhesive properties, and it was proposed that the peculiar cell morphology of ISC may further prevent the effective adhesive interaction and bond formation with endothelium cells. To investigate this postulation, we simulate the adhesive incubation process of sickle cells in a static condition.

### 7.2.2 Static incubation

Similar to the shear flow system, four different sickle cells are initially placed at a distance of  $0.12\mu m$  from a plate coated with ligand particles. The same adhesive parameters are adopted, as given in Tab. 7.1. The instantaneous contact area is computed for each cell until a steady state is achieved, as shown in Fig. 7.3. The subplot Fig. 7.3(a), Fig. 7.3(b) and Fig. 7.3(c) represent the incubation process of the discocytes with shear modulus  $\mu_0$ ,  $4\mu_0$  and  $10\mu_0$ , respectively. Fig. 7.3(d) represents the result of a ISC with shear modulus  $\mu = 10\mu_0$ . Three major points emerge from the simulation results.

First, we note that the contact area measured after the static incubation exhibits an inverse relationship with the cell rigidity. While the contact area for all of the cells increases sharply to  $25\mu m^2$  within the initial stage, the contact area between the deformable SS2 and the plate shows a further increase and reaches  $43\mu m^2$  at the final stage. In contrast, the contact area between the SS4 cell and the plate does not show further changes and keeps the value of  $26.5\mu m^2$  at the final stage. This inverse relationship is consistent with the different cell adhesive dynamics in shear flow system, and it can be understood by a qualitative analysis of the change of free energy during the incubation process. If we define the cell and the ligand particles as a single system, the change of total free energy  $\Delta E$  during the process can be written as

$$\Delta E = \Delta E_{deform} - \Delta E_{adhesion}, \quad (7.4)$$

where  $\Delta E_{deform}$  represents the increase of the cell free energy due to the deviation of cell shape from the equilibrium state during the incubation process.  $\Delta E_{adhesion}$  represents the absolute value of the energy decrease due to the adhesive bond formation between the cell membrane and the ligand particles. The final state is determined by the counter-balance between the two free energy terms. A deformable SS2 cell is prone to form larger contact area than the rigid cell can be understood as follows. For a SS2 cell with smaller cell rigidity, the energy barrier induced by the cell deformation is relatively small, and the decrease of free energy induced by the adhesive interaction plays a dominant role. After the initial incubation stage, the adhesive interaction forces the cell membrane to further deform and extend on the plate, resulting in the further increase of the contact area. In contrast, the rigid SS4 cell exhibits a “solid” like properties with a larger energy barrier for cell deformation. The adhesive interaction between the cell and plate is more like the attraction between two solid objects (two magnets, as a example of the extreme case), where the cell deformation plays a less important role. After the initial incubation stage, the adhesive interaction driven by the bond formation can not overcome the free energy increase induced by the cell deformation. Therefore, further increase of the contact area is avoided.

Second, for the deformable SS2 cell, we note that the equilibrium contact area obtained from the static incubation is smaller than the contact area obtained from the shear flow conditions. In contrast, the time required for static incubation to reach the equilibrium state is longer than the value of the shear flow condition. These discrepancies are mainly due to the further cell deformation under the shear flow condition, e.g., part of the deformation free energy  $\Delta E_{deform}$  discussed above is balanced by the hydrodynamic force exerted on the cell membrane under shear flow condition. The extended cell membrane facilitates the bond formation with the ligand particles and results in larger contact area. This result also provides a reasonable explanation for the experimental observations that the cell adhesion of

the deformable SS2 cell is more pronounced under flow conditions [12, 114].

Third, compared with the dense discocyte, the ISC shows smaller contact area with the plate although similar cell rigidities are applied on the two cells. This result validates that the cell morphology may also influence the cell adhesive properties. Compared with the biconcave shape, the peculiar elongated and curved characteristics of the ISC can further prevent the membrane receptors from interacting with the ligand particles, resulting in the different adhesive behavior among the SS4 cell groups, as reported in Ref. [80].

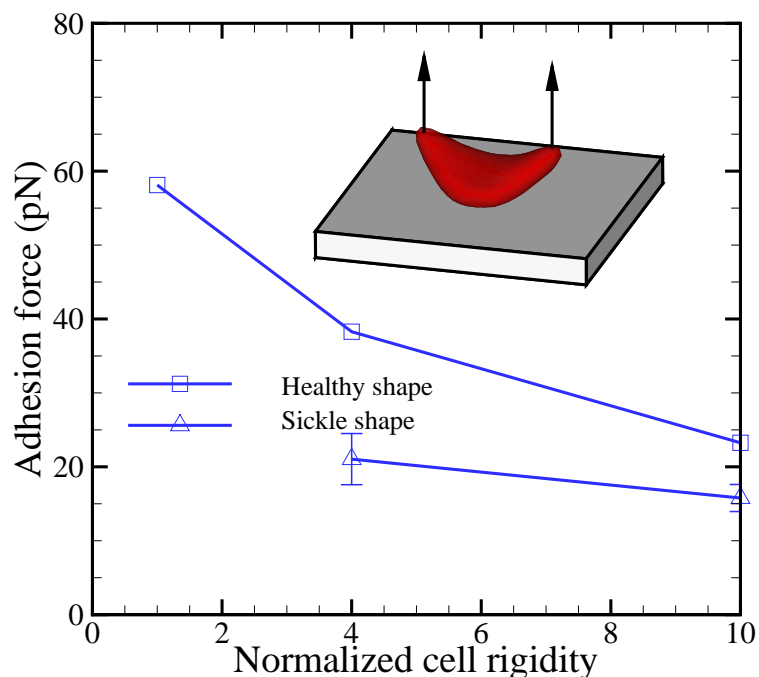


Figure 7.4: Adhesive force between a sickle cells and the wall as a function of the membrane rigidity for two cell morphologies. The subplot shows a sketch of the simulation set up, where a uniform lift force is applied on the upper part of an ISC.

To quantify the effect of the cell rigidity and morphology discussed above, we measure the adhesive force between the cell and the plate. Starting from the steady state obtained from the static incubation, lift force along the  $z$  direction is uniformly

applied to the upper part of cell membrane (40%, 200 vertices in total). A sketch of the simulation set up is shown in the inset plot of Fig. 7.4. The adhesive force is determined as the lift force that drives the cell detaching from the plate in the *quasi-static* state, as shown in Fig. 7.4. Similar to the contact area, the adhesive force also exhibits an inverse relationship with the cell rigidity. The adhesive force between the deformable SS2 cell and the plate is  $58.6pN$ . In contrast, the value decreases to  $23.0pN$  for the rigid SS4 cell. Moreover, the ISC exhibits smaller adhesive force than the discocyte within a wide range of cell rigidity, indicating a less adhesive property induced by the peculiar cell morphology.

The above result, combined with the heterogeneous cell adhesive dynamics under shear flow conditions, suggest that the deformable discocytes are the most adhesive cell group among the different sickle cell classes. The ISC group, on the contrary, is the least adhesive cell group. In microcirculation, the multiple cell groups play different role in the hematological disorders such as vaso-occlusion. We discuss this in the next section.

### 7.3 Sickle blood in tube flow

Sickle blood suspension is characterized by elevated flow resistance in microcirculation, which can lead to vaso-occlusion in *in vivo* venule [81], *ex vivo* micro-vasculatures [83] and micro-channels [69]. In a simplified example presented in Sec. 5.3.4, we showed that for sickle cell suspension in a tube flow with diameter  $9\mu m$ , vaso-occlusion is avoided unless certain adhesive interaction between the sickle cell and the tube wall is introduced. While this simplified example revealed the predominant role of cell adhesion to initialize the occlusion events, homogeneous cell morphology and membrane rigidity are adopted. The heterogeneous adhesive properties among the different cell classes were not incorporated in that simulation. In this section, we further investigate the abnormal hemodynamics of sickle blood sus-

pensions mixed with different cell density groups. Blood suspensions composed of different cell fractions are perfused into a tube system and the resultant hemodynamics is studied. Using this method, we want to identify the specific contributions of individual cell groups to the vaso-occlusion crisis.

This simulation work is motivated by the experimental study by Kaul *et al.* [83], who conducted a microcirculatory study in an isolated *ex vivo* mesoecum vasculature of rat. Following this experiment [83], we consider a sickle blood suspension of hematocrit  $H_t = 30\%$  in a tube with diameter of  $10\mu m$ , which is a typical value for post-capillaries. The set up of the system is shown in Fig. 7.5. The post-capillary is modeled by a cylinder tube with diameter of  $10\mu m$  and length  $40\mu m$ . Periodic boundary condition is applied along the flow direction. The cells are divided into two groups. The green particles represent the adhesive ligand particles coated on the tube wall within the region  $15\mu m < x < 25\mu m$ . The arrow represents the flow direction where a pressure gradient  $\Delta P/\Delta x = 8.7 \times 10^4$  Pa/m is applied. Blood suspension of different cell groups are perfused into the cylinder tube and the simulation results are discussed as below.

- *SS2 + ISC*

Five SS2 cells (labeled by blue color) and five ISCs (labeled by red color) are placed in the tube. Steady flow is achieved by turning off the adhesive interaction, as shown in Fig. 7.5 (a). The mean flow across the tube is about  $150\mu m/s$ . Starting from this state ( $t = 0$ ), the cell-ligand interaction is applied to both the SS2 cells and ISCs where adhesive parameters are similar to the cases of single cell (see Tab. 7.1). Fig. 7.6 shows the following instantaneous mean velocity across the tube. Steady flow is maintained until one of the SS2 cells get attached to the tube wall in the region coated with ligand particles, triggering a sharp decrease of the flow rate at ( $t = 0.3s$ ), as shown in Fig. 7.5 (b). As a positive feedback, the decreased blood flow rate induces more SS2 cells to adhere to the tube wall, leading to a further decrease of the flow rate at  $t = 0.4s$  and  $t = 0.53s$ . Moreover, these adherent cells decrease the effective

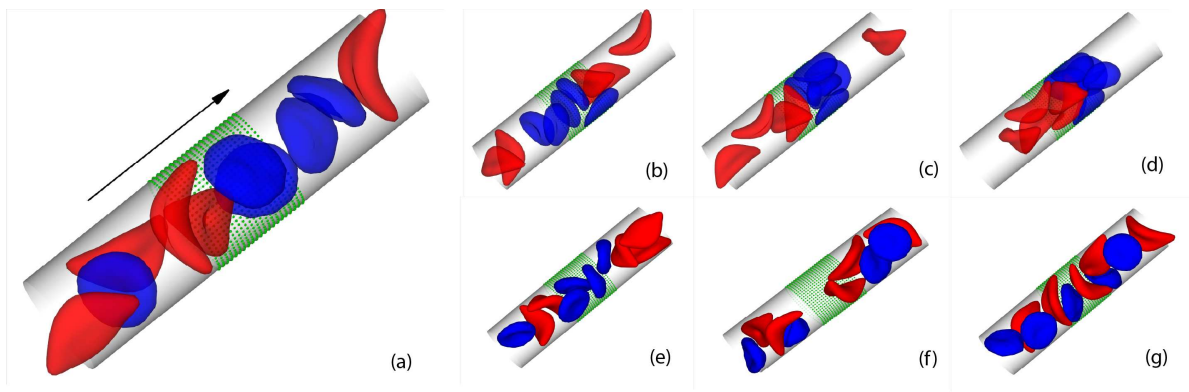


Figure 7.5: Snapshots of blood cells in a cylinder tube of  $D = 10\mu\text{m}$  with  $H_t = 30\%$ . The blue and red cells represent the SS2 cells and the ISCs, respectively. The subplot (a) represents the steady flow state free of adhesive interaction. Subplots (b-d) represent the snapshots of the blood flow where adhesive interaction is applied to both the SS2 cells and the ISCs. Specifically, (b) represents a snapshot where one SS2 cell adhere to the tube wall; (c) represents a snapshot where more cells adhere to the tube wall; (d) represents a snapshot of the blood occlusion state at the final stage of the simulation. The subplots (e-g) represent the snapshots of the blood flow where adhesive interaction is only applied to the ISCs. The subplot (f) shows a transient adhesion between ISC and the tube wall. Steady flow is recovered as the cell detaches from the tube wall, as shown in (g).

tube diameter near the adhesive sites, resulting in a secondary trapping of the other ISCs, as shown in Fig. 7.5(c). Full occlusion is achieved round  $t = 0.8s$ , as also shown in Fig. 7.5(d). The above simulation results show that, under physiological conditions similar to the blood flow in post-capillaries, the adhesive cell-endothelium interaction can potentially trigger the full blood occlusion state. Moreover, the final occlusion state exhibits a specific pattern similar to the experimental observations [83, 80]: the rigid, elongated ISCs trapped by the adherent SS2. To verify this unique phenomenon, three more identical independent simulations have been performed for this case. All of the final occlusion states exhibit this featured pattern. Although same adhesive parameters are applied to the two cell groups, no adherent ISC is observed in the present simulations.

- *Non-adhesive SS2 + ISC*

To explore if the above pattern is mainly due to the limited number of free ligands,

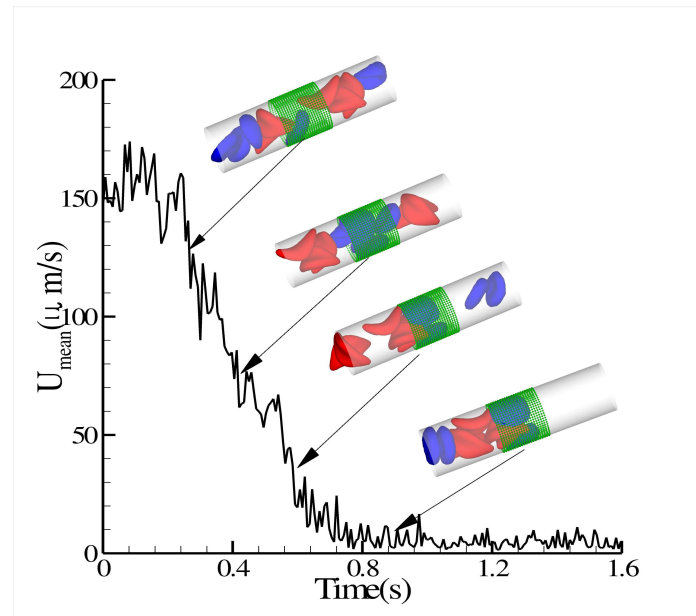


Figure 7.6: Instantaneous mean velocity of the blood flow in a cylinder tube of  $D = 10\mu\text{m}$  containing SS2 cells and ISCs. Adhesive interaction is applied to both cell groups. The inset plots show several snapshots of the blood flow in the simulation.

or the less adhesive feature of the ISCs, we've performed a similar simulation of the blood flow where the SS2-ligand interaction is turned off. Starting from the steady state shown in Fig. 7.5(a), the blood flow is simulated for 6s. The snapshots of the following states are shown in Fig. 7.5(e), Fig. 7.5(f) and Fig. 7.5(g). Due to the ISC-ligand interaction, occasional transient adhesion/contact can be formed between the ISC and the tube wall as shown in Fig. 7.5(f). The transient adhesion results in the decrease of the flow rate at  $t \approx 2\text{s}$  and  $t \approx 4\text{s}$ , as shown in Fig. 7.7. However, no firm adhesion has been observed; the blood flow can recover the initial flow rate when the adherent ISCs detach from the tube wall. Blood occlusion is avoided during the simulation. This result reveals the distinct role of the SS2 cell in vaso-occlusion: it is the major cell group that initializes the cell adhesion in post-capillaries. This is also consistent with the positive correlation between the red cell deformability index and the severity of the disease reported by clinical observation [11]. The ISC group, on the contrary, contribute differently to the occlusion process, as discussed in the

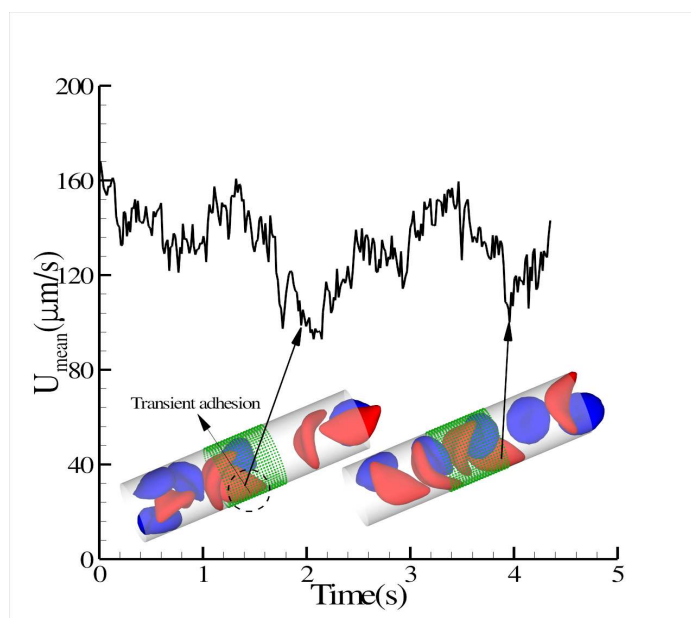


Figure 7.7: Instantaneous mean velocity of the blood flow in a cylinder tube of  $D = 10\mu m$  containing SS2 cells and ISCs. Adhesive interaction is only applied to the ISC group. The inset plots show two snapshots of the blood flow in the simulation.

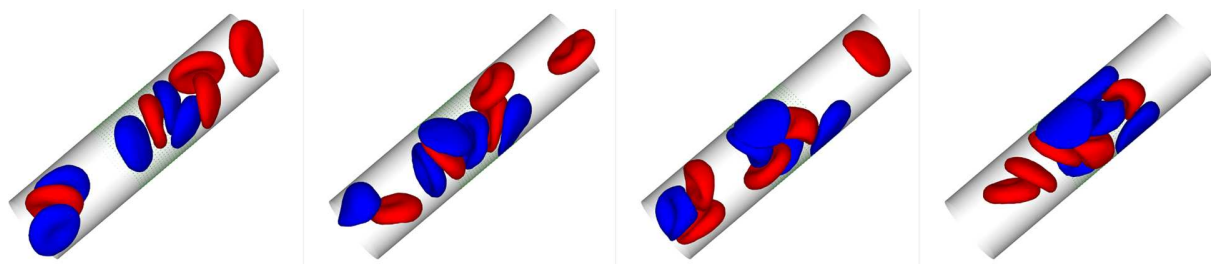


Figure 7.8: Snapshots of the red blood cells in a cylinder tube of  $D = 10\mu m$  with  $H_t = 30\%$ . The blue and red cells represent the SS2 cells and healthy cells, respectively. The subplot (a) represents the steady flow state free of adhesive interaction. The subplots (b-d) represent snapshots of the blood flow where adhesive interaction is applied to the SS2 cell group. The SS2 cells adhere to the tube wall, as shown in the (b) and (c). Healthy cells can squeeze through the adherent sites as shown in (d).

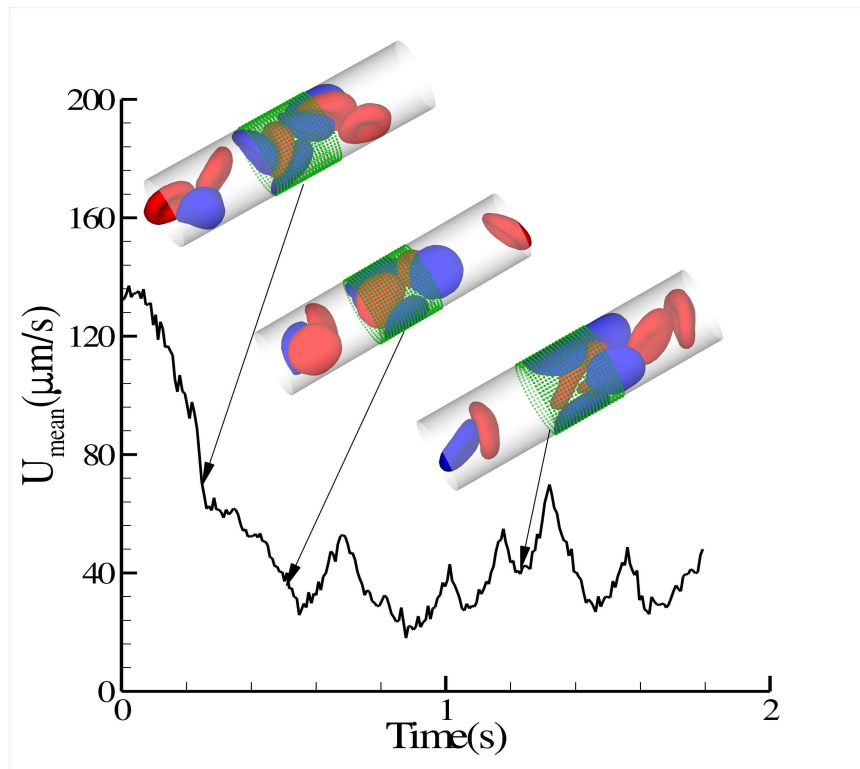


Figure 7.9: Instantaneous mean velocity of the blood flow in a cylinder tube of  $D = 10\mu\text{m}$  containing SS2 and healthy cells. Adhesive interaction is applied to the SS2 cell group. The inset plots show several snapshots of the blood flow in the simulation.

next simulation.

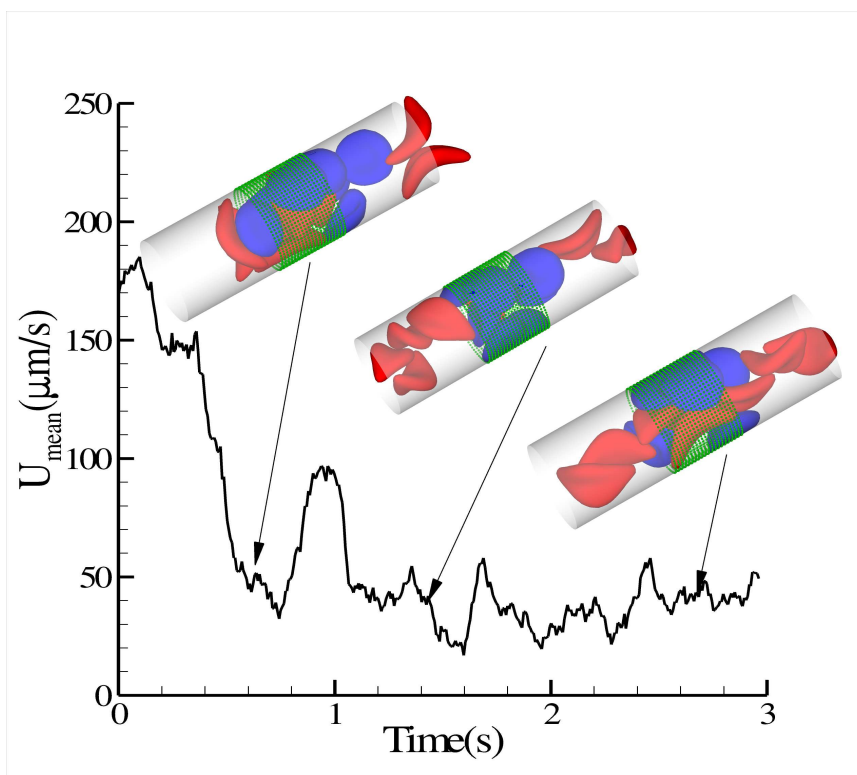


Figure 7.10: Instantaneous mean velocity of the blood flow in a cylinder tube of  $D = 12\mu\text{m}$ ,  $H_t = 30\%$ . Simulation parameters are similar to the case shown in Fig. 7.6.

- *SS2 + Healthy*

Equal amounts of healthy (labeled by red color) and SS2 (labeled by blue color) cells are mixed and perfused into the cylinder tube. The initial state (Fig. 7.8(a)) represents a steady flow free of adhesive interaction. Starting from this state, blood flow is simulated with adhesive interaction applied between the SS2 cells and the coated ligands. Fig. 7.8(b), Fig. 7.8(c) and Fig. 7.8(d) represent typical snapshots of the following flow states. Similar to the *SS2 + ISC* case, the SS2 cells show firm adhesion to the tube wall, resulting in the decrease of the flow rate at  $t = 0.25$  and  $t = 0.48$ . While blood flow exhibits sluggish characteristics, full occlusion is avoided as the adherent SS2 cells fails to trap the healthy cells, as shown in Fig. 7.8. This discrepancy is mainly due to the high deformability of the healthy red cells,

which enables the healthy cells to squeeze through the tube where large number of adherent SS2 cells accumulated. The result, in turn, reveals the distinct role of the ISC group in the vaso-occlusion process. Although the least adhesive, the ISC, due to this high membrane rigidity and elongated cell shape, serve as the particular cell group trapped by the adherent cells in the post-capillaries. This result explains the experimental observation that large number of dense cells accumulate in the occlusion region and disappear in the peripheral blood [83].

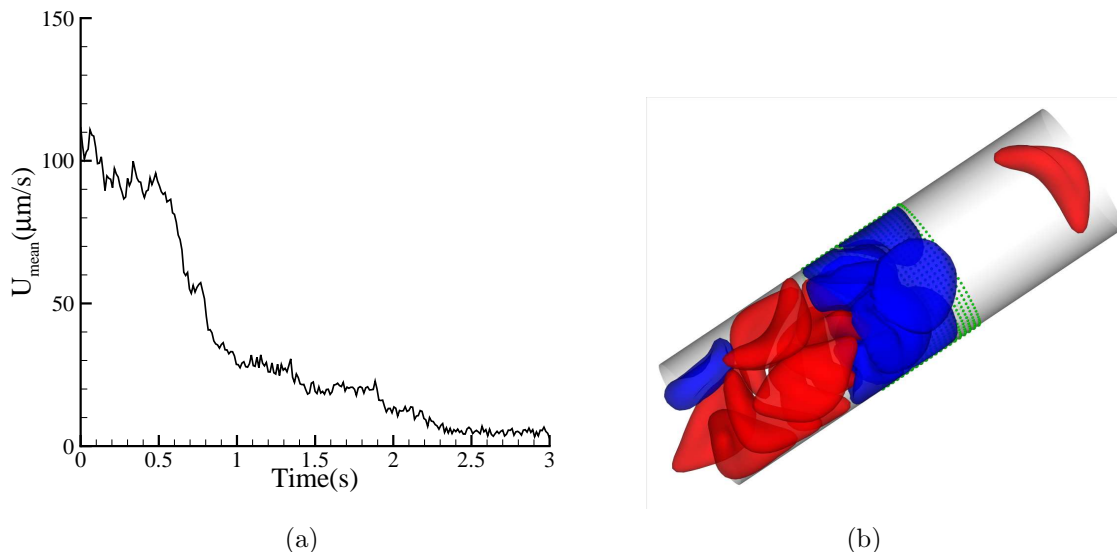


Figure 7.11: (a) Instantaneous mean velocity of the blood flow in a cylinder tube of  $D = 12\mu m$ ,  $H_t = 45\%$ . Simulation parameters are similar to the case shown in Fig. 7.10. (b) a snapshot of the blood occlusion at the final stage of the simulation.

- *Effect of the tube size*

Seven SS2 cells and seven ISCs are mixed and perfused into a cylinder tube with diameter of  $D = 12\mu m$ , where same pressure gradient and adhesive interaction are applied. Different from the case of  $D = 10\mu m$ , blood occlusion is avoided in the present simulation. The sieve-like pattern formed by the adherent SS2 cells do not fully trap the ISCs due to the larger spatial accommodation near the adhesion sites. The blood flow maintains a mean flow velocity round  $35\mu m/s$  at the final stage, as

show in Fig. 7.10.

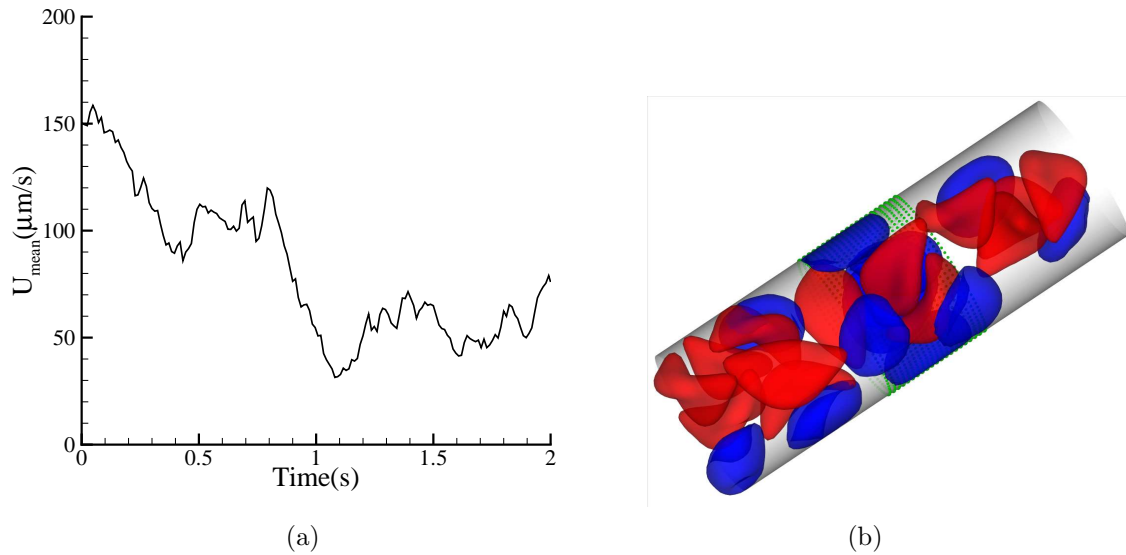


Figure 7.12: (a) Instantaneous mean velocity of the blood flow in a cylinder tube of  $D = 13.4\mu m$ ,  $H_t = 45\%$ . Simulation parameters are similar to the case shown in Fig. 7.10. (b) a snapshot of the blood flow at the final stage of the simulation.

- *Effect of the hematocrit*

Up to this point, the hematocrit of the blood flow is chosen as 30% according to the *ex vivo* experiments [83, 80]. As a sensitivity study, we have also conducted several simulations of blood flow with  $H_t = 45\%$ . Fig. 7.11 shows the instantaneous mean velocity of the blood flow in a tube of diameter of  $D = 12\mu m$ , where the pressure gradient and adhesive parameters are similar to the previous case. Different from the  $H_t = 30\%$  case, blood flow exhibits full occlusion state at the final stages. This is mainly due to the lower flow rate and smaller spatial accommodation at the adhesion sites, both induced by the high cell volume fraction in the tube system. However, as the tube diameter further increases, the blood flow systems exhibit similar trend to the cases of  $H_t = 30\%$ . As the tube diameter increases to  $D = 13.4\mu m$ , our simulation suggests that the full occlusion can be avoided, as shown in Fig. 7.12.

- *Effect of the inflammation stimulated leukocytes*

In the previous cases, we discuss the microcirculation of blood flow under normal physiological conditions. Simulation results indicate that the vaso-occlusion sites mainly distribute in blood vessels with diameter smaller than  $12\mu m$ . However, we note that in clinical, the vaso-occlusion crisis is not limited in post-capillaries. Recent studies [85] indicate that the sickle disease is often accompanied with an inflammatory endothelial phenotype, which results in elevated leukocyte recruitment. Further more, studies by Turhan *et al.* [147] in transgenic-knockout mice show that the inflammation stimulated (by cytokine  $TNF-\alpha$ ) adherent leukocytes interact with the sickle red blood cells, resulting in the vaso-occlusion crisis in blood vessels with larger diameter. Here, we briefly discuss this effect by imposing an *ad hoc* attractive interaction between the sickle cell and leukocyte.

Leukocyte recruitment on vascular endothelium is induced by the interaction of the adhesive molecules on Leukocytes such as L-selectin,  $\alpha M\beta 2$  integrin, *et al.* with endothelial adhesion molecules, including ICAM-1, VACAM-1, E-selectin and P-selectin. These adhesive interactions are further influenced by the inflammation stimuli such as IL-1,  $TNF-\alpha$ , CXCL8. Under similar physiological conditions, a leukocyte may exhibit various adhesive dynamics. For systematic investigation on the phase diagram of the adhesive dynamics, see Ref. [20]. In the present work, the leukocyte-endothelium adhesive interaction is modeled by the stochastic bond formation/dissociation between leukocyte cell vertices and the ligand particles, as defined by Eq. (5.7). Simulation parameters are similar to the ones for sickle cell-endothelium interaction presented Tab. 7.1 except for  $k_s$ , which is chosen between 100 and 3000 to represent the bond affinity under different inflammation stages.

Fig. 7.13 shows the instantaneous cell velocity of a single leukocytes in tube flow of diameter  $D = 13.4\mu m$  with pressure gradient  $\Delta P/\Delta x = 8.7 \times 10^4$  Pa/m. Fig. 7.13(a) corresponds to the free motion state, where the leukocyte detaches from the tube wall due to the low bond affinity ( $k_s = 100$ ). Fig. 7.13(b) represents the stable rolling on the tube wall with medium bond affinity ( $k_s = 300$ ). This is characterized

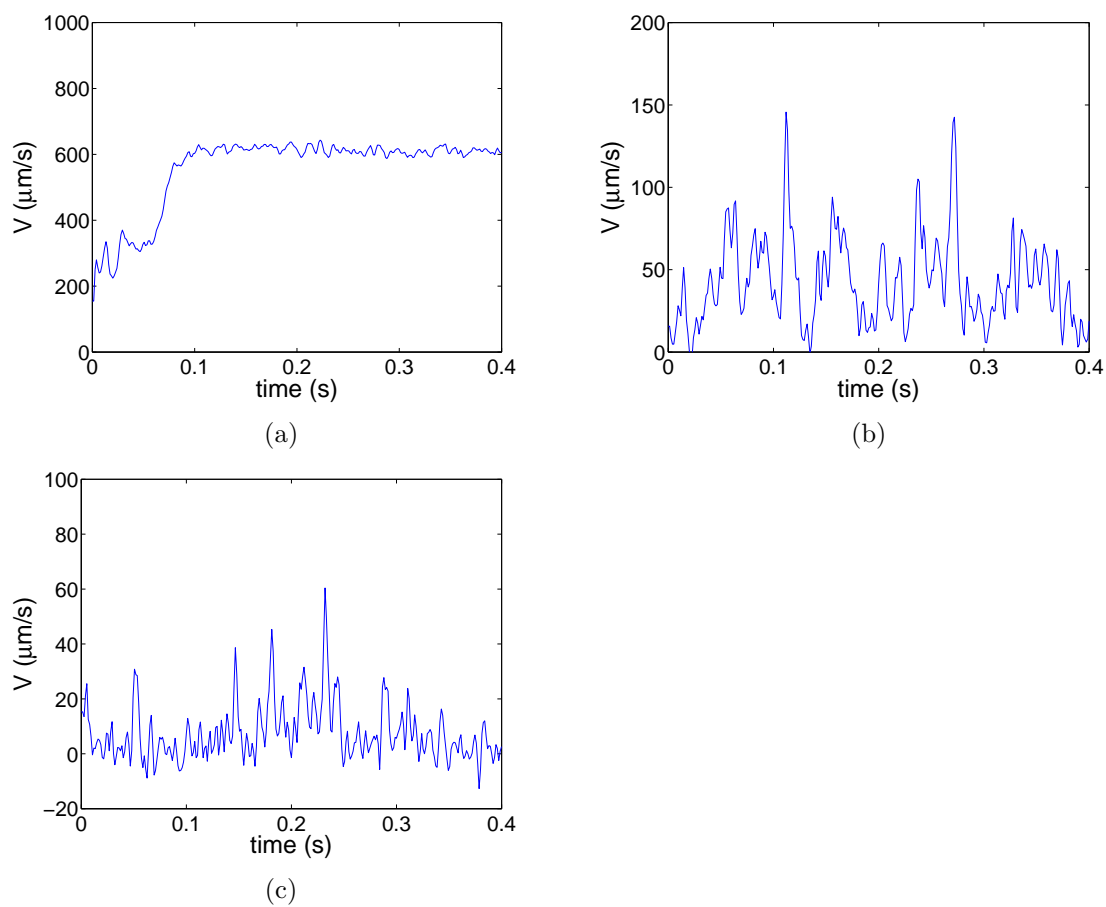


Figure 7.13: Instantaneous velocity of a single leukocyte with adhesive bond coefficient  $k_s = 100$ (a), 300(b), and 1000(c), respectively.

by the velocity oscillating between  $20\mu\text{m}/\text{s}$  and  $100\mu\text{m}/\text{s}$ . Fig. 7.13(c) represents the firm adhesion state with high bond affinity ( $k_s = 1000$ ). The cell velocity fluctuates around zero except few peaks representing the transient movement along the flow direction.

The adhesive interaction between the sickle red blood cells and the leukocytes are modeled by the Morse potential

$$U_M(r) = D_e[e^{2\beta(r_0-r)} - 2e^{\beta(r_0-r)}], \quad (7.5)$$

where  $r$  is the distance between cell-membrane vertices of adjacent cells,  $r_0$  and  $D_e$  are the zero force distance and well-depth of  $U_M(r)$ , respectively.  $\beta$  determines the range of interaction. In the present work, we choose  $r_0 = 0.3$ ,  $\beta = 1.5$ ,  $D_e = 80$  with cut-off distance  $r_M = 0.45$ . This yields adhesive forces between two cells in range  $55 - 63\text{pN}$ .

With the cell interaction defined above, we reconsider the blood flow circulation in larger tube flow. First, we consider blood flow in a tube with diameter  $D = 13.4\mu\text{m}$  with one leukocyte. Steady flow shown in Fig. 7.14(b) is achieved by turning off the adhesive interactions. To represent inflammation-induced cell adhesion, we turn on the adhesive interaction between the leukocyte and the adhesive ligands with  $k_s = 1000$  at  $t = 0\text{s}$ . Due to the cell margination effect, the leukocyte touches with the tube wall at  $t = 0.47\text{s}$  and shows stable adhesion as shown in Fig. 7.14(c). The adherent leukocyte decreases the effective tube diameter and the mean velocity drops from  $150\mu\text{m}$  to  $45\mu\text{m}$  during this stage. Finally, to represent the stimulated inflammation state in clinical (induced by various cytokine), we further turn on the sickle cell-leukocyte interaction defined by Eq. (7.5) at  $t = 1.47\text{s}$ . Multiple sickle cells get trapped on the adherent leukocyte as shown in Fig. 7.14(d). This results in the further decrease of the flow rate. Full occlusion state is achieved at  $t \approx 2.2\text{s}$ .

Finally, we note that for venular flow, multiple leukocytes may accumulate at the inflammation activated region, which may also result in vaso-occlusion. Here

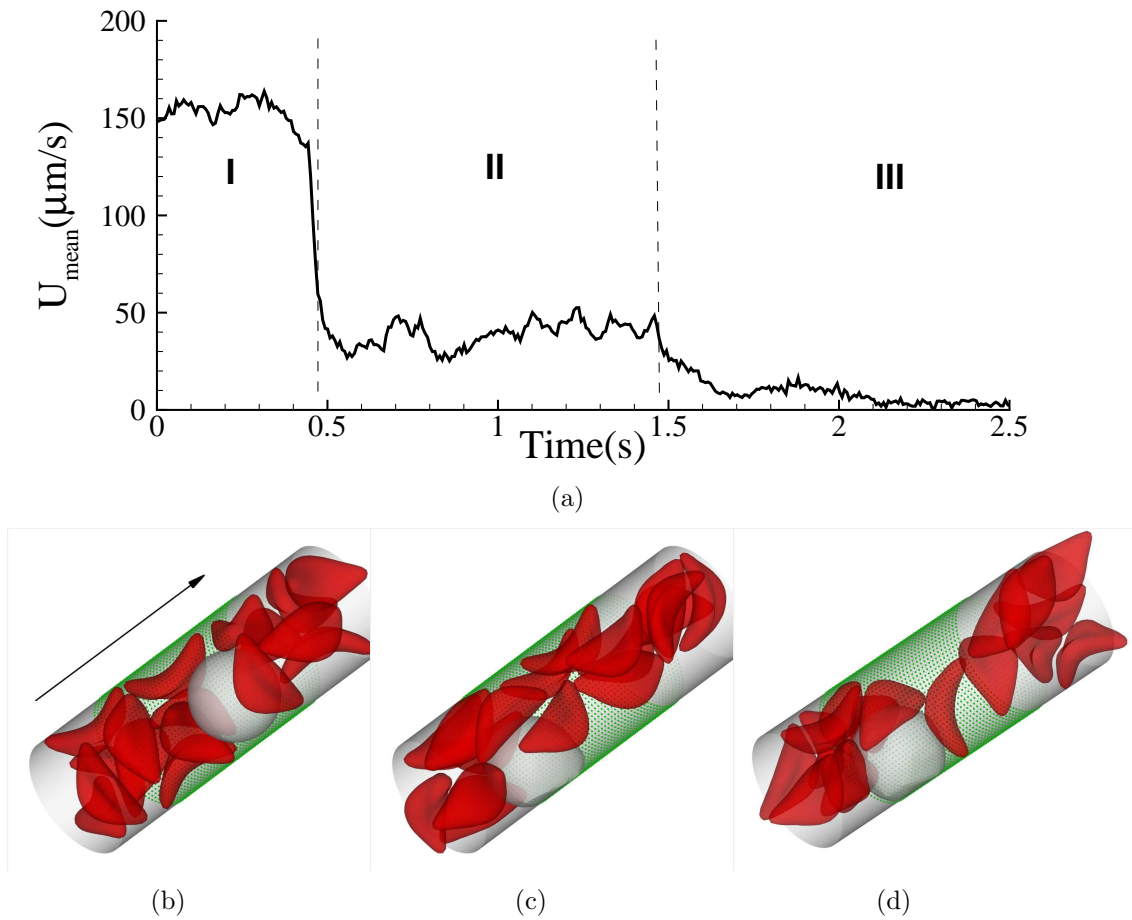


Figure 7.14: (a) Instantaneous mean velocity of the blood flow in a cylinder tube of  $D = 13.4\mu\text{m}$  with one leukocyte. (b-d) represent the blood cells in free motion, firm adhesion and flow occlusion states, respectively.

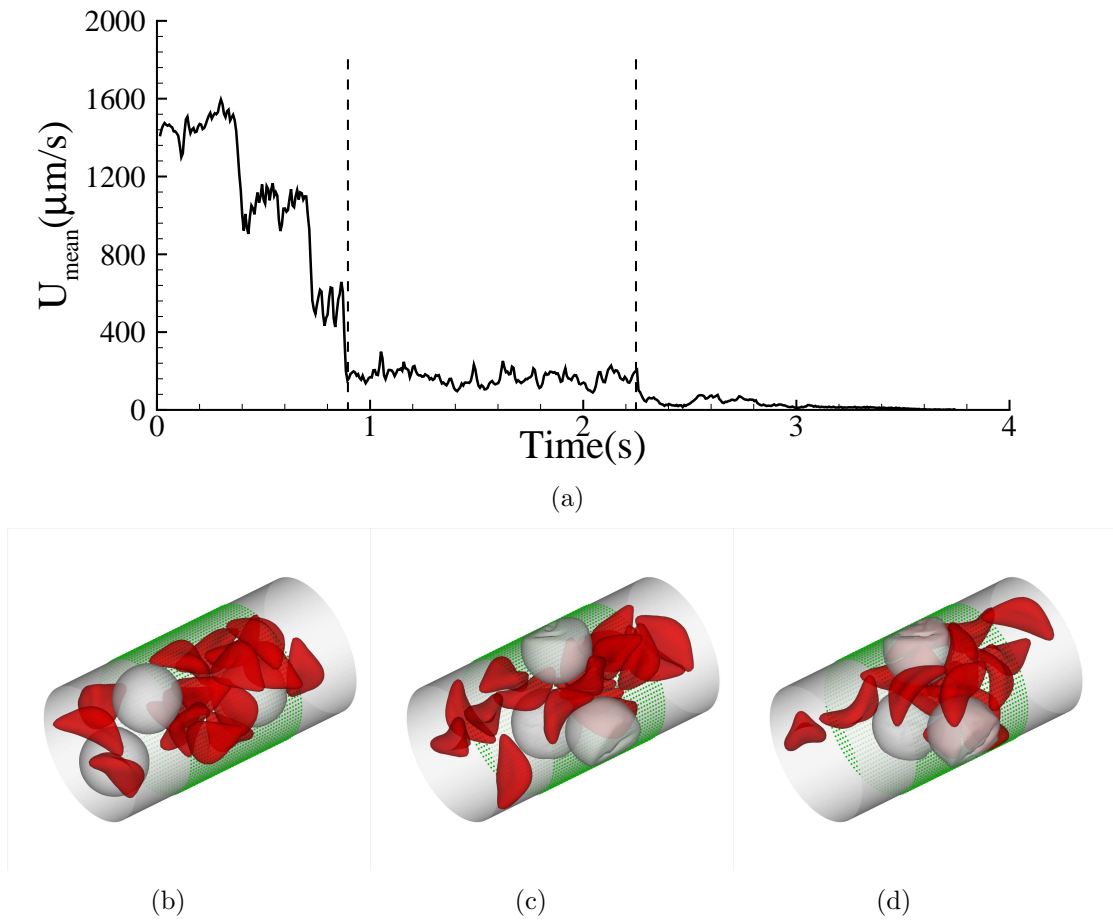


Figure 7.15: (a) Instantaneous mean velocity of the blood flow in a cylinder tube of  $D = 20.2\mu\text{m}$  with three leukocytes. (b-d) represent the blood cells in free motion, firm adhesion and flow occlusion states, respectively.

we consider a blood flow with diameter  $D = 20.2\mu m$  with multiple leukocytes as shown in Fig. 7.15. Starting from the steady flow at  $t = 0s$ , we turn on the adhesive interaction between the leukocytes and the ligands coated on the tube wall. In physiological aspect, this refers to the inflammation state (stimulated by cytokine such as TNF- $\alpha$ ). The blood flow can be roughly divided into three stages. During the first stage, the leukocytes adhere to the tube wall, resulting in the decrease of flow rate at  $t = 0.40, 0.71, 0.88s$ . During the second stage, the blood flow shows sluggish characteristics due to the adherent leukocytes. The mean flow velocity drops to  $162\mu m/s$ . At the end of the second stage, we further turn on the interaction between the leukocytes and the sickle red blood cells. This results in the further entrapment of the sickle red blood cells in the inflammation region and vaso-occlusion at  $t \approx 3.2s$ . Therefore, for vaso-occlusion induced by leukocytes, the key mechanism is the recruitment of adherent leukocytes. In a blood vessel deficient of the inflammation activated endothelium, vaso-occlusion can be successfully protected.

## 7.4 Summary

In this chapter, we employed a validated multi-scale model of sickle red blood developed in Chap. 5 to investigate the adhesive dynamics of individual cells as well as the abnormal hemodynamics of sickle blood flow in a cylinder tube. Under the same shear flow conditions, the sickle cells of different density groups exhibit different dynamic behaviors (firm adhesion, flipping movement, free motion, *etc.*), which is consistent with the experimental observations reported in Ref. [12, 114]. The different cell contact area and adhesive force measured from the static incubation and *quasi-static* detachment simulations illustrate that the cell adhesion is further influenced by both the cell morphology and membrane rigidity. The SS2 cell group, due to its high deformability characteristics, is the most adhesive cell group while the ISC group, due to the high membrane rigidity and peculiar elongated cell shape,

is the least adhesive cell group.

With regards to the abnormal hemodynamics of sickle blood suspension, the simulation results agree well with experimental measurements conducted in isolated vasculatures . The dynamic responses obtained from the different cell suspensions reveal that the SS2 cells and ISCs contribute differently to the vaso-occlusion process. The specific cell patterns (ISCs trapped by adherent SS2 cells) observed in the occlusion region indicate that the SS2 cells are the major cell group that initializes the cell adhesion in the post-capillaries, while the ISCs are the major cell group that induces the secondary cell entrapment in the adhesive regions. Sensitivity studies on the tube size and hematocrit value reveal that the blood flow rate and the venule diameter can further influence the pre-condition for the vaso-occlusion crisis. Given the typical physiological conditions of blood flow in post-capillaries, the present simulations suggest that most of the vaso-occlusion events occur in venules with diameter smaller than  $12\mu m$ . This result is also consistent with the experimental observation [83] that the blood occlusion sites concentrate in post-capillaries with diameter between 7 and  $10\mu m$ . ( $H_t = 30\%$  is adopted in that experiment.) For blood flow with larger vessel diameter, the present work validates that the adherent leukocytes may also results in vaso-occlusion crisis in venular flow by introducing the adhesive interaction between the leukocytes and the sickle red blood cells.

While the present work provides reasonable explanations for the heterogeneous cell adhesion and consistent simulation results with the experimental observation, we are cautious to claim that the present model can capture the whole features of the abnormal hemodynamics of the sickle blood flow. We note that the *in vivo* blood occlusion is a complex process involving the interplay of multiple physiological factors; several physical conditions simplified in the present work can potentially contribute to the abnormal hemodynamics. First, the proportion of the SS2 and SS4 cells is kept as a constant ratio (1:1) in the present work. However, different cell proportion may further influence the local cell entrapment in the microcirculation.

In this sense, the threshold value  $D = 12\mu m$  obtained from the present work should not be treated as the criterion of the vaso-occlusion in post-capillaries. Second, we assume that both the SS2 and the ISC cell membranes express the same “effective” protein receptors. However, the cell-endothelium interaction is actually composed of multiple ligand-receptor interactions. Further investigation is needed to identify the individual ligand-receptor interaction and the contribution to the cell adhesion among the different cell density groups. Third, we note that the rigid SS4 cells can contribute to the vaso-occlusion through two pathways. Although most of the occlusion events concentrate in the post-capillaries as an interplay of the SS2 and SS4 cell groups, a single SS4 cell may also contribute to vaso-occlusion by blocking the blood flow at the pre-capillary sites, which exhibits stochastic behavior and the occurrence can not be predicted in a given microvascular environment, as suggested by Kaul *et al.* [83, 84, 102]. Finally, we note that the blood occlusion is a dynamic process where the local oxygen saturation may further influence the blood flow circulation. This results in a dilemma competition between the extreme conditions of local cell concentration. On one hand, high local  $H_t$  can provide high oxygen saturation environment and prevent the cell sickling process. However, it results in lower blood flow rate which favors the cell adhesion process. On the other hand, the lower local  $H_t$  may facilitate the local blood flow circulation. However, the hypoxia condition may cause more cells involving in the “deoxygenation-sickling” process, as suggested by Kaul *et al.* [13]. Systematic investigation of these effects may further facilitate our understanding on this abnormal hematological disorder.

With regards to the therapeutic treatments, the present work suggests that vaso-occlusion, the major cause of clinical morbidity, is triggered by the adhesion of the deformable SS2 cells and propagated by the selective secondary entrapment of the rigid SS4 cells. While the present medical treatment by hydroxyurea can effectively prolong the delay time of cell sickling procedure, medical treatment on the target and blockage of the other procedures such as the vessel endothelium activation and cell-

endothelium adhesion may provide new paradigms on the treatment of this disease, which requires further experimental and numerical investigation.

# Chapter 8

## Summary and Perspective

### 8.1 Concluding remarks

In this dissertation, we have achieved the following goals:

- By constructing a coarse-grained particle system directly from the atomistic system governed by Lennard-Jones potential, we demonstrated that the Dissipative Particle Dynamics is originated from a further simplification of the Mori-Zwanzig theory applied to the coarse-grained molecular dynamics (MD). The dissipative and random forces appear naturally if the coarse-grained force field is approximated by the pairwise decomposition. When the many-body effect is not pronounced (e.g., low density, smaller cluster state), the pairwise DPD force terms provide a good approximation of the atomistic interactions, and the structural and dynamic properties of the atomistic systems can be successfully reproduced from the coarse-grained system.

- We demonstrated that the no-slip boundary condition in DPD fluid can be achieved by imposing an effective dissipative force on the DPD particles adjacent to the bounded wall, where the freezing wall particle discussed in Ref. [127] can be removed. We also developed an adaptive method that allows to target the prescribed outflow rate for open fluid systems. This method is examined in bifurcated flow where

different flow rate is prescribed on each outlet. The DPD simulation results agree well with the numerical results by Navier-Stokes Equation.

- We explored the fidelity of the continuum approximation for blood flow systems on mesoscopic level. By analyzing the simulation results of the blood flow in different tube size, we identify a non-continuum to continuum transition as the tube diameter increases to above  $100\mu m$ .

- We constructed a multi-scale model of the sickle red blood cell to represent different sickle cell morphologies based on a simulated annealing procedure and experimental observations. Cell distortion is quantified by the asphericity and the elliptical shape factors and agree with the medical image analysis. This model is examined in both homogeneous shear flow and tube flow systems. The shear viscosity and flow resistance obtained from the present work show reasonable agreement with the experimental measurements. The transition from shear-thinning to shear-independent flow reveals the profound effect of the cell membrane stiffening during deoxygenation.

- We developed a coarse-grained (CG) stochastic model to represent the growth of the intracellular aligned hemoglobin polymer domain. The CG model is calibrated based on the mechanical properties (Young's modulus, bending rigidity) of the sickle hemoglobin fibers reported in experiments. The process of the cell membrane transition is simulated for physiologic aligned hemoglobin polymer configurations and mean corpuscular hemoglobin concentration. Typical SS-RBC morphologies observed in experiments can be obtained from this model as a result of the intracellular aligned hemoglobin polymer development without introducing any further *ad hoc* assumptions.

- We examined the effect of the cell-endothelium interaction on the abnormal hemodynamics of the sickle blood suspensions. The heterogeneous sickle cell groups exhibit different adhesive dynamics due to the various cell morphologies and membrane rigidities. We demonstrated that the typical SS2 and SS4 cell groups contribute

differently to the vaso-occlusion crisis. This result explains the specific cell patterns widely observed at the occluded sites (SS4 cells trapped by adherent SS2 cells) as reported by *in vivo* and *ex vivo* experiments.

## 8.2 Future research

We conclude this thesis by providing some areas of future research which follow from some of the work presented herein.

- Systematic investigation of the many-body effect in the coarse-graining procedure. Construct more sophisticated coarse-grained force fields to incorporate the “many-body” information that lead to a more accurate prediction of the structural and dynamic properties of the atomistic system.
- Develop the outflow boundary method for complex fluid systems such blood suspensions.
- Develop proper models for the sickle hemoglobin (HbS) molecule/solution to capture the HbS polymerization process. This work may provide new insight to the polymerization kinetics and quantify the physical conditions that control the homogeneous/heterogeneous nucleation, polymer growth rate and final configuration of the polymer domain.
- Numerical simulation of diffusion of chemicals (e.g., hydroxyurea, decitibine, erythropoietin) to quantify the therapeutic effects of drug treatments on the micro-circulation of the sickle blood flow.
- Modeling of other types of disease cells such as HIV and diabetic red blood cell.

# Bibliography

- [1] <http://www.ncbi.nlm.nih.gov/pubmedhealth/PMH0001554/>.
- [2] M. Abkarian, M. Faivre, and A. Viallat. Swinging of red blood cells under shear flow. *Physical Review Letters*, 98:188302, 2007.
- [3] R. L. C. Akkermans and W. J. Briels. Coarse-grained dynamics of one chain in a polymer melt. *J. Chem. Phys.*, 113(15):6409–6422, 2000.
- [4] R. L. C. Akkermans and W. J. Briels. Coarse-grained interactions in polymer melts: A variational approach. *J. Chem. Phys.*, 115(13):6210–6219, 2001.
- [5] R. L. C. Akkermans and W. J. Briels. A structure-based coarse-grained model for polymer melts. *J. Chem. Phys.*, 114(2):1020–1031, 2001.
- [6] M. P. Allen and D. J. Tildsley. *Computer Simulation of Liquids*. Clarendon Press, Oxford, 1987.
- [7] M. Antia, T. Herricks, and P. K. Rathod. Microfluidic modeling of cell-cell interactions in malaria pathogenesis. *PLoS Pathogens*, 3(7):939–945, 2007.
- [8] A. Aprelev, Z Liu, and F. A. Ferrone. The growth of sickle hemoglobin polymers. *Biophysical Journal*, 101:885–891, 2011.
- [9] T. Asakura, J. A. Mattiello, K. Obata, K. Asakura, M. P. Reilly, N. Tomassini, E. Schwartz, and K. Ohene-Frempong. Partially oxygenated sickle cells: Sickle-

shaped red cells found in circulating blood of patients with sickle cell disease. *Proceedings of the National Academy of Sciences*, 91:12589–12593, 1994.

- [10] J. A. Backer, C. P. Lowe, H. C. J. Hoefsloot, and P. D. Iedema. Poiseuille flow to measure the viscosity of particle model fluids. *J. Chem. Phys.*, 122(15):6, 2005.
- [11] S. K. Ballas, J. Larner, E. D. Smith, S. Surrey, E. Schwartz, and E. F. Rappaport. Rheologic predictors of the severity of the painful sickle cell crisis. *Blood*, 72:1216–1223, 1988.
- [12] G. A. Barabino, L. V. McIntire, S. G. Eskin, D. A. Sears, and M. Udden. Endothelial cell interactions with sickle cells, sickle cell, sickle trait, mechanically injured, and normal erythrocytes under controlled flow. *Blood*, 70:152–157, 1987.
- [13] G. A. Barabino, M. O. Platt, and D. K. Kaul. Sickle cell biomechanics. *Annu. Rev. Biomed. Eng.*, 12:345–367, 2010.
- [14] Barber, J. and Alberding, J. and Restrepo, J. and Secomb, T. Simulated two-dimensional red blood cell motion, deformation, and partitioning in microvessel bifurcations. *Ann. Biomed. Engin.*, 36:1690–1698, 2008.
- [15] A. D. Becke. Density-functional thermochemistry. iii. the role of exact exchange. *Journal of Chemical Physics*, 98(7):5648–5652, 1993.
- [16] E. S. Boek, P. V. Coveney, H. N. W. Lekkerkerker, and P. van der Schoot. Simulating the rheology of dense colloidal suspensions using dissipative particle dynamics. *Phys. Rev. E*, 55(3):3124–3133, 1997.
- [17] M. M. Brandao, A. Fontes, M. L. Barjas-Castro, L. C. Barbosa, F. F. Costa, C. L. Cesar, and S. T. O. Saad. Optical tweezers for measuring red blood cell

- elasticity: application to the study of drug reponse in sickle cell disease. *Eur J. Haematol*, 70:207–211, 2003.
- [18] R. W. Briehl. Nucleation, fiber growth and melting and domain formation and structure in sickle cell hemoglobin gels. *Journal of Molecular Biology*, 245:710–723, 1995.
- [19] W. J. Briels and R. L. C. Akkermans. Representation of coarse-grained potentials for polymer simulations. *Mol. Simulat.*, 28(1-2):145–152, 2002.
- [20] K. C. Chang, D. F. J. Tees, and D. A. Hammer. The state diagram for cell adhesion under flow: Leukocyte rolling and firm adhesion. *Proceedings of the National Academy of Sciences*, 97:11262–11267, 2000.
- [21] E. Y. Chiang and P. S. Frenette. Sickle cell vaso-occlusion. *Hematology/Oncology Clinics of North America*, 19:771–784, 2005.
- [22] S. Chien, S. Usami, H.M. Taylor, J. L. Lundberg, and M. I. Gregersen. Effects of hematocrit and plasma proteins on human blood rheology at low shear rates. *Journal of Applied Physiology*, 21:81–87, 1966.
- [23] G. W. Christoph, J. Hofrichter, and W. A. Eaton. Understanding the shape of sickled red cells. *Biophysical Journal*, 88(2):1371–1376, 2005.
- [24] J. D. Corbett, W. E. Mickols, and M. F. Maestre. Effect of hemoglobin concentration on nucleation and polymer formation in sickled red blood cells. *J. Biol. Chem.*, 270:2708–2715, 1995.
- [25] D. R. Daniels, D. Marenduzzo, and M. S. Turner. Stall, spiculate, or run away: The fate of fibers growing towards fluctuating membranes. *Phys. Rev. Lett.*, 97:098101, 2006.

- [26] D. R. Daniels and M. S. Turner. The force generated by biological membranes on a polymer rod and its response: Statics and dynamics. *Journal of Chemical Physics*, 121:7401–7407, 2004.
- [27] M. Dao, J. Li, and S. Suresh. Molecularly based analysis of deformation of spectrin network and human erythrocyte. *Materials Science and Engineering C*, 26:1232–1244, 2006.
- [28] R. Delgado-Buscalioni and P.V. Coveney. USHER: an algorithm for particle insertion in dense fluid. *J. Chem. Phys.*, 119(2):978987, 2003.
- [29] D. E. Discher, D. H. Boal, and S. K. Boey. Simulations of the erythrocyte cytoskeleton at large deformation. II. Micropipette aspiration. *Biophysical Journal*, 75(3):1584–1597, 1998.
- [30] C. Dong, R. S. Chardwick, and A. N. Schechter. Influence of sickle hemoglobin polymerization and membrane properties on deformability of sickle erythrocytes in the microcirculation. *Biophysical Journal*, 63:774–783, 1992.
- [31] Q. Dou and F. A. Ferrone. Simulated formation of polymer domains in sickle hemoglobin. *Biophysical Journal*, 65:2068–2077, 1993.
- [32] B. Dunweg. Molecular dynamics algorithms and hydrodynamic screening. *J. Chem. Phys.*, 99(9):6977–6982, 1993.
- [33] M. M. Dupin, I. Halliday, C. M. Care, and L. L. Munn. Lattice boltzmann modelling of blood cell dynamics. *International Journal of Computational Fluid Dynamics*, 22(7):481–492, 2008.
- [34] D. M. Eckmann, S. Bowers, M. Stecker, and A. T. Cheung. Hematocrit, volume expander, temperature, and shear rate effects on blood viscosity. *Anesthesia & Analgesia*, 91:539–545, 2000.

- [35] A. Eriksson, M. N. Jacobi, J. Nystrom, and K. Tunstrom. Using force covariance to derive effective stochastic interactions in dissipative particle dynamics. *Phys. Rev. E*, 77(1):016707, 2008.
- [36] Pep Español. Hydrodynamics from dissipative particle dynamics. *Phys. Rev. E*, 52(2):1734–1742, 1995.
- [37] P. Espanol. Dissipative particle dynamics for a harmonic chain: A first-principles derivation. *Phys. Rev. E*, 53(2):1572–1578, 1996.
- [38] P. Espanol. Fluid particle model. *Physical Review E*, 57(3):2930–2948, 1998.
- [39] P. Espanol, M. Serrano, and I. Zuniga. Coarse-graining of a fluid and its relation with dissipative particle dynamics and smoothed particle dynamics. *Int. J. Mod. Phys. C*, 8:899–908, 1997.
- [40] P. Espanol and P. Warren. Statistical mechanics of dissipative particle dynamics. *Europhysics Letters*, 30(4):191–196, 1995.
- [41] E. Evans, N. Mohandas, and A. Leung. Static and dynamic rigidities of normal and sickle erythrocytes. major influence of cell hemoglobin concentration. *The Journal of Clinical Investigation*, 73:477–488, 1984.
- [42] E. A. Evans and R. Skalak. *Mechanics and thermodynamics of biomembranes*. CRC Press, Inc., Boca Raton, Florida, 1980.
- [43] X. Fan, N. Phan-Thien, S. Chen, X. Wu, and T. Y. Ng. Simulating flow of DNA suspension using dissipative particle dynamics. *Phys. Fluids*, 18(6):063102, 2006.
- [44] D. A. Fedosov. *Multiscale modeling of blood flow and soft matter*. PhD thesis, Brown University, USA, 2010.

- [45] D. A. Fedosov, B. Caswell, and G. E. Karniadakis. Dissipative particle dynamics simulation of depletion layer and polymer migration in micro- and nanochannels for dilute polymer solutions. *J. Chem. Phys.*, 128(14):144903, 2008.
- [46] D. A. Fedosov, B. Caswell, and G. E. Karniadakis. A multiscale red blood cell model with accurate mechanics, rheology, and dynamics. *Biophysical Journal*, 98(10):2215–2225, 2010.
- [47] D. A. Fedosov, B. Caswell, and G. E. Karniadakis. Wall shear stress-based model for adhesive dynamics of red blood cells in malaria. *Biophysical Journal*, 100(9):2084–2093, 2011.
- [48] D. A. Fedosov, B. Caswell, A. S. Popel, and G. E. Karniadakis. Blood flow and cell-free layer in microvessels. *Microcirculation*, 17:615–628, 2010.
- [49] D. A. Fedosov and G. E. Karniadakis. Triple-decker: Interfacing atomistic-mesososcopic-continuum flow regimes. *J. Comp. Phys.*, 228(4):1157 – 1171, 2009.
- [50] D. A. Fedosov, W Pan, B. Caswell, G. Gompper, and G. E. Karniadakis. Predicting human blood viscosity in silico. *Proceedings of the National Academy of Sciences*, 108(29):11772–11777, 2011.
- [51] F. A. Ferrone, J. Hofrichter, and W. A. Eaton. Kinetics of sickle hemoglobin polymerization : I. studies using temperature-jump and laser photolysis techniques. *Journal of Molecular Biology*, 183(4):591 – 610, 1985.
- [52] F. A. Ferrone, J. Hofrichter, and W. A. Eaton. Kinetics of sickle hemoglobin polymerization : Ii. a double nucleation mechanism. *Journal of Molecular Biology*, 183(4):611 – 631, 1985.
- [53] E. G. Flekkøy and P. V. Coveney. From molecular dynamics to dissipative particle dynamics. *Phys. Rev. Lett.*, 83(9):1775–1778, 1999.

- [54] J. B. Freund and M. M. Oresanin. Cellular flow in a small blood vessel. *Journal of Fluid Mechanics*, 671:466–490, 2011.
- [55] R. M. Fuchslin, H. Fellermann, A. Eriksson, and Hans-Joachim Ziock. Coarse graining and scaling in dissipative particle dynamics. *J. Chem. Phys.*, 130(21):214102, 2009.
- [56] H. Fukunaga, J. Takimoto, and M. Doi. A coarse-graining procedure for flexible polymer chains with bonded and nonbonded interactions. *J. Chem. Phys.*, 116(18):8183–8190, 2002.
- [57] O. Galkin and P. G. Vekilov. Mechanisms of homogeneous nucleation of polymers of sickle cell anemia hemoglobin in deoxy state. *Journal of Molecular Biology*, 336:43–59, 2004.
- [58] R. A. Gingold and J. J. Monaghan. Smoothed particle hydrodynamics - theory and application to non-spherical stars. *Mon. Not. R. Astro. Soc.*, 181(2):375–389, 1977.
- [59] L. Grinberg and G. E. Karniadakis. Outflow boundary conditions for arterial networks with multiple outlets. *Ann. Biomed. Engin.*, 36:1496–1514, 2008.
- [60] R. D. Groot and P. B. Warren. Dissipative particle dynamics: Bridging the gap between atomistic and mesoscopic simulation. *J. Chem. Phys.*, 107(11):4423–4435, 1997.
- [61] R. D. Groot and P. B. Warren. Dissipative particle dynamics: Bridging the gap between atomistic and mesoscopic simulation. *Journal of Chemical Physics*, 107(11):4423–4435, 1997.
- [62] D. A. Hammer and S. M. Apte. Simulation of cell rolling and adhesion on surfaces in shear flow: general results and analysis of selectin-mediated neutrophil adhesion. *Biophysical Journal*, 63:35–57, 1992.

- [63] V. A. Harmandaris, N. P. Adhikari, N. F. A. van der Vegt, and K. Kremer. Hierarchical modeling of polystyrene: From atomistic to coarse-grained simulations. *Macromolecules*, 39(19):6708–6719, 2006.
- [64] R. P. Hebbel. Adhesion of sickle red cells to endothelium: Myths and future directions. *Transfusion Clinique et Biologique*, 15:14–18, 2008.
- [65] R. P. Hebbel, O. Yamada, C. F. Moldow, H. S. Jacob, J. G. White, and J. W. Eaton. Abnormal adherence of sickle erythrocytes to cultured vascular endothelium: possible mechanism for microvascular occlusion in sickle cell disease. *Journal of Clinical Investigation*, 65:154–160, 1980.
- [66] W. Helfrich. Elastic properties of lipid bilayers: theory and possible experiments. *Z. Naturforschung C*, 28:693–703, 1973.
- [67] J. B. Herrick. Peculiar elongated sickle-shaped red blood corpuscles in a case of severe anemia. *Arch. Intern. Med.*, 6:517–521, 1910.
- [68] T. Hidenori, Shoken M. M., and Minoru S. Numerical simulation of viscous flow by smoothed particle hydrodynamics. *Prog. Theor. Phys.*, 95:939–960, 1994.
- [69] J. M. Higgins, D. T. Eddington, S. N. Bhatia, and L. Mahadevan. Sickle cell vasoocclusion and rescue in a microfluidic device. *Proceedings of the National Academy of Sciences*, 104(51):20496–20500, 2007.
- [70] P. Hohenberg and W. Kohn. Inhomogeneous electron gas. *Physical Review*, 136:B864–B871, 1964.
- [71] P. J. Hoogerbrugge and J. M. V. A. Koelman. Simulating microscopic hydrodynamic phenomena with dissipative particle dynamics. *Europhysics Letters*, 19(3):155–160, 1992.

- [72] R. Hoover, R. Rubin, G. Wise, and R. Warren. Adhesion of normal and sickle erythrocytes to endothelial monolayer cultures. *Blood*, 54:872–876, 1979.
- [73] K. Horiuchi, J. Ohatak, Y. Hirano, and T. Asakura. Morphologic studies of sickle erythrocytes by image analysis. *J. Lab. Clin. Med.*, 115:613, 1990.
- [74] C. Hupert and M. Baumann. Local membrane curvature affects spontaneous membrane fluctuation characteristics. *Molecular membrane Biology*, 20:155–162, 2003.
- [75] V. M. Ingram. Abnormal human haemoglobins. i. the camparison of normal human and sickle-cell haemoglobins by fingerprinting. *Biochim. Biophys. Acta.*, 28:539–545, 1958.
- [76] T. Itoh, S. Chien, and S. Usami. Effects of hemoglobin concentration on deformability of individual sickle cells after deoxygenation. *Blood*, 85:2245–2253, 1995.
- [77] M. Ivanova, R. Jasuja, S. Kwong, R. W. Briehl, and F. A. Ferrone. Nonideality and the nucleation of sickle hemoglobin. *Biophysical Journal*, 79:1016–1022, 2000.
- [78] C. Junghans, M. Praprotnik, and K. Kremer. Transport properties controlled by a thermostat: An extended dissipative particle dynamics thermostat. *Soft Matter*, 4(1):156–161, 2008.
- [79] G. E. Karniadakis and S. J. Sherwin. *Spectral/hp element methods for CFD*. Oxford University Press, Oxford, 2005.
- [80] D. K. Kaul, D. Chen, and J. Zhan. Adhesion of sickle cells to vascular endothelium is critically dependent on changes in density and shape of the cells. *Blood*, 83:3006–3017, 1994.

- [81] D. K. Kaul and M. E. Fabry. In *in vivo* studies of sickle red blood cells. *Microcirculation*, 11:153–165, 2004.
- [82] D. K. Kaul, M. E. Fabry, and R. L. Nagel. Erythrocytic and vascular factors influencing the microcirculatory behavior of blood in sickle cell anemia. *Ann. NY. Acad. Sci.*, 565:316–326, 1989.
- [83] D. K. Kaul, M. E. Fabry, and R. L. Nagel. Microvascular sites and characteristics of sickle cell adhesion to vascular endothelium in shear flow conditions: Pathophysiological implications. *Proceedings of the National Academy of Sciences*, 86:3356–3360, 1989.
- [84] D. K. Kaul, M. E. Fabry, P. Windisch, S. Baez, and R. L. Nagel. Erythrocytes in sickle-cell-anemia are heterogeneous in their rheological and hemodynamic characteristics. *Journal of Clinical Investigation*, 72(1):22–31, 1983.
- [85] D. K. Kaul and R. P. Hebbel. Hypoxia/reoxygenation causes inflammatory response in transgenic sickle mice but not in normal mice. *Journal of Clinical Investigation*, 106:411–420, 2000.
- [86] D. K. Kaul and X. Liu. Rate of deoxygenation modulates rheologic behavior of sickle red blood cells at a given mean corpuscular hemoglobin concentration. *Clinical Hemorheology and Microcirculation*, 21:125–135, 1999.
- [87] D. K. Kaul and H. Xue. Rate of deoxygenation and rheologic behavior of blood in sickle cell anemia. *Blood*, 77:1353–1361, 1991.
- [88] E. E. Keaveny, I. V. Pivkin, M. R. Maxey, and G. E. Karniadakis. A comparative study between dissipative particle dynamics and molecular dynamics for simple and complex-geometry flows. *The Journal of chemical physics*, 123(10):104107, 2005.

- [89] T. Kinjo and S. Hyodo. Linkage between atomistic and mesoscale coarse-grained simulation. *Mol. Simulat.*, 33(4-5):417–420, 2007.
- [90] T. Kinjo and S. A. Hyodo. Equation of motion for coarse-grained simulation based on microscopic description. *Phys. Rev. E*, 75(5):051109, 2007.
- [91] S. H. L. Klapp, D. J. Diestler, and M. Schoen. Why are effective potentials “soft”? *J. Phys-Condens. Mat.*, 16(41):7331–7352, 2004.
- [92] W. Kohn and L. J. Sham. Self-consistent equations including exchange and correlation effects. *Physical Review*, 140:A1133–A1138, 1965.
- [93] K. Kremer, G. S. Grest, and I. Carmesin. Crossover from Rouse to reptation dynamics: A molecular-dynamics simulation. *Phys. Rev. Lett.*, 61(5):566, 1988.
- [94] P. L. LaCelle. Oxygen delivery to muscle cells during capillary vascular occlusion by sickle erythrocytes. *Blood Cells*, 3:263–272, 1977.
- [95] F. Lahmar and B. Rousseau. Influence of the adjustable parameters of the DPD on the global and local dynamics of a polymer melt. *Polymer*, 48(12):3584–3592, 2007.
- [96] A. W. Lees and S. F. Edwards. The computer study of transport processes under extreme conditions. *Journal of Physics C*, 5:1921–1928, 1972.
- [97] H. Lei, B. Caswell, and G. E. Karniadakis. Direct construction of mesoscopic models from microscopic simulations. *Phys. Rev. E*, 81:026704, 2010.
- [98] H. Lei and G. E. Karnidakis. Quantifying the rheological and hemodynamic characteristics of sickle cell anemia. *Biophysical Journal*, 102:185–194, 2012.
- [99] H. Li and G. Lykotrafitis. A coarse-grain molecular dynamics model for sickle hemoglobin fibers. *Journal of Mechanical Behavior of Biomedical Materials*, 4:162–173, 2011.

- [100] Z. Li and E. E. Dormidontova. Equilibrium chain exchange kinetics in block copolymer micelle solutions by dissipative particle dynamics simulations. *Soft Matter*, 7:4179–4188, 2011.
- [101] C. C. Liew and M. Mikami. A coarse-grained model for particle dynamics simulations of complex fluids. *Chem. Phys. Lett.*, 368(3-4):346–351, 2003.
- [102] H. H. Lipowsky, S. Usami, and S. Chien. Human ss red cell rheological behavior in the microcirculation of cremaster muscle. *Blood Cells*, 8:113, 1982.
- [103] S. Lomholt and M. R. Maxey. Force-coupling method for particulate two-phase flow : Stokes flow. *Journal of Computational Physics*, 184(2):381–405, 2003.
- [104] C. Loudon and A. Tordesillas. The use of the dimensionless womersley number to characterize the unsteady nature of internal flow. *J. Theor. Biol.*, 191(1):63–78, 1998.
- [105] A. A. Louis, P. G. Bolhuis, J. P. Hansen, and E. J. Meijer. Can polymer coils be modeled as “soft colloids”? *Phys. Rev. Lett.*, 85(12):2522–2525, 2000.
- [106] L. B. Lucy. Numerical approach to testing of fission hypothesis. *Astron. J.*, 82(12):1013–1024, 1977.
- [107] A. P. Lyubartsev and A. Laaksonen. Calculation of effective interaction potentials from radial distribution functions: A reverse Monte Carlo approach. *Phys. Rev. E*, 52(4):3730–3737, Oct 1995.
- [108] V. Marry and G. Ciccotti. Trotter derived algorithms for molecular dynamics with constraints: Velocity Verlet revisited. *J. Comput. Phys.*, 222(1):428–440, 2007.
- [109] M. Matsumoto, S. Saito, and I. Ohmine. Molecular dynamics simulation of the ice nucleation and growth process leading to water freezing. *Nature*, 416(6879):409–413, 2002.

- [110] M. R. Maxey and B. K. Patel. Localized force representations for particles sedimenting in stokes flow. *International Journal of Multiphas Flow*, 27:1603–1626, 2001.
- [111] E. W. Merrill, E. R. Gilliland, G. Cokelet, H. Shin, A. Britten, and R. E. Wells. Rheology of human blood, near and at zero flow: Effects of temperature and hematocrit level. *Biophysical Journal*, 3:199 – 213, 1963.
- [112] W. Mickols, M. F. Maestre, I. JR. Iinoco, and S. H. Embury. Visualization of oriented hemoglobin s in individual erythrocytes by differential extinction of polarized light. *Proceedings of the National Academy of Sciences*, 82:6527–6531, 1985.
- [113] J. P. Mills, L. Qie, C. T. Lim, M. Dao, and S. Suresh. Nonlinear elastic and viscoelastic deformation of the human red blood cell with optical tweezers. *Mech Chem Biosyst*, 1(3):169–180, 2004.
- [114] N. Mohandas and E. Evans. Sickle erythrocyte adherence to vascular endothelium. *Journal of Clinical Investigation*, 76:1605–1612, 1985.
- [115] H. Mori. Transport, collective motion, and Brownian motion. *Prog. Theor. Phys*, 33:423, 1965.
- [116] M. A. Moyers-Gonzalez and R. G. Owens. Mathematical modelling of the cell-depleted peripheral layer in the steady flow of blood in a tube. *Biorheology*, 47:39–71, 2010.
- [117] J. T. Padding and W. J. Briels. Uncrossability constraints in mesoscopic polymer melt simulations: Non-Rouse behavior of  $C_{120}H_{242}$ . *J. Chem. Phys.*, 115(6):2846–2859, 2001.
- [118] W. Pan, B. Caswell, and G. E. Karniadakis. A low-dimensional model for the red blood cell. *Soft Matter*, 6:4366–4376, 2010.

- [119] W. Pan, B. Caswell, and G. E. Karniadakis. Rheology, microstructure and migration in brownian colloidal suspensions. *Langmuir*, 26(1):133–142, 2010.
- [120] W. Pan, I. V. Pivkin, and G. E. Karniadakis. Single-particle hydrodynamics in dpd: A new formulation. *Europhys. Lett.*, 84(1):10012, 2008.
- [121] R. Panton. *Incompressible Flow*. John Wiley & Sons, Inc., New York, 1996.
- [122] C. Pastorino, T. Kreer, M. Muller, and K. Binder. Comparison of dissipative particle dynamics and langevin thermostats for out-of-equilibrium simulations of polymeric systems. *Phys. Rev. E*, 76(2):026706, 2007.
- [123] L. Pauling, H. A. Itano, S. J. Singer, and I. C. Wells. Sickle cell anemia, a molecular disease. *Science*, 110:543–548, 1949.
- [124] C. S. Peskin, G. M. Odell, and G. F. Oster. Cellular motions and thermal fluctuations: the brownian ratchet. *Biophysical Journal*, 65:316–324, 1993.
- [125] I. V. Pivkin and G. E. Karniadakis. Accurate coarse-grained modeling of red blood cells. *Physical Review Letters*, 101(11):118105, 2008.
- [126] I. V. Pivkin and George Em Karniadakis. A new method to impose no-slip boundary conditions in dissipative particle dynamics. *J. Comp. Phys.*, 207(1):114 – 128, 2005.
- [127] I. V. Pivkin and George Em Karniadakis. Controlling density fluctuations in wall-bounded dissipative particle dynamics systems. *Phys. Rev. Lett.*, 96(20):206001, 2006.
- [128] I. V. Pivkin and George Em Karniadakis. Accurate coarse-grained modeling of red blood cells. *Phys. Rev. Lett.*, 101(11):118105, 2008.
- [129] I. V. Pivkin, Peter D. Richardson, and George E. Karniadakis. Effect of red blood cells on platelet aggregation. *Engin. Med. Biol. Magazine, IEEE*, 28(2):32 –37, march-april 2009.

- [130] M. Revenga, I. Zuniga, and P. Espanol. Boundary model in DPD. *J. Mod. Phys. C*, 9(1):1319, 1998.
- [131] M. Revenga, I. Zuniga, and P. Espanol. Boundary conditions in dissipative particle dynamics. *Comp. Phys. Comm.*, 121-122(1):309–311, 1999.
- [132] R. E. Samuel, E. D. Salmon, and R. W. Briehl. Nucleation and growth of fibers and gel formation in sickle cell haemoglobin. *Nature*, 345:833–835, 1990.
- [133] R. E. Samuel, E. D. Salmon, and R. W. Briehl. Nucleation and growth of fibres and gel formation in sickle cell haemoglobin. *Nature*, 345:833–835, 1990.
- [134] I. H. Sarelius and B. R. Duling. Direct measurement of microvessel hematocrit, red cell flux, velocity and transit time. *Am. J. Physiol*, 243:H1018–H1026, 1982.
- [135] T. Schneider and E. Stoll. Molecular-dynamics study of a three-dimensional one-component model for distortive phase transitions. *Phys. Rev. B*, 17(3):1302, 1978.
- [136] M. Sharan and A. S. Popel. A two-phase model for flow of blood in narrow tubes with increased effective viscosity near the wall. *Biorheology*, 38:415–428, 2001.
- [137] J. P. Shelby, J. White, K. Ganesan, P. K. Rathod, and D. T. Chiu. A microfluidic model for single-cell capillary obstruction by *Plasmodium falciparum*-infected erythrocytes. *Proceedings of the National Academy of Sciences USA*, 100:14618–14622, 2003.
- [138] J. R. Silbermann, M. Schoen, and S. H. L. Klapp. Coarse-grained single-particle dynamics in two-dimensional solids and liquids. *Phys. Rev. E*, 78(1):011201, 2008.
- [139] R. Skalak, S. R. Keller, and T. W. Secomb. Mechanics of blood flow. *Journal of Biomechanical Engineering*, 103:102–115, 1981.

- [140] J. Smiatek, M.P. Allen, and F. Schid. Tunable-slip boundaries for coarse-grained simulations of fluid flow. *Europ. Phys. J. E: Soft Matter Biol. Phys.*, 26(1):115, 2008.
- [141] M. L. Smith, M. J. Smith, M. B. Lawrence, and K. Ley. Viscosity-independent velocity of neutrophils rolling on p-selectin *in vitro* or *in vivo*. *Microcirculation*, 9:523–536, 2002.
- [142] T. Soddemann, B. Dunweg, and K. Kremer. Dissipative particle dynamics: A useful thermostat for equilibrium and nonequilibrium molecular dynamics simulations. *Phys. Rev. E*, 68(4):046702, 2003.
- [143] A. K. Soper. Empirical potential Monte Carlo simulation of fluid structure. *Chem. Phys.*, 202(2-3):295 – 306, 1996.
- [144] N. A. Spenley. Scaling laws for polymers in dissipative particle dynamics. *Europhys. Lett.*, 49(4):534, 2000.
- [145] H. R Sunshine, J. Hofrichter, and W. A. Eaton. Requirements for therapeutic inhibition of sickle haemoglobin gelation. *Nature*, 275:238–240, 1978.
- [146] V. Symeonidis, G. E. Karniadakis, and B. Caswell. Dissipative particle dynamics simulations of polymer chains: Scaling laws and shearing response compared to DNA experiments. *Phys. Rev. Lett.*, 95(7):076001, 2005.
- [147] A. Turhan, L. A. Weiss, N. Mohanda, B. S. Coller, and P. S. Frenette. Primary role for adherent leukocytes in sickle cell vascular occlusion: A new paradigm. *Proceedings of the National Academy of Sciences*, 99:3047–3051, 2002.
- [148] S. Usami, S. Chien, P. M. Scholtz, and J. F. Bertles. Effects of deoxygenation on blood rheology in sickle cell disease. *Microvascular Research*, 9:324–334, 1975.

- [149] N. G. Vankampen and I. Oppenheim. Brownian-motion as a problem of eliminating fast variables. *Physica A*, 138(1-2):231–248, 1986.
- [150] J. G. Wang, M. S. Turner, G. Agarwal, S. Kwong, R. Jesepts, F. A. Ferrone, and R. W. Briehl. Micromechanics of isolated sickle cell hemoglobin fibers: bending moduli and persistence lengths. *Journal of Molecular Biology*, 315:601–612, 2002.
- [151] T. Werder, J. H. Walther, and P. Koumoutsakos. Hybrid atomistic-continuum method for the simulation of dense fluid flows. *J. Comp. Phys.*, 205(1):373 – 390, 2005.
- [152] S. M Willemsen, H. C. J. Hoefsloot, and P. D. Iedema. No-slip boundary conditions in dissipative particle dynamics. *J. Mod. Phys. C*, 11(5):881, 2000.
- [153] R. Zwanzig. Ensemble method in the theory of irreversibility. *J. Chem. Phys.*, 33:1338, 1960.